Characterization and optimization of microionization chambers

by

Jessica R. Miller

A dissertation submitted in partial fulfillment of
the requirements for the degree of

Doctor of Philosophy

(Medical Physics)

at the

University of Wisconsin-Madison

2013

Date of final oral examination: 11/27/13

This dissertation is approved by the following members of the Final Oral Committee:
Larry A. DeWerd, Professor, Medical Physics
Bruce R. Thomadson, Professor, Medical Physics
Michael W. Kissick, Professor, Medical Physics
Bryan P. Bednarz, Assistant Professor, Medical Physics
Douglass L. Henderson, Professor, Engineering Physics

To my parents, Pam and Gary Snow. My dad taught me to reach for the stars and my mom showed me a love that would endure any fall.

Abstract

An increase in the delivery of small and non-standard radiation fields has led to the development of small-volume ionization chambers (< 0.02 cm^3), called microchambers. Microchambers are used for dosimetry measurements in radiation therapy clinics around the world, and the University of Wisconsin Accredited Dosimetry Calibration Laboratory has experienced a significant increase in requests for the calibration of microchambers for low- and medium-energy x-ray beams as well as the ^{60}Co beam. This indicates that these chambers are being used for reference-dosimetry measurements in a wide range of therapy and imaging applications and beam energies.

Unfortunately, microchambers demonstrate a series of anomalous behaviors not seen in larger-volume chambers. In this work, a comprehensive characterization of five microchamber models was performed for a ^{60}Co beam, high-energy pulsed beams, and low- and medium-energy x-ray beams. In all cases a lower signal-to-noise ratio was measured for the microchambers compared to larger-volume chambers; however, for high-energy pulsed beams and often for the ^{60}Co beam, the leakage current comprised less than 0.1% of the chamber signal. For all beams investigated, the microchambers exhibited large voltage-independent and dependent polarity effects which caused an inverse proportionality between the chamber response and the applied voltage and anomalous ion recombination correction factors. Furthermore, the microchambers exhibited a strong energy dependence for kilovoltage x-ray beams relative to ^{60}Co. These anomalous behaviors varied from microchamber to

microchamber, even among the same chamber model; however, the behavior of an individual chamber was consistent.

A series of investigations were performed to determine the cause of these behaviors. The energy dependence was attributed to high-Z materials inside the collecting volume of the microchambers. The source of the voltage-dependent polarity effects was isolated to a potential difference between the collecting and guard electrodes, distorting the electric field lines and altering the collecting volume of the chamber. It was determined that a difference in the conductance of materials of the electrodes was likely causing the potential difference.

An optimized microchamber design was created and manufactured. The microchamber was composed of a low-Z conductive plastic to eliminate the energy dependence. Furthermore, the electrodes were composed of the same batch of plastic which was manufactured to reduce inhomogeneities in the conductance of the material. With the optimized design, the chamber demonstrated negligible energy dependence and a significant reduction in the voltage-dependent polarity effects.

Acknowledgments

It is impossible to express in a few short paragraphs the immense gratitude that I have for each and every person who has contributed to this work. I would like to begin by thanking my advisor, Dr. Larry DeWerd. During my graduate school search, I had the opportunity to visit the UWMRRC and meet with the students, staff, and Larry. These interactions played a large role in my decision to attend the University of Wisconsin. At the UWMRRC, I observed an outgoing group of happy and well-supported students who were given every opportunity to succeed. The success of the students was, in large part, due to leadership and patience of Larry. It was Larry who brought this project to my attention, and it was with his guidance and knowledge that I was able to define the scope of this dissertation. Furthermore, with Larry's encouragement and support I was able to travel to a wide-range of conferences, discuss this work with the leading experts in the field, and collaborate with manufacturers to optimize chamber designs. For this, and so much more, I thank Dr. DeWerd.

John Micka, who is always good for a laugh and some Christmas whiskey, also deserves a huge debt of gratitude. John has been an invaluable resource for the laboratory. For many students, myself included, John has stood apart; he is always available, approachable, and above all, concerned for the well being of the students. With his long history of performing ionization chamber calibrations and advising UWADCL customers and ionization chamber manufacturers, John was a fountain of practical knowledge.

The students at the UWMRRC are all very privileged with access to many wonderful resources, the greatest of which is the amazing team of staff. Specifically, I must thank Frank Grenzow for his invaluable wisdom of electrometers and all things electronic. Frank generously volunteered his time reviewing electrometer design and collaborating with me to create several chamber/electrometer setups that are unique to this work. Furthermore, his continued interest and insight were critical to the completion of this project. In a similar manner, I would like to thank Dan Anderson for his computer support and assistance with Monte Carlo installation. I also would like to thank Benjamin Palmer and Cliff Hammer who were always upbeat and willing to help with student projects even when the students were mercilessly defeating them in all laboratory competitions. A final thank you to Wendy Kennan for making the laboratory a clean and safe environment and to Keith Kunugi for his general assistance with many of the laboratory resources and procedures.

This work would not have been possible without the collaboration of a few people outside of the UWMRRC family. First and foremost, I must thank everyone from Standard Imaging, particularly Brian Hooten. Brian is the king of ionization chambers and shared in the frustration of this microchamber journey. We spent countless hours scratching our heads and brainstorming isolation techniques. Without Brian's considerable knowledge of microchamber design and manufacturing, this project would not have been possible. Above all else, Brian exhibited an enthusiasm and excitement for discovery that was contagious. He was an absolute joy to work with and I am infinitely thankful for the opportunity to collaborate with him. I would also like to thank Dr. Malcolm McEwen from the NRC. He contributed through many insightful conversations and project defining ideas. He also generously lent us his custom A2 chambers.

The UWMRRC students were also a tremendous source of support and often guidance throughout this project. I am particularly thankful to Megan Wood, Martha Malin, Travis McCaw, Jessica Fagerstron, Mike Lawless, Qing Lang, and Joshua Reed for editing this

lengthy novel. In particular, I would like to thank Martha Malin for spending many late nights with me here at the Carbone Canter Center and at the East Clinic performing a variety of QA measurements. I could not have asked for a more responsible, intelligent, and kind partner in crime. I would also like to thank Mike Lawless who has become a wonderful friend and brought much laughter to many long days in the basement cubicles. I must also thank an honorary UWMRRC student, Dr. Dustin Jacqmin who danced his way into my heart and the hearts of my family and friends. He is absolutely one of a kind and I am constantly inspired by his fearlessness. I would like to say a very special thanks to Dr. Stephanie Junell and Dr. Laura Bartol, for not only helping with this research, but becoming some of my greatest friends. Friendships like these are few and far between, and I am so thankful to have both of you in my life. Throughout our time here in Madison, we have seen each other through many tribulations and celebrated many of life's greatest moments from marriages to motherhood. I know that no matter where medical physics takes us, the bond we have created in Madison will endure.

Lastly, I would like to thank my family, and for them there are no words great enough. To my parents, Gary and Pam Snow, and my little sister, Mckenzie Snow, I owe this all to you. God has given me many blessings throughout my life, but the greatest of all was to be born into this family. I cannot imagine a happier childhood in a home more filled with love and laughter. It is only through your support and encouragement that I have achieved anything. I do not say it enough, but thank you.

As of September seventh of this year, I am honored to acknowledge one more family member, my husband, Andy Miller. Andy has filled my graduate school days with an abundance of joy, laughter, and love; for that, I will be forever thankful. He has unwaveringly supported me through the highs and lows of a lengthy graduate career and across the miles of highway that stand between us. Andy, you are my rock. You inspire me everyday with

your strength, integrity, and patience. I could not feel more lucky or be more excited to spend the rest of my life with you.

Contents

List of Figures

List of Tables

Chapter 1

Introduction

1.1 Overview

Cavity ionization chambers are the most common devices used in clinical radiation-therapy dosimetry. Current reference-dosimetry protocols published by the American Association of Physicist in Medicine (AAPM) and the International Atomic Energy Agency (IAEA) rely on the response of an ionization chamber to determine the dose to media. Typical Farmer-type and scanning ionization chambers (collecting volumes greater than 0.02 cm^3) behave in a predictable manner corresponding to current ionization chamber theory. Thus, with several well understood correction factors and accurate calibration factors, the current dosimetry protocols are able to correctly account for and utilize the response of these larger-volume chambers.

With an increase in the delivery of small and non-standard radiation fields in patient treatments, a need for smaller-volume ionization chambers has arisen. In response, small-volume ionization chambers, called microionization chambers or microchambers, were created with collecting volumes of less than 0.02 $cm^3$and are used for dosimetry measurements in radiation therapy clinics around the world. Furthermore, the University of Wisconsin Accredited Dosimetry Calibration Laboratory (UWADCL) has experienced an increase in

requests for the calibration of microchambers for low- and medium-energy x-ray beams as well as the ^{60}Co beam. This indicates that these chambers are being used in reference-dosimetry measurements for a wide range of therapy applications and beam energies.

Unfortunately, microchambers demonstrate a series of anomalous behaviors not seen in larger-volume chambers. There are no current AAPM or IAEA recommendations dedicated to microchamber dosimetry, and therefore, microchambers are often used with the same dosimetric techniques and relationships as large-volume chambers. Several publications have highlighted the undesirable behaviors of microchambers, such as large polarity effects (McEwen, 2010; Agostinelli et al., 2008; Martens et al., 2000; Stasi et al., 2004) and an inverse proportionality between chamber response and applied voltage (McEwen, 2010; Le Roy et al., 2011). However, a comprehensive characterization of microchamber behavior does not exist. Furthermore, no work has been done to determine the cause of these behaviors. Without an understanding of the processes that compete with the collection of the true radiation-induced gas ionization in microchambers, the reliability and applicability of these chambers is uncertain.

Herein lies the motivation for this work; while microchambers are used in reference-dosimetry measurements and relied upon for accurate dose determination, it is necessary that the behavior of these chambers is either optimized or accounted for correctly. The goal of this work can be categorized into three main components:

1. Perform a thorough characterization of the current microionization chamber models for low- and high-energy photon beams to determine their dosimetric issues and limitations (see Chapters 3, 4, 5, and 5).

2. Identify the cause of the anomalous behaviors to gain an understanding of the processes occurring in microchambers (see Chapters 6, 7, and 8).

3. Determine a method to accurately account for these behaviors or eliminate the behaviors through optimized microchamber design (see Chapter 9).

The dosimetric challenges of small and non-standard-radiation fields are great. The first step to achieving accurate reference-dosimetry measurements in these complex radiation fields is to ensure the reliability and accuracy of the employed dosimeter. The aim of this work is to identify and resolve the obstacles impeding the performance of microchambers for small and non-standard radiation therapy dosimetry.

Chapter 2

Background

This chapter provides a review of the current dosimetry issues facing cylindrical microionization chambers and the impact these issues may have on clinical reference dosimetry. To effectively assess microionization chamber behavior, this chapter also discusses current cylindrical ionization chamber dosimetry, including reference-class ionization chamber qualifications and the ionization chamber requirements of current AAPM clinical reference dosimetry protocols. It should be noted that the IAEA TRS-398 protocol is similar to the AAPM protocols, but this work will henceforth refer to AAPM nomenclature for simplicity. With an understanding of the current dosimetry needs and typical ionization chamber performance, an objective evaluation of microionization chamber behavior can be performed.

2.1 Dosimetry

2.1.1 Dosimetry quantities

Accurate radiation dosimetry relies on the determination of the dose, dose rate, or other radiologically relevant quantities resulting from the interaction of ionizing radiation with matter. To fully understand dosimetry it is essential to recognize two fundamental quantities that are used to describe the interactions of radiation with matter: dose and kerma.

Energy deposition in matter by ionizing radiation, such as x- or γ-ray photons, is a two-step process. The first step in energy dissipation is called kerma, which is defined as the energy transferred to charged particles in a material by indirectly ionizing radiation. For a monoenergetic photon beam, kerma is defined by

$$K = \Psi \cdot (\frac{\mu_{\rm tr}}{\rho})_{E,Z}, \tag{2.1}$$

where Z is the atomic number of the absorbing material, Ψ is the energy fluence of the photon beam of energy E, and $(\frac{\mu_{tr}}{\rho})_{E,Z}$ is the mass energy-transfer coefficient in units of cm^2/g. The energy received by charged particles can result in local excitations and ionizations or can be carried away by photons from radiative processes.

The energy imparted to matter by all types of ionizing radiation, but delivered by charged particles, is called the absorbed dose, D. D represents the energy per unit mass which remains in the matter to produce any effects that are attributable to the radiation and is, consequently, considered the most important quantity in radiological physics. Consider a finite volume with mass m. The absorbed dose at any point in that volume is defined by

$$D = \frac{d\epsilon}{dm}, \tag{2.2}$$

where $d\epsilon$ is the expectation value of the energy imparted in an infinitesimal volume of mass dm (Attix, 2004).

2.1.2 Measurement Techniques

Determination of kerma and dose can be a significant challenge. Kerma cannot be measured directly and the methods available for the direct measurement of dose are limited. Calorimetric dosimeters, which measure the radiation-induced temperature change in a media, are the closest practical means to directly determine D. Unfortunately, radiation induced

temperature rises are very small and calorimeters are extremely sensitive to changes in ambient conditions making them impractical for clinical dosimetry. All other techniques used to measure D rely on coefficients of conversion to infer absorbed dose from a secondary effect of ionizing radiation.

One of these secondary effects is the radiation-induced creation of ion pairs in air, the details of which are described in Section 2.2.2. The number of radiation-induced ion pairs created in a volume of air, under certain conditions, is proportional to the absorbed dose in the volume of air, D_{air}. With accurate coefficients of conversion, ion pair production can be used to directly calculate D_{air}. As mentioned in Section 1, the most popular dosimeter for clinical dosimetry is the ionization chamber, which is designed to measure this radiation-induced ion pair production. Ionization chambers consists of a gas cavity, usually of air, surrounded by a solid envelope. The absorbed dose in the air cavity is calculated by

$$D_{\text{air}} = \frac{Q}{m}(\frac{\overline{W}}{e})_{\text{air}}, \tag{2.3}$$

where Q, expressed in coulombs, represents the charge (of either sign) produced by ionizing radiation in a collecting volume of mass, m. $\overline{W}$ is the mean energy expended per ion pair produced in gas and e is the charge of an electron. For x- and γ-rays in dry air, $\overline{W}/e$ is equal to 33.97 J/C.

Once the absorbed dose in the cavity is determined and charged particle equilibrium (CPE) is obtained, it is possible to calculate the absorbed dose in the wall of the chamber, as well as in other desired media, using cavity theory. If CPE exists throughout a defined volume then every charged particle carrying energy out of that volume is compensated by an identical charged particle carrying the same energy into the volume. The presence of CPE is not absolutely necessary for cavity theory calculations, but in its absence the charged particle spectrum must be well known. The spectrum must also be the same in the cavity and in the medium in which the dose is to be determined. Thus, it is desirable for CPE to

exist throughout the cavity of an ionization chamber to avoid these complications (Attix, 2004).

2.2 Cylindrical ionization chambers

Cylindrical ionization chambers, as opposed to parallel-plate or spherical ionization chambers, are the most common type of ionization chamber used in clinical reference dosimetry for external photon beams. Therefore, this work is limited to the investigation of cylindrical chambers. The following sections describe the typical components, classifications, and behavior of cylindrical chambers.

2.2.1 Schematics

The volume of air inside of an ionization chamber, in which ion pair production is measured, is called the collecting volume. The collecting volume is contained and defined by three electrodes; the thimble or wall electrode of the chamber, the collecting electrode, and the guard electrode. Each electrode is separated from the other electrodes by an insulating material, as shown in Figure 2.1. The chamber electrodes are connected to an electrometer through a low-noise triaxial cable. The electrometer, which is discussed in further detail in Section 2.2.1.5, is responsible for measuring charge or current produced by the ionization chamber, while applying a constant biasing voltage to the electrodes (DeWerd et al., 2009).

2.2.1.1 Wall electrode

The wall electrode of the chamber, often referred to as the thimble or shell of the chamber, serves as a barrier that contains the gas inside the cavity while functioning as an electrically conducting electrode. As discussed previously, CPE is desirable for ionization measurements and the wall of the chamber provides mass to allow an equilibrium charged particle fluence

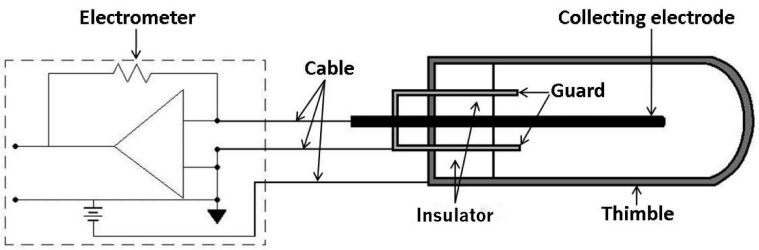

(a)

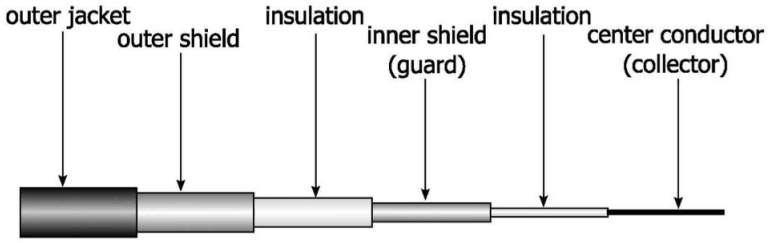

(b)

Figure 2.1: (a) Schematic cross section of a cylindrical ionization chamber connected to an analog electrometer. (b) Schematic of a triaxial cable.

within the cavity. In the case where the thickness of the wall does not meet this criterion, a build-up cap composed of the same, or a similar, material can be placed over the thimble to provide adequate thickness. It is also important to note that minimal inhomogeneity between the wall and cavity media is ideal; therefore, the effective atomic number $\overline{Z}$ of the wall material should be close to that of the cavity gas (Attix, 2004).

2.2.1.2 Collecting electrode

The center collecting electrode, in combination with the wall electrode, produces an electric potential difference within the cavity that permits ion collection and defines the active collecting volume. In addition to maintaining the applied potential bias, the central electrode also collects the radiation-induced ions of one sign produced in the collecting volume. If possible, the same material should be used for the wall and the collecting electrode to avoid

perturbations caused when interaction cross sections in the collector are much higher than that of the wall (Attix, 2004).

2.2.1.3 Guard electrode

The third primary component of an ionization chamber is the guard electrode. The guard electrode is biased to the same electric potential as the collecting electrode and serves to intercept unwanted electric leakage current flowing between the wall and the collecting electrode. The guard electrode also influences the shape of the electric field lines in the chamber cavity and can alter the shape of the collecting volume (Attix, 2004).

2.2.1.4 Insulating materials

Two separate insulators are required in the assembly of a cylindrical ionization chamber. The insulating material placed between the guard and wall electrodes is commonly referred to as the high-voltage (HV) insulator. The insulating material between the guard and collecting electrodes will be referred to in this work as the collector/guard insulator. In both cases, the insulating materials should electrically isolate the conductive electrodes while providing a physical space between the electrodes. Thus, it is important that the materials chosen for the insulators have high insulating properties as well as the necessary rigidity.

2.2.1.5 Electrometers

The current produced by an ionization chamber can be as low as 0.01 pA to 1 μA depending on the strength of the radiation source. Due to the relatively low impedance of a digital multimeter (DMM), the minimum current measuring capability of a high end DMM is 20 μA (Grenzow, 2009). To overcome this limitation, a refined, high-impedance dc multimeter, known as an electrometer, can be used to measure the current or charge produced by an

ionization chamber (Keithley Instruments, 2004). In the 1960s the development of the first MOSFET amplifier led to the introduction of the modern electrometer. Today, electrometers are used in nearly all clinics performing radiation therapy. To create a high impedance input with a low impedance output, an operational amplifier composed of an inverting amplifier and a negative feedback is typically placed in the preamplifier of an electrometer (DeWerd et al., 2009).

The preamplifier circuitry within an electrometer performs two functions. First, the circuitry applies a bias to each of the ionization chamber electrodes through a low-noise triaxial cable as shown in Figure 2.1. The potential bias between the wall electrode and the guard electrode is supplied by a HV power supply usually located within the electrometer. The inverting amplifier configuration forces the bias applied to the collecting electrode to maintain equal potential with that of the guard electrode. Therefore, the collecting electrode and the guard electrode should "float" at the same voltage, which is applied by the HV power supply with respect to the wall electrode. Second, the circuitry must measure and display the output charge or current of the ionization chamber. Current and charge measurements are performed with a feedback picoammeter and coulombmeter, respectively. Every electrometer has one or both of these measuring circuits.

A picoammeter contains a feedback resistor, R_{F}, ranging from 10^7 ohms to 10^{12} ohms, which is used to measure the amplifier output voltage. The output voltage, V_{out}, is a measure of input current, I , related by

$$V_{\mathrm{out}} = -V_{\mathrm{R}} = -IR_{\mathrm{F}}, \tag{2.4}$$

where $-V_{\mathrm{R}}$ is the voltage drop across R_{F}.

Similarly, a coulombmeter is formed by replacing the resistor with a feedback capacitor, C_{F}, ranging from 0.001 μF to 1.0 μF. The output voltage of the electrometer, V_{out} is proportional to the voltage across the feedback capacitor, V_{C}, by

$$V_{\text{out}} = -V_{\text{C}} = -\frac{IT}{C_{\text{F}}}, \tag{2.5}$$

where I is the ionization current of the chamber and T is the integration time of the capacitor (DeWerd et al., 2009).

Currently, there is no protocol published by the American Association of Physicists in Medicine (AAPM) regarding the behavior requirements of a suitable electrometer. Instead, many electrometer manufacturers assure conformity to the International Electrotechnical Commission (IEC) Report Number 60731 (IEC, International Electrotechnical Commission, 1997), which contains a series of guidelines for reference-class electrometers. All electrometers used in this work meet these IEC requirements according to the manufacturers.

2.2.2 Charge collection

Ionizing radiation enters a chamber cavity with enough energy to remove electrons from the neutral molecules in the gas, converting them into positive ions. The majority of the free electrons created in the ionization process will attach to oxygen molecules to create negative ions (Boag et al., 1996; Boag and Wilson, 1952). In the absence of an electric field, the majority of negative and positive ions recombine, either with each other or other ions produced in the cavity, and an inadequate amount of charge is collected by the chamber. When a polarizing voltage is applied to the chamber, an electric field is induced which sweeps the positive and negative ions to opposite electrodes. As the polarizing voltage increases, the number of ions carried to the electrodes and collected increases until 100% collection efficiency is achieved and the chamber response plateaus at a saturation current (DeWerd et al., 2009).

It should be noted that a portion of the ionized free electrons reach the collecting electrode without attaching to an oxygen molecule and therefore do not form negative ions. This process reduces the amount of recombination between positive and negative ions and

can increase the collection efficiency of the ionization chamber. Furthermore, these free electrons have a high level of mobility when compared to positive ions. This can lead to space charge effects which may alter the magnitude of the electric field within the chamber collecting volume (Boag et al., 1996; Boag and Wilson, 1952; Bielajew, 1985; Hochhäuser and Balk, 1986). The effects of this phenomenon on chamber response will be discussed further in Section 2.3.2.2.

If the polarizing voltage is great enough to induce an electric field of 1000 V/mm or greater, charge multiplication may begin to occur at which point the ions are given enough energy to further ionize the gas inside the chamber (Zankowski and Podgorsak, 1998; Attix, 2004; Boag et al., 1987; Jeffery et al., 1974). The increase in chamber response due to charge multiplication is not an accurate representation of the initial radiation-induced gas ionization. Therefore, ionization chamber measurements are often made in the near-saturation region to eliminate any effects due to charge multiplication.

2.2.3 Classification

For the purpose of this work, ionization chambers are classified in one of three categories. Farmer-type chambers are defined as standard cylindrical ionization chambers having a collecting volume of 0.6–0.65 cm^3. Ionization chambers with an intermediate volume of approximately 0.1 cm^3 are classified as scanning chambers. The definition of a microchamber is not well delineated in the literature, but for this work, microchambers will be classified as having a collecting volume of $\leq$0.02 cm^3 and are discussed further in Section 2.5.

2.3 Ionization chamber reference dosimetry

Another important classification for this work is that of a reference-class dosimeter. The qualifications of a reference-class ionization chamber have yet to be published by the AAPM. However, a publication by McEwen (2010) establishes a series of recommendations for de-

termining if a chamber should be used as a reference-class dosimeter. The recommendations are outlined below and the details of each constraint are discussed in detail in Section 2.3.2.

- The chamber response should stabilize in less than 5 min with a change of less than 0.5% in the chamber reading from beam-on to stabilization.
- Leakage currents should contribute less than 0.1% to the chamber reading.
- The polarity correction should be less than 0.4%.
- For practical ranges of applied voltage, the inverse of the chamber response should vary linearly with the inverse of the applied voltage.
- A plot of the ion recombination correction factor as a function of dose per pulse should be linear with a intercept of less than 1.002 for an applied voltage of 300V.
- Initial recombination obtained with opposite polarities should agree to within 0.1% .
- The calibration coefficients obtained at a primary or secondary standard calibration laboratory should be consistent to within 0.3% between calibrations (typically 2 years).(McEwen, 2010)

An update to the current AAPM task group for high-energy external-beam reference dosimetry is in progress (the AAPM task group number 51 addendum). This updated protocol will contain reference-class qualifications recommended by the AAPM. For the purpose of this work, the aforementioned published qualifications will be used to determine the applicability of a chamber for reference dosimetry measurements.

2.3.1 Current AAPM external beam protocols

While there is no AAPM protocol dedicated to reference-class ionization chamber requirements, there are several clinical reference dosimetry protocols for external photon beams

that have been published by the AAPM. These protocols rely on ionization chamber reference dosimetry and include several recommendations for ionization chamber behavior. A detailed discussion of each of these chamber behaviors and the ability of typical ionization chambers to meet these recommendations is provided in Section 2.3.2. However, first, a brief overview of the current protocols is provided as reference for current ionization chamber requirements and to highlight the importance of accurately accounting for chamber behavior.

2.3.1.1 Megavoltage radiation therapy sources

The AAPM task group 51 (TG-51) published a protocol to address clinical reference dosimetry of high-energy photon beams (nominal energies ranging from ^{60}Co to 50 MV) and electron beams (nominal energies ranging from 4 MeV to 50 MeV). This protocol relies on ionization chamber measurements to calculate the absorbed dose to water in the beam of interest. To perform this calculation for photon beams, three ionization chamber dependent quantities are needed: the fully corrected ionization chamber reading, M, the absorbed-dose-to-water calibration factor for a ^{60}Co beam, $N_{D,w}^{^{60}\mathrm{Co}}$, and a beam quality conversion factor k_Q. With these three parameters, the dose to water in the beam of interest, $D_{D,w}^{Q}$, can be calculated as

$$D_{D,w}^{Q} = M k_Q N_{D,w}^{^{60}\mathrm{Co}}. \tag{2.6}$$

The calibration factor measured in reference conditions must be directly traceable to national standards of absorbed dose to water. In the United States, this means calibrations must be performed at the National Institute of Standards and Technology (NIST) or at an Accredited Dosimetry Calibration Laboratory (ADCL) traceable to NIST. The beam quality conversion factors converts the absorbed-dose-to-water calibration factor for a ^{60}Co beam to an absorbed-dose-to-water calibration factor for a radiation beam of quality Q. The

k_Q values for several common ionization chambers are published in the TG-51 protocol. To obtain M, several correction factors must be applied to the chamber reading, M_{raw}, to accurately account for the radiation-induced ionization in the chamber cavity. Therefore, M can be written as

$$M = M_{\text{raw}} P_{\text{TP}} P_{\text{pol}} P_{\text{ion}} P_{\text{elec}}, \tag{2.7}$$

where P_{TP} corrects the ionization chamber reading to standard temperature and pressure conditions for which the calibration factor applies. The correction factor P_{elec} accounts for the electrometer calibration and should be applied only when the chamber and electrometer are calibrated separately. The correction factors P_{pol} and P_{ion} are chamber specific and correct for polarity effects and the incomplete ion collection efficiency, respectively (Almond et al., 1999).

With the incorporation of Equation 2.7, Equation 2.6 can be expanded as

$$D^Q_{D,w} = M_{\text{raw}} P_{\text{TP}} P_{\text{pol}} P_{\text{ion}} P_{\text{elec}} k_Q N^{^{60}\text{Co}}_{D,w}. \tag{2.8}$$

It is clear from this equation that any errors in the correction factors can directly effect the determined absorbed dose. Therefore, it is essential that these correction factors are accurately determined and applied. The two chamber dependent effects and their corresponding correction factors, P_{pol} and P_{ion}, are discussed in detail in Sections 2.3.2.2 and 2.3.2.3, respectively. However, as a reference, the TG-51 protocol recommends that P_{ion} for a given chamber must be less than 1.05 and P_{pol} must be no greater than 0.3% from unity.

Additional AAPM task group protocols, such as TG-148 for quality assurance (QA) in helical tomotherapy and TG-142 for QA of medical linear accelerators, have extended the TG-51 protocol for other high energy dosimetry modalities as well as additional QA procedures. These protocols still rely on ionization chamber readings, calibration coefficients, and P_{ion} and P_{pol} correction factors as defined in the TG-51 protocol. Thus, it is important that

these calibration and correction factors are accounted for properly in ionization chamber measurements for high-energy radiation therapy beams.

2.3.1.2 Kilovoltage and orthovoltage x-ray sources

The AAPM Task Group 61 (TG-61)(Ma et al., 2001) has developed a reference dosimetry protocol for low- and medium-energy x-ray beams (<300 kV) that is based on the air-kerma response of ionization chambers. The protocol contains two approaches for determining the dose to the water either at the surface of a water phantom (called the in-air method) or at a point of interest (called the in-phantom method). Both methods rely on the fully corrected ionization chamber reading, M, and an air-kerma calibration coefficient, N_{K}, for the chamber of interest. For measurements performed in the United States, N_{K} must be NIST traceable. Using these parameters, the absorbed dose to water at the phantom surface shall be determined as

$$D_{\mathrm{w,z=0\,cm}} = M N_{\mathrm{K}} B_{\mathrm{w}} P_{\mathrm{stem,air}} \left[\left(\frac{\overline{\mu}_{\mathrm{en}}}{\rho} \right)^{\mathrm{w}}_{\mathrm{air}} \right]_{\mathrm{air}}, \tag{2.9}$$

where B_{w} and $P_{\mathrm{stem,air}}$ are the backscatter and chamber stem correction factors, respectively, and $[(\overline{\mu}_{\mathrm{en}}/\rho)^{\mathrm{w}}_{\mathrm{air}}]_{\mathrm{air}}$ is the ratio of the mean mass energy-absorption coefficients for water-to-air averaged over the incident photon spectrum.

The absorbed dose to water at a 2 cm depth shall be determined using the in phantom method as

$$D_{\mathrm{w,z=2\,cm}} = M N_{\mathrm{K}} P_{\mathrm{Q,cham}} P_{\mathrm{sheath}} \left[\left(\frac{\overline{\mu}_{\mathrm{en}}}{\rho} \right)^{\mathrm{w}}_{\mathrm{air}} \right]_{\mathrm{water}}, \tag{2.10}$$

where $P_{\mathrm{Q,cham}}$ and P_{sheath} are the overall chamber and waterproofing sleeve correction factors, respectively, and $[(\overline{\mu}_{\mathrm{en}}/\rho)^{\mathrm{w}}_{\mathrm{air}}]_{\mathrm{air}}$ is the ratio of the mean mass energy-absorption coefficients for water-to-air averaged over the incident photon spectrum at a reference point in

water in the absence of the chamber. The in-phantom method is only applicable for tube potentials greater than 100 kV.

For both methods, the fully corrected chamber reading M is obtained using the same correction factors defined in the TG-51 protocol, see Equation 2.7. Therefore, it is once again imperative for accurate dose determination that the chamber reading and the corresponding calibration and correction factors are accurately and correctly applied.

The TG-61 protocol also requires that the ionization chamber meet several additional conditions that are not specified in the TG-51 protocol. The specifics of these requirements are discussed in Section 2.3.2.5. For this summary it is sufficient to state that it is necessary to determine the variation in N_{K} with calibration beam quality for a chamber prior to performing reference dosimetry measurements in x-ray beams below 300 kV.

2.3.2 Ionization chamber behavior and performance

As mentioned in the previous sections, reference-class ionization chambers must meet certain behavioral criteria. A properly functioning ionization chamber should perform in a well-understood and predictable manner when exposed to ionizing radiation. The responses and associated correction factors of a chamber not only provide a good indication of whether the chamber is working correctly, but they are also essential for accurate dose determination in current reference dosimetry protocols. The following sections discuss several of these behaviors and how they affect the suitability of an ionization chamber for reference-class dosimetry measurements.

2.3.2.1 Leakage

Leakage is a broad term, accounting for the current originating from the ionization chamber, connectors, triaxial cable, and electrometer which is unrepresentative of the true radiation-induced gas ionization current. Typically leakage current is categorized as either intrinsic

or radiation-induced. In both cases, the magnitude and stability of the effect is dependent upon a series of factors, such as the applied chamber bias, the chamber dimensions and materials, the beam geometry and the radiation type (DeBlois et al., 2000).

There is little guidance from the AAPM concerning leakage current limits; however, due to the IAEA TRS-398 Code of Practice recommendations, McEwen (2010) suggested that the chamber leakage current should compose less than 0.1% of the chamber signal. This limit is achievable for many chambers on the market today. Several authors have reported leakage currents of less than 0.1% for typical ionization chambers (McEwen, 2010; Le Roy et al., 2011; Leybovich et al., 2003). Leybovich et al. (2003) measured the leakage induced error in dose calculation for a tomographic and step-and-shoot IMRT plan using a variety of chambers. Without correcting for leakage, the Farmer-type and scanning chambers measured doses equal to the calculated dose to within 0.5% and 2.6%, respectively. With leakage correction, the measurement error with the scanning chamber was reduced to 0.5%. This demonstrated that leakage currents can have a significant effect on dosimetric measurements if not accounted for properly. Furthermore, several studies have indicated that the relative effect of leakage currents tend to increase with decreasing chamber size (McEwen, 2010; Leybovich et al., 2003; Le Roy et al., 2011).

2.3.2.2 Polarity effects

A polarity effect is defined as any change in chamber response that is caused by the polarity of the chamber and is therefore unrepresentative of the true gas ionization. No single parameter can be identified as both the physical source and absolute predictor of this effect (Williams and Agarwal, 1997). There are a multitude of causes of the polarity effect and they can be categorized as either voltage-dependent effects or voltage-independent effects (Abdel-Rahman et al., 2006).

Voltage-dependent effects occur when the absolute value of the signals for measurements made with opposing polarities vary with the magnitude of the applied voltage (Abdel-Rahman et al., 2006). A comprehensive understanding of the origins of voltage-dependent effects does not exist, but it is suggested that a difference in the potential of the guard electrode with respect to the collecting electrode, could be a significant contributor. Altering the potential of the guard with respect to the collector induces a change in the shape of electric field lines in the chamber cavity, therefore altering the size and placement of the active collecting volume. When the collecting electrode is biased, the potential of the guard may lag or lead that of the collector, the amount of which is dependent on the polarity and magnitude of the collector potential (Boag, 1964; Kim et al., 2005). Space charge effects may also play a significant role in voltage-dependent polarity effects. Since the mobility of free electrons is roughly 1000 times greater than the mobility of positive ions, electrons are pulled to the electrode at a faster rate, leaving behind a cloud of positive ions. This cloud of slowly moving positive ions can have a significant effect on the strength and uniformity of the electric field. Since stronger electric fields are able to pull ions to the electrodes more quickly, this effect decreases with increasing voltage (Lapsley, 1953; Boag, 1963; Boag et al., 1996; Hochhäuser and Balk, 1986; Bielajew, 1985). Another possible contributor to voltage-dependent polarity effects, is the net transfer of electrons between the collecting electrode and the wall electrode. These transferred electrons are independent of the radiation-induced air ionization and may be attributed to differences in the dimensions or materials between the electrodes, non-uniform dose-rate throughout the collecting volume, or asymmetry in electron emission between the electrodes. Greening et al.(1953) demonstrated this effect by performing saturation curves at low-pressures where air ionization plays a negligible role in an ionization chamber's signal. At low pressures, the chamber signal (i.e. the net electron transfer between electrodes) was voltage- and polarity-dependent.

Voltage-independent polarity effects do not vary with the magnitude of the applied voltage and are attributed mainly to Compton currents. These currents are caused by secondary electron production in individual chamber components, particularly the cable and collecting electrode (Abdel-Rahman et al., 2006; Johns et al., 1958). Due to the length of the chamber stem and cable irradiated, voltage-independent effects can be highly dependent on the field size of the radiation beam (Martens et al., 2000; Stasi et al., 2004; Agostinelli et al., 2008).

To correct for errors in measurements due to polarity effects, the TG-51 protocol (see Section 2.3.1.1) suggests the application of a polarity correction factor, P_{pol}, which is defined as

$$P_{\text{pol}} = \left| \frac{M^{+}_{\text{raw}} - M^{-}_{\text{raw}}}{2M_{\text{raw}}} \right|, \tag{2.11}$$

where M^{+}_{raw} and M^{-}_{raw} are the uncorrected chamber readings when positive and negative charge is collected, respectively. TG-51 states that the difference between P_{pol} and unity should typically be no greater than 0.3% for most chambers (Almond et al., 1999). McEwen (2010) recommends that P_{pol} should be less than 0.4% to qualify as a reference-class dosimeter. For many commercially available Farmer-type and scanning chambers, these limits have been achievable (Seuntjens et al., 2000). However, it is important to note that this correction factor accounts only for unwanted signal due specifically to Compton currents (Abdel-Rahman et al., 2006). Currently, there is no widely accepted method to comprehensively account for voltage-dependent polarity effects.

2.3.2.3 Ion recombination

Ion recombination is an effect that is often misrepresented and, consequently, accounted for incorrectly (McEwen, 2010; Palmans et al., 2010). This broad term accounts for three separate phenomena: initial recombination, ion diffusion, and general recombination. Each

of these processes reduces the number of ions that are collected by the chamber, causing an under-representation of the true radiation-induced gas ionization.

Initial ion recombination occurs when ions created along the path of a single particle combine either due to coulomb attraction between oppositely charged ions or motion caused by the applied electric field (Zankowski and Podgorsak, 1998). The number of particle tracks occurring per unit volume of gas does not influence the recombination occurring within a given track. Since initial recombination applies only to the individual tracks, this effect is independent of the dose rate of the radiation beam (Attix, 2004). Ion diffusion is a process in which identical ions move against the applied potential to obtain a uniform distribution. Similar to initial recombination, this effect is dose-rate independent. General recombination accounts for ion recombination which occurs between ions that were created along different ionizing particle tracks. Therefore, general recombination is a function of the dose rate of the radiation beam.

For a standard ionization chamber, the reduction in chamber response due to ion recombination losses can be corrected for by multiplying the chamber response by a correction factor, P_{ion}, which is defined as the saturation charge, Q_{sat}, divided by the measured charge Q.

$$P_{\text{ion}} = \frac{Q_{\text{sat}}}{Q} \tag{2.12}$$

The saturation charge is defined as the charge collected when 100% of the ions in the collecting volume are measured. It should be noted that for the calculation of P_{ion}, the measured current, I, and saturation current, I_{sat} are interchangeable with Q and Q_{sat}, respectively, and depend only on what is measured by the electrometer. Throughout this section, charge will be used to discuss ion recombination.

As mentioned in Section 2.2.2, a portion of the ionized electrons reach the collecting electrode without attaching to oxygen molecules and therefore do not form negative ions.

These free electrons have a high level of mobility and can increase the collection efficiency of the ionization chamber. Several authors have created theoretic models to account for this effect in both continuous (Bielajew, 1985) and pulsed radiation beams (Boag et al., 1996; Boag and Wilson, 1952). However, the increase in collection efficiency is often insignificant and cannot increase the chamber signal above Q_{sat}(Di Martino et al., 2005; DeBlois et al., 2000); therefore, it is not accounted for in dosimetry protocols and will not be corrected for in this work.

To calculate P_{ion}, Q must be measured for at least two applied voltages and Q_{sat} must be determined. Since general recombination is dependent on the ionization intensity the method for determining Q_{sat} is different for continuous and pulsed radiation beams. The following sections describe the calculations, and corresponding derivations, for calculating Q_{sat} for continuous and pulsed beams.

Continuous radiation To assess ion recombination effects in a continuous radiation beam such as ^{60}Co, the collection efficiency, f, is evaluated for each of the three ion recombination processes. The charge collection efficiency is defined as the charge collected, Q, divided by the saturation charge, Q_{sat}.

$$f = \frac{Q}{Q_{\text{sat}}} \tag{2.13}$$

The collection efficiency, f_{i}, accounting for only initial ion recombination is defined as

$$f_{\text{i}} = \frac{1}{1 + \Lambda_{\text{i}}/V}, \tag{2.14}$$

where V is the polarizing voltage and Λ_{i} is the initial recombination coefficient that accounts for various chamber and air parameters. Similarly, the ion diffusion collection efficiency, f_{d}, for all beams and can be written as

$$f_{\mathrm{d}} = \frac{1}{1 + \Lambda_{\mathrm{d}}/V}, \tag{2.15}$$

where the diffusion parameter, Λ_{d}, is proportional to the temperature of the cavity divided by the electronic charge of the ions.

The general recombination collection efficiency, f_{g}, for a continuous radiation beam is proportional to the square of the voltage by

$$\mathrm{f_g} = \frac{1}{1 + \Lambda_{\mathrm{g}}/V^2}, \tag{2.16}$$

where the general recombination coefficient, Λ_{g}, is proportional to the dose rate and contains several chamber and air parameters.

Unlike initial recombination, which occurs independently, ion diffusion and general recombination can be mutually competing processes. However, when the total collection efficiency f is greater than 0.7, each component functions as an independent process and f can be expressed as the product of the individual components, ignoring the higher order terms, as

$$f = f_{\mathrm{i}} f_{\mathrm{d}} f_{\mathrm{g}} = \left\{ 1 + \frac{\Lambda_{\mathrm{i}} + \Lambda_{\mathrm{d}}}{V} + \frac{\Lambda_{\mathrm{g}} + \Lambda_{\mathrm{i}}\Lambda_{\mathrm{d}}}{V^2} \right\}^{-1}. \tag{2.17}$$

Substituting Equation 2.17 into Equation 2.13 gives

$$\frac{1}{Q} = \frac{1}{Q_{\mathrm{sat}}} + \frac{\alpha}{V} + \frac{\beta}{V^2}, \tag{2.18}$$

where $\alpha = \frac{(\Lambda_{\mathrm{i}} + \Lambda_{\mathrm{d}})}{Q_{\mathrm{sat}}}$ and $\beta = \frac{(\Lambda_{\mathrm{g}} + \Lambda_{\mathrm{i}}\Lambda_{\mathrm{d}})}{Q_{\mathrm{sat}}}$ (Zankowski and Podgorsak, 1998).

Traditionally, Equation 2.18 is used to calculate Q_{sat}. The equation can be fit to a plot of the inverse charge as a function of the inverse voltage. This plot is known as a Jaffé plot, and Q_{sat} can be extracted from the fit of the equation to the data, but this technique

has limitations. The fit can only be applied to the linear portion of the Jaffé plot to avoid errors caused by including data points outside of the ionization recombination region where processes such as charge multiplication can occur.

Charge multiplication has been shown to play a significant role in ionization chamber measurements at clinically applied voltages, especially in small-volume chambers where strong electric fields are present. Agostinelli et al. (2008) observed excess current collection for a PTW 31014 microionization chamber at voltages greater than 150 V, particularly at 400 V (the manufacturer-recommended operating voltage). Palmans et al. (2010) showed that the effect of charge multiplication is greater than that of ion recombination for an Exradin A1SL scanning chamber at polarizing voltages as low as 150 V, and Le Roy et al. (2011) suggested reducing the operating voltage of the Exradin A1SL to ±150 V to reduce excess charge collection due to charge multiplication at higher voltages. In these situations the chamber reading should be corrected for both the charge lost due to ion recombination and the excess charge collected due to charge multiplication. To account for charge multiplication, as well as any radiation-induced conductivity in the stem of the chamber, Zankowski and Podgorsak (1998) suggested the addition of the multiplicative exponential term, $e^{-\gamma V}$ to Equation 2.18 as shown in Equation 2.19 (Zankowski and Podgorsak, 1998).

$$\frac{1}{Q} = \left(\frac{1}{Q_{\text{sat}}} + \frac{\alpha}{V} + \frac{\beta}{V^2} \right) e^{-\gamma V} \tag{2.19}$$

Equation 2.19 can also be used to determine Q_{sat} by fitting the equation to a Jaffé plot of the data. This equation provides a robust fit for a wide range of applied voltages while accounting for initial recombination, ion diffusion, general recombination, and any exponential effects such as charge multiplication.

Unlike the robust calculation methods discussed thus far, the TG-51 protocol suggests a simplified two-voltage technique for the determination of P_{ion}. The two-voltage technique ignores the effects of initial recombination and ion diffusion, assuming that the contribution

from both processes is negligible when compared to that of general recombination. This method requires the chamber response, M_H, at some clinically relevant voltage, V_H, and another reading, M_L, at a lower voltage, V_L, which is typically around half the magnitude of, V_H. The two measurements are used to calculate the ion recombination correction factor, P_{ion}, for continuous beams as (Almond et al., 1999)

$$P_{\text{ion}} = \frac{1 - \left(\frac{V_H}{V_L}\right)^2}{\frac{M^H_{\text{raw}}}{M^L_{\text{raw}}} - \left(\frac{V_H}{V_L}\right)^2}. \tag{2.20}$$

This techniques provides a simple and time efficient method for determining P_{ion}, but ignoring the effects of initial recombination and ion diffusion and can lead to errors. Therefore, the applicability of this technique should be validated for every chamber prior to application (Di Martino et al., 2005).

Pulsed radiation General ion recombination collection efficiency, f_{g}, for an ionization chamber exposed to pulse radiation was first determined by Langevin in 1902 (Langevin, 1902) and later expanded and benchmarked by J. W. Boag (Boag, 1950; Boag and Wilson, 1952; Boag and Currant, 1980; Boag, 1982). For an ideal theoretical case,

$$f_{\text{g}} = \frac{1}{u} ln(1+u), \tag{2.21}$$

where

$$u = \frac{\Lambda_{\text{g}}}{V}, \tag{2.22}$$

and $\Lambda_{\text{g}} = \mu\rho d^2$. In this expression, $\mu = 3.2x10^{10}$ Vm/C, ρ is the initial charge density per pulse in the collecting volume of the chamber, d is the equivalent spacing of the electrodes, and V is the voltage applied to the chamber. For small charge densities and collection effi-

ciencies greater than 90%, u becomes significantly small. With small values of u, Equation 2.21 can be approximated by

$$f_{\mathrm{g}} \approx 1 + \frac{\lambda_{\mathrm{g}}}{V}, \tag{2.23}$$

where $\lambda_{\mathrm{g}} = \Lambda_{\mathrm{g}}/2Q_{\mathrm{sat}}$. However, this equation only accounts for general recombination. Several authors have measured the effects of initial recombination and ion diffusion in pulsed beams and have found that these components also vary approximately linearly with voltage (Burns and Rosser, 1990; Derikum and Roos, 1993; Havercroft and Klevenhagen, 1993). Thus, Equation 2.23 can be rewritten as

$$f = 1 + \frac{\lambda_{\mathrm{i,d}}}{V} + \frac{\lambda_{\mathrm{g}}}{V}, \tag{2.24}$$

where λ_{i} and λ_{d} account for initial ion recombination and ion diffusion, respectively. Combining Equation 2.13 with Equation 2.24 gives,

$$\frac{1}{Q} = \frac{1}{Q_{\mathrm{sat}}} + \frac{\lambda_{\mathrm{i,d}}}{V} + \frac{\lambda_{g}}{V}. \tag{2.25}$$

Due to Equation 2.25, McEwen (2010) recommended that the inverse chamber response should vary linearly with the inverse applied voltage over the range of practical applied voltages to meet the criteria of a reference-class ionization chamber. A variety of cylindrical chambers have been found to fulfill this criteria (McEwen, 2010). Similar to methods employed for continuous radiation beams, DeBlois et al. (2000) included an exponential factor, $e^{-\gamma V}$, to account for the effects such as charge multiplication and cable irradiation. The addition of this factor to Equation 2.25 can be written as

$$\frac{1}{Q} = \left(\frac{1}{Q_{\mathrm{sat}}} + \frac{\lambda_{\mathrm{i,d}}}{V} + \frac{\lambda_{g}}{V} \right) e^{-\gamma V}. \tag{2.26}$$

Equation 2.26 provides a robust fit for a wide range of applied voltages accounting for initial recombination, ion diffusion, general recombination, and any exponential effects such as charge multiplication. Once again, the saturation current can be easily derived from a Jaffé plot fit, and a more accurate ion recombination correction factor can be applied to the chamber reading.

The TG-51 protocol suggests a two-voltage technique to calculate P_{ion} in a pulsed radiation beam, similar to that of continuous beams. The two-voltage technique once again ignores the effects of initial recombination and ion diffusion, and requires the chamber responses M_H and M_L at some clinically relevant applied voltage, V_H, and a lower applied voltage, V_L, respectively. The two measurements are used to calculate the ion recombination correction factor, P_{ion}, for pulsed beams (Almond et al., 1999) as:

$$P_{\text{ion}}(V_H) = \frac{1 - \frac{V_H}{V_L}}{\frac{M^H_{\text{raw}}}{M^L_{\text{raw}}} - \frac{V_H}{V_L}}. \tag{2.27}$$

As with continuous beams, this techniques is simple and time efficient but can lead to errors due to the incomplete account of ion recombination.

2.3.2.4 Ion recombination as a function of dose per pulse

A more robust indicator that a chamber is behaving properly is the variation of the collection efficiency of the chamber as a function of the dose per pulse (McEwen, 2010; Bruggmoser et al., 2007). As stated in the previous section, the collection efficiency varies linearly with λ_{g}, which is equal to $\mu\rho d^2/2Q_{\text{sat}}$. The initial charge density per pulse, ρ, can be converted to dose-to-water per pulse, $D_{\text{w,pp}}$, by

$$\rho = \frac{D_{\text{w,pp}}}{vN_{D,\text{w}}}, \tag{2.28}$$

where v is the collecting volume of the chamber and $N_{\mathrm{D,w}}$ is the chamber calibration coefficient, described in Section 2.3.1.1. Therefore, we can rewrite Equation 2.25 as

$$P_{\mathrm{ion}} = 1 + \frac{\left[\lambda_{\mathrm{i,d}} + \frac{\mu d^2}{2Q_{\mathrm{sat}}}\left(\frac{D_{\mathrm{w,pp}}}{vN_{D,\mathrm{w}}}\right)\right]}{V}. \tag{2.29}$$

Equation 2.29 can be simplified using the formalism of Bruggmoser et al. (2007) as

$$P_{\mathrm{ion}} = 1 + (\gamma + \delta D_{\mathrm{w,pp}})/U, \tag{2.30}$$

where U is the polarizing voltage, γ is a measure of initial ion recombination and δ is the coefficient of general ion recombination. This simplified equation can be used to benchmark the methodology in this work with published data. As a result of Equation 2.30, it is recommended that for a reference-class chamber, the plot of P_{ion} as a function of $D_{\mathrm{w,pp}}$ should vary linearly, with a y-intercept of less than 1.002. The initial recombination coefficient, γ, should also remain constant to within 0.1% for opposite polarities (McEwen, 2010). Several authors have demonstrated commercial Farmer-type and scanning chambers that meet these requirements (Berg and Noerrevang, 2004; Bruggmoser et al., 2007; McEwen, 2010).

2.3.2.5 Energy dependence

It is well established that the response and energy dependence of an ionization chamber is highly dependent on the materials and dimensions of the chamber components (Kristensen, 1983; Smyth and McEwan, 1984; Ma and Nahum, 1993; Muir and Rogers, 2010; Palm and Mattsson, 1999). This dependency becomes even more significant for lower-energy x-ray beams where the photoelectric effect, which relies strongly on the atomic number (Z) of the chamber materials, is dominant (Muir and Rogers, 2011; Hill et al., 2009; Rosser, 1998; Ubrich et al., 2008; Allen Li et al., 1997). As a result, the AAPM TG-61 Protocol (see

Section 2.3.1.2) published a set of recommendations and requirements pertaining to the energy dependence of chambers for lower-energy photon-beams.

First, the chamber response must remain consistent to within ±2% and 0.2% for a Sr-90 check source and a ^{60}Co beam, respectively. Second, the protocol contains recommendations and requirements pertaining to the chamber's dependence on the energy of the calibration beams. It is recommended that the uncertainty in the air-kerma calibration coefficient (N_{K}) for any clinical beam quality between two calibration qualities should be less than or equal to 2%, and N_{K} should be consistent for medium-energy x-ray beams relative to ^{60}Co to within ±2%. These recommendations serve as guidelines which may be modified by the user provided they do not compromise the accuracy of the dosimetry determination. The protocol requires that reference dosimetry for medium-energy x-ray beams shall be performed with a chamber that has N_{K} values that vary with beam quality by less than 3% between 100 and 300 kV (Ma et al., 2001). The protocol also states that cylindrical chambers shall only be used above 70 kV, however, the demand for cylindrical chamber calibration factors for kilovoltage x-rays indicates there is an interest in the response of these chambers to lower-energy x-ray beams as well. Many Farmer-type and scanning chamber models, which contain low-Z components (Z≤13), have been shown to produce flat responses to low- and medium-energy x-ray beam qualities that meet these specifications (Ubrich et al., 2008; Hill et al., 2009; Muir and Rogers, 2011; Rosser, 1998; Allen Li et al., 1997).

2.4 Small-field external beam radiation therapy

As mentioned previously, advances in radiation therapy such as stereotactic radiosurgery and intensity-modulated radiotherapy, have led to a reduction in the size of treatment fields and an increase in the use of nonstandard fields. Small and nonstandard radiation fields present a variety of dosimetry challenges. In order to accurately perform dosimetry for these fields, a dosimeter is required that can provide high spatial resolution in areas of steep

dose gradients (Stasi et al., 2004; Martens et al., 2000; Westermark et al., 2000). Current small field AAPM task groups, such as TG-42 for stereotactic radiosurgery, recommend using small volume chambers (with collecting volume diameters of 2 mm to 3 mm) but give no further guidance on the selection or qualifications of the chamber. The AAPM has created task group number 155 (TG-155) to address small field and non-equilibrium condition photon beam dosimetry. At this time, TG-155 has not published a protocol. As a result, small field dosimetry measurements are often performed with the same techniques as large field dosimetry measurements, but with smaller dosimeters.

Furthermore, it is likely that future protocols relying on small-volume ionization chambers will still require accurate determination of the radiation-induced gas ionization in the chamber collecting volume in order to compute dose. As discussed in the previous sections, ionization chambers must meet a series of behavior criteria in order to accurately account for dose. Therefore, for this work, chambers produced for small-field dosimetry measurements will be characterized by the same standards as typical-reference class chambers.

Herein lies the premise for this work; it has been demonstrated that small-volume ionization chambers, called microionization chambers or microchambers, exhibit a series of behaviors not seen in typical reference-class chambers. Microchambers exhibit anomalous ion recombination and polarity effects, low signal-to-noise ratios, and significant dependence on the energy of the radiation beam. Until these effects are characterized and either better understood and accounted for or eliminated, microchambers cannot be relied on for accurate dosimetry measurements in reference- or small- and nonstandard-fields.

2.5 Microionization chambers

The definition of a microchamber is not well delineated; the published values for the maximum collecting volume of these chambers ranging from 0.01cm^3 to 0.10 cm^3 (McEwen, 2010; Stasi et al., 2004). For the purpose of this work, microchambers will be classified

as having a collecting volume of $\leq 0.02\,\mathrm{cm}^3$. Currently, there are three manufacturers of cylindrical microionization chambers; Standard Imaging, PTW, and IBA Dosimetry. The majority of these chambers are characterized in this work. The materials and dimensions of the chamber models are discussed in Chapter 3 and are listed in Table 3.1. Images and general schematics provided by each manufacturer are shown in Figure 2.2.

Standard Imaging offers three chamber models that fit the microchamber criteria. The chambers are marketed as microionization chambers for assessing radiation fields for IMRT, stereotactic, orthovoltage x-rays, and superficial skin therapy. The chamber models offered include the Exradin A16 developed for use in field sizes as small as 3.4 mm by 3.4 mm, and the Exradin A14 and A14SL, developed for use in field sizes down to 4 mm by 6 mm. The A14SL and A14 models have the same internal dimensions and cavity volume; however, the A14SL model is the Slim-Line version of the A14 model with a uniform outer diameter of 6.4 mm.

The line of PinPoint® ionization chambers offered by PTW, contains two chamber models with cavity volumes of less than 0.02 cm^3; the 31014 model and the 31016 model. These chambers are marketed as both reference and absolute dosimeters for nominal beam energies ranging from ^{60}Co to 50 MV in field sizes ranging from 2 cm by 2 cm to 30 cm by 30 cm. Both models are composed of identical materials but have different dimensions. The shell of the 31016 model, which is not characterized in this work, has a larger outer diameter and shorter length, creating a nearly spherical collecting volume which is stated to reduce the angular variations in chamber response. PTW also manufactured a 31006 model, which was the predecessor of the 31014 model. According to the manufacturer, the only difference between the two chamber models is the material of the collecting electrode. The 31006 model contained a collecting electrode composed of steel, opposed to aluminum for the 31014 model. This 31006 model is no longer sold, but for investigative purposes is characterized in the work.

IBA Dosimetry manufactures one microionization chamber, the CC01. Little guidance is provided by the manufacturer as to the application of this chamber model. It is stated that this chamber is intended for areas of steep dose gradients such as small stereotactic fields.

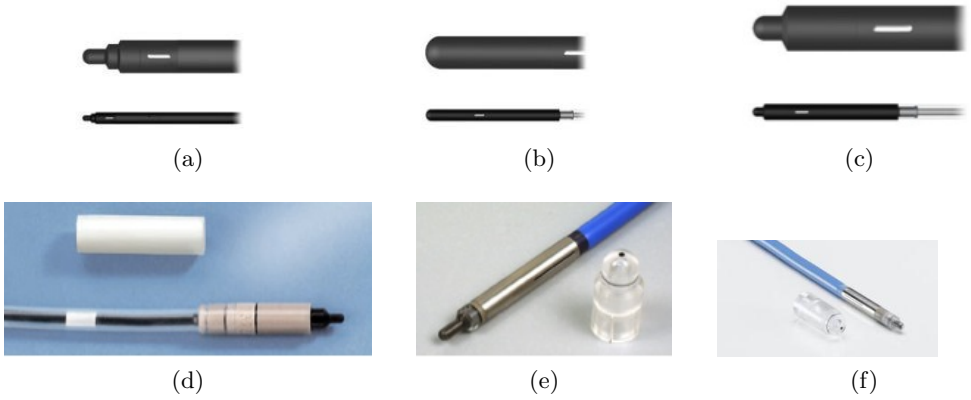

Figure 2.2: Manufacturer images of the five microionization chambers characterized in this work; (a) an Exradin A16, (b) an Exradin A14SL, (d) an Exradin A14, (d) an IBA CC01, (e) a PTW TN31006, and (f) a PTW TN31014.

Contrary to each of the manufacturer claims, these chambers demonstrate behaviors different than typical reference-class chambers, which may render them inapplicable for reference dosimetry measurements. The following section will review the published data pertaining to the performance of each of these microchambers.

2.5.1 Performance

In theory, microchambers are an ideal solution for small-field dosimetry. Several commercially available microchambers are used in radiation therapy dosimetry measurements, and improvements in spatial resolution and improved accuracy in output factor measurements for small fields have been reported for several microchamber models (Agostinelli et al., 2008; Martens et al., 2000; Stasi et al., 2004).

Unfortunately, microchambers also demonstrate behaviors different than typical reference-class chambers. In particular, microchambers have substantially smaller collecting volumes. A consequence of this volume reduction is a decrease in the number of ions available for collection. This results in a drop in chamber sensitivity, thereby reducing the signal-to-noise ratio, leaving these chambers more vulnerable to common chamber issues such as leakage (Leybovich et al., 2003; Martens et al., 2000; Le Roy et al., 2011). Furthermore, microchambers demonstrate a variety of problems and anomalous behaviors not seen in their larger counterparts, including large pre-irradiation and polarity effects, poor measurement reproducibility and stability, anomalous ion recombination correction factors (Stasi et al., 2004; McEwen, 2010; Agostinelli et al., 2008; Shimono et al., 2009; Le Roy et al., 2011), and strong energy dependence (Hill et al., 2009; Martens et al., 2000; Muir and Rogers, 2011).

2.5.1.1 Leakage

Since chamber sensitivity is proportional to the volume of the chamber, the fraction of the measured signal composed of leakage current is relatively greater for small-volume chambers. The published leakage values for microchambers vary significantly. Le Roy et al. (2011) measured the inherent and radiation-induced leakage for a variety of microchamber models and found that the leakage comprised less than 0.01% of the signal for each model. McEwen (2010) found the inherent leakage for a variety of microchambers to be less than 0.2% of the chamber signal, with the leakage of the smallest chambers (volume < 0.015 cm^3) greater than the recommended 0.1%. Similar results were reported for the radiation-induced leakage. Agostinelli et al. (2008) reported that the inherent leakage for the PTW 31014 microchamber contributed less than 0.02% to the chamber signal for high-energy photons. However, the radiation-induced leakage due to stem irradiation was significant, as great at 0.4 pC (Gy cm)$^{-1}$ and it was recommended that the effect be accounted for to achieve accurate dose measurements. Leybovich et al. (2003) determined that the error in dose

calculation for a tomographic and a step-and-shoot IMRT plan using a small 0.009 cm^3 custom microchamber was 16% and 7% , respectively; compared to less than 1.7% for both plans when leakage was corrected for.

While the reported magnitude of the inherent and radiation-induced leakage for each of these chamber models varies significantly in the literature. It is clear, that leakage current can have a significant effect on dose calculation, especially in complex IMRT and small-field treatment deliveries where treatment times are long. It is also apparent that the chamber leakage should be measured for each individual chamber prior to dosimetry measurements, regardless of the chamber model. Furthermore, it is necessary for further guidance in leakage limitations and measurement techniques for microchambers.

2.5.1.2 Ion recombination

Very little work has been published investigating ion recombination in microchambers. Le Roy et al. (2011) showed a series of saturation curves for several PTW 31006, CC01, Exradin A14SL, and Exradin A16 microchamber models. For both Exradin microchambers as well as the PTW 31006 microchamber, an increase in chamber response with decreasing voltage was reported in the ion recombination region for several of the chambers. However, no explanation or further investigation into the cause of these effects was supplied. The final recommendation was that none of the microchambers qualified as reference-class chambers. McEwen (2010) also reported an increase in charge collection with decreasing applied voltage for several chambers, but mentioned only the Exradin A14SL model specifically.

McEwen (2010) also investigated the fit of P_{ion} as a function of dose per pulse for several microchamber models. The response of the microchambers varied, with large y-intercept values to y-intercepts below unity, suggesting ion recombination increased the chamber response beyond the saturation current. Furthermore, several microchambers exhibited no significant change in P_{ion} with dose per pulse and, for other models, the slopes varied

greatly depending on the polarity. It was stated that this behavior may be due to an electrical breakdown of the chamber caused by strong electric fields between the closely spaced electrodes, but no further investigation was performed.

2.5.1.3 Polarity effects

Polarity effects for microchambers are consistently reported to be greater than those of their larger counterparts. McEwen (2010) measured average $P_{\text{pol}}(300\,\text{V})$ values for IBA, PTW, and SI microchambers for 10 cm by 10 cm high-energy photon beams (^{60}Co, 6 MV, 10 MV and 25 MV). In all cases, the correction factors were greater than the TG-51 recommended 0.3% from unity. Similarly, Agostinelli et al. (2008) measured $P_{\text{pol}}(400\,\text{V})$ values of 1.008 to 1.009 ± 0.003 for the PTW 31014 microchamber in high energy photon beams.

This effect is of considerable concern in microchambers measurements, where the reduced signal-to-noise ratio, coupled with Compton currents caused by cable irradiations, produces polarity effects that can be highly dependent on the field size of the radiation beam (Martens et al., 2000; Stasi et al., 2004; Agostinelli et al., 2008). Agostinelli et al. (2008) performed measurements with a PTW 31014 microchamber which demonstrated deviations in $P_{\text{pol}}(400\,\text{V})$ of up to 3% and 0.5% for field sizes greater than and less than 10 cm by 10 cm, respectively. Similarly, P_{pol} values measured by Stasi et al. (2004) for the Exradin A16 and A14SL microchambers varied by more than 0.5% with a reduction in the field size from 10 cm by 10 cm to 1 cm by 1 cm.

2.5.1.4 Energy dependence

Unlike for larger-volume chambers, the energy response for microchambers has not been established. Several commercially available microchambers contain collecting electrodes composed of high-Z materials, such as steel and silver-plated copper-clad steel (SPC). These high-Z materials, as well as the larger fraction of the cavity volume occupied by the collecting

electrode, have been shown to cause large collecting electrode perturbations and variations in chamber response with beam quality (Muir and Rogers, 2011; Crop et al., 2009).

2.6 Monte Carlo

2.6.1 Ionization chamber simulations

Monte Carlo simulations have proven extremely useful in the characterization of ionization chambers and related dosimetry protocols (Capote et al., 2004; Borg and Rogers, 1999; Ferreira et al., 1999; Hill et al., 2009; Kawrakow, 2000b). For this investigation, an extended version of the Electron Gamma Shower (EGS) transport code was used, called EGSnrc (Kawrakow, 2000a; Kawrakow et al., 2010). The Stanford Linear Accelerator Center (SLAC) created EGS for use in high-energy Monte Carlo simulations. EGSnrc was later developed by the National Research Council (NRC) to incorporate enhancements such as improved implementation of the condensed history technique and better low-energy cross sections. As a result, EGSnrc is currently applicable for energies of 1 keV to 10 GeV. It has been demonstrated that with these improvements, EGSnrc offers the ability to simulate ionization chamber response with an accuracy level of 0.1% with respect to the underlying cross sections used by the code (Kawrakow, 2000b).

For this investigation it is important to note that EGSnrc source codes are traditionally written in Mortran3, which is an extended Fortran language developed at SLAC for its powerful macro capabilities. To create an executable file, the Mortran source code is converted into Fortran with the Mortran pre-processor in a step called Mortran compiling. The Fortran source code is then compiled into an executable with a standard Fortran compiler. Although it is possible to write EGSnrc user codes entirely in Fortran, the NRC Report PIRS-701 encourages users to continue the use of Mortran3 computing language due to ease of in-line documentation, structure, and macro facility.(Kawrakow et al., 2010)

2.6.2 Charge particle transport in EGSnrc

Monte Carlo simulations rely on a random sampling of probability functions to solve a problem. According to Kawrakow et al. (1998), a typical fast electron will undergo 10^5 to 10^6 elastic and inelastic interactions with the surrounding material while in the process of slowing down. Analog Monte Carlo techniques exist which track each of these collisions along the particle track; however, these simulations are often not possible due to limitations in computing power and time. To improve the efficiency of these simulations, many Monte Carlo codes today use a Condensed History (CH) technique for charged particle transport. This technique was developed by Berger in 1960 (Berger, 1963). Instead of tracking the exact path of an electron and every elastic and inelastic collision that the particle undergoes, the CH Technique relies on a cumulative statistical treatment of the collisions over a specific distance called the step size. Collisions are accounted for with a multiple scattering distribution and the energy and direction of motion at the end of the particle step are altered accordingly (Kawrakow and Bielajew, 1998). Simulations employing the CH technique have been well benchmarked, specifically for ionization chamber simulations (Kawrakow, 2000a).

CH Techniques can be categorized as either Class I or Class II schemes. Monte Carlo codes, such as MCNP, rely on Class I schemes to track charged particles along a predetermined energy grid. This technique is advantageous for multiple scattering events, but can be troublesome when correlating energy loss and secondary particle production during inelastic events. Class II Monte Carlo codes, such as EGSnrc, account for the creation and transport of secondary charged particles (bremsstrahlung and delta particles) with energies above set thresholds (Kawrakow, 2000a).

Charged particle transport in EGSnrc is performed in a subroutine called ELECTR. When a charged particle is created the subroutine is called and the particle goes through a loop called NEWELECTRON. Within this loop, the elastic and inelastic interactions are

accounted for in each charged particle step until the particle is absorbed or reaches a certain energy threshold.

2.6.3 Charge particle transport in an external field

To investigate the effects of electric field perturbations in ionization collection, a novel Monte Carlo (MC) simulation is proposed which incorporates EGSnrc transport in conjunction with an algorithm implemented to account for the electric field deflection and energy alteration of charged particles. EGSnrc is published with an independent Mortran3 macro template developed by Bielajew (1987; 1993), called emf_macros.mortran. This macro is not fully implemented into the EGSnrc source code and is designed only as a start for those wishing to simulate transport in a magnetic or electric field (Kawrakow et al., 2010). The macro has been successfully implemented in several magnetic field investigations (Bielajew, 1987; Kirkby et al., 2008; Takata and Sugita, 2000) including the influence of transverse and longitudinal magnetic fields on dose distributions from MRI-linac and MRI-^{60}Co integrated units (Kirkby et al., 2008, 2010), conformal photon- and electron-beam radiation therapy with magnetic fields (Allen Li et al., 2001), and the effects of fringe magnetic fields from the bending magnet in the linear accelerator treatment head (O'Shea, 2011; O'Shea et al., 2011). In each case, this method was benchmarked against similar simulations performed using a Monte Carlo code called PENELOPE or against measured results.

While the applicability of magnetic fields in EGSnrc applications has been well established, little work has been done to integrate an external electric field into EGSnrc charge particle transport. Originally, the macro was updated and benchmarked by Alex F. Bielajew in Jenkins et al. (1988) for both electric and magnetic fields simulations in EGS4 Monte Carlo code. However, further work published by Bielajew concerning the macro pertained only to magnetic fields.

The transport of a charged particle in a medium in the presence of an electric field can be difficult to model. However, by relying on several macroscopic approximations and the information available at the beginning and end of each EGSnrc CH charged particle step, the presence of the electric field can be accounted for with a high level of accuracy. The theoretical steps to arrive at this conclusion are detailed is Section 6.2.1.

.

Chapter 3

Microionization chamber characterization in a ^{60}Co beam

3.1 Methods and Materials

3.1.1 Ionization chamber selection

The microchambers characterized in this work were all cylindrical, air-filled ionization chambers. As a reference for the behavior of these microchambers, a comparison with several of their larger-cylindrical counterparts was also performed. The chambers were organized into three groups according to a categorization scheme discussed in Section 2.2.3, and are shown with their manufacturer stated dimensions and materials in Table 3.1.

All Exradin chambers used in this work were manufactured by Standard Imaging (SI) of Middleton, WI, the PTW chambers were manufactured by PTW-Frieburg of Frieburg, Germany, and the CC01 chamber was manufactured by IBA Dosimetry of Schwarzenbruck, Germany.

Table 3.1: Each ionization chamber model used in this work and the corresponding nominal collecting volume, the inner diameter (ID) and outer diameter (OD) of the wall, the OD of the collecting electrode, and the thickness of the build-up cap. The materials are PMMA, graphite (Gr), aluminum (Al), air equivalent plastic (C552), steel, and silver-plated copper-clad steel (SPC).

Classification	Chamber model	Collecting volume (cm^3)	Wall		Electrode		Build-up cap	
			Material	ID/OD (mm)	Material	OD (mm)	Material	Thickness (mm)
Farmer-type	PTW N23333*	0.600	PMMA/Gr	6.1/7.1	Al	1.00	PMMA	4.6
	Exradin A12	0.650	C552	6.1/7.1	C552	1.00	C552	2.8
Scanning	Exradin A1SL	0.057	C552	4.15/6.35	C552	1.00	C552	2.0
Micro	PTW TN31006**	0.015	PMMA/Gr	2.0/3.4	Steel	0.18	PMMA	3.0
	PTW TN31014	0.015	PMMA/Gr	2.0/3.4	Al	0.30	PMMA	3.0
	Exradin A14SL	0.016	C552	4.15/6.35	SPC	0.33	C552	2.0
	Exradin A16	0.007	C552	2.4/3.4	SPC	0.33	C552	2.5
	IBA CC01	0.010	C552	2.0/3.0	Steel	0.35	PMMA	3.0
	Proof-of-concept	0.015	C552	3.3/4.3	C552	0.76	N/A	N/A

** PTW N23333 is the predecessor to the PTW N30001 and PTW N30010. The PTW N23333 and N30001 are no longer manufactured.*

*** PTW TN31006 is the predecessor to the PTW TN31014 and is no longer manufactured.*

3.1.2 Saturation curve measurements

Saturation curves were measured for at least one of each of the ionization chamber models displayed in Table 3.1 using the University of Wisconsin Accredited Dosimetry Calibration Laboratory's (UWADCL) Theratron 1000 ^{60}Co irradiator. To minimize the effects of temperature fluctuations of the air in the ^{60}Co vault, all measurements were performed in a $(50x50x47)\,cm^3$ water tank. The PTW N23333 was not inherently waterproof and was placed inside a 1-mm-thick PMMA sleeve. No corrections were applied for the presence of the sleeve because sleeve effects have been shown to be negligible for these measurements (Ross and Shortt, 1992; McEwen, 2010; Buckley and Rogers, 2006).

Irradiations were performed with the ionization chamber perpendicular to the central axis of the beam with a field size of $(10x10)\,cm^2$ at the center of the chamber volume, as

shown in Figure 3.1(a). Ceiling- and wall-mounted lasers were used to position the center of the collecting volume at a distance of 100 cm from the source at a depth of 5 cm in water.

To isolate the effects of the electrometer on chamber response, saturation curves were measured with two electrometer models. Saturation curves were performed for all chambers with a SI MAX 4000 electrometer (Standard Imaging, Middleton, WI) and several saturation curves were reproduced with a Keithley 6517A electrometer (Keithley Instruments, Inc., Cleveland, OH).

3.1.2.1 Standard Imaging MAX 4000 electrometer

Ionization current for each of the ionization chamber models displayed in Table 3.1 was measured using a customized SI MAX 4000 electrometer. In order to apply the desired range of applied voltages, a conventional SI MAX 4000 was altered to supply either the standard internal bias or allow for an external voltage supply. For all saturation curve measurements, a Harshaw High-Voltage (HV) Power Supply was used to supply the entire range of voltages. Photographs of the altered electrometer and HV power supply are shown in Figures 3.1(b) and (c). Using the Harshaw HV power supply, the outer wall of each chamber was held at ground while the collecting and guard electrodes were biased to the voltage of interest. The electrometer was used in conjunction with Standard Imaging's MAX COMM^{TM} Version 2 software to acquire current readings at a sampling rate of 2 Hz.

For each saturation curve the chamber was pre-irradiated for 20 minutes at an applied voltage of $\pm$300 V depending on the polarity of the curve to be measured. For all saturation curves, measurements were performed during negative and positive charge collection with voltages applied in the following order: (300, 150, 75, 35, 10, 300, 400, 500, 600, and 300) V. This semi-randomized order and the repetition of the 300 V measurement provided a check for chamber response consistency and bias trending (McEwen, 2010). The maximum voltage

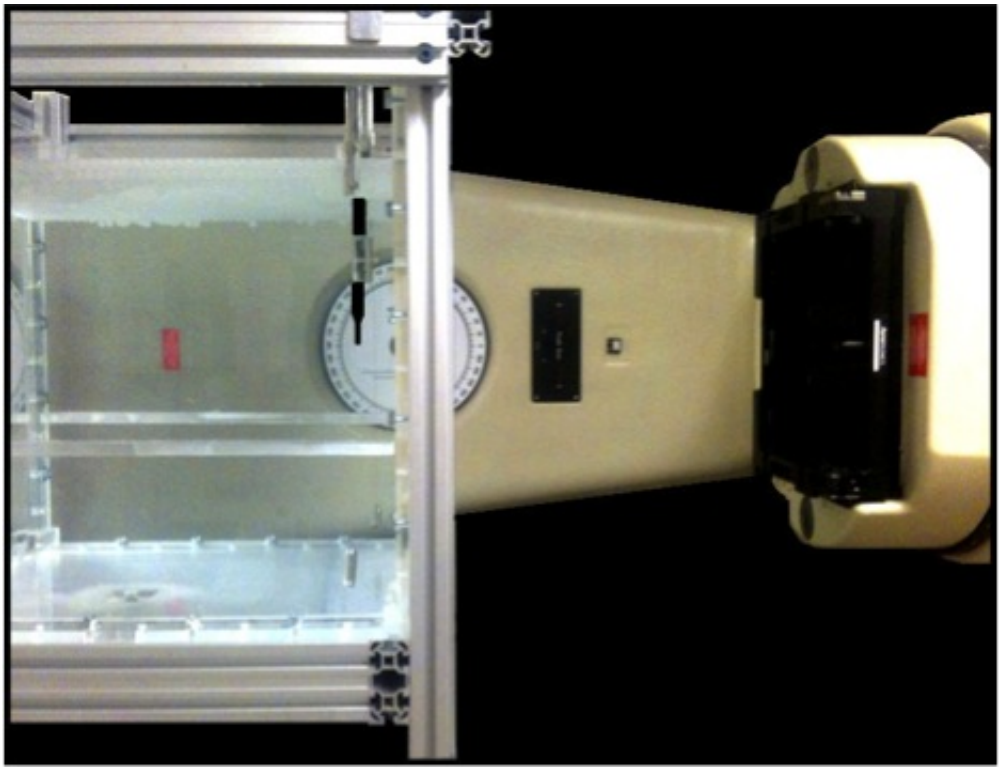

(a)

(b)

(c)

Figure 3.1: Photographs of (a) the chamber set up for saturation curve measurements performed with the UWADCL ^{60}Co irradiator, (b) the altered exterior of SI MAX 4000 electrometer, and (c) the MAX 4000 electrometer and Harshaw HV power supply setup.

applied to the PTW microchambers was 500 V in accordance with the manufacturer stated limits. For each applied voltage the chamber leakage was recorded before and after each irradiation. At each of the ten applied voltages, the chamber was irradiated for 16 minutes allowing for 10 minutes of pre-irradiation followed by 6 minutes of data acquisition.

During data collection, the atmospheric pressure and the temperature of the water were monitored, and a temperature and pressure correction was applied to each data set. Six minutes of data acquisition at a rate of 2 Hz provided 720 separate current readings, which were averaged for each applied voltage.

3.1.2.2 Keithley 6517A electrometer

Saturation curves for the Exradin A14SL microchamber and the Exradin A1SL scanning chamber were reproduced with a Keithley 6517A electrometer. The same chamber setup and external Harshaw HV power supply were used for the SI and Keithley electrometer measurements.

During saturation curve measurements with the Keithley 6517A electrometer, the chambers were pre-irradiated for a minimum of 5 minutes at an applied voltage of ± 300 V depending on the polarity of the curve to be measured. The chamber response was measured with voltages applied in the following order: (300, 150, 75, 35, 10, and 300) V during negative and positive charge collection. For each applied voltage the chamber leakage was recorded before and after each irradiation. At each of the six applied voltages, the Exradin A14SL and A1SL chambers were irradiated for approximately 9 minutes and 5 minutes, respectively.

To collect data, the current was monitored until a rough stabilization in chamber response was achieved. The stabilized current was recorded. The atmospheric pressure and the temperature of the water were also monitored, and a temperature and pressure correction was applied to each current measurement.

3.2 Results and discussion

3.2.1 Leakage and chamber response reproducibility

During each saturation curve measurement performed with the SI MAX 4000 electrometer, three separate 300 V data sets were acquired at each polarity. Figure 3.2 displays the results for each 300 V data set normalized to the first 300 V measurement at the corresponding polarity. For both polarities, the Farmer-type and scanning chambers demonstrated a high level of reproducibility, with a maximum difference of less than 0.07% between any two readings. A slightly larger discrepancy was seen among the microchambers, as was expected due to the decreased signal-to-noise ratio inherent in smaller-volume chambers. A difference as great as 0.65% was seen between measurements performed with the CC01 microchamber, but generally the microchamber measurements were reproducible to within 0.25%.

This investigation also suggested that the sequence of applied voltages did not effect the chamber response reproducibility. In the most extreme case, the CC01 microchamber, the chamber response for the third measurement was reduced by approximately 0.65% for both polarities. Among the remaining chambers, there was a lack of trending between chamber response reproducibility and polarity.

The variation in the chamber response during each of the 6 minutes of data acquisition for each 300 V measurement was also analyzed using the relative standard deviation of each set of 720 current readings. The average relative standard deviation in the response of the chambers was 0.01% for Farmer-type chambers, 0.03% for the scanning chamber, and 0.05% for microchambers.

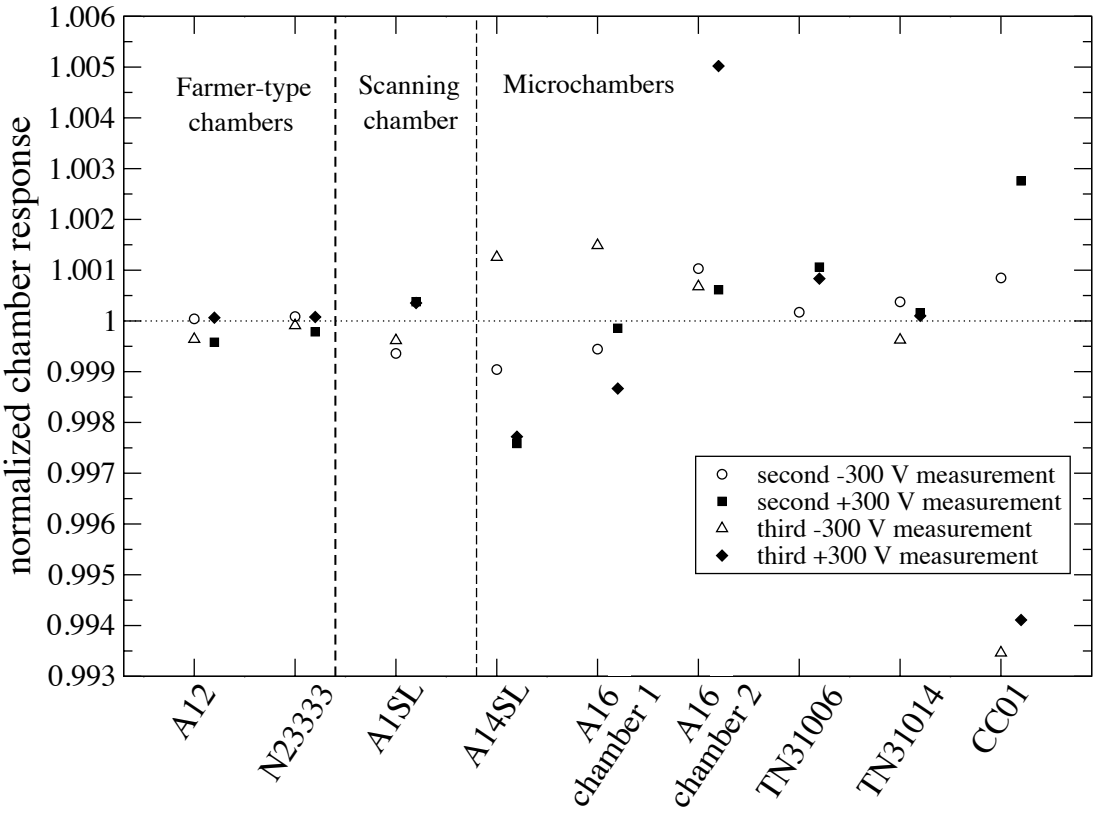

Figure 3.2: Normalized variations in chamber response at applied voltages of ±300 V during saturation curve measurements. All data were normalized to the first 300 V measurement performed at the corresponding polarity. Measurements performed during positive and negative charge collection are represented with open and solid symbols, respectively.

The leakage current for each of the chambers biased to ±300 V was below 10 fA, which corresponded to a maximum of 0.003%, 0.034% and 0.25% of the chamber signal for Farmer-type, scanning, and microchambers, respectively. According to the reference-class chamber guidelines presented in Section 2.3, the leakage signal should compromise less than 0.1% of the chamber signal. The Farmer-type and scanning chambers produced leakage currents well below this limit. For microchambers, a leakage signal of less than 5-7 fA would be

required to limit leakage to less than 0.1% of the chamber signal. While leakage currents less than 5 fA were often achieved, it was difficult to maintain this low leakage current over long periods of irradiation time and large changes in chamber bias. Therefore, a maximum leakage current of 0.010 pA was chosen for this work.

3.2.2 Saturation curves

To gain greater insight into the behavior of each individual microchamber, the shape and relative magnitude of the saturation curves for opposing polarities were analyzed. The average chamber response at each applied voltage was normalized to the average response of the chamber when negative charge was collected at a polarizing voltage of +300 V.

3.2.2.1 Farmer-type ionization chambers

To illustrate the behavior of an ideal ionization chamber, Figure 3.3 displays two normalized saturation curves measured with the Exradin A12 and PTW N23333 Farmer-type chambers. The presence of ion recombination was observed at lower applied voltages. As the applied voltage increased, the collection efficiency improved until a saturation current was achieved. A stable linear plateau in chamber response occurred over a range of applicable voltages and the effects of charge multiplication and cable/stem irradiations were minimal. It is also important to note that for both polarities, each chamber's response was nearly identical suggesting negligible polarity effects, as expected.

3.2.2.2 Scanning ionization chamber

Figure 3.4 shows the relative saturation curves for the Exradin A1SL. The shape of the curves were similar to those of the Farmer-type chambers and the polarity-induced differences in magnitude were relatively small, particularly at the recommended operating voltage of 300 V. However, the response of the chamber failed to reach a consistent satu-

ration plateau over the range of voltages tested. It appeared that excess charge collection was occurring at lower applied voltages with the scanning chamber compared to typical Farmer-type chambers. This excess charge collection may have been in part due to charge multiplication enhancements that can occur at lower applied voltages with smaller-volume chambers, where smaller electrode separations produce stronger electric field strengths inside the chamber cavity. It is possible that this excess charge collection was produced in the Exradin A1SL at low enough applied voltages to compete with ion recombination. This characteristic has been verified in several scanning chambers and microchambers, as discussed in Section 2.3.2.3 (Agostinelli et al., 2008; Palmans et al., 2010), and reinforces the importance of accounting for this excess charge collection in P_{ion} calculations for small-volume chambers.

3.2.2.3 Microionization chambers

The saturation curves measured for each microchamber (shown in Figures 3.6, 3.7, and 3.8) were unique, even for multiple chambers of the same model. The microchambers exhibited anomalous behaviors not seen in typical Farmer-type and scanning chambers. The anomalous microchamber behaviors included: large voltage-independent and -dependent polarity effects, an increase in the slopes of the saturation curves over the entire range of applied voltages, and an inverse proportionality between the chamber response and the applied voltage.

The PTW TN31006 and the IBA CC01 microchambers exhibited strong polarity effects, as demonstrated in Figure 3.6. The magnitude of the polarity effect for each of the chambers was large but relatively consistent for applied voltages less than 300 V, indicating voltage-independent polarity effects at lower applied voltages. At applied voltages greater than 300 V, the chamber response during negative charge collection rapidly increased with the applied voltage, while the chamber response during positive charge collection remained

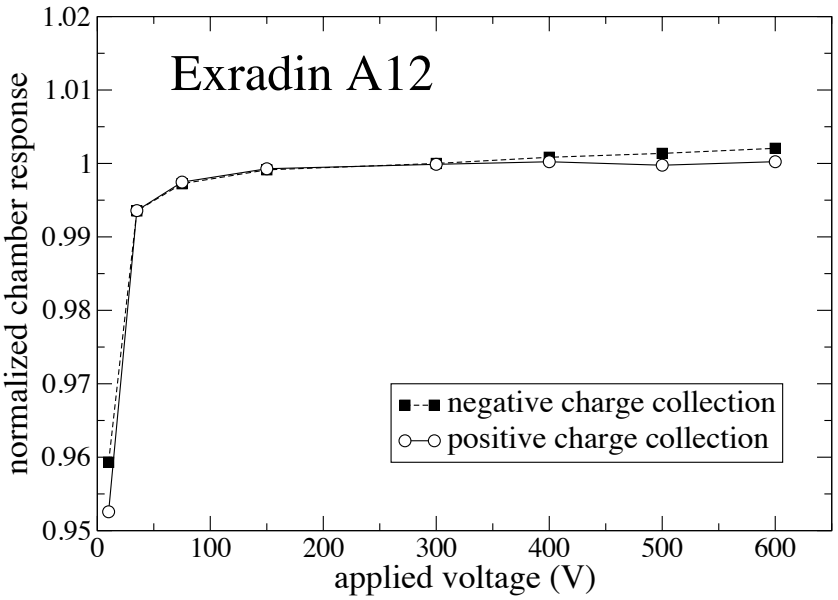

(a)

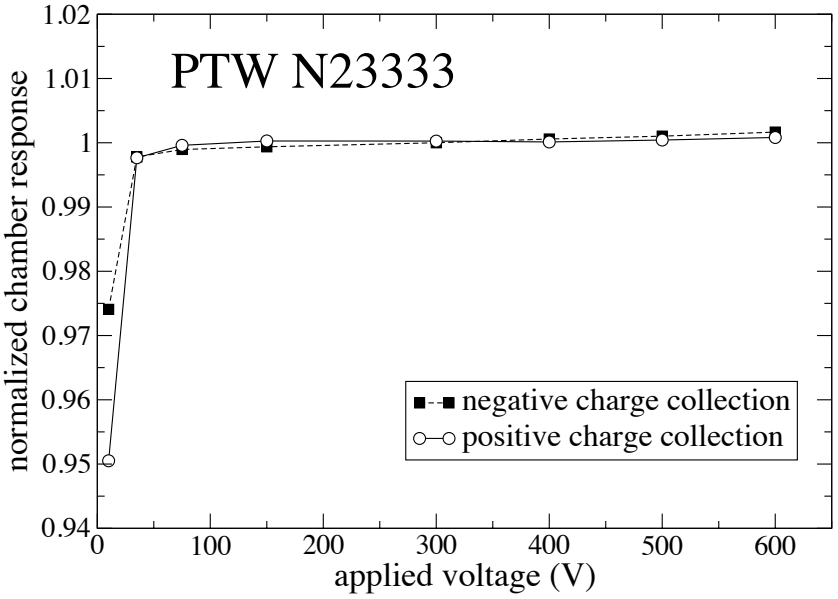

(b)

Figure 3.3: Normalized saturation curves measured with two Farmer-type ionization chambers, (a) an Exradin A12 and (b) a PTW N23333. All data were normalized to the average signal received when the chamber was biased to a polarizing voltage of +300 V (negative charge collection).

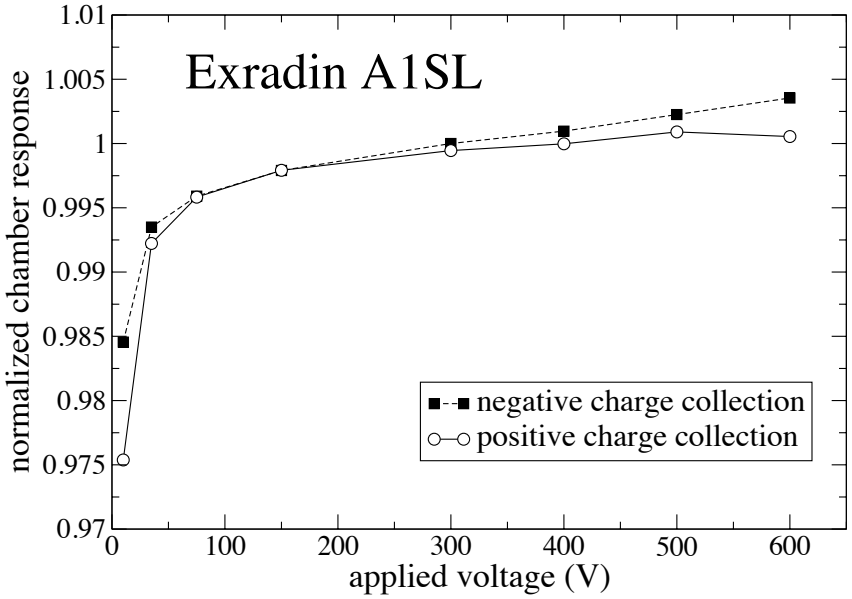

Figure 3.4: Same as Figure 3.3 except for an Exradin A1SL scanning ionization chamber.

relatively constant, even at applied voltages as high as 600 V. This suggested that at applied voltages greater than 300 V, an anomalous voltage-dependent effect occurred.

Further complications occurred during saturation curve measurements with the PTW TN31006 microchamber. Applying a voltage of greater than approximately 450 V caused the chamber response and leakage current to spike. A jump in the leakage current from ± 0.010 pA to ± 0.500 pA would occur when the applied voltage was increased from 400 V to 500 V. This behavior remained for several hours after reducing the applied voltage. To determine the cause of this behavior, radiograph images of the internal components of the chamber were taken. From the radiograph image shown in Figure 3.5, it was clear that the tip of the collecting electrode frayed producing a cluster of burr like strands. It is likely that at applied voltages greater than 450 V the electric field between the frayed collecting electrode burrs and the wall electrode became strong enough to produce arcing across the electrodes creating a path for large, unstable leakage currents. Therefore, all measurements

performed with the PTW TN31006 microchamber were performed with an applied voltage of $\leq$400 V.

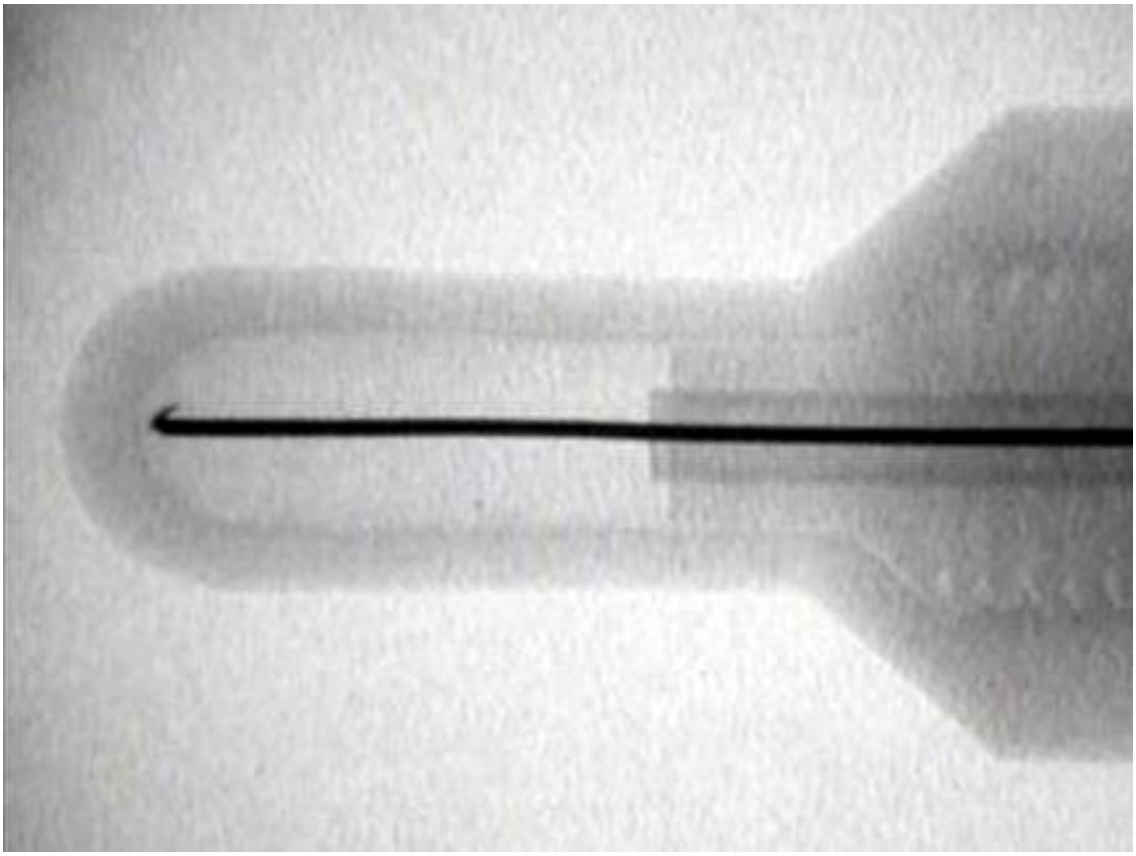

Figure 3.5: A radiograph of the PTW TN31006 microionization chamber characterized in this work.

The saturation curves measured with the PTW TN31014 microchamber, shown in Figure 3.7(a), exhibited strong voltage-dependent polarity effects for applied voltages less than 300 V. At applied voltages greater than 300 V the magnitude of the chamber response varied with polarity; however, it is uncertain if the polarity effect was voltage dependent or voltage independent. The most anomalous behavior exhibited by the PTW TN31014 microchamber was the inverse proportionality between the chamber response and the applied voltage for negative charge collection at applied voltages less than 300 V. This phenomenon masked the effects of ion recombination, making conventional ion recombination correction methods

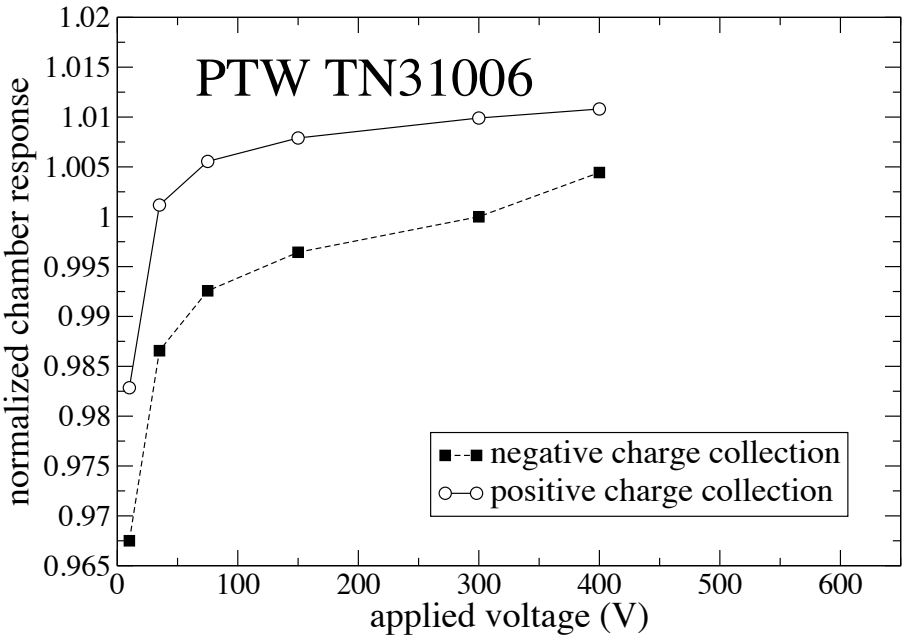

(a)

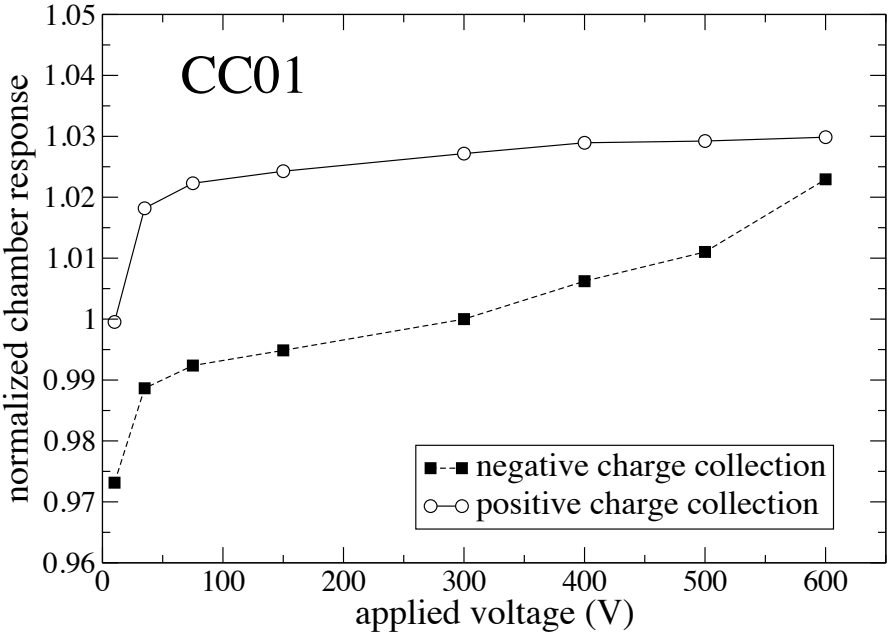

(b)

Figure 3.6: Same as Figure 2 except for two microionization chambers; (a) a PTW TN31006 and (b) an IBA CC01.

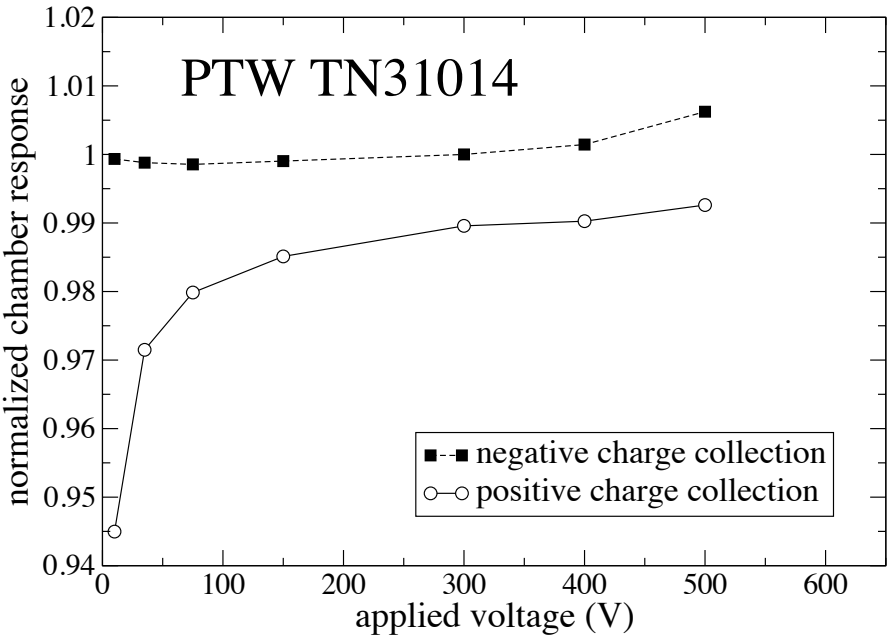

(a)

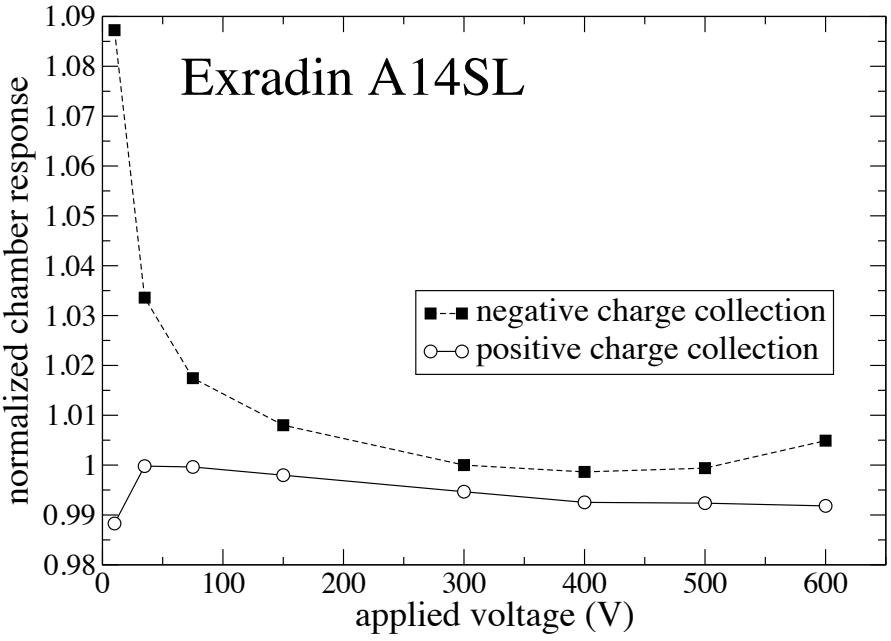

(b)

Figure 3.7: Same as Figure 2 except for two microionization chambers; (a) a PTW TN31014 and (b) an Exradin A14SL.

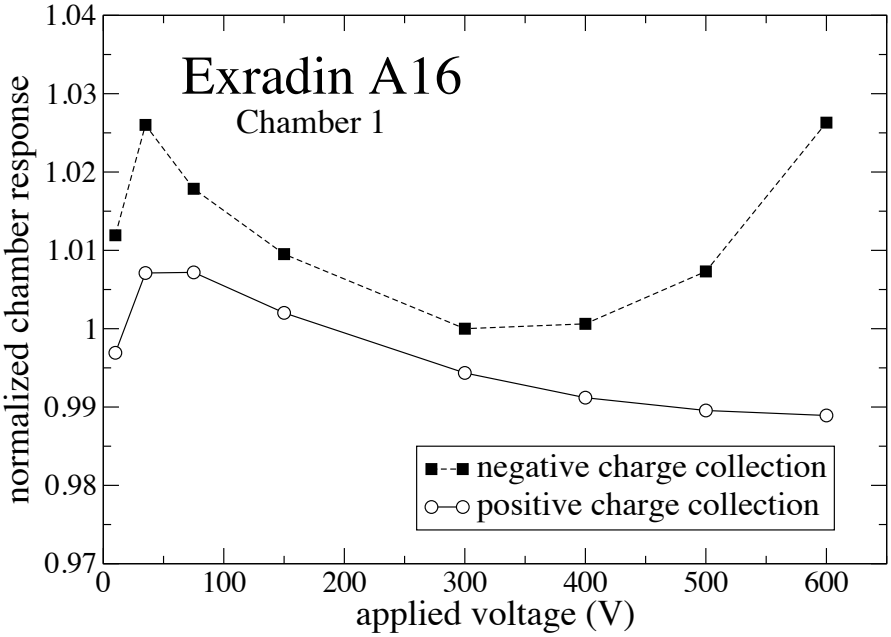

(a)

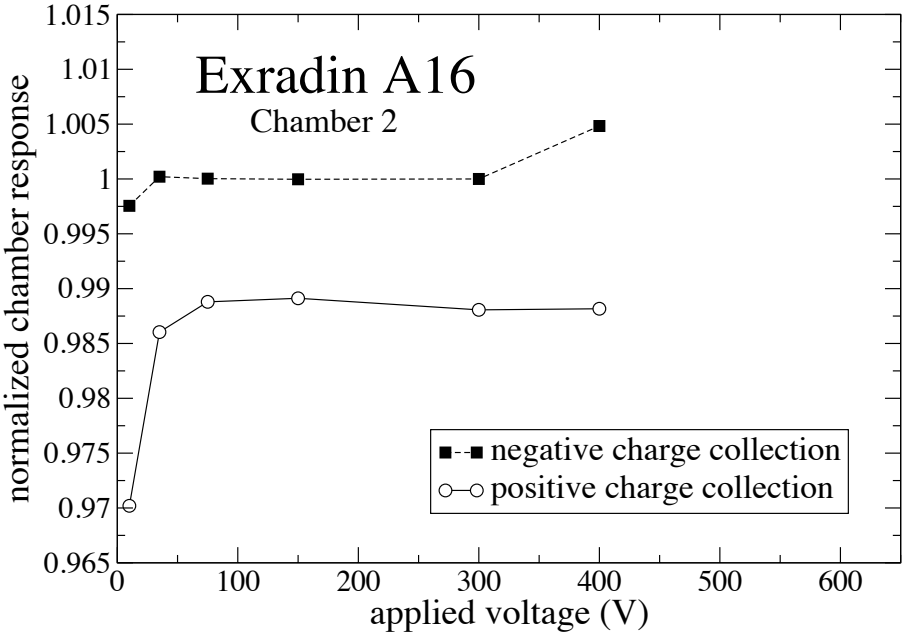

(b)

Figure 3.8: Same as Figure 2 except for two Exradin A16 microchambers.

ineffective. While this unexplained increase in chamber response with decreasing applied voltage has been reported for a few microchambers (Le Roy et al., 2011), the cause of this behavior is unknown.

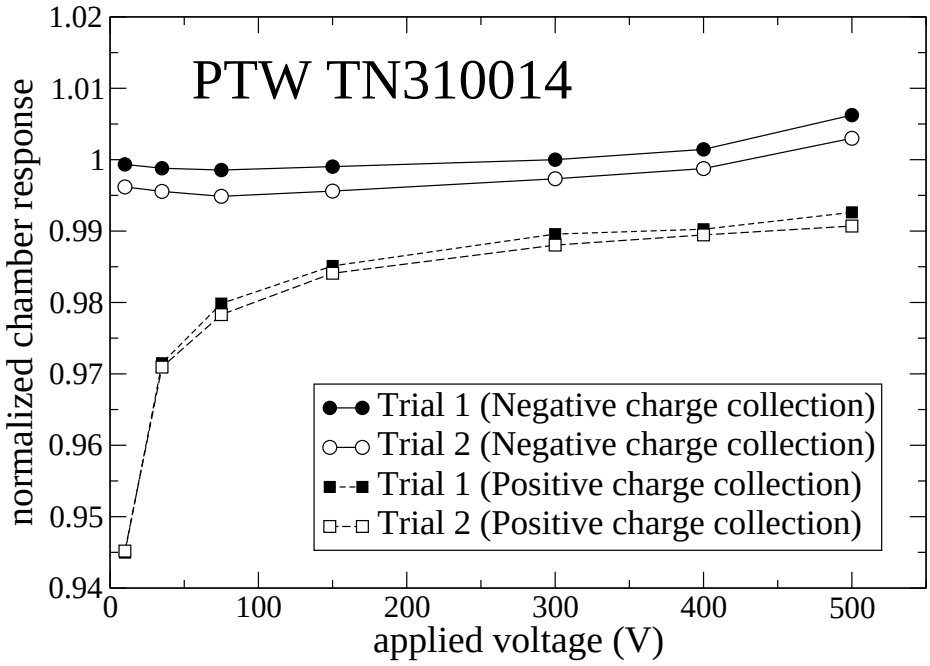

Figure 3.9: Two sets of normalized voltage curves measured 24 hours apart with a PTW TN31014 microchamber. The initial (Trial 1) and repeated (Trial 2) measurements are shown with solid and open symbols, respectively. All data were normalized to the average signal received during Trail 1 when the chamber was biased to a polarizing voltage of +300 V (negative charge collection).

The Exradin A14SL microchamber, shown in Figure 3.7(b) exhibited the anomalous increase in chamber response with decreasing voltage, similar to the PTW TN31014. However, unlike the PTW TN31014, the Exradin A14SL exhibited this behavior during both positive and negative charge collection. While the chamber response varied inversely with applied voltage for both polarities, the effect was more extreme during negative charge collection, suggesting that the polarity effect was still voltage dependent. Significant excess charge collection occurred at voltages greater than 300 V when negative charge was collected. However, there was no evidence of this effect during positive charge collection. In

fact, the chamber response continued to decrease with increasing voltage during positive charge collection, even at applied voltages as great as 600 V.

The saturation curves from two Exradin A16 chambers (Chambers 1 and 2) were measured to compare variations within chamber models. The first Exradin A16, shown in Figure 3.6(c), exhibited behavior similar to the Exradin A14SL. Most notable was the shape of the saturation curve at lower applied voltages where the chamber response increased with decreasing voltage by more than 1.3% and 2.6% for negative and positive charge collection, respectively. The chamber response also varied significantly with polarity for applied voltages greater than 300 V. The second Exradin A16, shown in Figure 3.6(d), demonstrated a more standard saturation curve. From 35 V to 300 V, the offset due to polarity was relatively constant indicating a large voltage-independent polarity effect. However, the response still demonstrated a slight increase in the chamber response with decreasing voltage of 0.11% and 0.02% for negative and positive charge collection, respectively. Both Exradin A16 chambers demonstrate anomalous behaviors; however, the magnitude and character of these behaviors varied between the two chambers.

To check the reproducibility and consistency in the shape of these microchamber saturation curves, the PTW TN31014 measurements were repeated 24 hours after the initial saturation curve measurements. The same methodology was used except that the order of the polarity in which the signal was measured was reversed to evaluate any variations resulting from pre-irradiation effects or bias trending. As shown in Figure 3.9 the relative magnitude in the chamber response varied slightly, as was expected from the chamber reproducibility study discussed in Section 3.2.1, but the shapes of the curves were consistent in all cases. Measurements were repeated with several of the microchambers, and similar results were obtained. This suggests that, while the behavior of microchambers varies significantly from chamber to chamber, the response of an individual chamber is consistent and reproducible.

3.2.3 Electrometer isolation

As mentioned in Section 3.1.2, it was necessary to isolate the behavior of the chambers from any effects of the electrometer. Therefore, measurements were repeated for the Exradin A1SL scanning chamber and the Exradin A14SL microchamber using a Keithley 6517A electrometer. The saturation curves measured with both the altered SI MAX 4000 and the Keithley 6517A electrometers are shown in Figure 3.10. For each chamber, the relative shapes of the saturation curves were consistent and independent of the electrometer type. These results suggest that the characterizations performed with the SI MAX 4000 electrometer represent an accurate assessment of the chamber behavior, and the anomalous behaviors of the microchambers were not a consequence of the electrometer setup.

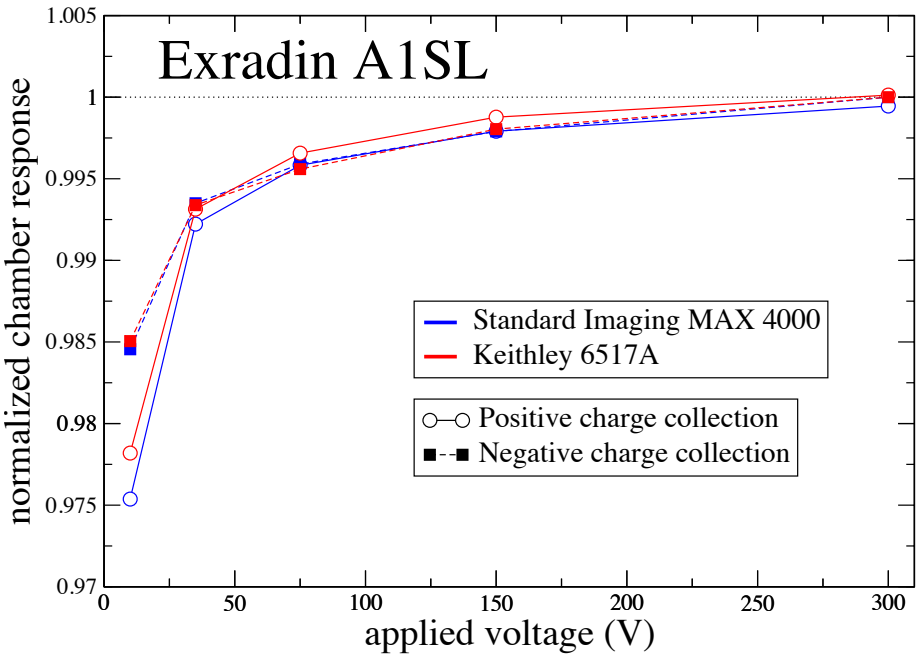

Figure 3.10: Normalized saturation curves measured for the Exradin A1SL scanning chamber using an altered SI MAX 4000 electrometer and a Keithley 6517A electrometer shown in blue and red, respectively. All data were normalized to the +300 V measurement (negative charge collection) for each electrometer.

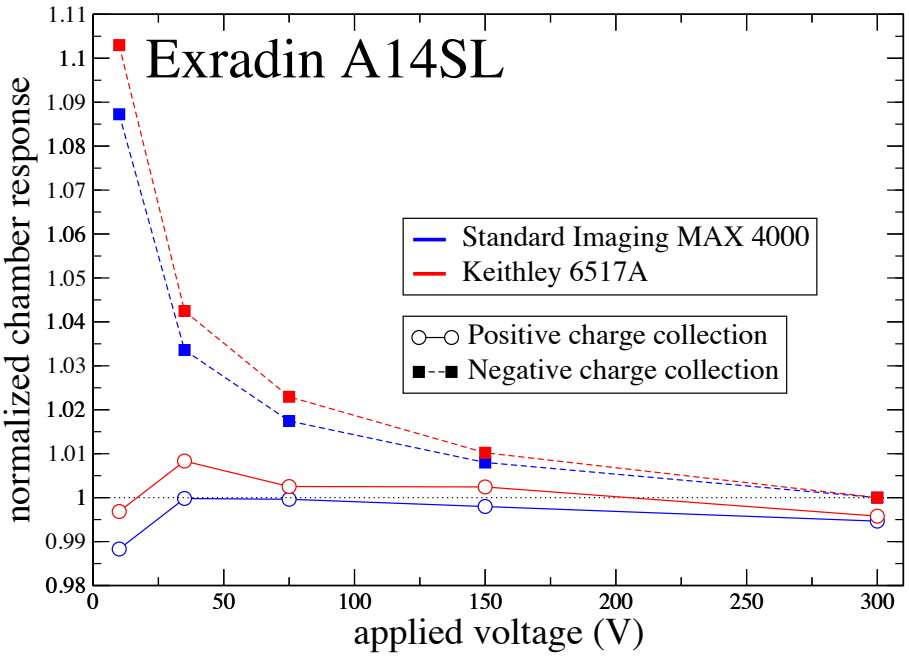

Figure 3.11: Same as Figure 3.10 except for the Exradin A14SL microchamber

3.2.4 Polarity correction factors

The polarity correction factor, P_{pol}, was calculated for each chamber using the method suggested by TG-51 (described in Section 2.3.1.1) for the three 300 V data sets collected during the saturation curve measurements. All P_{pol} values were calculated for negative charge collection, $P_{\text{pol}}(+300\,\text{V})$, corresponding to the UWADCL calibration conditions (i.e., $M_{\text{raw}} = M_{\text{raw}}^{-}$). The resulting P_{pol} values are shown in Table 3.2.

TG-51 states that P_{pol} values should differ from unity by no more than 0.3% for most chambers (Almond et al., 1999). To qualify as a reference-class chamber, P_{pol} should be within 0.4% of unity (McEwen, 2010). The correction factors for all Farmer-type and scanning chambers were well within 0.3% from unity. Furthermore, the percent standard deviation of the three P_{pol} measurements was no greater than 0.03% for any chamber.

Polarity effects for microchambers were significantly greater than those of their larger counterparts, which is consistent with other published data (McEwen, 2010; Le Roy et al.,

Table 3.2: Polarity correction factors calculated using the TG-51-recommended method (see Equation 2.11). Three 300 V measurements were performed during each saturation curve measurement, at the beginning (1), middle (2), and end (3) of data acquisition, which were used to calculate the reported correction factors.

Chamber classification	Chamber model	P_{pol}(+300 V)				
		1	2	3	Mean	Standard deviation (%)
Farmer-type	PTW N23333	1.000	1.000	1.000	1.000	0.01
	Exradin A12	1.001	1.002	1.002	1.002	0.07
Scanning	Exradin A1SL	1.000	1.000	1.000	1.000	0.03
Micro	PTW TN31006	1.009	1.009		1.009	0.03
	PTW TN31014	0.9948	0.9949	0.9946	0.9948	0.02
	Exradin A14SL	0.9965	0.9972	0.9983	0.9973	0.09
	Exradin A16	0.9968	0.9966	0.9982	0.9972	0.09
	IBA CC01	1.014	1.013	1.014	1.014	0.05

2011; Agostinelli et al., 2008). The P_{pol} values for all microchambers fell outside the 0.3% range with the exception of one Exradin A16 model and the Exradin A14SL model, which demonstrated the largest variations in P_{pol} values with a percent standard deviation of nearly 0.1%. Although the correction factor for these two Exradin chambers fit the requirements for TG-51 reference dosimetry and those of a reference-class chamber, it is clear from the saturation curves shown in Section 3.2.2 that the polarity effects for these chambers are significant and voltage-dependent. To accurately assess the behavior of a microchamber, it is not sufficient to take a snap shot of the polarity effect at one applied voltage. The issue with current dosimetry protocols is that in determining the applicability of a chamber, they fail to consider whether the polarity effect of the chamber remains consistent over the range of applicable voltages.

3.2.5 Ion recombination correction factors

Ion recombination correction factors, P_{ion}, for applied voltages of ±300 V were determined for each chamber using both the two-voltage technique ($|V_H|$=300 V and $|V_L|$=150 V) and Equation 2.19. Equation 2.19 was fit to a range of applied voltages (35 V to 300 V). Since ion recombination becomes negligible at higher voltages, the 400 V, 500 V, and 600 V data sets were excluded from this technique. Furthermore, Equation 2.19 relies on the assumption that higher order terms are negligible and therefore omitted. It has been shown that for polarizing voltages less than 30 V, these higher order terms may be significant and Equation 2.19 may no longer be valid (Palmans et al., 2010); therefore, the 10 V measurements were excluded as well. The results of this analysis are shown in Table 3.3.

Table 3.3: Ion recombination correction factors calculated using the TG-51-recommended two-voltage technique and a fit of the data to Equation 2.19. Correction factors were calculated for an applied voltage of 300 V at both polarities and the percent standard deviation of the factors was calculated.

Chamber	Chamber	P_{ion}(Equation 2.19)		P_{ion}(two-voltage)		Standard
classification	model	+300 V	-300 V	+300 V	-300 V	deviation (%)
Farmer-type	PTW N23333	1.000	1.000	1.000	1.000	0.00
	Exradin A12	1.001	1.000	1.001	1.000	0.01
Scanning	Exradin A1SL	1.001	1.001	1.001	1.001	0.01
Micro	PTW TN31006	1.001	1.001	1.001	1.001	0.02
	PTW TN31014	0.9998	1.002	1.000	1.000	0.1
	Exradin A14SL	1.015	1.003	0.9979	0.9989	0.4
	Exradin A16	1.013	1.008	0.9970	0.9974	0.8
	IBA CC01	1.000	1.000	1.002	1.002	0.2

Table 3.3 shows that the Farmer-type and scanning chambers responded as expected, producing consistent P_{ion} values among the different calculation techniques, all of which were greater than unity and significantly less than the TG-51 recommended value of 1.05. Furthermore, P_{ion} for each chamber was consistent to within 0.1% for both polarities. According to the reference-class requirements discussed in Section 2.3, it was also important

that the Jaffé plots for these chambers remained linear over a range of applicable applied voltages. For continuous beams, the inverse chamber response relies on an additional term containing the square of the applied voltage, as shown in Equation 2.18; however, this term accounts for general recombination, which is considered negligible for continuous beams. Therefore, the linearity between the inverse chamber response and the inverse applied voltage may still be held as an approximate guideline for continuous beams. Figure 3.12(a) shows the Jaffé plots for the Exradin A12 chamber as well as a fit of Equation 2.19 to the data. For both polarities, the curves were linear. The coefficients calculated with Equation 2.19 demonstrated negligible exponential excess charge, with $e^{-\gamma V} = 1$ for all applied voltages in this work (i.e., $\gamma \approx 0$). These results agreed well with the observations from the A12 saturation curves, which demonstrated a plateau in the chamber response at a saturation current. This stable plateau suggests the absence of excess charge due to exponential effects, such as charge multiplication and stem effects, were negligible.

The Jaffé plots for the Exradin A1SL scanning chamber are shown in Figure 3.12(b). The fit of Equation 2.19 to the data demonstrated that the inverse chamber response was not linear with the inverse applied voltage. This nonlinearity agreed with the saturation curve results for this chamber shown in Figure 3.4. The saturation curves suggested excess charge collection over a range of applied voltages, likely due to an exponential term such as charge multiplication or stem effects. The coefficients calculated from the fit of Equation 2.19 to the Jaffé plots further validate this assumption, with $\gamma = 1.04E-5$ and $\gamma = 7.84E-6$ for positive and negative charge collection, respectively. These values of γ correspond to the exponential excess charge accounting for 0.3% and 0.2% of the chamber signal at an applied voltage of -300 V and +300 V, respectively. A corrected Jaffé plot for the Exradin A1SL which uses these results to account for the exponential excess charge is shown in Figure 3.13(a). With the exponential correction, the curves were linear and satisfied the reference-class requirement. To demonstrate the benefits of this technique further, the

original and corrected saturation curves for the Exradin A1SL are shown in Figure 3.13(b). The curves corrected for exponential excess charge collection demonstrated a desirable flat plateau in chamber response over a range of applied voltages, as was expected in the absence of charge multiplication or stem effects. These results show the advantage of this robust fit for smaller volume chambers, such as the A1SL scanning chamber, where excess exponential charge becomes significant.

Unlike the Farmer-type and scanning chambers, the P_{ion} values for microchambers varied significantly, often falling below unity which is nonsensical by the definition of ion recombination. Each microchamber in this work, with the exception of the PTW TN31006, also demonstrated P_{ion} values which varied by more than 0.1% with polarity. However, it is important to note that several of the microchambers in this work exhibited P_{ion} values greater than unity and below 1.05, thus meeting the TG-51 requirements regarding ion recombination. These results could be very misleading. From the saturation curves presented in Section 3.2.2.3, it was clear that none of the chambers exhibited typical ion recombination effects. Without a thorough chamber characterization, it may not be clear if these chambers exhibit reference-class behavior. Specifically, if only one polarity is examined, which is often the case in clinical situations, several of these anomalous behaviors may be missed. This work emphasizes the importance of investigating P_{ion} at both polarities, as well as the importance of the reference-class guideline which requires the inverse chamber response to vary linearly with the inverse applied voltage in a Jaffé plot. While some of the microchamber P_{ion} values in Table 3.3 may appear correct, one must look at the Jaffé plot to determine if the P_{ion} calculation technique is properly accounting for ion recombination.

The Jaffé plots for each microchamber [Figures 3.14(a) and (b)] were unique and varied significantly with polarity. Several microchambers, such as the Exradin A14SL shown in Figure 3.14(b), exhibited fits with negative slopes, which suggested that contributions from initial recombination, ion diffusion, and general recombination caused an inverse propor-

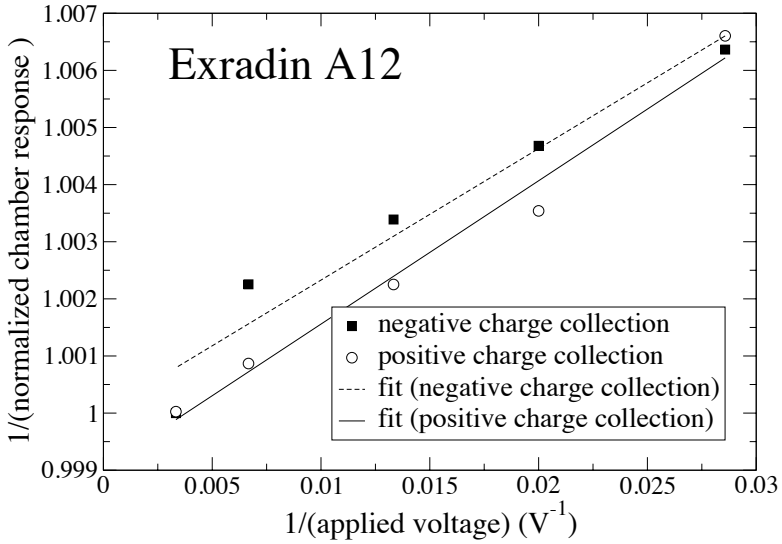

(a)

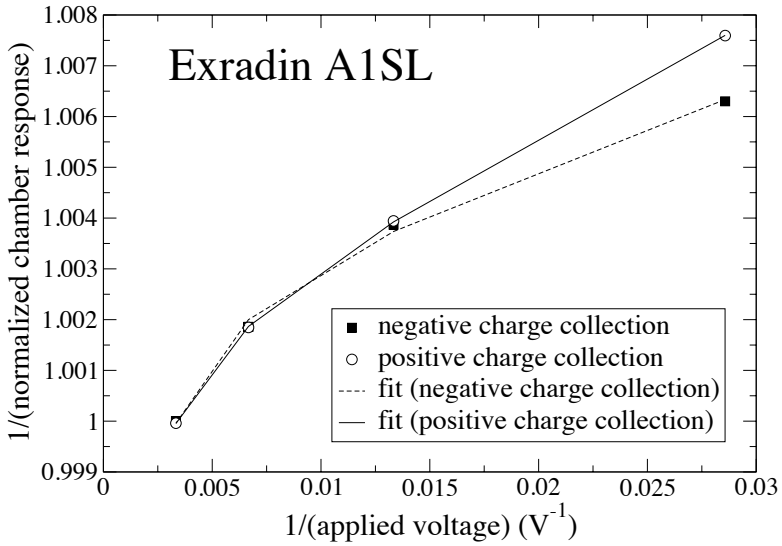

(b)

Figure 3.12: Jaffé plots for (a) an Exradin A12 Farmer-type chamber and (b) an Exradin A1SL scanning chamber normalized to the average signal received when each chamber was biased to +300 V. The fit of Equation 2.19 to the data is represented by the dashed and solid lines for negative and positive charge collection, respectively.

tionality between the chamber response and applied voltage. Applying constraints to the fit of Equation 2.19 to prevent this anomalous behavior, produced fits with poor agreement

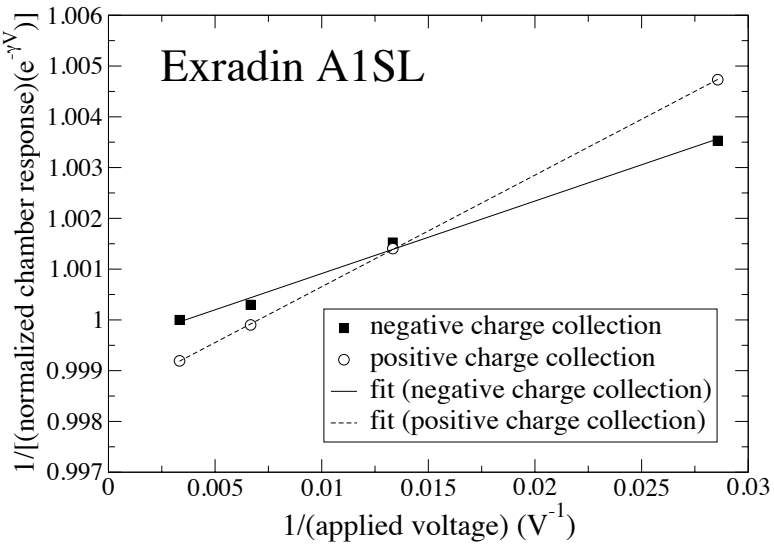

(a)

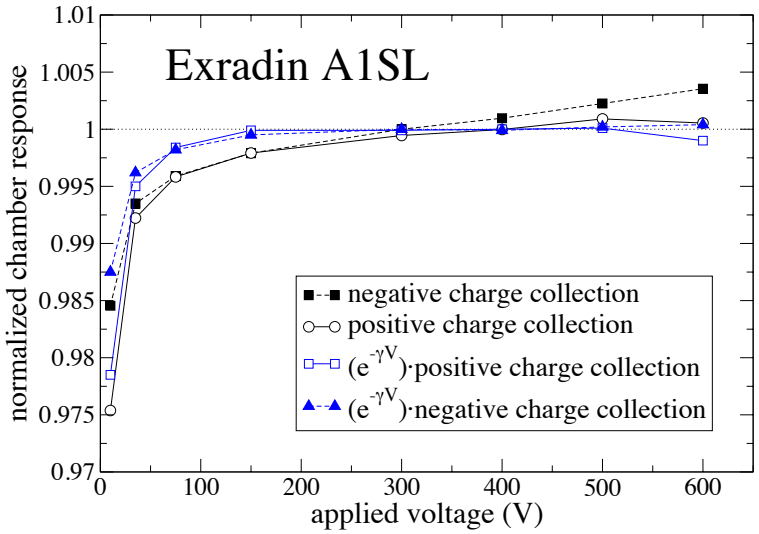

(b)

Figure 3.13: (a) The normalized Jaffé plot of the Exradin A1SL shown in Figure 3.12(a) except all data were corrected for any multiplicative effects, $e^{-\gamma V}$. (b) The saturation curve of the Exradin A1SL before (from Figure 3.4) and after all data were corrected for any multiplicative effects, represented with black and blue symbols, respectively.

to the data, which ultimately failed to account for ion recombination. These figures high-

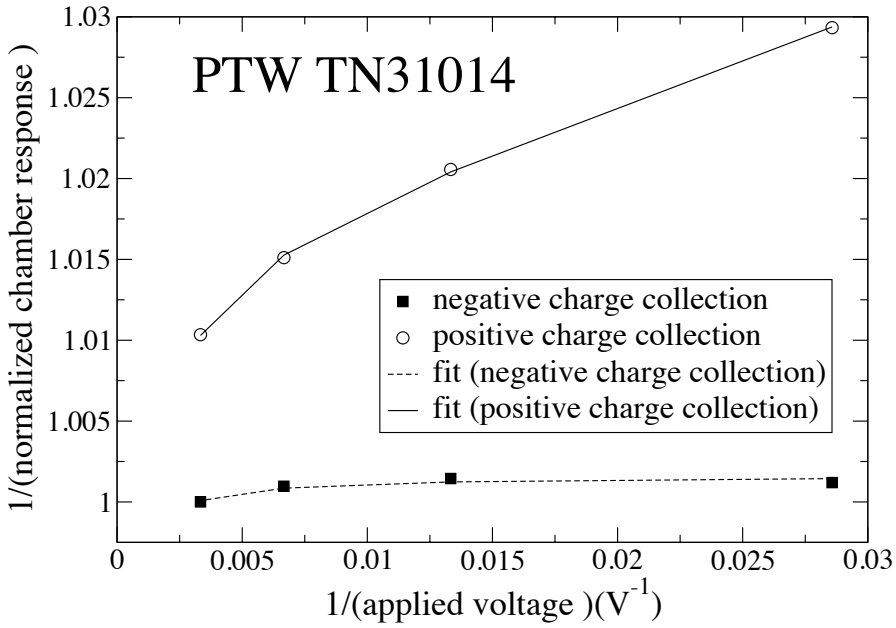

(a)

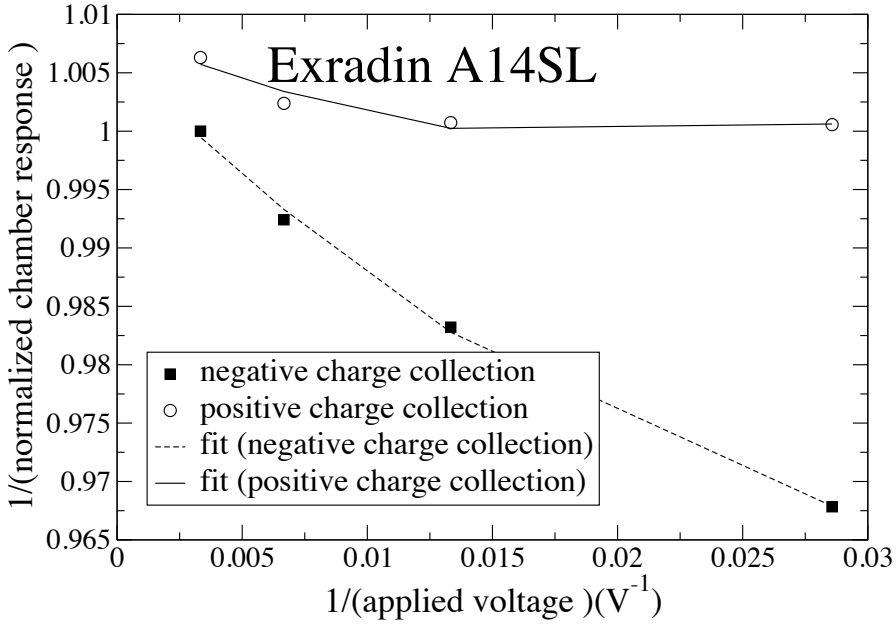

(b)

Figure 3.14: The same as Figure 3.12 except for (a) a PTW TN31014 microchamber, and (b) an Exradin A14SL microchamber.

light the importance of ion recombination correction guidelines and the inability of even the current robust methods to accurately account for ion recombination for microchambers.

3.3 Conclusions

For the microchambers investigated in this work, the chamber response for a given polarity at 300 V was reproducible to within 0.25%. The average relative standard deviation in the chamber current over a given measurement set, once the chamber response stabilized, was 0.05%. Prior to any measurement, a leakage current of less than 0.010 pA was achieved, corresponding to a maximum of 0.25% of the microchamber signal; however, in most cases, the leakage current was less than 0.010 pA and within the 0.1% limit of the reference-class guidelines outlined in Section 2.3.

The microchambers exhibited anomalous behaviors not seen in typical Farmer-type and scanning chambers. The undesirable microchamber behaviors included: large voltage-independent and -dependent polarity effects, an inconsistent increase in the slopes of the saturation curves over the entire range of applied voltages, and an inverse proportionality between the chamber response and the applied voltage. The behavior of the microchambers varied from chamber to chamber, even among the same model; however, the behavior of an individual chamber was consistent.

The polarity correction factors for the microchambers in this work were greater than those of the scanning and Farmer-type chambers. However, several chambers exhibited P_{pol} values within the recommended limits. The saturation curves showed that the polarity effects for these chambers were highly voltage dependent. Thus, P_{pol} values calculated for only the applied voltage of interest, were not sufficient to assess whether the polarity effects of the chamber were acceptable. A larger range of voltages must be measured for both polarities, and the change in chamber response must be analyzed to deduce if the chambers meet reference-class dosimetry requirements.

During ion recombination calculations, excess charge collection due to exponential terms, such as charge multiplication and stem effects, were observed for the Exradin A1SL scanning chamber. The excess charge may have occurred at low enough applied voltages to compete with ion recombination. It was demonstrated that the robust ion recombination correction technique, employing a fit of Equation 2.19 to the Jaffé plot, was beneficial for smaller volume chambers where exponential excess charge occurred. However, for the microchambers in this work, it was clear from the the saturation curves and Jaffé plots that even this robust method could not account for ion recombination. Although several of the microchambers produced reasonable P_{ion} values that were above unity and below 1.05, the Jaffé plots showed that Equation 2.19 could not accurately account for ion recombination. Therefore, P_{ion} calculations alone are not sufficient to deduce the applicability of a microchamber. A full saturation curve must be measured for microchambers prior to reference-dosimetry measurements. Furthermore, ion recombination correction was not possible using current methods for several of the microchambers. The cause of these anomalous behaviors must be better understood and accounted for or eliminated through optimized microchamber design.

Chapter 4

Microionization chamber characterization in high-energy pulsed photon beams

Although ^{60}Co is used to treat patients in the clinic and is the standard for chamber calibrations, the majority of external beam treatments are delivered with a high-energy pulsed photon beam using a linear accelerator (linac). Therefore, it is important to characterize microchambers for linac beams to determine if the anomalous behaviors demonstrated by microchambers for ^{60}Co beams translate to high-energy pulsed photon beams. To achieve this goal, saturation curves for each of the chambers characterized in Chapter 3 were measured in a 6 MV pulsed photon beam.

As stated in Section 2.3.2.4, a robust assessment of a chamber's behavior is the variation of P_{ion} with the dose per pulse of the radiation beam McEwen (2010). Several authors have investigated this relationship for Farmer-type chambers, providing a comprehensive method to benchmark this work against literature values. Therefore, in this chapter, P_{ion} was measured with a Farmer-type chamber and a microchamber for a continuous beam and

several pulsed linac beams with dose-per-pulse values ranging from 0.27 mGy/pulse to 0.40 mGy/pulse.

4.1 Methods and Materials

Saturation curves were measured for a Varian Clinac iX linear accelerator beam at the University of Wisconsin Carbone Cancer Center using a similar methodology to that of the ^{60}Co saturation curve measurements discussed in Chapter 3. Measurements were made in a $(32x28x36)\,\mathrm{cm}^3$ SI water tank. A reference ionization chamber was used to monitor variations in output from the linear accelerator. The reference chamber, an Exradin A12 Farmer-type chamber, was placed inside the water tank at the edge of the field as shown in Figure 4.2. During irradiation the response of the reference chamber and chamber of interest were recorded simultaneously. Irradiations were performed with the ionization chamber of interest perpendicular to the central axis of the beam with a field size of $(10x10)\,\mathrm{cm}^2$ at the center of the chamber volume. The light field cross hairs and the optical distance indicator of the linear accelerator were used to position the center of the collecting volume at a distance of 100 cm from the source at a depth of 5 cm in water. Ionization current of the chamber of interest was measured using the same customized SI MAX 4000 electrometer and Harshaw HV Power Supply as used in the ^{60}Co measurements [shown in Figure 3.1(b)]. Reference chamber measurements were performed with a standard (non-altered) SI Max 4000 electrometer. Both electrometers were used in conjunction with Standard Imaging's MAX COMM$^{\mathrm{TM}}$ Version 2 software to acquire current readings at a sampling rate of 2 Hz.

4.1.1 Characterization in a 6 MV photon beam

One of each of the ionization chamber models displayed in Table 3.1 was characterized for the 6 MV pulsed photon beam. For each saturation curve, the chamber was pre-irradiated for a

Figure 4.1: Photograph of the experimental setup for ionization chamber measurements with the Varian Clinic iX linear accelerator.

Figure 4.2: Photograph of the measurement setup with an Exradin A12 chamber of interest and reference chamber.

minimum of 20 minutes with an applied voltage of ±300 V corresponding to the polarity of the curve to be measured. For the 6 MV saturation curve measurements, additional voltages were measured to ensure accurate ion recombination calculations. The measurements were performed in the following order: (300, 150, 100, 75, 50, 35, 10, 300, 400, 500, 600, and 300) V for positive and negative charge collection. The maximum voltage applied to the PTW TN31006 microchamber was 400 V due to the arcing issue described in Section 3.2.2.3. For each applied voltage the chamber leakage was recorded before and after irradiation. At each of the twelve applied voltages, the chamber was irradiated for 16 minutes allowing for 10 minutes of pre-irradiation followed by 6 minutes of data acquisition. During data collection the atmospheric pressure and the temperature of the water were monitored, and a temperature and pressure correction was applied to each data set. Six minutes of data acquisition at a rate of 2 Hz provided 720 separate current readings, which were averaged for each applied voltage.

4.1.2 Variations in ion recombination with the dose per pulse

Saturation curves were measured for an Exradin A12 Farmer-type chamber and A14SL microchamber at both polarities, for three dose-per-pulse, D_{pp}, values in addition to the curves measured in the ^{60}Co beam (Section 3.2.5) and the 6 MV pulsed photon beam (Section 4.2). The same set-up described in Section 4.1.1 was used, with the exception of the data acquisition time. Due to the higher dose rate of the linear accelerator beams measured in this section, the chambers were irradiated at each applied voltage for 10 minutes allowing for 8 minutes of pre-irradiation followed by 2 minutes of data acquisition. To achieve the different D_{pp} values, the energy and source-to-surface distance (SSD) of the water tank were altered.

An additional Exradin A12 Farmer-type chamber was used to measure the dose to water, D_{w}, in each beam at each SSD. The charge measured by the Exradin A12 chamber was

recorded over a period of time, t, of 30 sec, and D_{w} was calculated using Equation 2.8. For a given dose rate, the D_{pp} was calculated as

$$D_{\mathrm{pp}} = \frac{D_{\mathrm{w}}/t}{\dot{P}}, \tag{4.1}$$

where $\dot{P}$ is the pulse rate in Hz or pulses per sec. The final pulse rate of the beam is dependent on several parameters, including the klystron and console gun trigger frequencies which are constant for a given energy mode, the repetition rate or dose rate specified by the linac operator, and the gun pulse repetition frequency (GPRF) logic by which the machine skips pulses to create the desired pulse and dose rate. According to the Varian Systems Manual, the klystron and the gun triggers are pulsed at a constant repetition rate for a given energy mode. For the low energy mode, which includes the 6 MV and 10 MV x-ray beams, the frequency of the triggers is 360 Hz. To control the dose rate the system drops or disables specified pulses. To drop a pulse, the system alters the timing of the gun pulses so that specified gun pulses are not coincident with the klystron trigger. The amount of pulses dropped is determined by the dose rate selected by the operator at the console. Dose rates ranging from 100 MU/min to 600 MU/min are available for the Varian Clinac iX. For each selected dose rate, the gun trigger is timed to drop a percentage of pulses in a six pulse sequence. For saturation curve measurements, a dose rate of 300 MU/min was chosen. With a dose rate of 300 MU/min three of every six pulses are dropped. Thus, a maximum of 180 pulses occur per second in the linac beams used in this work.

4.2 Results and discussion

4.2.1 Characterization in a 6 MV photon beam

4.2.1.1 Leakage and chamber response reproducibility

During each saturation curve measurement, three separate 300 V data sets were acquired at each polarity. Figure 4.3 displays the results for each 300 V data set normalized to the first 300 V measurement at each polarity. For both polarities, each of the chambers demonstrated a difference of less than 0.5% between any two 300 V readings. The variation in the chamber response during each of the 6 minutes of data acquisition for each 300 V measurement was also analyzed. The relative standard deviation of each set of 720 current readings was 0.08% for Farmer-type chambers, 0.07% for the scanning chamber, and 0.06% for microchambers. Similar to the leakage current with the ^{60}Co measurements, the leakage current for each of the chambers biased to ±300 V in the 6 MV linac beam was below 10 fA. However, unlike the ^{60}Co measurements, 10 fA of leakage current met the reference-class requirement of less than 0.1% of the chamber signal in the 6 MV linac beam. The leakage current corresponded to 0.001%, 0.012% and 0.057% of the chamber signal for Farmer-type chambers, the scanning chamber, and microchambers, respectively.

4.2.1.2 Saturation curve shape

The shape and relative magnitude of the saturation curves for opposing polarities were analyzed for the same Farmer-type chambers, scanning chamber and microchambers as discussed in the previous chapter. The average chamber response at each applied voltage was normalized to the average response of the chamber when negative charge was collected at a polarizing voltage of +300 V.

Farmer-type ionization chambers Figure 4.4 displays two normalized saturation curves measured with the Exradin A12 and PTW N23333 Farmer-type chambers for a 6 MV pulsed

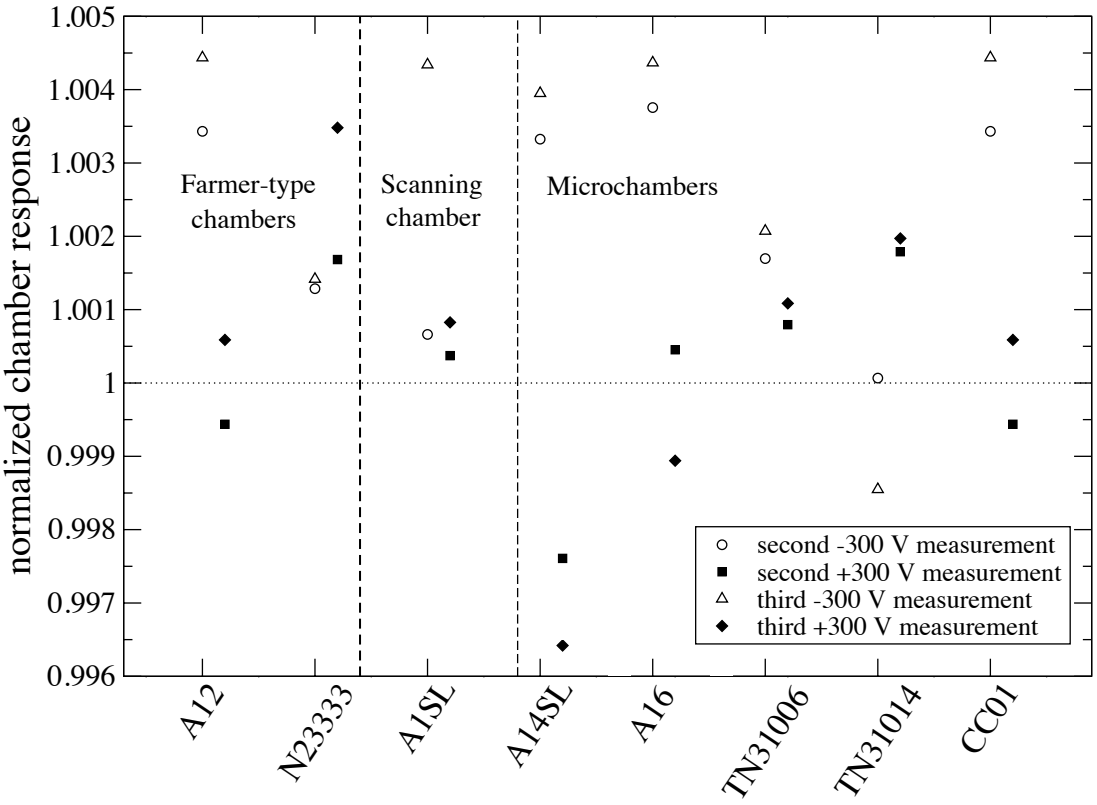

Figure 4.3: Normalized variations in chamber response among the three measurements performed when the chambers were biased to 300 V during each saturation curve. All data were normalized to the first 300 V measurement performed at that polarity. Measurements performed during positive charge collection (-300 V) and negative charge collection (+300 V) are represented with open circles and solid symbols, respectively.

photon beam. Similar to the ^{60}Co curves, the collection efficiency improved as the applied voltage increased until a saturation current was achieved. A stable linear plateau in chamber response occurred over a range of applicable voltages and the effects of charge multiplication and cable/stem irradiations were minimal. For both polarities, the shape of each chamber's response was nearly identical with a slight difference in magnitude, suggesting a voltage-independent polarity effect which could be accounted for using the TG-51-recommended application of P_{pol}, which will be discussed further in Section 4.2.1.3. As expected, effects

of ion recombination were greater for these chambers in the pulsed beam compared to the ^{60}Co beam.

Scanning ionization chambers Figure 4.5 shows the relative saturation curves for the Exradin A1SL. The shapes of the curves were similar to those measured in the ^{60}Co beam, with the response of the chamber failing to reach a consistent saturation plateau over the range of applied voltages tested. The polarity-induced differences in magnitude were relatively small over the entire range of applied voltages tested. Like the Farmer-type chambers, the effects of ion recombination were greater in the 6 MV beam compared to the ^{60}Co beam.

Microionization chambers The saturation curves measured for each microchamber (shown in Figures 4.6, 4.7, and 4.8) varied significantly between chamber models. For an individual microchamber the magnitude of the polarity effects varied slightly between the ^{60}Co and 6 MV pulsed beam; however, the anomalous behaviors and relative shapes of the curves were consistent. The anomalous microchamber behaviors demonstrated in both radiation beams included: large voltage-independent and -dependent polarity effects, an increase in the slopes of the saturation curves over the entire range of applied voltages, and an inverse proportionality between the chamber response and the applied voltage. With the exception of the Exradin A14SL during negative charge collection, the expected increase in ion recombination in the 6 MV beam was not demonstrated in any of the microchamber saturation curves. The consequence of this is discussed further in Section 4.2.2.

The PTW TN31006 and IBA CC01 microchambers exhibited strong polarity effects [Figures 4.6(a) and (b)], similar to the ^{60}Co saturation curves. The shapes of the curves were nearly identical between the two radiation beams; however, there was a significant shift in the difference in magnitude for opposing polarities. The saturation curves measured with the PTW TN31014 microchamber, shown in Figure 4.7(a), exhibited the same strong

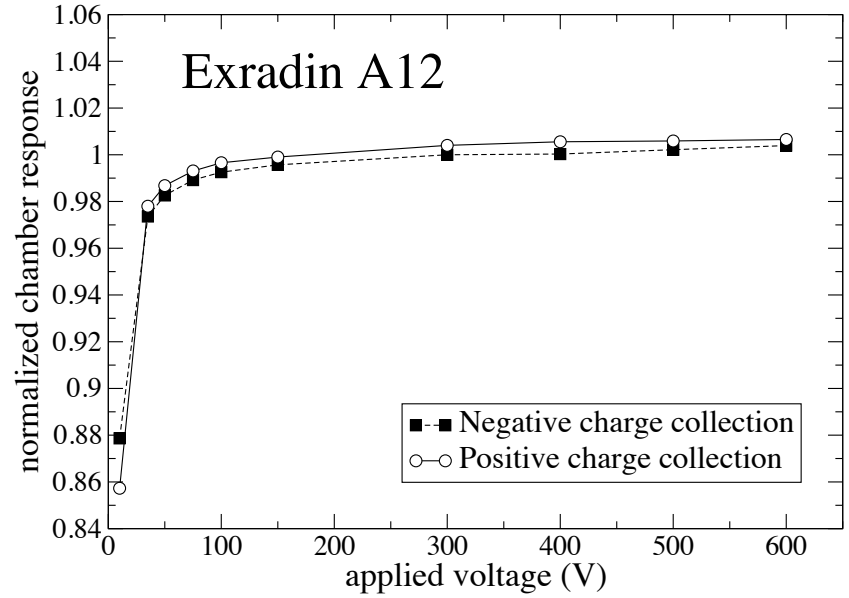

(a)

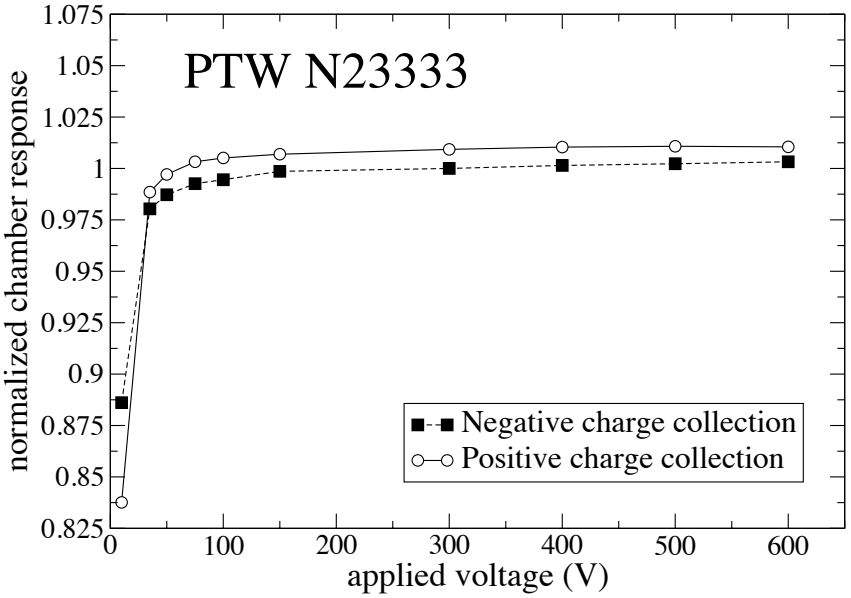

(b)

Figure 4.4: Normalized saturation curves measured with two Farmer-type ionization chambers, (a) an Exradin A12 and (b) a PTW N23333. All data were normalized to the average signal received when the chamber was biased to a polarizing voltage of +300 V (negative charge collection).

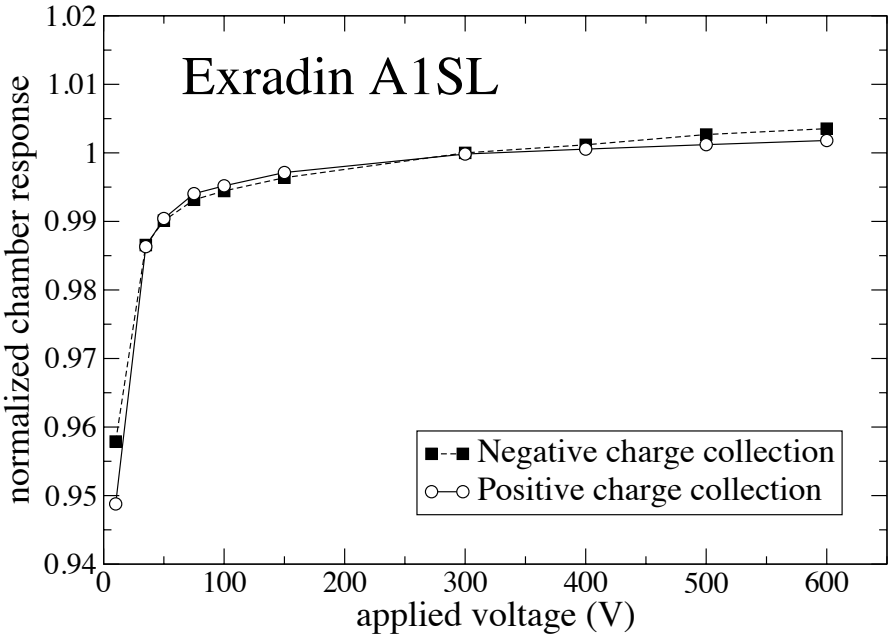

Figure 4.5: Same as Figure 4.4 except for an Exradin A1SL scanning chamber.

voltage-dependent polarity effects as seen in the ^{60}Co beam. Specifically, the chambers demonstrated the inverse proportionality between the chamber response and the applied voltage for negative charge collection at applied voltages less than 300 V. The Exradin A14SL and A16 microchambers also retained the anomalous voltage-dependent polarity effects and inverse proportionality between chamber response and applied voltage for both polarities. The extent of the increase in chamber response with decreasing applied voltage was reduced slightly with the 6 MV pulsed beam, but the effects were still significant.

4.2.1.3 Polarity correction factors

The polarity correction factor, P_{pol}, was calculated for each chamber using the method suggested by TG-51 (see Equation 2.11) for the 300 V data sets collected during saturation curve measurements. All P_{pol} values were calculated for negative charge collection, $P_{\text{pol}}(+300\,\text{V})$, corresponding to the UWADCL calibration conditions (i.e., $M_{\text{raw}} = M^{-}_{\text{raw}}$). The resulting P_{pol} values are shown in Table 4.1. The correction factors for all Farmer-

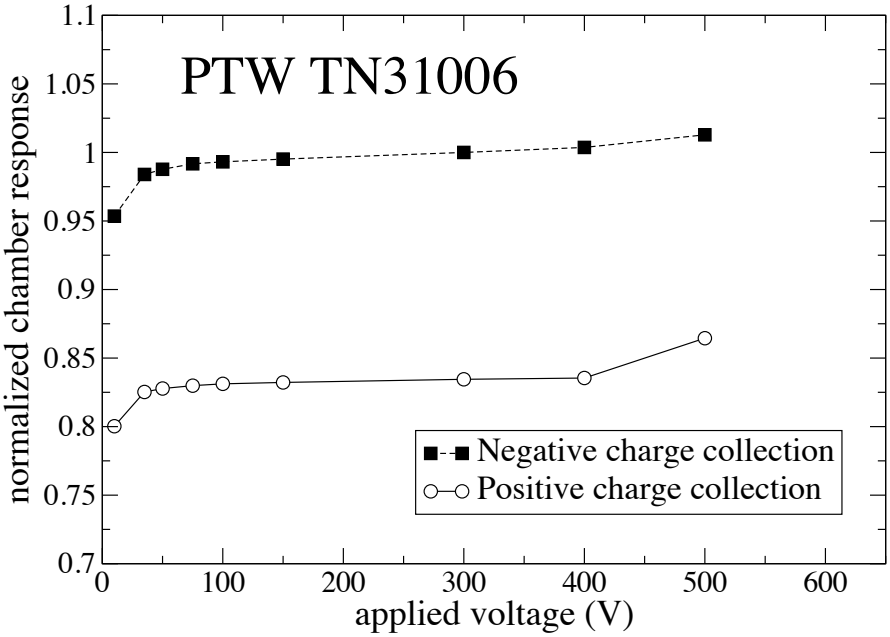

(a)

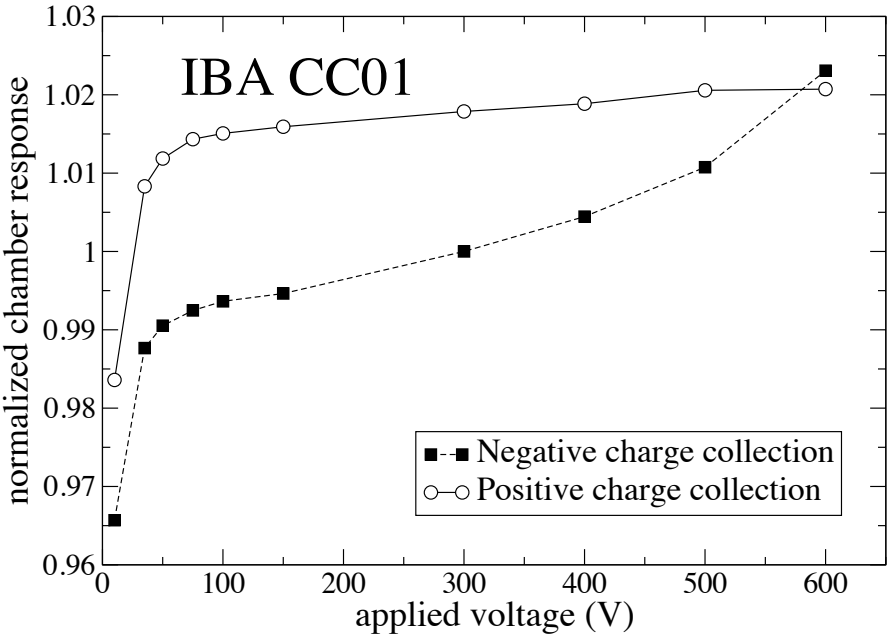

(b)

Figure 4.6: Same as Figure 4.4 except for two microionization chambers; (a) a PTW TN31006 and (b) an IBA CC01.

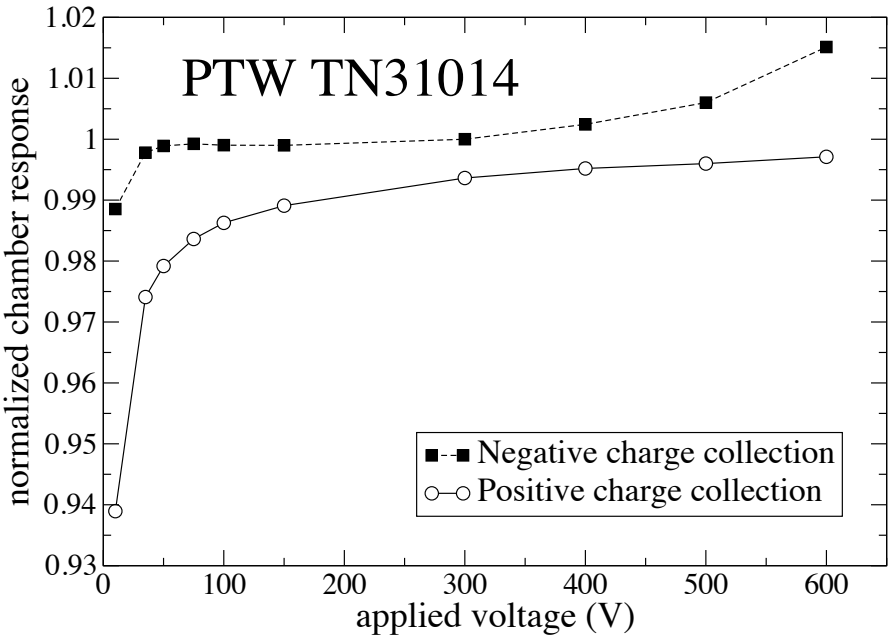

(a)

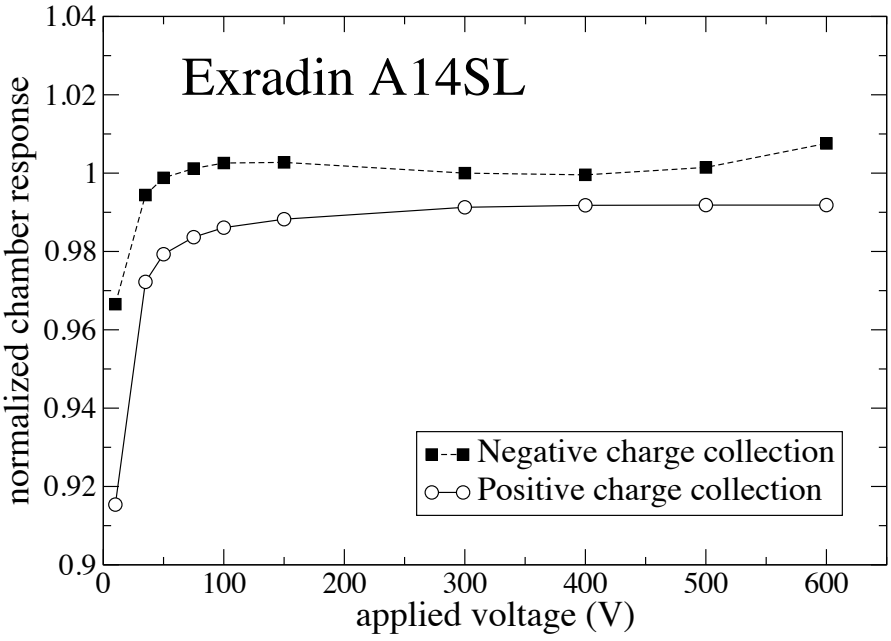

(b)

Figure 4.7: Same as Figure 4.4 except for two microionization chambers; (a) a PTW TN31014 and (b) an Exradin A14SL.

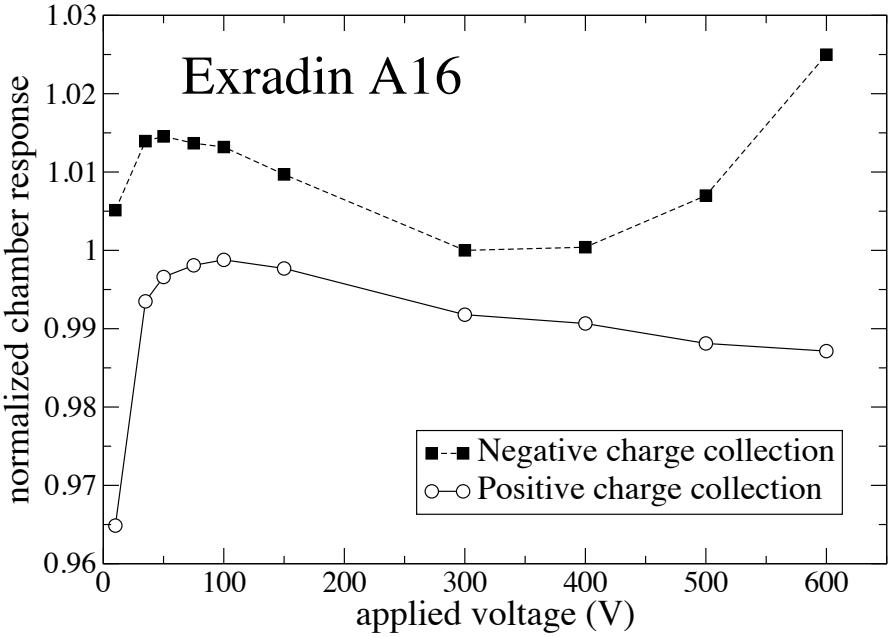

(a)

Figure 4.8: Same as Figure 4.4 except for an Exradin A16 microionization chamber.

type and scanning chambers were well within 0.2% from unity, with the exception of the PTW N23333 Farmer-type chamber, which was slightly greater at 0.5% from unity. For all larger-volume chambers, the magnitude of the polarity effects were voltage-independent, indicating the the TG-51-recommended polarity correction factors are applicable.

Polarity effects were voltage-dependent for all microchambers in this work and varied with each model. The P_{pol} values were all within the TG-51-recomended 0.4% from unity, with the exception of the PTW [36]006 microchamber. These results, along with the ^{60}Co P_{pol} calculations, demonstrate that while the P_{pol} values for a particular voltage may be within the recommended limits, it is necessary to characterize the polarity effects for a range of applied voltages.

Table 4.1: Polarity correction factors calculated using the TG-51-recommended method (see Equation 2.11). Three 300 V measurements were performed during each saturation curve, at the beginning (1), middle (2), and end (3) of data acquisition, which were used to calculate the reported correction factors.

Chamber classification	Chamber model	P_{pol}(+300 V)				
		1	2	3	Mean	Standard deviation (%)
Farmer-type	PTW N23333	1.005	1.005	1.004	1.005	0.06
	Exradin A12	1.001	1.003	1.003	1.002	0.1
Scanning	Exradin A1SL	1.000	1.000	1.000	1.000	0.02
Micro	PTW TN31006	0.9170	0.9174	0.9174	0.9173	0.02
	PTW TN31014	0.9977	0.9968	0.9960	0.9968	0.08
	Exradin A14SL	0.9935	0.9963	0.9972	0.9956	0.2
	Exradin A16	0.9945	0.9961	0.9971	0.9959	0.1
	IBA CC01	1.001	1.003	1.003	1.002	0.1

4.2.1.4 Ion recombination correction factors

As discussed in Section 2.3.2.4, the effects of ion recombination on chamber response are proportional to the dose per pulse of the radiation beam. Therefore, P_{ion} should be greater for the 6 MV photon beam with a D_{pp} of 0.27 mGy/pulse, than for the continuous ^{60}Co beam. The saturation curves shown in Section 4.2.1.2 demonstrated this increase in ion recombination for Farmer-type and scanning chambers. However, only the P_{ion} values calculated with the fit to Equation 2.19 consistently accounted for this increase in ion recombination. Using the robust method, P_{ion} increased by roughly a factor of 10 from the ^{60}Co beam to the 6 MV beam. The two-voltage technique provided similar P_{ion} values for both radiation beams. This highlights the importance of using the more robust techniques to characterize ionization chambers.

As with the ^{60}Co measurements, the P_{ion} values for the microchambers in the 6 MV pulsed beam were unrepresentative of any true ion recombination effects. Even the most

Table 4.2: Ion recombination correction factors calculated using the TG-51-recommended two-voltage technique and a fit of the Jaffé plot to Equation 2.26. Correction factors were calculated for an applied voltage of 300 V at both polarities and the percent standard deviation of the factors was calculated.

Chamber classification	Chamber model	P_{ion}(Equation 2.19)		P_{ion}(two-voltage)		Standard deviation (%)
		+300 V	-300 V	+300 V	-300 V	
Farmer-type	PTW N23333	1.003	1.004	1.000	1.001	0.04
	Exradin A12	1.003	1.003	1.001	1.001	0.01
Scanning	Exradin A1SL	1.001	1.002	1.001	1.001	0.03
Micro	PTW TN31006	1.001	1.001	1.001	1.001	0.02
	PTW TN31014	1.000	1.002	0.9999	1.002	0.2
	Exradin A14SL	1.004	1.002	0.9997	1.000	0.2
	Exradin A16	1.011	1.005	0.9969	0.9971	0.6
	IBA CC01	1.001	1.001	1.001	1.002	0.03

robust method failed to account for ion recombination accurately due to the anomalous behavior. Several P_{ion} values calculated with the two-voltage technique were below unity which was nonsensical and a good indication that the chamber was not behaving correctly. As mentioned in Section 4.2.1.2, it is important to note that the relative shape of the saturation curves remained roughly the same for an individual chamber for both radiation beams. The increased effects of ion recombination in the 6 MV beam were not evident. This observation further validated the theory that there were alternative processes occurring, which overwhelmed and masked the effects of ion recombination.

4.2.2 Variations in ion recombination with the dose per pulse

Saturation curves were measured with an Exradin A12 Farmer-type chamber and an Exradin A14SL microchamber for five D_{pp} values. The parameters and D_{pp} values achieved in this work are displayed in Table 4.3.

Table 4.3: The D_{pp} values (mGy/pulse) achieved for a ^{60}Co beam and two Varian Clinac iX beams at a dose rate of 300 MU/min. The D_{pp} was measured using an additional Exradin A12 Farmer-type chamber at a depth of 5 cm in water with a SSD of 79 cm and 95 cm.

Radiation beams	Source-to-surface distance (cm)	Dose per pulse (mGy/pulse)
^{60}Co	95	continuous
6 MV linac	95	0.27
	79	0.38
10 MV linac	95	0.28
	79	0.40

4.2.2.1 Farmer-type chamber

The normalized saturation curves and Jaffé plots measured during negative charge collection with the Farmer-type chamber are shown in Figures 4.9(a) and (b), respectively. It is clear from both figures that the effects of ion recombination increased with the D_{pp}. Furthermore, Figure 4.9(b) shows the fits of Equation 2.19 to the ^{60}Co data and Equation 2.26 to the pulsed linac data. The fits agreed well with the measured data and produced P_{ion}(+300 V) values which are shown in Figure 4.10 as a function of D_{pp}. The P_{ion} values in Figure 4.10 were fit to Equation 2.30 and the coefficients of initial, γ, and general, δ, recombination were calculated. The results are shown in Table 4.4. From these results it can be concluded that the Exradin A12 Farmer-type chamber met the ion recombination requirements of the reference class chamber:

1. The fits of Equations 2.19 and 2.26 to the Jaffé plots were linear for all D_{pp} values [see Figure 4.9(a)].

2. The fits of Equation 2.30 to the P_{ion} values as a function of the D_{pp} of the beam were linear (see Figure 4.10).

3. The apparent initial recombination, or y-intercepts, of P_{ion} vs. D_{pp} were within 0.1% for both polarities and were between unity and 1.002 (see Figure 4.10).

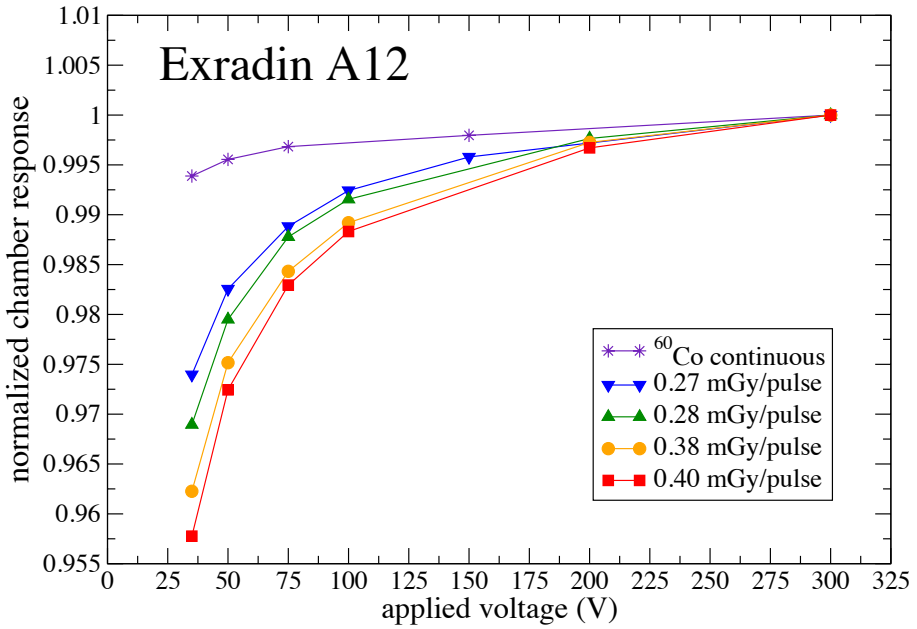

(a)

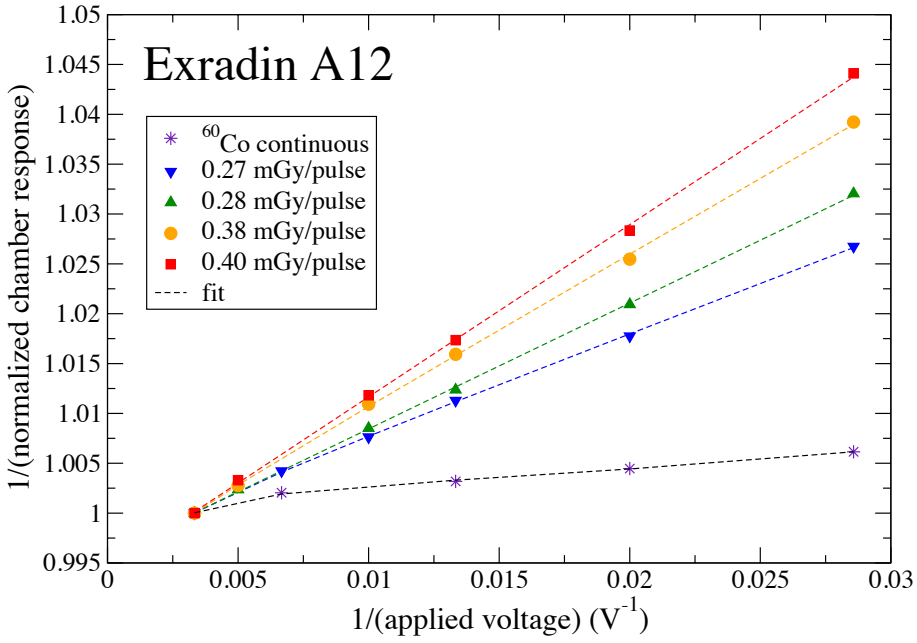

(b)

Figure 4.9: Normalized (a) saturation curves and (b) Jaffé plots for the Exradin A12 Farmer-type chamber for D_{pp} values ranging from a continuous beam to a 0.40 mGy/pulse linac beam. All data was measured during negative charge collection and is normalized to the 300 V measurement for each D_{pp}.

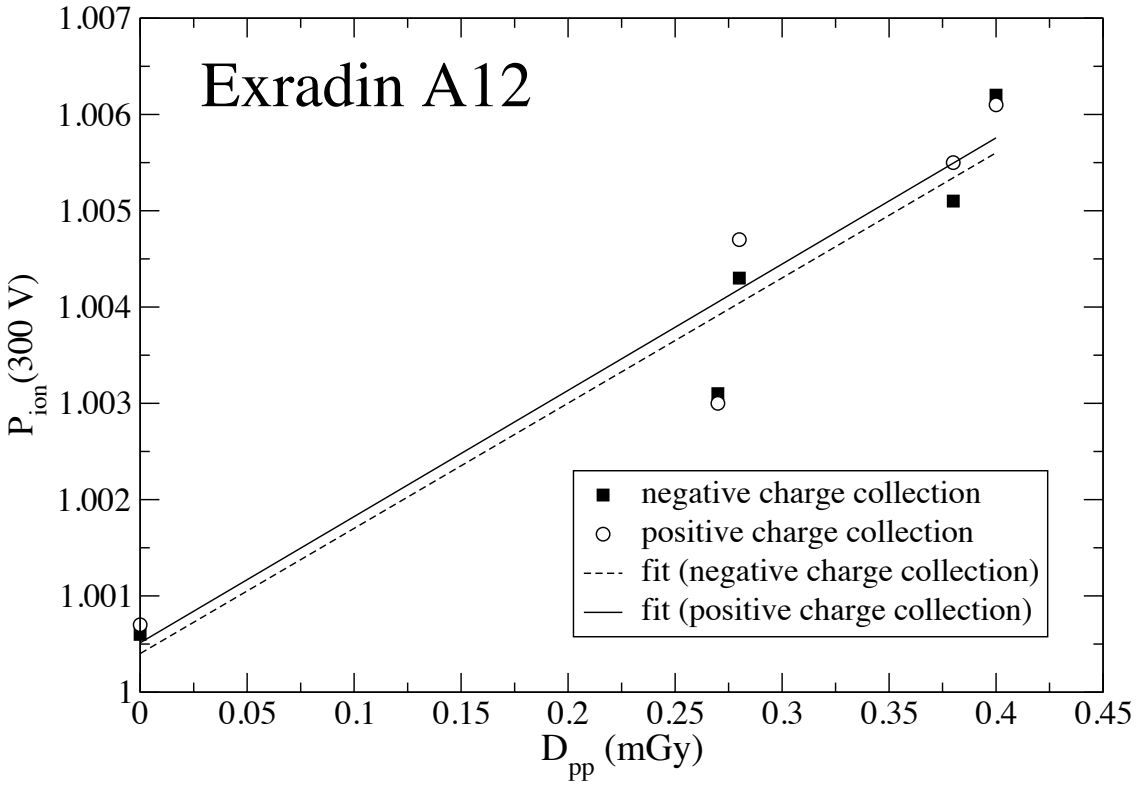

Figure 4.10: P_{ion} as a function of D_{pp} for an Exradin A12 Farmer-type chamber for D_{pp} values ranging from a continuous beam to a 0.40 mGy/pulse linac beam. The fit of Equation 2.30 to P_{ion} values measured during negative and positive charge collection is represented by dashed and solids lines, respectively.

As mentioned in Section 2.3.2.4, the variation of P_{ion} as a function of D_{pp} also offers a robust method for benchmarking this work against literature values. Several authors have reported similar results for Farmer-type chambers (McEwen, 2010; Bruggmoser et al., 2007; Berg and Noerrevang, 2004). However, only McEwen (2010) has reported values for γ and δ for the Exradin A12 Farmer-type chamber. Kry et al. (2012) published P_{ion} values for the Exradin A12 for several D_{pp} values which agreed fairly well with those of McEwen (2010); however, a fit to the data was not provided. The coefficients γ and δ for this

Table 4.4: The coefficients of initial, γ, and general, δ, recombination calculated with fit of Equation 2.30 to P_{ion} at five D_{pp} values. The P_{ion} values were measured for an Exradin A12 Farmer-type chamber and an Exradin A14SL microchamber and calculated with a robust exponential fit to the Jaffé plots. The coefficients in this work are compared to the published values of McEwen (2010).

Model	This study				McEwen (2010)	
	γ (V)		δ (V mGy^{-1})		γ (V)	δ (V mGy^{-1})
	+300 V	-300 V	+300 V	-300 V	-300 V	+300 V
Exradin A12	0.22	0.25	3.90	3.93	0.23±0.039	4.1±0.33
Exradin A14SL	2.01	1.02	0.00	0.50	–	–

work and that of McEwen (2010) are shown in Table 4.4. Table 4.4 also contains the recombination coefficients calculated in this work using the TG-51 recommended two-voltage (2V) technique. The values calculated with the robust fit of the Jaffé plot in this work and the linear fit of the Jaffé plot by McEwen (2010) are in good agreement, well within the uncertainty provided by McEwen (2010). This agreement validates the accuracy of the robust Jaffé plot fit for the characterization of ionizations chambers, even for large volume chambers where the exponential effects are small. This agreement also provides a benchmark for the chamber setup and irradiation techniques used in this work.

4.2.2.2 Microchambers

The D_{pp} results for the Exradin A14SL microchamber perpetuate the previous conclusions of this and the previous chapter; even the most robust methods for ion recombination fail to accurately account for ion recombination in microchambers. The saturation and Jaffé plots for negative and positive charge collection are shown in Figures 4.11 and 4.12, respectively. For both polarities, the fits of Equation 2.19 and Equation 2.26 did not agree well with the current ion recombination theory for the ^{60}Co and the pulsed linac beams,

respectively. Furthermore, the fits of Equation 2.30 to P_{ion} as a function of D_{pp} were nonsensical, as shown in black in Figure 4.13. The slopes of the fits varied significantly with polarity, with negative charge collection producing a slope of zero. The fits also provided significantly different values for the apparent initial recombination (>0.1%). The corresponding ion recombination coefficients, γ and δ, are shown in Table 4.4. These results mirror the saturation curve measurements, and it is clear that additional processes must be accounted for to accurately correct the response of microchambers.

It is important to note that in the absence of the P_{ion} values for the ^{60}Co beam, the fit of Equation 2.26 to the pulse linac data produced reasonable curves, as shown in Figure 4.13 in red. This result could be misleading; it would suggest that ion recombination correction factors are accurately accounted for in this chamber, which is clearly not the case. This investigation emphasizes the importance of understanding and carefully analyzing saturation and Jaffé plots for each chamber prior to reference-dosimetry measurements.

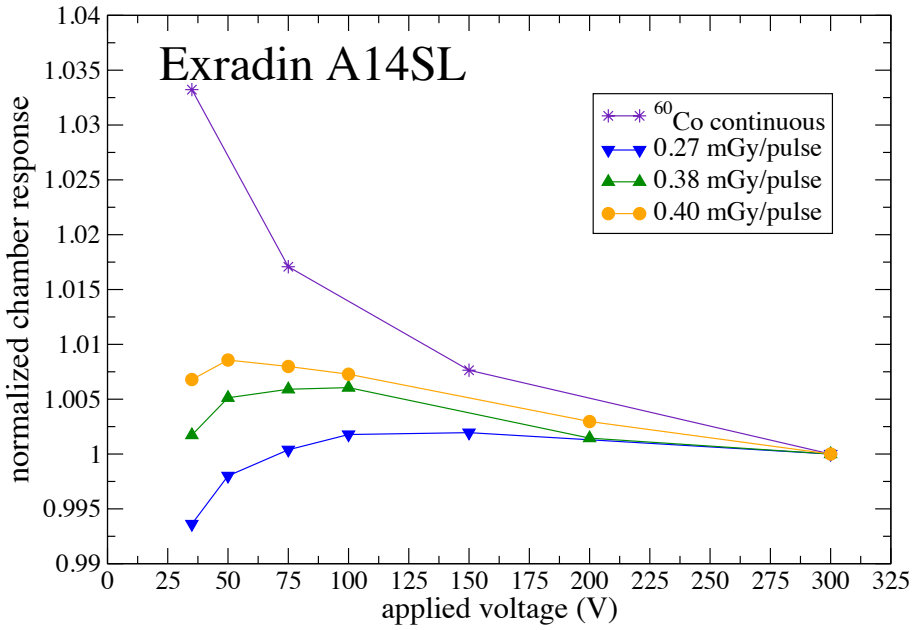

(a)

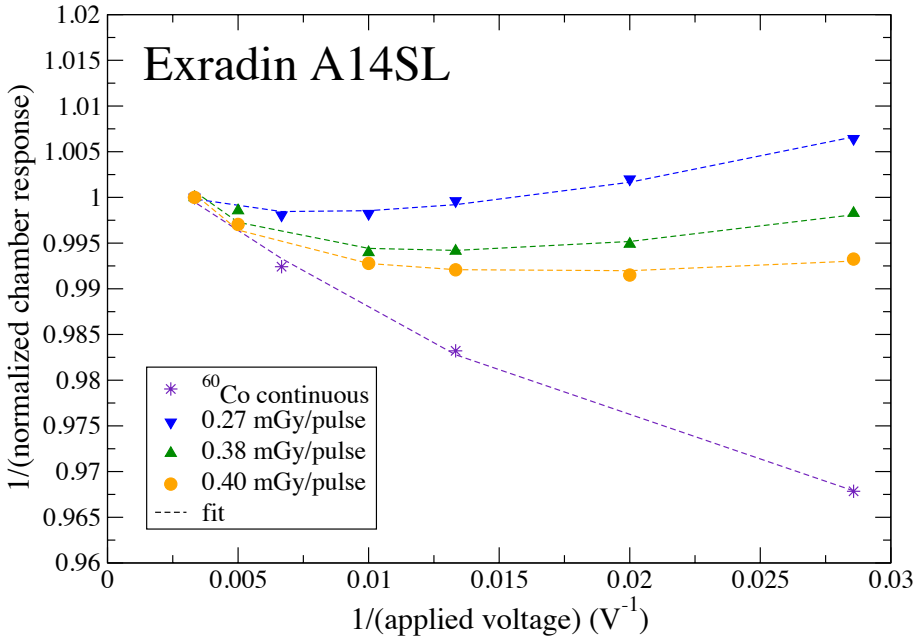

(b)

Figure 4.11: Normalized (a) saturation curves and (b) Jaffé plots for the Exradin A14SL microchamber for D_{pp} values ranging from a continuous beam to a 0.40 mGy/pulse linac beam. All data were measured during negative charge collection and were normalized to the 300 V measurement for each D_{pp}.

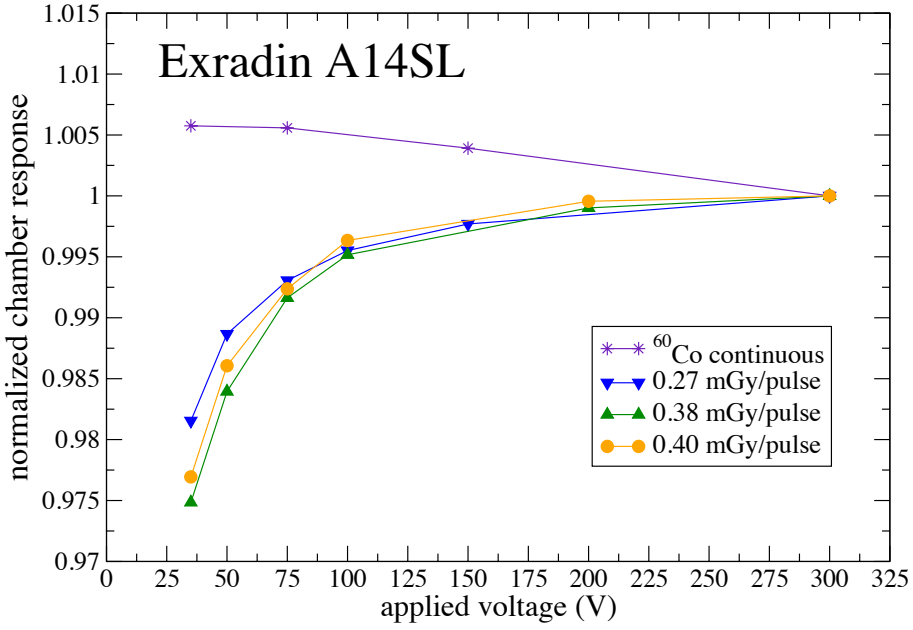

(a)

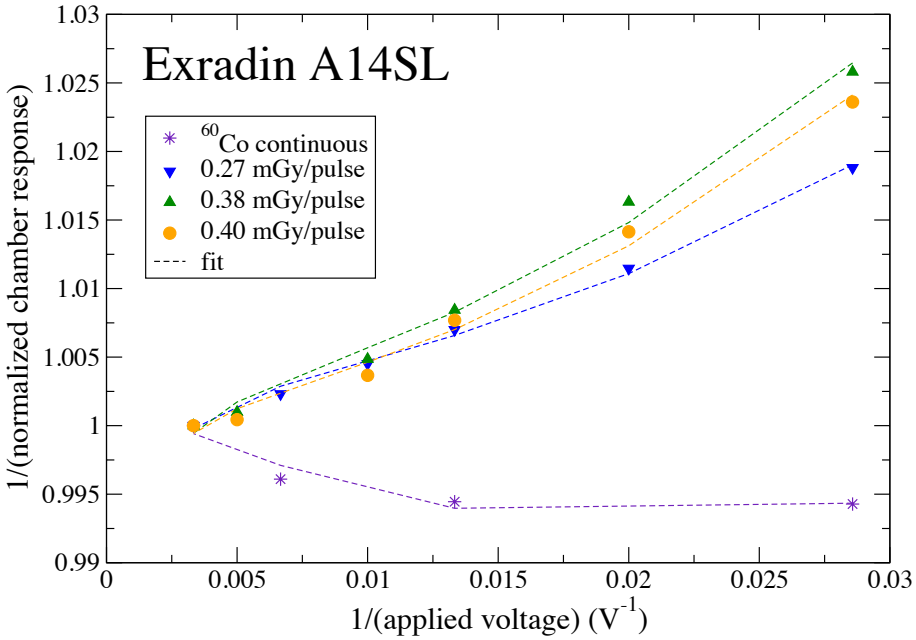

(b)

Figure 4.12: Same as Figure 4.11, except measurements were performed during positive charge collection.

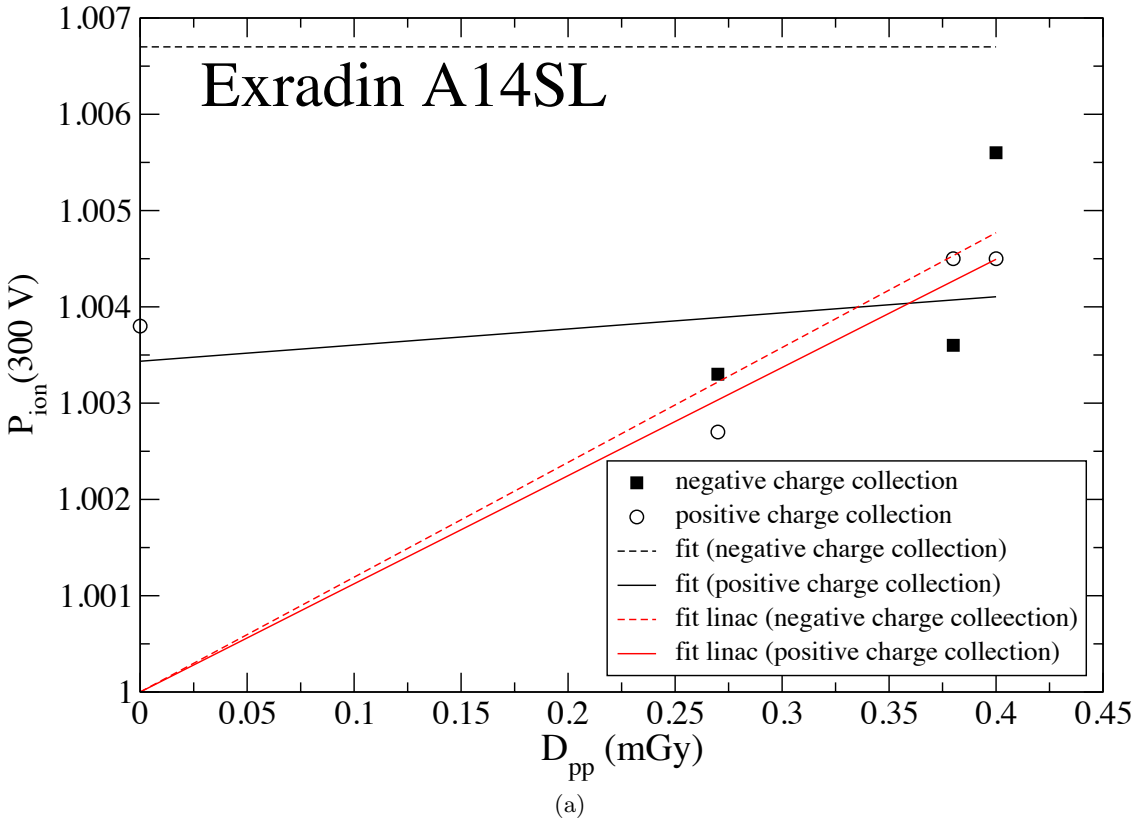

(a)

Figure 4.13: The fit of Equation 2.30 to P_{ion} as a function of D_{pp} for an Exradin A12 Farmer-type chamber for D_{pp} values ranging from a continuous beam to a 0.40 mGy/pulse linac beam. Lines in red represent a fit to the P_{ion} values measured for the linac beams only.

4.3 Conclusions

The chamber response for each chamber investigated in this work was reproducible to within 0.5% for a given polarity at an applied voltage of 300 V. Once the chamber response of the microionization chambers stabilized, the average relative standard deviation in the chamber current was 0.06%. The leakage current composed less than 0.1% of the chamber signal for all chambers.

The anomalous behaviors demonstrated by the microchambers in the ^{60}Co saturation curves were also exhibited in the 6 MV linac saturation curves. The magnitude of the polarity effects was reduced slightly with the high-energy pulsed beam, but the polarity-dependent effects were still present. Similar to the ^{60}Co characterization, several of the P_{pol} values for the microchambers were within the recommended limits; however, the saturation curves demonstrated significant voltage-dependent effects indicating the presence of additional effects which P_{pol} may not account for correctly. Thus, P_{pol} values calculated for the applied voltage of interest alone were not sufficient to assess whether the polarity effects of the chamber were acceptable.

The voltage-dependent effects prevented the most robust methods for P_{ion} calculation to accurately account for ion recombination in microchambers. Furthermore, the expected increase in ion recombination with D_{pp} was not demonstrated for microchambers. To benchmark the methodology of this work, P_{ion} was calculated for five D_{pp} values. The coefficients γ and δ for the Exradin A12 Farmer-type chamber were in good agreement with published values. These results validated the P_{ion} calculation technique used in this work, which accounts for additional exponential effects such as charge multiplication. This study also demonstrated that the Exradin A12 Farmer-type chamber met each of the ion recombination requirements for a reference-class chamber. The Exradin A14SL microchamber, on the other hand, failed to meet any of the reference-class requirements pertaining to ion recombination. This investigation further demonstrates the need for an understanding of the source of these voltage-dependent polarity effects in order to either account for them in dose calculations or eliminate them through optimized microchamber design.

Chapter 5

Microionization chamber characterization in low- and medium-energy x-ray photon beams

Although microionization chambers are more commonly used in high-energy photon beams, the UWADCL has experienced an increase in the demand for air-kerma calibrations of microchambers for low- and medium-energy x-ray beams. This indicates that these small-volume chambers are being used as dosimeters for kilovoltage x-ray applications, such as superficial skin therapy and intraoperative treatments, where high spatial resolution and minimal perturbation of the beam are desired. Thus, the response and calibration requirements for microchambers to x rays with a tube potential below 300 kV is of interest.

As discussed in Chapter 2, the TG-61 protocol requires polarity and ion recombination correction factors to accurately determine the the absorbed dose for the beam of interest. Thus it is necessary to characterize the saturation curves for microchambers in kilovoltage

x-ray beams. Furthermore, TG-61 contains recommendations and requirements pertaining to the chamber's dependence on the energy of the calibration beams. It is recommended that the uncertainty in the air-kerma calibration factor (N_K) for any clinical beam quality between two calibration qualities should be less than or equal to 2%, and N_K should be consistent for medium-energy x-ray beams relative to ^{60}Co to within ±2%. These recommendations serve as guidelines which may be modified by the user provided they do not compromise the accuracy of the dosimetry determination. The protocol requires that reference dosimetry for medium-energy x-ray beams shall be performed with a chamber that has N_K values that vary with beam quality by less than 3% for tube potentials between 100 and 300 kV (Ma et al., 2001). The protocol also states that cylindrical chambers shall only be used above 70 kV, however, the demand for cylindrical chambers calibration factors for kilovoltage x-rays indicates there is an interest in the response of these chambers to lower-energy x-ray beams as well. Thus, it is necessary to determine the variation in N_K with calibration beam quality for a chamber prior to performing reference dosimetry measurements in x-ray beams below 300 kV.

5.1 Saturation curve measurements

5.1.1 Methods and Materials

Saturation curves were measured for a NIST-defined M120 x-ray beam with a first half value layer (HVL) of 6.96 mm Al, a homogeneity coefficient of 78, and an effective energy of 49.9 keV. The same ionization chamber models from Chapter 3 were characterized with the UWADCL Advanced X-Ray constant potential x-ray system with a Gulmay CP320 generator and a Comet 320 tungsten anode tube. Measurements were performed in air, using a methodology similar to that of the ^{60}Co measurements described in Section 3.1.2, with the exception of the water tank. The center of the chamber volume was positioned with

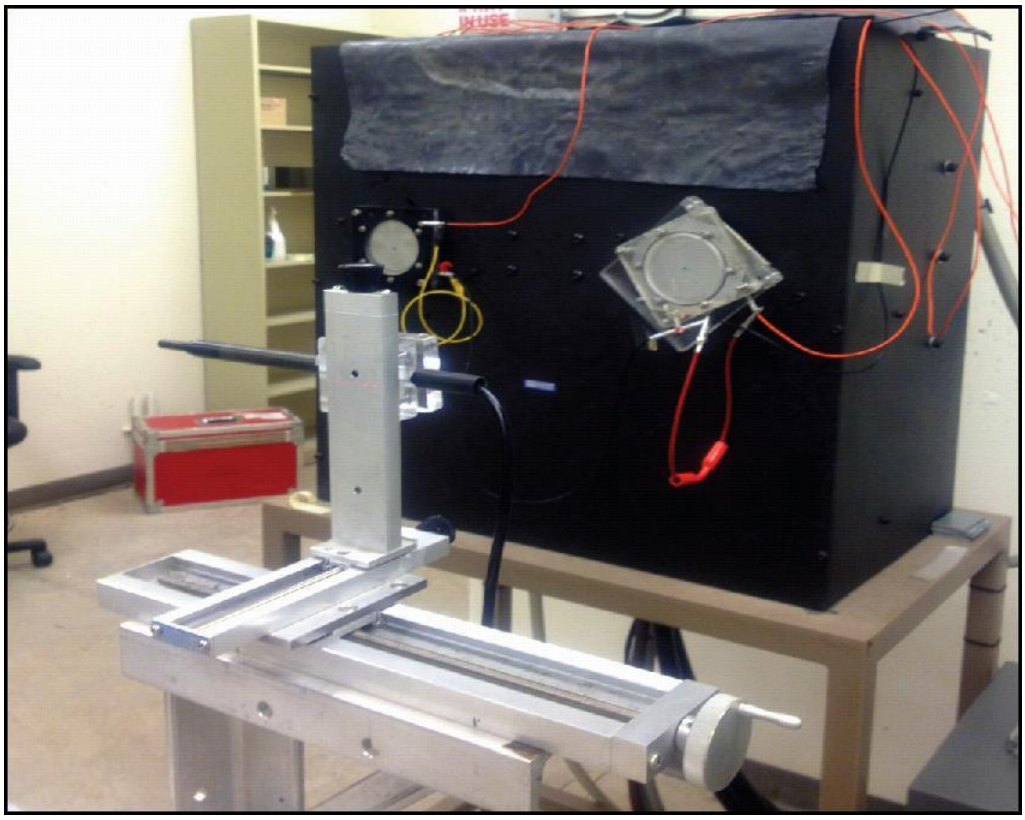

Figure 5.1: Photograph of the experimental setup for ionization chamber measurements with the UWADCL Advanced X-Ray constant potential x-ray system.

ceiling- and wall-mounted lasers at distance of 100 cm from the tube anode. Irradiations were performed with the ionization chamber perpendicular to the central axis of the beam with a field size of (10 x 10) cm^2 at the center of the chamber volume as shown in Figure 5.1. A parallel-plate transmission chamber was used to monitor the variations in output from the x-ray source during saturation curve measurements.

Ionization current from the chamber of interest was measured using the customized SI MAX 4000 electrometer and Harshaw HV Power Supply, shown in Figure 3.1(b). SI's MAX COMM^{TM} Version 2 software was used to acquire current readings at a sampling rate of 2 Hz. For each saturation curve, the chamber was pre-irradiated for at least 20 minutes with an applied bias of $\pm$300 V depending on the polarity of the curve to be measured. The

measurements were performed in the following order: 300, 150, 75, 35, 10, 300, 400, 500, 600, and 300 V. For each applied voltage the chamber leakage was recorded before and after each irradiation. At each of the ten applied voltages, the chamber was irradiated for 16 minutes allowing for 10 minutes of pre-irradiation followed by 6 minutes of data acquisition. During data collection, the atmospheric pressure and the temperature of the air were monitored, and a temperature and pressure correction was applied to each data set.

5.1.2 Results and discussion

5.1.2.1 Leakage and chamber response reproducibility

During each saturation curve measurement, three separate 300 V data sets were acquired at each polarity. Figure 5.2 displays the results for each 300 V data set normalized to the first 300 V measurement at each polarity. For both polarities, the Farmer-type and scanning chambers demonstrated a maximum difference of less than 0.5% between any two readings, the same value as with the 6 MV linac measurements. For the microchambers, a maximum difference of less than 1.2% between any two readings was measured, compared to 0.5% and 0.25% for the 6 MV and ^{60}Co beam, respectively. This increase in variation between the 300 V measurements for the microchambers was likely due, in part, to the increased signal-to-noise ratio for several of the chambers in the M120 x-ray beam. While the limit for the leakage current of each chamber was maintained at 10 fA for all radiation beams, the decreased signal for several of the microchambers in the M120 x-ray beam led to a maximum percent leakage-to-signal ratio of 0.48%, as opposed to 0.057% and 0.25% for the 6 MV and ^{60}Co beam, respectively. For the Farmer-type and scanning chambers, a leakage value of 10 fA corresponded to the maximum percentage of 0.021% and 0.233% of the chamber signal, respectively.

The variation in the chamber response during each of the 6 minutes of data acquisition for each 300 V measurement was also analyzed. The relative standard deviation in the

response of the chambers was 0.04% for Farmer-type chambers, 0.10% for the scanning chamber, and 0.17% for microchambers.

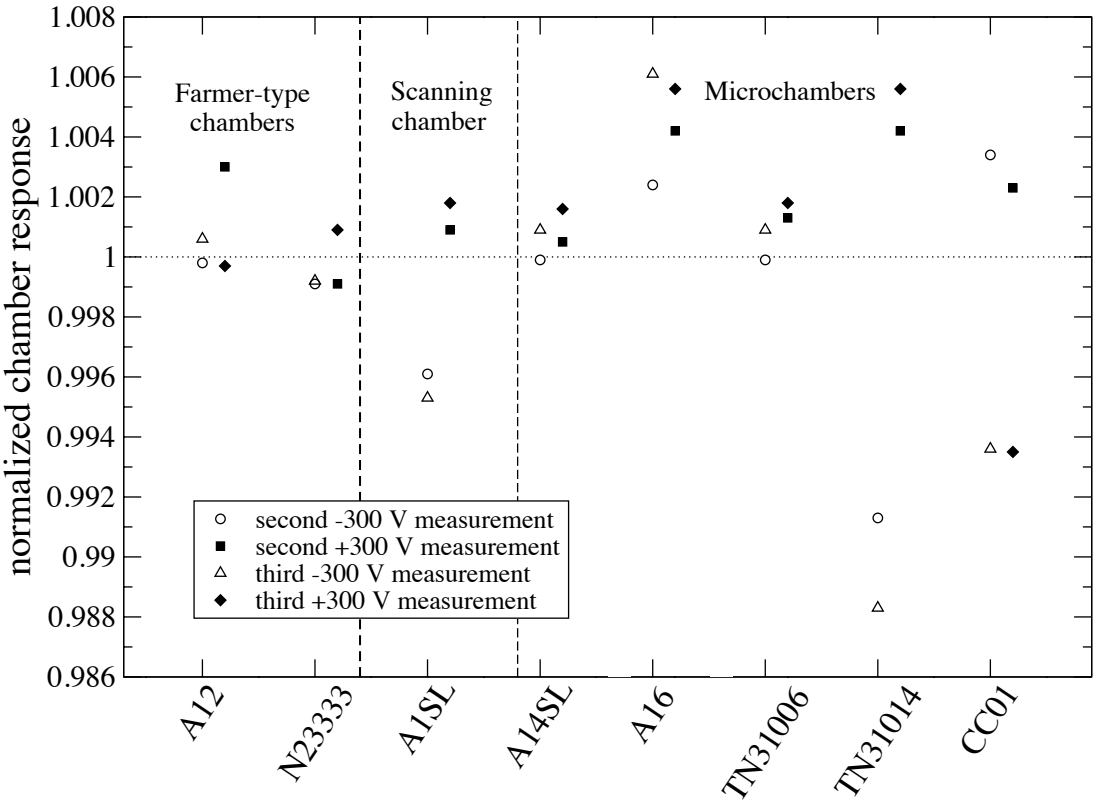

Figure 5.2: Normalized variations in chamber response at applied voltages of ±300 V during saturation curve measurements. All data were normalized to the first 300 V measurement performed at the corresponding polarity. Measurements performed during positive and negative charge collection are represented with open circles and solid symbols, respectively.

5.1.2.2 Saturation curve shape

The saturation curves for each chamber investigated are shown in the following sections. For each set of measurements, the average chamber response at each applied voltage was normalized to the average response of the chamber when negative charge was collected at a polarizing voltage of +300 V.

Farmer-type and scanning ionization chambers The saturation curves for the Farmer-type and and scanning chambers are shown in Figures 5.3 and 5.4, respectively. Unlike the Farmer-type and scanning chamber saturation curves measured for high-energy photon beams, the saturation curves for the M120 x-ray beam exhibited slight voltage-dependent polarity effects and less stability in chamber response. It was likely that the low beam energy and dose rate of the M120 x-ray beam led to a lower chamber signal and an increased sensitivity to material compositions and dimensions.

Microionization chambers The microchambers also exhibited an increased magnitude in polarity effects for the M120 x-ray irradiations as shown in Figures 5.5, 5.6, and 5.7. Even with the increase in polarity differences, the same general trends and shapes were exhibited by each chamber in the M120 x-ray beam, the 6 MV pulsed linac beam, and the ^{60}Co beam. This indicates that the anomalous processes occurring inside microchambers are important for all external-beam reference-dosimetry measurements. Furthermore, the additional processes are not a result of the dose-rate or energy of the photon beam.

5.1.2.3 Polarity correction factors

As mentioned in the previous section, the polarity effects for all chambers were greater in the M120 x-ray beam compared to the higher-energy photon beams. The P_{pol} values for the Farmer-type and scanning chambers met the reference-dosimetry requirements; however, further investigation into the voltage-dependent effects for standard sized chambers in low-energy x-ray beams is required.

The microchambers exhibited P_{pol} values that far exceeded the 0.4% from unity requirement established in TG-51. In most cases, the magnitude of the polarity effects were greater in the M120 x-ray beam than the high-energy photon beams.

Table 5.1: Polarity correction factors calculated using the TG-51-recommended method (see Equation 2.11). Three 300 V measurements were performed during each saturation curve, at the beginning (1), middle (2), and end (3) of data acquisition, which were used to calculate the reported correction factors.

Chamber classification	Chamber model	P_{pol}(+300 V)				
		1	2	3	Mean	Standard deviation (%)
Farmer-type	PTW N23333	0.9989	0.9989	0.9980	0.9986	0.05
	Exradin A12	1.001	0.9991	1.001	1.000	0.1
Scanning	Exradin A1SL	1.000	0.9975	0.9967	0.9980	0.2
Micro	PTW TN31006	0.8638	0.8634	0.8633	0.8635	0.03
	PTW TN31014	1.021	1.014	1.012	1.016	0.4
	Exradin A14SL	1.012	1.012	1.012	1.012	0.02
	Exradin A16	1.011	1.010	1.011	1.010	0.06
	IBA CC01	1.022	1.023	1.022	1.022	0.03

5.1.2.4 Ion recombination correction factors

The P_{ion} values measured for the Farmer-type and scanning chambers were within 0.1% of the P_{ion} values for the higher-energy photon beams. However, $P_{ion}(-300\,V)$ for the PTW N23333 chamber calculated with the fit of Equation 2.19 to the Jaffé plot was less than unity. This highlighted the increased voltage-dependent polarity effects demonstrated with Farmer-type chambers for the M120 x-ray beam. Similar to the high-energy beams, the P_{ion} values for the microchambers in the M120 beam showed greater variety, with several P_{ion} values calculated with the two-voltage technique below unity.

Table 5.2: Ion recombination correction factors calculated using the TG-51-recommended two-voltage technique and a fit of the Jaffé plot to Equation 2.19. Correction factors were calculated for an applied voltage of 300 V at both polarities and the percent standard deviation of the factors was calculated.

Chamber	Chamber	P_{ion}(Equation 2.19)		P_{ion}(two-voltage)		Standard
classification	model	+300 V	-300 V	+300 V	-300 V	deviation (%)
Farmer-type	PTW N23333	1.0002	0.9999	1.0009	1.0006	0.07
	Exradin A12	1.0000	1.0000	1.0005	1.0001	0.03
Scanning	Exradin A1SL	1.0007	1.0007	1.0010	1.0011	0.02
Micro	PTW TN31006	1.0000	1.0012	1.0022	0.9990	0.07
	PTW TN31014	0.9989	1.0035	1.0012	1.0026	0.2
	Exradin A14SL	1.0059	1.0032	0.9994	0.9990	0.3
	Exradin A16	1.0106	1.0089	0.9969	0.9965	0.9
	IBA CC01	1.0005	1.0000	1.0031	1.0005	0.22

5.2 Energy dependence in air-kerma calibration coefficients

5.2.1 Methods

To assess the energy dependence of each chamber, air-kerma calibration coefficients were measured for ^{60}Co and x-ray beams (20–250 kVp) with effective energies ranging from 11.5 keV to 1.05 MeV.

5.2.1.1 Low- and medium-energy x-ray irradiations

All x-ray irradiations were performed with the UWADCL Advanced X-Ray constant potential x-ray system described in Section 5.1.1. A series of beam qualities were selected that were matched for first and second half-value layers (HVL) with comparable beam qualities offered by the National Institute of Standards and Technology (NIST). For simplicity, the NIST beam codes are used here (Lamperti and O'Brien, 2001). The numeric value in the beam code corresponds to the kVp of the x-ray unit. The beam codes, first HVL, homo-

geneity coefficients, and effective energies of the x-ray beams used in this work are shown in Table 5.3.

Table 5.3: Beam code (Lamperti and O'Brien, 2001), first HVL, homogeneity coefficient and effective energy of the x-ray beams used in this work. The effective energy is an estimate of the monoenergetic photon energy that gives the same first HVL as the polyenergetic spectrum (Nunn et al., 2008).

Beam code	1^{st} HVL (mm Al)	Homogeneity coefficient	Effective energy (keV)
M20	0.148	75	11.5
M30	0.356	65	15.5
M40	0.728	66	19.8
M50	1.02	66	22.4
M60	1.68	66	26.9
M80	2.96	68	33.5
M100	4.98	72	42.1
M120	6.96	78	49.9
M150	10.2	87	67.0
M200	14.9	98	99.8
M250	18.5	98	145

The center of the chamber volume was positioned at distance a of 100 cm from the tube anode. Irradiations were performed with the ionization chamber perpendicular to the central axis of the beam with a field size of (10 x 10) cm^2 at the center of the chamber volume. Prior to data collection, each chamber was irradiated for a minimum of 10 minutes at a chamber bias of ± 300 V, corresponding to the bias that would be used for the set of measurements immediately following. Charge collections were performed using two reference-class electrometers (IEC, International Electrotechnical Commission, 1997). A SI MAX 4000 and SuperMAX electrometer were used for ^{60}Co and x-ray measurements, respectively. The chamber leakage was monitored before and after each irradiation, and had negligible impact on the measured calibration coefficients. Prior to chamber measurements of each x-ray beam, the air-kerma rate of the beam was measured with a NIST-calibrated ionization chamber. The air-kerma calibration coefficient for each chamber in each x-ray beam was calculated as (Aitken and Henry, 1964; Ehrlich et al., 1976; Mora et al., 1999;

Scrimger and Cormack, 1963)

$$N_{\mathrm{K}} = \left[\frac{N_{\mathrm{K,std}}(Q_{\mathrm{std}}/Q_{\mathrm{m,std}})}{(Q/Q_{\mathrm{m}})} \right], \tag{5.1}$$

where N_{K} and $N_{\mathrm{K,std}}$ are the air-kerma calibration coefficients measured for the chamber of interest and the NIST-traceable standard, respectively. Similarly, Q and Q_{std} are the average values of the uncorrected charge readings for the chamber of interest and the standard, respectively. The average value of the uncorrected charge readings from the monitor chamber during exposure of the chamber of interest and the standard are Q_{m} and $Q_{\mathrm{m,std}}$, respectively. For each chamber measurement, a series of three or more charge readings was performed and averaged to ensure a lack of trending. The chamber leakage was monitored before and after each measurement.

5.2.1.2 ^{60}Co irradiations

A methodology similar to that of the x-ray irradiations was used for all ^{60}Co air-kerma calibration coefficient measurements. The center of the chamber volume was positioned in air, at a distance of 100 cm from the UWADCL Theratron 1000 ^{60}Co source. To provide adequate build-up for the ^{60}Co irradiations in air, each chamber was irradiated with a build-up cap specified by the manufacturer for the corresponding chamber model. The material and thickness of each build-up cap are shown in Table 3.1. Each chamber was oriented perpendicular to the central axis of the beam and irradiated with a (10 x 10) cm^2 field size at the center of the chamber volume. All chambers were irradiated at $\pm$300 V for 10 minutes prior to data acquisition. Charge collections were performed using a SI MAX 4000 electrometer and the temperature and pressure were recorded during each irradiation. Prior to each chamber measurement, the air-kerma rate was measured with a NIST-calibrated ionization chamber. The air-kerma calibration coefficient, N_{K}, was calculated for each beam

as

$$N_{\mathrm{K}} = \left[\frac{N_{\mathrm{K,std}} \cdot Q_{\mathrm{std}} \cdot P_{\mathrm{TP,std}}}{Q \cdot P_{\mathrm{TP}}} \right], \tag{5.2}$$

where P_{TP} and $P_{\mathrm{TP,std}}$ are the temperature and pressure correction factors for the chamber of interest and the NIST-traceable standard, respectively.

5.2.2 Results and discussion

To determine the relative energy dependence among the different chambers, the measured air-kerma calibration coefficients, N_{K}, were normalized to the N_{K} values measured with the ^{60}Co beam for each chamber in Table 3.1. Figures 5.8(a) and (b) show the relative N_{K} values for negative and positive charge collection, respectively. The collecting volumes calculated from the N_{K} values measured for the ^{60}Co beam were consistent with the manufacturer-specified volumes.

5.2.2.1 Low-Z ionization chambers

The relatively flat energy response of the Farmer-type and scanning chambers, which contain low-Z components (Z$\leq$13), agreed well with other studies that have examined the variation in chamber response to kilovoltage x-ray beams for similar chambers (Ubrich et al., 2008; **?**; Hill et al., 2009; Muir and Rogers, 2011; Rosser, 1998). For all of the low-Z chambers, with the exception of the PTW TN31014 microchamber, N_{K} varied with the beam quality by less than 3% for tube potentials between 100 kV and 250 kV, as required by TG-61. The PTW TN31014, which was the only commercial microchamber in this work composed of low-Z materials, exhibited N_{K} values which varied by 4% and 10% for positive and negative charge collection, respectively, for tube potentials between 100 kV and 250 kV.

5.2.2.2 High-Z ionization chambers

Unlike the low-Z chambers, a significant dependence on the beam quality was seen for all microchambers containing steel or silver-plated copper-clad steel (SPC), with N_K varying with the beam quality by greater than 50% for tube potentials between 100 and 250 kV in all cases. This variation is well beyond the maximum value of 3% required by TG-61. Furthermore, the average variation in air-kerma calibration coefficients between any two adjacent calibration beams was nearly 25% over the entire range of beam qualities investigated. Similar increases in energy dependence for chambers containing high-Z materials have been reported for this range of photon beam energies (La Russa et al., 2007; Hill et al., 2009; Muir and Rogers, 2011; Rosser, 1998). Specifically, Hill *et al.* (2009) showed that the variation in the relative chamber response of a PTW 31006 microchamber was much greater than that of several Farmer-type and scanning chambers for x-ray energies ranging from 50 kVp to 280 kVp. This was attributed to the steel electrode and the dominance of the photoelectric effect at lower energies and higher atomic numbers. Muir and Rogers (2011) demonstrated that the effect of the central collecting electrode on the response of an Exradin A16 in a 200 kVp x-ray beam was large, on the order of 50%, compared to less than 1% for the Exradin A12 Farmer-type chamber. However, they found that the magnitude of this effect varied little (2%) with changes in the photon spectrum caused by varying the depth of the chamber in water. It was concluded that the variations in chamber response depend in a complex way on the surroundings of the electrode, the electrode material, and the relative fraction of the cavity volume occupied by the electrode (Muir and Rogers, 2011).

Between the two Exradin microchambers, which contain the same SPC collecting electrodes and have similar chamber designs, the A14SL exhibited a slightly smaller variation in N_K with the quality of the beam. This reduction in energy dependence is likely due to the relative dimensions of the chamber components, particularly the smaller fraction of the

cavity volume that is occupied by the collecting electrode in the Exradin A14SL (0.4%) as compared to the Exradin A16 (1.0%). Similarly, Muir and Rogers (2011) reported that collecting electrode perturbations simulated in high-energy photon beams were greater for the Exradin A16 than the Exradin A14SL due to the larger fraction of the cavity volume occupied by the collecting electrode. It is clear that the energy dependence of these ionization chambers is not unique to small-volume chambers, but rather is a function of the materials and relative dimensions of the chamber components.

5.2.2.3 Proof-of-concept chambers

The impact of high-Z materials on chamber response in low- and medium-energy beams was further confirmed with the N_K measurements performed with the proof-of-concept microchamber with and without silver epoxy painted on the C552 collecting electrode. The measured air-kerma calibration coefficients were normalized to the N_K values measured with the M250 x-ray beam for each measurement set, as shown in Figure 5.9. The response of the chamber containing only low-Z components is similar to that of the previously discussed low-Z chambers. The maximum variation in N_K over the range of beam qualities measured was less than 2%. However, the measurements performed with the collecting electrode coated in silver showed a significantly greater variation in N_K over the same range of beam qualities. With the high-Z collector, the chamber exhibited a variation in N_K of greater than 50%. These results support the previous conclusions and highlight the impact of high-Z materials on ionization chamber response with beam quality for x-ray beams for tube potentials below 300 kV.

5.3 Conclusions

The reproducibility in the chamber response at an applied voltage of 300 V was increased from 0.25% to 1.2% for microchambers in the low energy-beams compared to the ^{60}Co

beam. The variation in chamber response during a single 300 V measurement increased from 0.05% for ^{60}Co to 0.17% for the M120 beam. This increase in variability was likely due to the decreased signal-to-noise ratio of chambers in low-dose rate beams and the increased sensitivity to chamber dimensions and materials in low-energy beams. The leakage of the microchambers composed approximately 0.5% of the chamber signal. A degradation in reproducibility was also seen with the Farmer-type and scanning chambers in the M120 beam. The saturation curves measured with Farmer-type and scanning chambers also exhibited voltage-dependent effects not seen in higher-energy beams. Further investigation into these effects is required. The microchamber saturation curves for the M120 x-ray beam demonstrated the same anomalous behaviors which occurred in high-energy photon beams. The relative magnitude of the polarity effects increased with the lower-energy beam, but the relative shapes of the saturation curves remained constant. These results support the theory that a significant voltage-dependent process is occurring in microchambers. This investigation also suggests that the anomalous process may occur in Farmer-type and scanning chambers as well, but under typical high-energy, high-dose-rate irradiations the chamber signal is high enough that the effect is negligible.

Air-kerma calibration coefficients were measured for ^{60}Co and x-ray beams (with effective photon energies ranging from 11.5 keV to 145 keV) with a variety of cylindrical ionization chambers varying in size and collecting electrode material. All chambers containing low-Z materials ($Z \leq 13$) exhibited chamber responses with little dependence on the beam quality, independent of the size of the chamber. These chambers typically exhibited variations in calibration coefficients of less than 3% with the beam quality in the range of medium-energy beams. However, variations greater than 50% in N_{K} were found for all microchambers containing high-Z collecting electrodes ($Z > 13$), specifically, the Exradin A14SL and A16 chambers, the IBA CC01 chamber, the PTW TN31006 chamber, and the proof-of-concept chamber containing silver. Between the two Exradin microchambers that were

nearly identical with the exception of the size of the thimble, the chamber with the smallest cavity (and thus the largest fraction of the cavity occupied by the collecting electrode) exhibited greater variations in N_K.

These results demonstrate that the energy dependence of these ionization chambers is not inherent to small-volume chambers, but rather is a complex function of the material of the chamber components as well as the relative dimensions of each component. Only the microchambers containing high-Z collecting electrodes showed variations in N_K with beam quality outside of the required TG-61 limits. As a result, it is recommended that only microchambers containing low-Z collecting electrodes be considered for reference dosimetry measurements in low- and medium- energy x-ray beams.

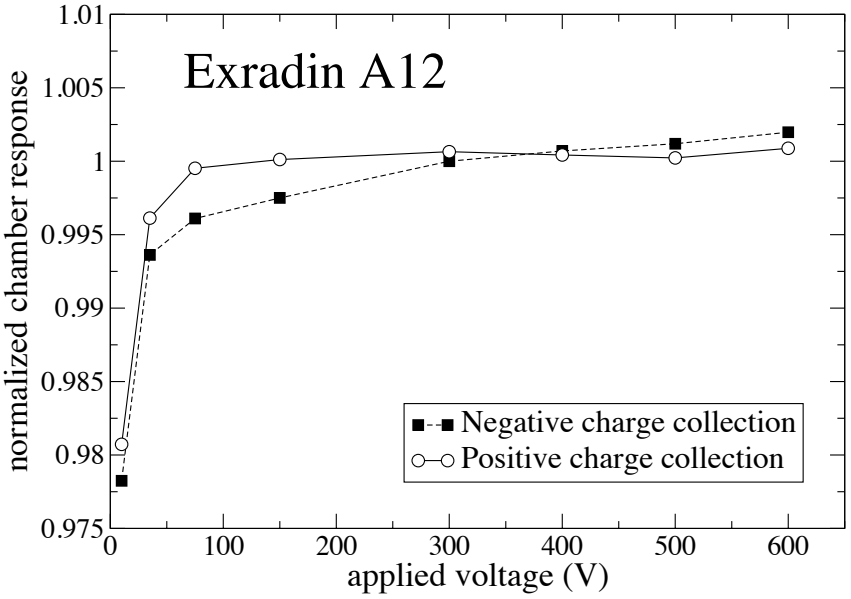

(a)

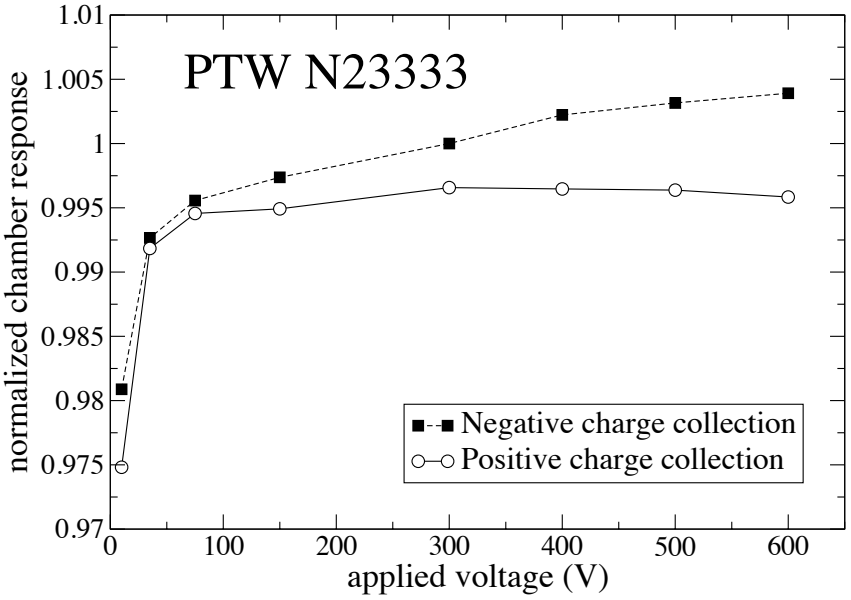

(b)

Figure 5.3: Normalized saturation curves measured with two Farmer-type ionization chambers, (a) an Exradin A12 and (b) a PTW N23333. All data were normalized to the average signal received when the chamber was biased to a polarizing voltage of +300 V (negative charge collection).

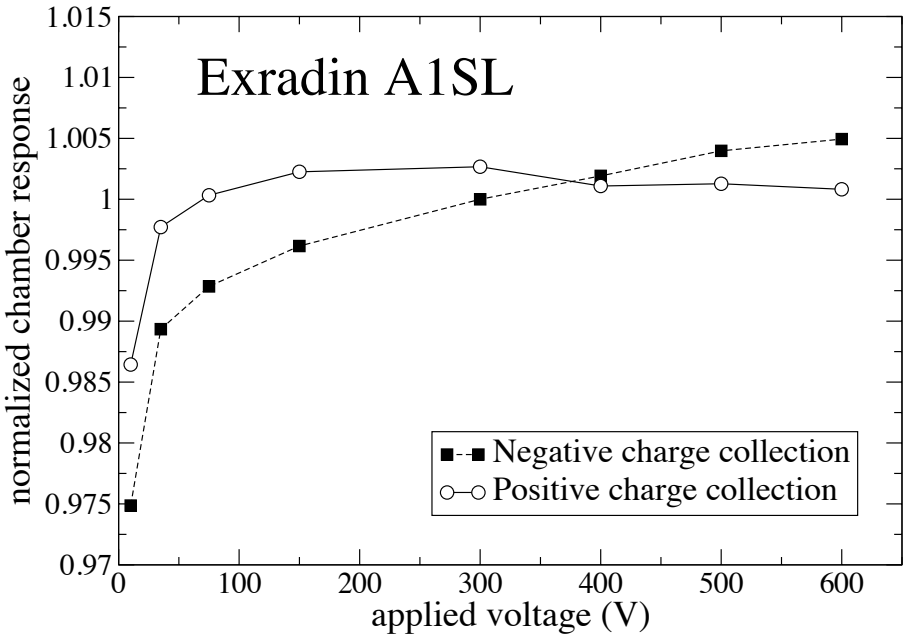

Figure 5.4: Same as Figure 5.3 except for an Exradin A1SL ionization chamber.

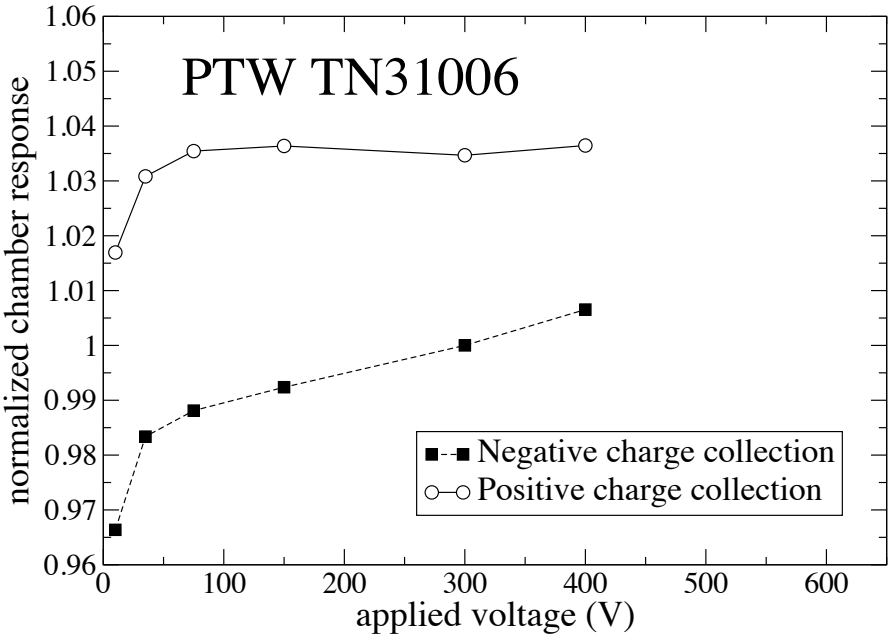

(a)

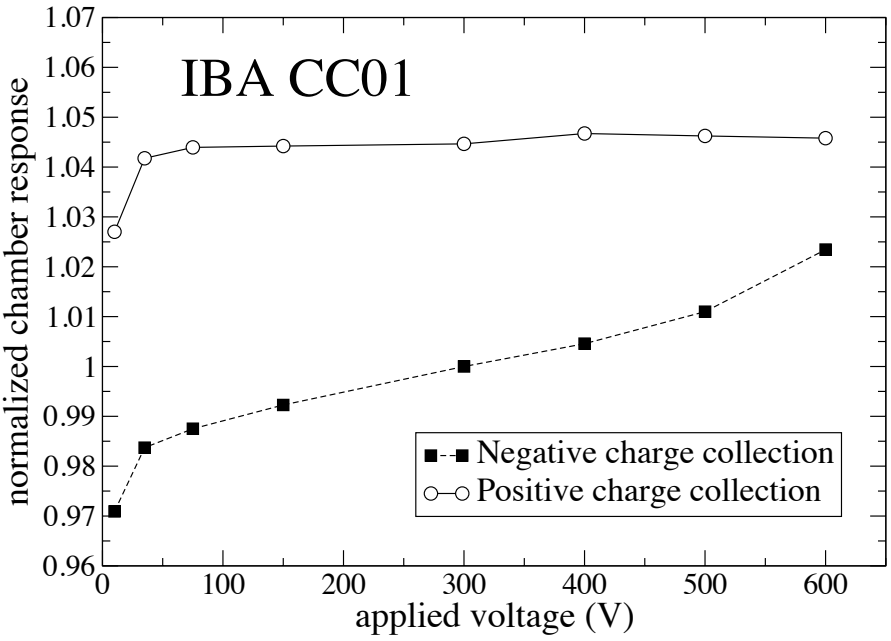

(b)

Figure 5.5: Same as Figure 5.3 except for two microionization chambers; (a) a PTW TN31006 and (b) an IBA CC01.

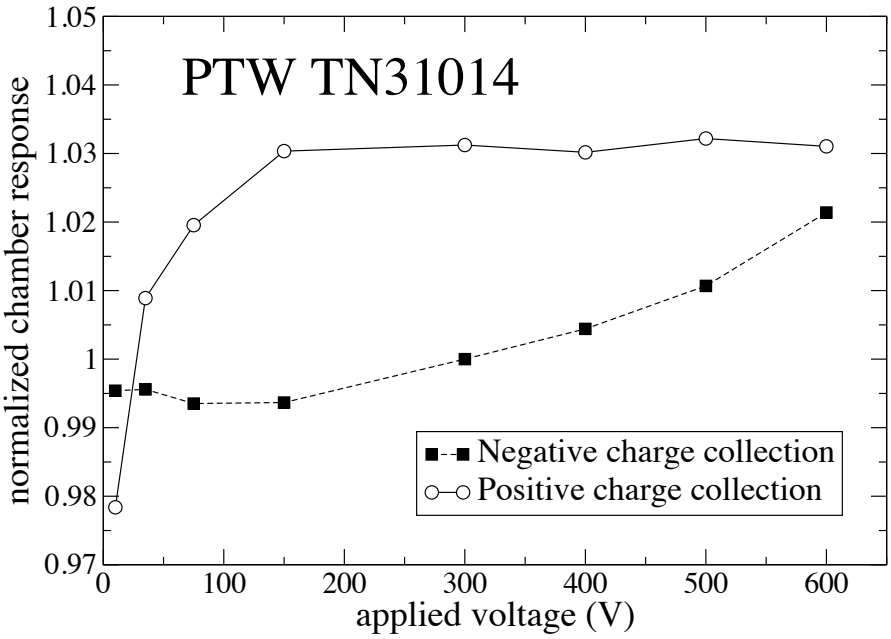

(a)

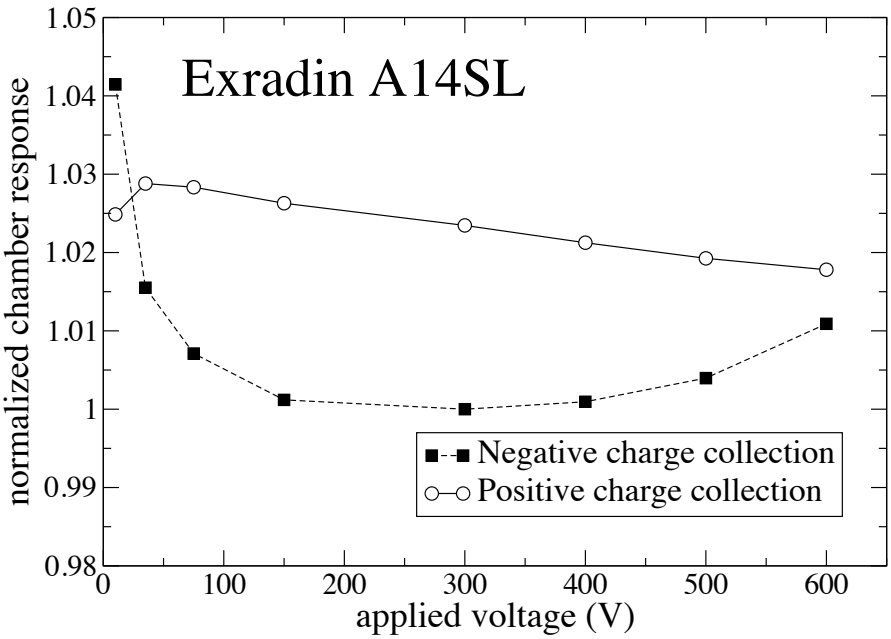

(b)

Figure 5.6: Same as Figure 5.3 except for two microionization chambers; (a) a PTW TN31014 and (b) an Exradin A14SL.

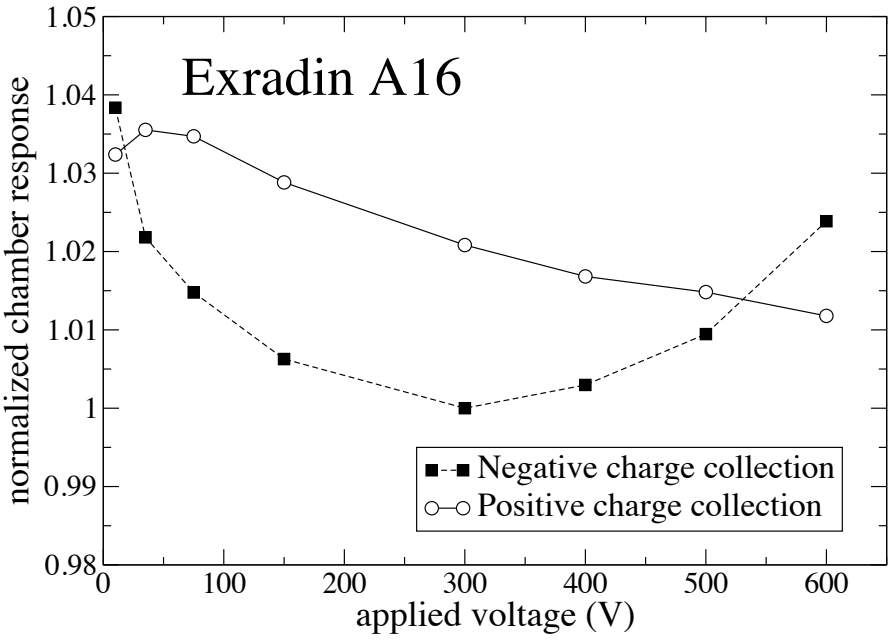

(a)

Figure 5.7: Same as Figure 5.3 except for an Exradin A16 microchambers.

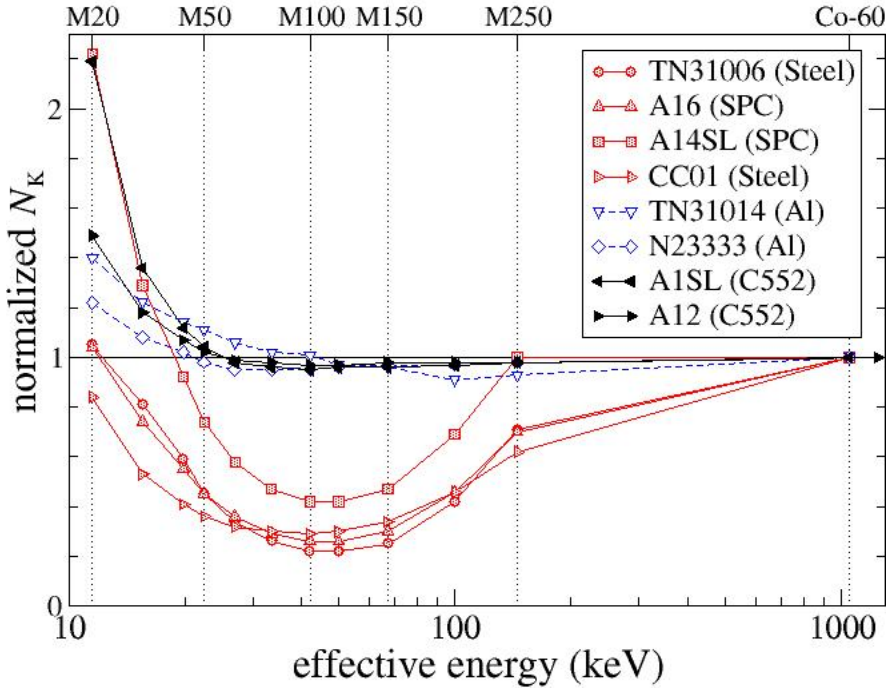

(a)

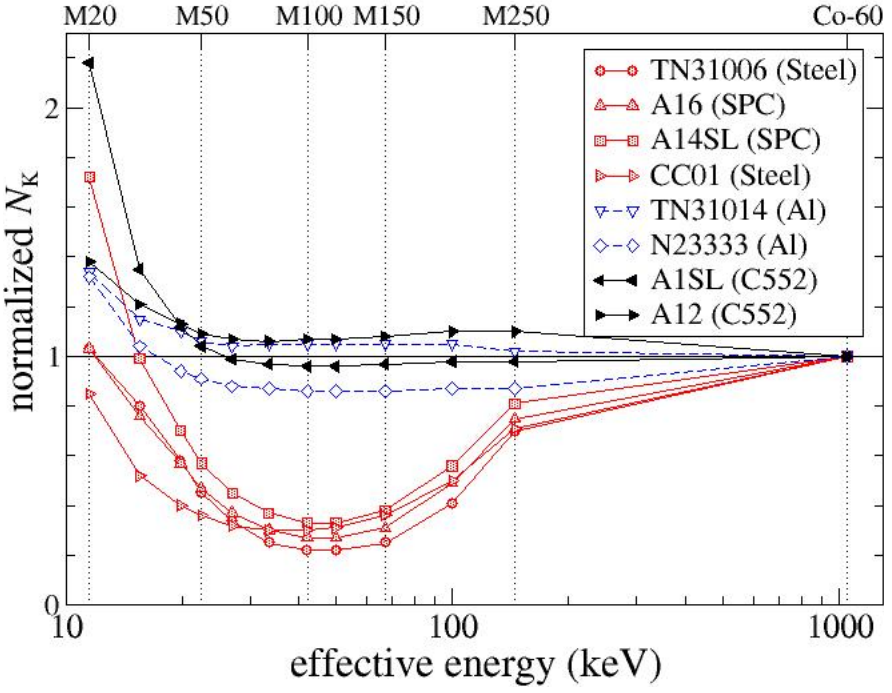

(b)

Figure 5.8: Normalized air-kerma calibration coefficients, N_K, measured with ionization chambers biased to (a) +300 V (negative charge collection) and (b) -300 V (positive charge collection) for x-ray beams with effective energies ranging from (11.5 to 145) keV. The material specification next to each chamber model in the legend denotes the collecting electrode material. The uncertainty at the k=2 level for the N_K measurements was 1.5%.

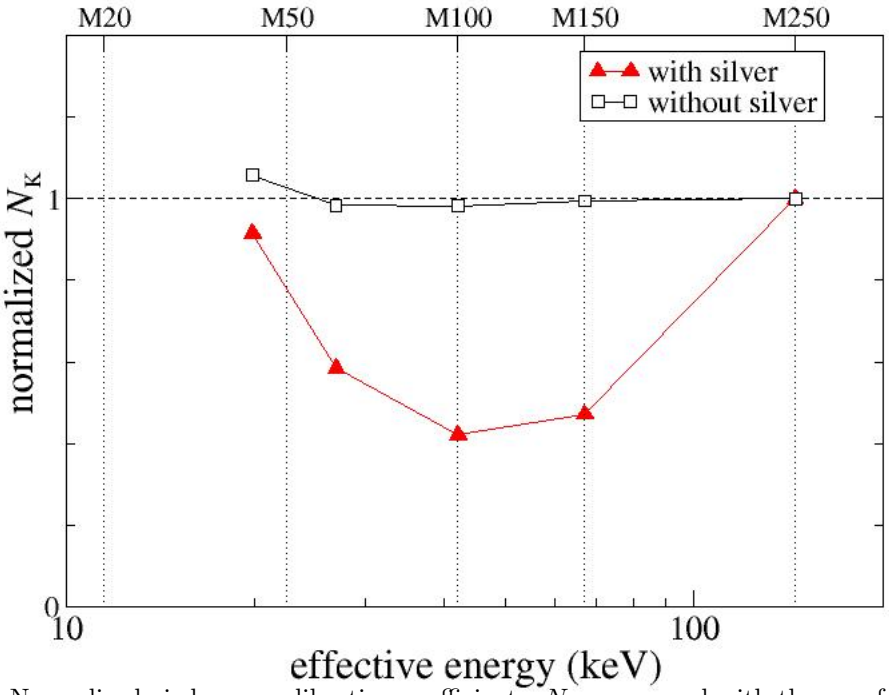

Figure 5.9: Normalized air-kerma calibration coefficients, N_K, measured with the proof-of-concept low-Z microchamber biased to +300 V (negative charge collection) for photon beams with effective energies ranging from 19.8 keV to 145 keV. Each N_K value is normalized to the N_K value measured in the M250 beam during each measurement set. The uncertainty at the k=2 level for the N_K measurements was 1.5%.

Chapter 6

Electric field characterization

It has been suggested that the anomalous behavior exhibited by microchambers may be a result of secondary electron emission in the presence of strong electric fields. It has been shown that secondary electron emission varies with the incident charged particle energy. Therefore, the strong electric fields induced in microchamber cavities may alter the energy of the charged particles such that the secondary electron emission varies, creating voltage-dependent polarity effects. This chapter investigates the ability of validity of this theory and the capability of EGSnrc Monte Carlo code to model these effects.

6.1 Electric field modeling

The electric field inside the cavity of several ionization chambers was modeled using COMSOL Multiphysics® finite element analysis software. To determine the geometric specifications of individual chambers, three-dimensional (3D) computed tomography (CT) images of each chamber were taken using the University of Wisconsin Carbone Cancer Center's Inveon microCT/microPET hybrid scanner from Siemens. Unfortunately, the high-Z components inside each microchamber caused significant artifacts, resulting in images that could not be used to derive accurate chamber dimensions. Therefore, only the Exradin ionization cham-

ber models were created, using proprietary manufacturing CAD diagrams provided by SI. Figure 6.1 shows a cross-sectional view of the electric potential and corresponding electric field lines inside a parallel plate chamber that was created in house. Due to the cylindrical symmetry of an ionization chamber, all the information needed to reconstruct a 3D field can be simulated with an axisymmetric two-dimensional model created using the AC/DC Electrostatic Application Module 3.5a. The AC/DC Module is an optional add-on package that extends the COMSOL Multiphysics® modeling environment to assist in modeling and solving electromagnetic problems.

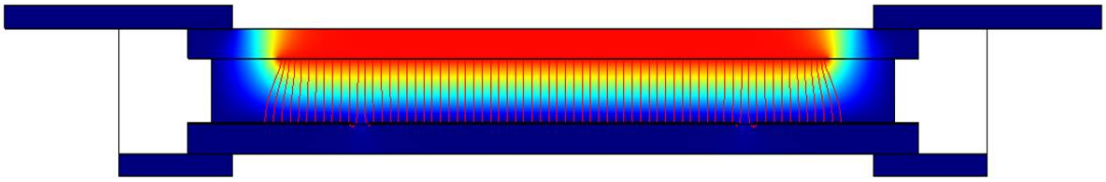

Figure 6.1: A COMSOL Multiphysics® model of the electric potential inside a parallel plate chamber. The electric potential ranges from 300 V in red to 0 V, or ground, in blue. The vertical red lines represent electric field lines that define the collecting volume.

In the AC/DC module, an electric potential was applied to the guard and collecting electrodes with respect to the wall electrode held at ground. This was accomplished by specifying material properties in active chamber volumes, or subdomains, and applying boundary conditions to the geometry interfaces. The wall, guard, and collecting electrode subdomains were inactivated to maximize efficiency and eliminate unnecessary mesh artifacts. A relative permittivity of 2.1 and 1.00059 were applied to the subdomains composed of insulation and air, respectively. An electric potential boundary condition was applied at the interface of all the electrode surfaces to specify the voltage at each boundary. The boundaries between the insulation and air volumes were set to allow continuous charge distribution by specifying the normal component of the electric displacement to be continuous across the boundary.

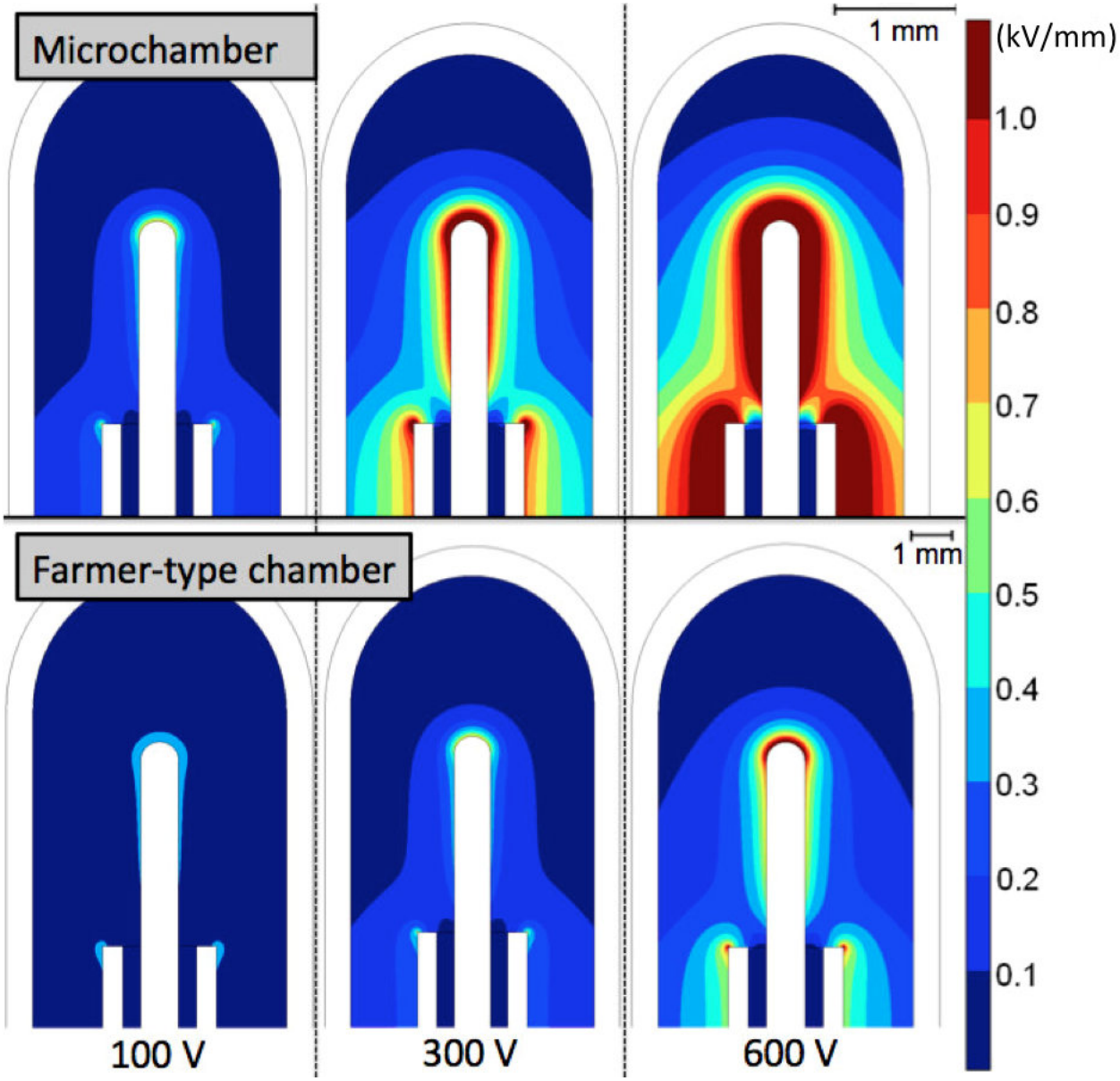

Figure 6.2: A COMSOL Multiphysics® model of the contoured normalized electric field inside a generic microchamber (top) and Farmer-type chamber (bottom). The electric potential difference applied to the electrodes was 100 V (left), 300 V (middle) and 600 V (right).

To maximize accuracy, a refined free mesh was applied to the active subdomains to partition the geometry into smaller units of simple shapes. None of the coefficients or material properties contained dependent variables thus eliminating the need for a complex nonlinear solver. The electric potential and electric field were calculated by Gaussian elimination using COMSOL's linear system UMFPACK direct solver. Figure 6.2 demonstrates the normalized electric-field contours inside a generic microchamber (top) and Farmer-type chamber (bottom) using this methodology. The columns, from left to right, show the chambers simulated with applied voltages of 100 V, 300 V, and 600 V. It has been suggested that charge multiplication may be negligible in ionization chamber measurements for electric field strengths of less than 2000 V/mm. However, charge multiplication effects can begin to occur at electric field strengths of 1000 V/mm (Zankowski and Podgorsak, 1998; Attix, 2004; Boag et al., 1987; Jeffery et al., 1974). In Figure 6.2 the dark red contours represent electric field strengths of 1000 V/mm or greater. At a typical operating voltage of 300 V, the microchamber, unlike the Farmer-type chamber, demonstrated electric-field strengths capable of producing charge multiplication. At 600 V, a substantial portion of the collecting volume contained an electric field of greater than 1000 V/mm. These results agreed well with the Exradin A1SL scanning chamber measurements presented in Chapter 3, where the additional exponential charge collection, theorized as charge multiplication, can be seen at operating voltages as low as 150 V. This also further validates the need to account for additional exponential charge collected in smaller-volume chambers for ion recombination corrections.

To use this data in Monte Carlo simulations, the r and z coordinates and corresponding components of the electric field (E_r and E_z) and electric potential (V_r and V_z) were exported as a matrix of data points. The integration of this data into the EGSnrc source code is discussed further in Section 6.2.1.2

6.2 Charged particle transport in the presence of an electric field

6.2.1 Development

6.2.1.1 Integration of external field macros

Deflection The change in the momentum, **p**, of a particle is proportional to the force, **F**, acting upon it. In traditional Monte Carlo techniques, the forces acting upon a particle can be separated into two categories: inelastic forces, $\mathbf{F}_{\mathrm{i}}$, and elastic forces, $\mathbf{F}_{\mathrm{e}}$. Thus, in the absence of an external electric or magnetic field, the equation of motion for a charged particle in a homogeneous medium can be written as

$$\frac{d\mathbf{p}}{dt} = \mathbf{F}_{\mathrm{i}}[E(t)] + \mathbf{F}_{\mathrm{e}}[E(t)], \tag{6.1}$$

where t is the time and E is the energy of the charged particle. The addition of an external electric or magnetic field introduces a third term, $\mathbf{F}_{\mathrm{em}}$, which is dependent on the position, x, the direction, u, and E of the charged particle. To account for the presence of an external field, Equation 6.1 must be extended as

$$\frac{d\mathbf{p}}{dt} = \mathbf{F}_{\mathrm{i}}[E(t)] + \mathbf{F}_{\mathrm{e}}[E(t)] + \mathbf{F}_{\mathrm{em}}[\mathbf{x}(t), E(t), \mathbf{u}(t)]. \tag{6.2}$$

By integrating over t, Equation 6.2 can be written as

$$\mathbf{v} = \mathbf{v}_0 + \frac{1}{m_0\gamma(E)}\{\mathbf{F}_{\mathrm{i}}[E(t^{'})] + \mathbf{F}_{\mathrm{e}}[E(t^{'})] + \mathbf{F}_{\mathrm{em}}[\mathbf{x}(t^{'}), E(t^{'}), \mathbf{u}(t^{'})]\}dt^{'} \tag{6.3}$$

where $\mathbf{v}$ and $\mathbf{v}_0$ are the initial and final velocities of the particle. m_0 is the rest mass of the particle and γ is the relativistic factor. A further integration gives

$$\mathbf{x} = \mathbf{x}_0 + \mathbf{v}_0 t + \mathbf{v}(t'')dt'' \tag{6.4}$$

These equations are rather complex and difficult to theoretically model because several components depend on the same variables, and therefore, are coupled together. For example, the inelastic, elastic, and electromagnetic forces all rely on the energy of the particle as it varies with time. If the particle undergoes an inelastic interaction, the effect of the interation on the particle's energy will coincide with a change in the electromagnetic and elastic forces. To further complicate the issue, during a condensed-history transport step, the exact trajectory and interactions of the particle are not known. Prior to the condensed step, the particle has a known position, $\mathbf{x}_0$, velocity, $\mathbf{v}_0$ (and thus direction vector, $\mathbf{u}_0$), and energy, E_0. In order to uncouple these parameters and allow for condensed-history Monte Carlo transport, this work relies on a statistical treatment of each component using the initial known parameters.

Using this method, the charge particle step is decoupled into two main components: (a) particle transportation using traditional EGSnrc transport algorithms in the absence of an external field, and (b) particle transportation accounting solely for the external electric or magnetic field. At the completion of each field-free charged-particle step, the influence of the external field is accounted for. To preserve accuracy of charged particle transport while employing this decoupled technique, the external field must not change significantly over the trajectory of the particle. The charged particle step must be small enough that the external field, as well as the energy and direction of the particle, does not vary greatly over the course of the step.

By decoupling the parameters in equation 6.3 and converting the total time of a step to the total path length of a step, s, Equation 6.3 becomes

$$\mathbf{v} = \mathbf{v}_0 + \frac{s}{m_0\gamma(E)v_0}\mathbf{u}_0 \cdot [\mathbf{F}_{\mathrm{i}}(E_0) + \mathbf{F}_{\mathrm{e}}(E_0) + \mathbf{F}_{\mathrm{em}}(\mathbf{x_0}, E_0, \mathbf{u}_0)]. \tag{6.5}$$

Using the simple relationship, $\mathbf{v} = \mathbf{v}_0 + \Delta\mathbf{v}$, the change in velocity of the particle, $\Delta\mathbf{v}$, can be written as

$$\triangle\mathbf{v}(E_0) = -\frac{s}{m_0\gamma(E_0)v_0}\mathbf{u}_0 \cdot [\mathbf{F}_{\mathrm{i}}(E_0) + \mathbf{F}_{\mathrm{e}}(E_0) + \mathbf{F}_{\mathrm{em}}(\mathbf{x_0}, E_0, \mathbf{u}_0)]. \tag{6.6}$$

As mentioned in Section 2.6.1, the ability of EGSnrc to accurately account for the inelastic and elastic forces in charged particle transport has been well established. The focus of this work is to maintain that high level of accuracy while incorporating the additional effects of an external electric field. With the previously discussed assumptions in place, the decoupled forces can be calculated separately so the influence of the elastic and inelastic forces will not be discussed further in this section. By ignoring the traditional EGSnrc forces and focusing on the contributions of external electric and magnetic fields, Equation 6.6 can be simplified as

$$\triangle\mathbf{v}(E_0) = -\frac{s}{m_0\gamma(E_0)v_0}\mathbf{u}_0 \cdot \mathbf{F}_{\mathrm{em}}(\mathbf{x_0}, \mathrm{E}_0, \mathbf{u}_0)_{\mathrm{i}}. \tag{6.7}$$

The change in the direction vector can be calculated using the definition of the direction vector, $\mathbf{u} = \mathbf{v}/|v|$, were $|v|$ is the norm. Therefore, we can calculate the change in the direction vector over the course of a step as follows

$$\Delta\mathbf{u}_{\mathrm{em}} = \frac{s}{m_0\gamma(E_0)v_0^2}\mathbf{F}_{\perp,\mathrm{em}}(\mathbf{x_0}, E_0, \mathbf{u}_0) \tag{6.8}$$

where, $\mathbf{F}_{\perp,\mathrm{em}}$ denotes the components of the electromagnetic force perpendicular to the initial direction vector $\mathbf{u}_0$. Using Equation 6.4 and Equation 6.8, we can calculate the change in the position of the particle as

$$\Delta\mathbf{x}_{\mathrm{em}} = \mathbf{u}_0 s + \frac{s}{2}\Delta\mathbf{u}_{\mathrm{em}}. \tag{6.9}$$

In this form, the changes in the position and the direction of the particle are dependent upon the electric field. The total force acting on a charged particle from an electromagnetic field is called the Lorentz force ($F = qE = qv \times B$). This fundamental equation can be be manipulated [as shown in Jenkins et al. (1988)] into the following form.

$$\mathbf{F}_{\perp,\mathrm{em}}(\mathbf{x_0}, E_0, \mathbf{u}_0) = e[\mathbf{E}_0 - \mathbf{u}_0(\mathbf{u}_0 \cdot \mathbf{E}_0) + \mathbf{v}_0 \times \mathbf{B}_0], \tag{6.10}$$

where $\mathbf{E}_0$ and $\mathbf{B}_0$ are the electric and magnetic fields. By integrating the components of $\mathbf{F}_{\perp,\mathrm{em}}$ into Equations 6.8 and 6.9, the final equations of displacement used in the updated macros are

$$\mathbf{u}_\mathrm{f} = \mathbf{u}_0 + \frac{se}{m_0\gamma(E_0)v_0^2}[\mathbf{E}_0 - \mathbf{u}_0(\mathbf{u}_0 \cdot \mathbf{E}_0) + \mathbf{v}_0 \times \mathbf{B}_0], \tag{6.11}$$

and

$$\mathbf{x}_\mathrm{f} = \mathbf{x}_0 + \mathbf{u}_0 s + \frac{s^2 e}{2m_0\gamma(E_0)v_0^2}[\mathbf{E}_0 - \mathbf{u}_0(\mathbf{u}_0 \cdot \mathbf{E}_0) + \mathbf{v}_0 \times \mathbf{B}_0]. \tag{6.12}$$

To incorporate this updated version of the macros into EGSnrc, the EGSnrc source code was altered. Since magnetic fields were not needed for this work, the source code was not modified to incorporate magnetic fields. To account for electric fields, the ELECTR subroutine (as discussed in Section 2.6.2) was altered to incorporate the macros accordingly. The ELECTR subroutine conducts charged particle transport separately in vacuum and dense media. Therefore, the macros were integrated separately for charged particle steps in vacuum and dense media. In both cases, the macros were called after the field-free inelastic and elastic collisions in each charged particle step.

Energy The energy of a charged particle is not affected by an external magnetic field, but can change drastically in a strong electric field. Simplistically, the change in the electric

potential difference of an external field experienced by a charged particle is directly proportional to the change in the kinetic energy of the particle. For the sake of the EGSnrc code, the change in the energy of the particle was accounted for as

$$\Delta E = e\mathbf{E}(\mathbf{x}_\mathrm{f} - \mathbf{x}_\mathrm{i}) \tag{6.13}$$

or

$$\Delta E = \mathbf{V}_\mathrm{f} - \mathbf{V}_\mathrm{i}, \tag{6.14}$$

where, $\mathbf{V}_\mathrm{i}$ and $\mathbf{V}_\mathrm{f}$ represent the potential energy at the initial and final positions of the charged particle step, respectively. For charged particle steps in vacuum, the source code was altered to call upon the energy macros for the electric field immediately after the change in energy for the particle was assigned to zero for traditional EGS transportation. In dense media, the macros were implemented immediately after the change in energy due to inelastic scattering was accounted for in the field-free transport. Further updates were made throughout the source code when the energy of the particles was updated or assigned to a new variable, specifically after the elastic scattering was simulated and at the end of the ELECTR subroutine when discarded electrons were assigned an energy.

6.2.1.2 Integration of COMSOL simulated electric fields

The CAVRZnrc and DOSRZnrc user codes were chosen for ease of verification and implementation. The RZ user codes are part of a system of user codes created to allow easier input of cylindrical geometries (Rogers et al., 2003). DOSRZnrc scores dose in right cylindrical geometries and has been extensively benchmarked. CAVRZnrc, which scores dose as well as other quantities used in dosimetry calculations, is used primarily for cavity ion-

ization chamber simulations to determine correction factors that account for scatter and attenuation in the wall of the chamber (Kawrakow et al., 2010; Rogers et al., 2011).

The source code was modified to comply with the CAVRZnrc user code and the COMSOL electric field data was reformatted and inserted into the macros as six separate Mortran data arrays (r coordinates, z coordinates, E_r, E_z, V_r, and V_z). It is also worth noting that COMSOL data was provided in units of m, V, and V/m, but EGSnrc required cm, MeV, and cm^{-1} for the position coordinates, electric potential, and electric field (Table 6.1). All data was converted accordingly.

Further coding was performed to accurately identify the data sets and integrate each array into the macros. An interpolation code was written to define the electric field between the input data points. After completion of each charged particle step the code identified the position of the particle (P_x, P_y, and P_z). If P_z matched any of the z coordinates for which the electric field, E_z, was defined, the code output the corresponding E_z value. If the particle was positioned outside of the defined electric field, E_z was defined as zero. If the particle fell in between two z coordinates for which E_z was defined, a linear interpolation is performed between the corresponding E_z values. A similar interpolation was performed to calculate E_r.

Table 6.1: The components of the electrostatic parameters of interest, and their corresponding units, for the ionization chamber models created in COMSOL and EGSnrc.

	COMSOL		EGSnrc	
Parameters	Matrices	Units	Matrices	Units
Coordinates	$z(i)$ $r(j)$	m	$x(i)$ $y(j)$ $z(k)$	cm
Electric potential	$V_r(i,j)$ $V_z(i,j)$	V	$V_x(i,j,k)$ $V_y(i,j,k)$ $V_z(i,j,k)$	MeV
Electric field	$E_r(i,j)$ $E_z(i,j)$	V/m	$E_x(i,j,k)$ $E_y(i,j,k)$ $E_z(i,j,k)$	1/cm

As shown in Table 6.1, CAVRZnrc simulations are performed in a three-dimensional Cartesian coordinate system so the radial component of the electric field, E_r, was further subdivided into the corresponding Cartesian x and y components (E_x and E_y). To accurately define E_x and E_y when the particle was in the positive x and y quadrant, the angle between the particle position and the positive x-axis was calculated as follows:

$$\theta = tan^{-1}\left(\frac{P_x}{P_y}\right). \tag{6.15}$$

If the particle stopped in one of the other three x and y quadrants, a slightly altered but similar calculation was performed to obtain the appropriate angle. E_x and E_y were defined as

$$E_x = E_r cos\left(\theta\right), \tag{6.16}$$

and

$$E_y = E_r sin\left(\theta\right). \tag{6.17}$$

The interpolation code was first written in MATLAB® and Fortran and extensively tested for any mathematical errors. Upon verification that the code was correctly interpolating data and accurately defining the external field for every point in the simulation geometry, the code was translated to Mortran. The complete Mortran macros were integrated into the CAVRZnrc and DOSRZnrc user codes through the Makefiles and were called upon throughout the ELECTR subroutine as previously discussed.

6.2.2 Simulations

6.2.2.1 Benchmarking

To benchmark the modified source code, a method similar to that of Bielajew in Jenkins et al. (1988) was used to insure the particle transport was accurate in vacuum. Five charged particles were simulated using the CAVRZnrc usercode, three positrons and two electrons, in the presence of a constant 511 keV/cm electric field. The electrons entered the vacuum perpendicular to the field with energies of 2 MeV and 20 MeV. The three positrons entered the vacuum at a 45 degree angle from the perpendicular bisector of the electric field against the direction of the field. The positrons entered the field with energies of 0.1 MeV, 1.0 MeV and 10.0 MeV. These parameters were chosen to coincide exactly with those published by Bielajew in Jenkins et al. (1988).

For this work, the electric field was modeled using (1) theoretical equations and (2) data transferred from a COMSOL simulation. The theoretical calculations for a static 511 keV/cm field were implemented into the macros as

$$E_{\mathrm{x}} = 0.0\,\mathrm{cm}^{-1}, \tag{6.18}$$

$$E_{\mathrm{y}} = 0.0\,cm^{-1}, \tag{6.19}$$

and

$$E_{\mathrm{z}} = -1.0\,cm^{-1}, \tag{6.20}$$

where 1.0 cm^{-1} was equivalent to 511 kV/cm for an electron. The electric potential was modeled as

$$V(z) = z\mathrm{em_e}, \tag{6.21}$$

where z was the position of the particle along the z-axis, e was the charge of the particle (-1 for electrons and +1 for positrons), and $\mathrm{m_e}$ was the rest mass of the charged particle (0.511 MeV for electrons and positrons). To simulate the electric field in COMSOL, a parallel-plate design shown in Figure 6.3(a) was created. The COMSOL electric field data was implemented into the EGSnrc source code, directed parallel to the z axis in the CAVRZnrc simulation. The results of the EGSnrc transport in the presence of both the analytically calculated and the COMSOL simulated electric fields are shown in Figure 6.3(b). The charge particle trajectories agree well for both electric field models. Furthermore, these agree perfectly with the trajectories analytically calculated by Bielajew in Jenkins et al. (1988). These results not only benchmark the implementation of the external electric field effects in EGSnrc, but also benchmark the COMSOL electric field simulations and the methods used to transfer and incorporate the COMSOL data into EGSnrc.

6.2.2.2 Ionization chamber simulations

Prior to running simulations with full ionization chamber geometries, a simplified geometry was used to determine if the anomalous behavior of microchambers, specifically the voltage-dependent polarity effect, was reproducible with EGSnrc electric-field simulations.

The DOSRZnrc user code was used to model a cylindrical water phantom with a radius of 5 cm and a length of approximately 6 cm. The water phantom was positioned at an SSD of 100 cm from a collimated ^{60}Co point source. A simplified chamber geometry was inserted into the water phantom (see Figure 6.4). In Chapters 3, 4, and 5 it was shown that the voltage-dependent polarity effects were significant in the Exradin A16 microchamber, which had the smallest collecting volume. The small chamber size was accompanied by a reduction in the radiation-induced gas ionization and a small electrode plate separation,

which produced strong electric field. Therefore, this chamber was chosen to investigate the possibility of modeling the anomalous behavior in EGSnrc. As shown in Figure 6.4, the simplified geometry contained a series of thin cylindrical plates, corresponding to the Exradin A16 chamber dimensions, as shown in Table 3.1. The plates consisted of two cylinders of air separated by a cylinder of steel representing the collecting electrode. The air volumes were positioned between two thin C552 cylinders mimicking the wall electrodes of the Exradin A16 chamber.

The corresponding electric field and electric potential were modeled between each of the plates and the collecting electrode. The dose was scored in the air volumes within a 5 mm diameter cylinder. This geometry allowed for EGSnrc to model charged particle transport in the presence of strong electric fields and high-Z materials. Identical simulations were performed with the collecting electrode composed of C552 low-Z plastic for comparison.

The results shown in Table 6.2 demonstrate differences between simulations run with opposing polarities and different applied voltages (ranging from 25 V to 300 V). The differences were, however, only significant for the 300 V simulations with respect to the dose uncertainties and the differences were not consistent with the voltage-dependent polarity effects investigated in this work. It is possible that EGSnrc is not capable of modeling the cause of the investigated behavior. While EGSnrc has been shown to accurately simulate ionization chamber response for well-behaving ionization chambers, current MC methods do not simulate many ionization chamber behaviors, such as ion recombination and charge multiplication. These results suggest that either the source of the anomalous behavior for microchambers was due to an effect that EGSnrc was not capable of modeling, or the secondary charged particles creating the effect had energies below 1 kV, beyond which EGSnrc cannot be relied upon for accurate electron transport. It is interesting to note that the voltage-dependent behavior that was modeled by the EGSnrc simulations was slightly

Table 6.2: The normalized dose and corresponding uncertainties simulated in EGSnrc for a simplified Exradin A16 geometry with a collecting electrode composed of silver and of C552 plastic for applied voltages ranging from ±300 V. The dose was normalized to the dose simulated for each geometry in the absence of an electric field. For each simulation the voltage was applied to the collecting and guard electrodes.

Material	Voltage (V)	Collected charge	Normalized dose	Uncertainty (%)
Silver	300	+	0.9968	0.13
		-	1.002	0.13
	50	+	0.9988	0.13
		-	1.000	0.13
	25	+	0.9997	0.13
		-	0.9993	0.13
C552	300	+	0.9978	0.10
		-	1.001	0.10
	50	+	0.9997	0.10
		-	0.9997	0.10
	25	+	1.000	0.10
		-	1.001	0.10

larger for simulations performed with a high-Z, silver collecting electrode compared to the low-Z, C552 collecting electrode.

6.2.3 Conclusions

The electric field and electric potential were modeled using COMSOL Multiphysics software for several commercial ionization chambers. The models were used to investigate electric field strengths and the potential for charge multiplication effects in a variety of chamber volumes. It was discovered that for microchambers, at an applied voltage of less than 300 V the induced electric fields were strong enough over a significant portion of the chamber volume to create charge multiplication. For Farmer-type chambers, this was not the case.

The EGSnrc source code was altered to account for the effects of external electric fields on charged particle transport. The COMSOL-generated electric field and electric potential were imported into the EGSnrc macros. The altered source code and the COMSOL models were benchmarked against analytical calculations. The COMSOL models were shown to correctly

model the induced chamber fields. The EGSnrc source code was shown to accurately account for charged particle deflection and energy change in electric fields.

The benchmarked methodology was used to simulate the effects of polarity at several applied voltages for a simplified Exradin A16 geometry in a water phantom. The simulated dose varied with the applied voltage and polarity; however, the trend in the voltage-dependent polarity effects demonstrated by the microchambers characterized in this work was not observed in the EGSnrc simulations. This suggests that either the current EGSnrc code does not account for or accurately model the processes causing the polarity effects investigated in this work, or the voltage-dependent polarity effects are due to secondary charged particles, created in chamber components, which have energies below the energy threshold of the code. In either case, the source of the anomalous polarity effects for the microchambers investigated in this study was not identified through MC simulations. The following chapters describe the empirical investigation used to isolate and investigate this behavior.

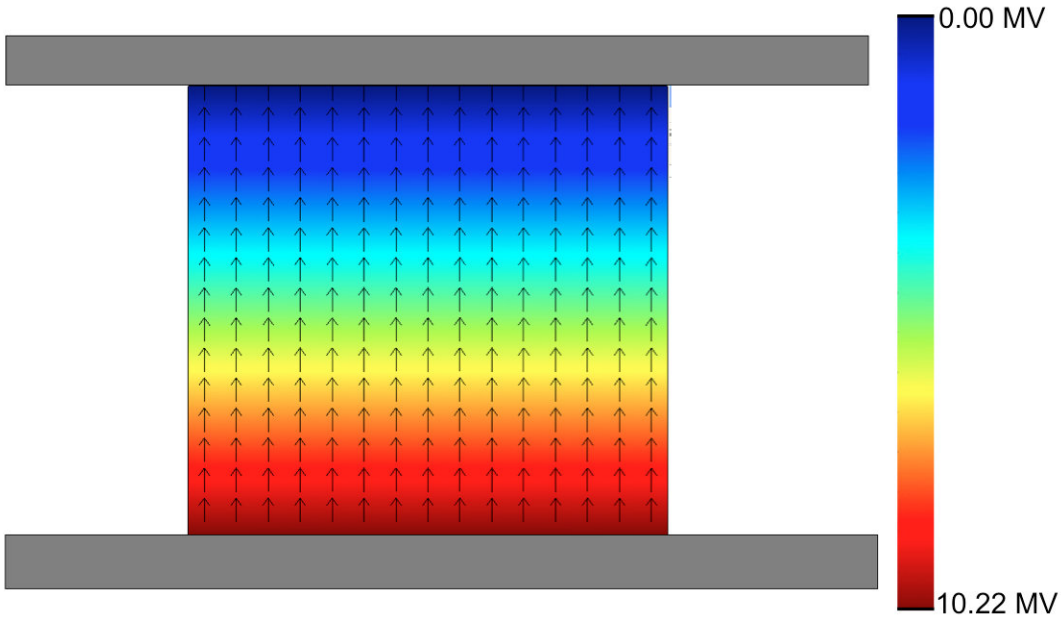

(a)

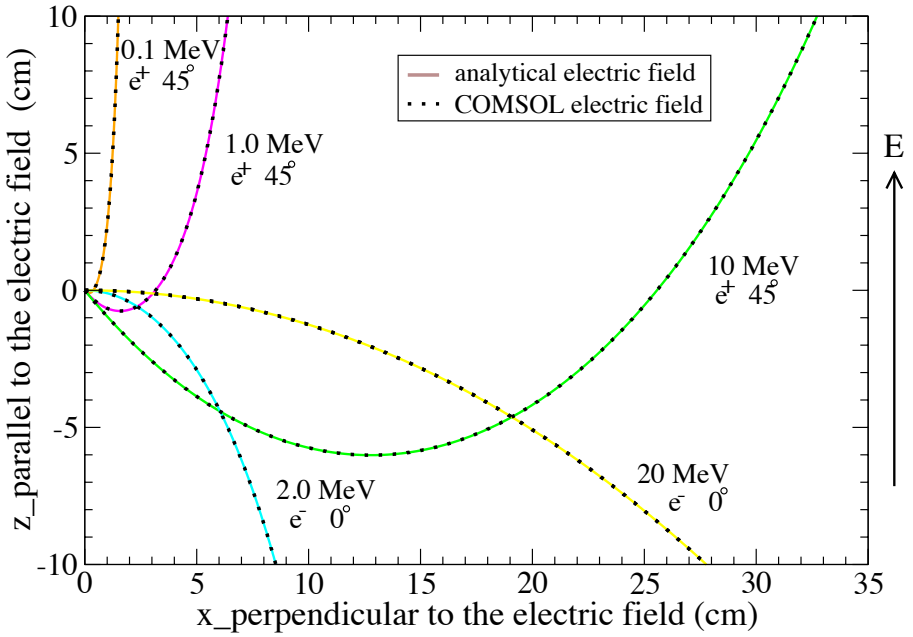

(b)

Figure 6.3: (a) COMSOL-generated electric field lines and electric potential for a parallel-plate chamber creating a 511 kV/cm field, and (b) a graph of the EGSnrc-generated and theoretically calculated charged particle tracks in vacuum in the presence of the COMSOL-generated 511 kV/cm field. The charged particles include three positrons and two electrons that entered the vacuum at a 45 degree angle and perpendicular to the electric field, respectively.

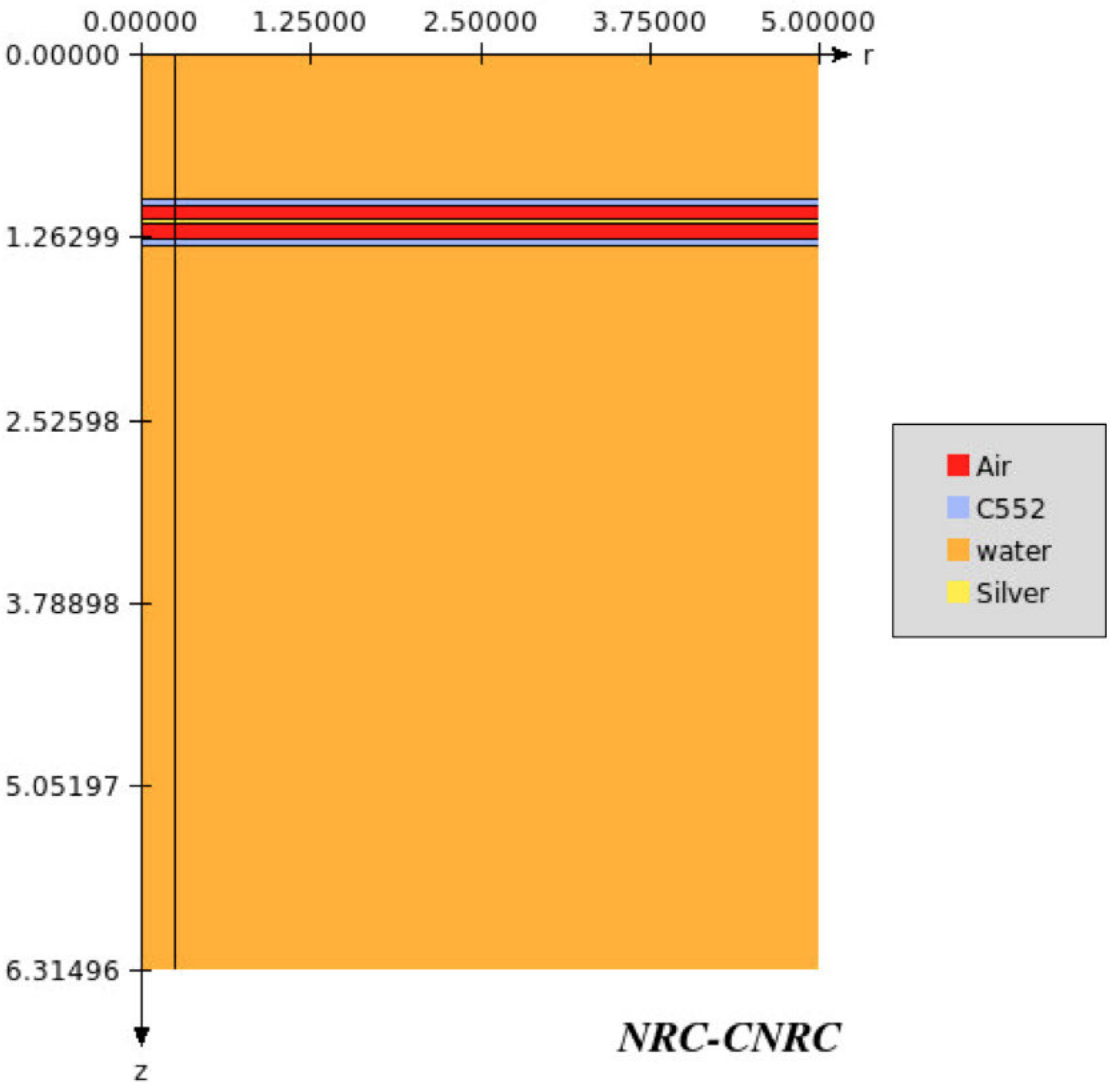

Figure 6.4: Schematic of the DOSRZnrc geometry of a simplified Exradin A16 in water.

Chapter 7

Isolating the source of voltage-dependent polarity effects

As demonstrated in Chapters 3, 4, and 5, an inverse proportionality in chamber response with applied voltage and large voltage-dependent polarity effects were found in all commercial microchambers investigated in this work. These anomalous behaviors render small-volume chambers unsuitable for reference-dosimetry measurements. In Chapter 6 it was demonstrated that current Monte Carlo methods are unable to simulate this behavior. Therefore, this chapter discusses the measurement techniques used to isolate the source of these voltage-dependent polarity effects. A series of investigations were performed with two prototype models, a microchamber and a larger-volume chamber referred to as prototype models J1 and A2, respectively.

7.1 Methods and Materials

For each prototype, saturation curve measurements were performed with the UWADCL Theratron 1000 ^{60}Co irradiator using the methodology described in Chapter 3. Once the behavior for each chamber was established, a series of controlled investigations were pre-

formed to isolate the cause of the voltage-dependent polarity effects. Due to time restraints during these investigations, a subset of applied voltages were selected for several measurements and the chamber response was measured in either air or water using the same methods previously discussed. Measurements were performed to ensure that the relative anomalous behavior of a chamber was consistent in air and water.

7.1.1 Microchamber: J1 prototypes

A set of five microchamber prototypes were manufactured at SI and given the model name J1. The shell, guard, and collecting electrodes of the J1 chambers were composed of a low-Z conductive plastic. The chambers were identical in design with a collecting volume of 0.014 cm^3. The dimensions of the chambers are shown in Table 7.1. The following sections discuss the empirical steps performed with these chambers to determine the source of the voltage-dependent polarity effects.

Table 7.1: Each ionization chamber model used in this work and the corresponding collecting volume, the inner diameter (ID) and outer diameter (OD) of the wall, and the OD of the collecting electrode.

Chamber model	S/N	Collecting volume (cm^3)	Wall		Electrode	
			Material	ID/OD (mm)	Material	OD (mm)
J1 Prototype	1, 2, 3, 4, and 5	0.014	low-Z plastic	0.28/0.33	low-Z plastic	0.08

7.1.1.1 Volume threshold

To better understand the source of the anomalous behavior it was important to determine if a volume threshold existed at which the voltage-dependent polarity effects started to occur or if the voltage-dependent polarity effects were completely independent of the volume of the chamber. To perform this investigation, a series of chamber shells were constructed to fit one of the J1 prototypes, serial number 5. The shell sizes varied, creating collecting volumes

ranging from 0.016 cm^3 to 0.06 cm^3 while maintaining roughly the same inner-radius-to-length ratio. Saturation curve measurements were performed first with the original shell, producing a collecting volume of 0.014 cm^3. The shell was removed and replaced and the measurements were repeated to ensure that removing and placing a new shell on the chamber would not significantly affect the chamber behavior. The remaining shells were placed on the chamber and the chamber was re-characterized.

7.1.1.2 Stem effects and cable irradiation

Several authors have demonstrated that the magnitude of polarity effects for a microchamber are highly dependent on the size of the irradiation field (Agostinelli et al., 2008; Stasi et al., 2004). Larger radiation field sizes often lead to larger portions of the chamber stem and triaxial cable being irradiated. Since the signal collected by small-volume chambers is significantly less than larger volume-chambers, the relative contribution to the chamber response due to extracranial effects, such as stem and cable irradiations, is much larger. To ensure that the voltage-dependent polarity effects demonstrated by the J1 prototypes were not a result of extracranial effects, a series of investigations were performed with the J1 prototype 3. The initial characterization of the J1 prototypes (see Section 7.2.1.2) showed that Prototype 3 demonstrated voltage-dependent polarity effects. Thus, if extracranial effects were the primary source of the voltage-dependent polarity effects, reducing the volume of stem and cable irradiated should in theory significantly reduce the polarity effects.

To isolate the effect of cable irradiations, the chamber was placed at the center of the radiation field. The chamber response was recorded at applied voltages of +10 V, +35 V, +50 V, and +300 V for beam field sizes of 5 x 5 cm^2, 10 x 10 cm^2, 15 x 15 cm^2 and 20 x 20 cm^2 at the center of the chamber volume. The total length of the stem of the chamber was 4 cm. Therefore, in each setup the primary variable was the length of the

cable irradiated. For each of these field sizes, the chamber response was measured at applied voltages of +35 V, and +300 V (negative charge collection).

To isolate the effects of stem irradiation, the chamber response was measured in a 10 x 10 cm^2 field, with the center of the chamber collecting volume in the center of the field and at the edge of the field. In this case, the primary variable was the length of the chamber stem irradiated. For each of these chamber positions, the chamber response was measured at applied voltages of +25 V, and +300 V (negative charge collection).

7.1.1.3 Chamber assembly and contamination

Additional experiments were performed with the J1 prototype 3 to investigate the effects of dust, oil, and other contaminants on the chamber behavior. Similarly, investigations were performed to determine the effect of chamber assembly on the response of the chamber.

First, the shell of the chamber was removed and cleaned with alcohol. Compressed air was used to eliminate any dust or loose contaminants on the surface of the insulators and electrodes. The shell was replaced. The chamber response was measured at applied voltages of +25 V and +300 V.

To investigate the effect of chamber assembly, the electrodes and the insulating material between the electrodes were removed from the chamber. The chamber was then reassembled with the same components. The chamber was placed in a hot box for 36 hours to allow the insulating materials to relax. The chamber response was again measured at applied voltages of +25 V and +300 V.

Finally, the chamber was once again disassembled, and each of the electrodes and the insulating materials between the electrodes were removed. Each component was washed with alcohol and then placed in an ultrasonic cleaner. The components were dried and the chamber was reassembled. The chamber was placed in a hot box for 36 hours to allow the

insulating materials to relax. The chamber response was again measured at applied voltages of +25 V and +300 V.

7.1.1.4 Presence of high-Z materials

A set of experiments were performed to investigate of the effects of the presence of high-Z materials on chamber response. These experiments can be divided into two parts: (1) to determine if high-Z materials were present in chambers exhibiting voltage-dependent polarity effects, and (2) to introduce high-Z materials into the collecting volume of a well-behaving microchamber to determine if the high-Z material caused voltage-dependent polarity effects.

Several methods were used to detect high-Z materials in chambers exhibiting voltage-dependent polarity effects. In Section 7.1.1.3, the presence of loose high-Z materials would have been eliminated in the disassembly and cleaning of each chamber component. To determine if high-Z materials were present in the material of the chamber components, radiographs were taken of each of the chambers. Radiograph images of the full chamber assembly, the internal assembly (insulators, guard electrode, and collecting electrode), and the guard and high-voltage insulator assembly (guard/HV) of prototype 3 are shown in Figure 7.1. In the Figures 7.1(b) and (c) a piece of high-Z silver was placed beside the chamber components for a contrast reference.

To introduce high-Z materials into the collecting volume of a microchamber, the collecting electrode of J1 prototype 5, which demonstrated mild voltage-dependent polarity effects, was coated with a silver epoxy. The silver epoxy, referred to as TIGA 901 resin, was manufactured by the Resin Technology Group (Easton, MA). The TIGA 901 resin mixture, composed of roughly 80% refined pure silver and 20% epoxy resin, was sold as part of a two-part silver epoxy adhesive formulation called TIGA 901 room temperature curing silver conductive epoxy. The TIGA 901 formulation, recommended for electrical bonding and sealing applications, consisted of the TIGA 901 resin in the form of a paste and a TIGA

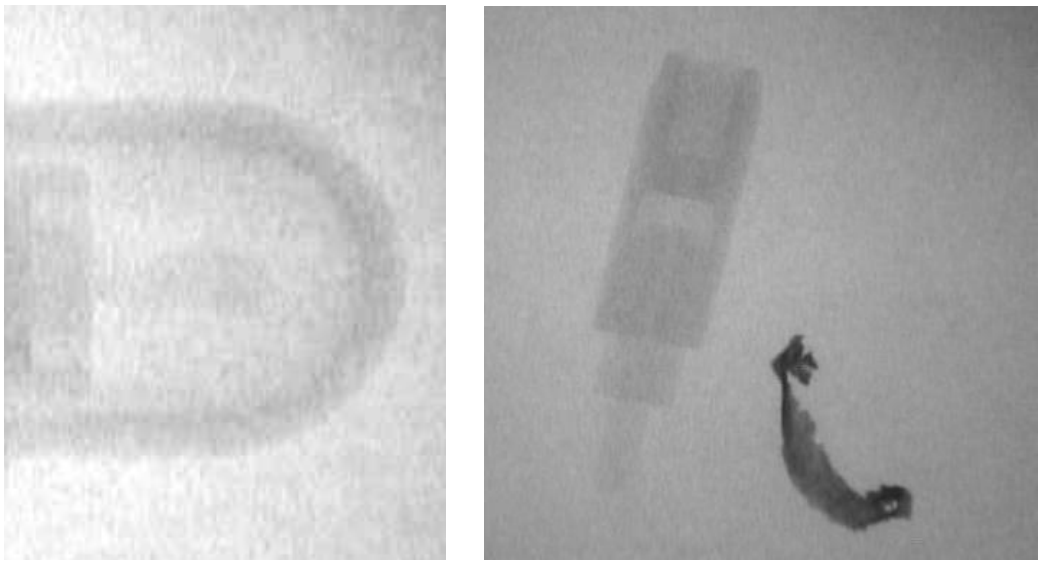

(a) (b)

(c)

Figure 7.1: Radiograph images of (a) the full chamber assembly, (b) the insulators and the guard and collecting electrodes, and (c) the guard/HV assembly. A piece of high-Z silver was placed beside the chamber components in (b) and (c) as a reference for the contrast of a high-Z material.

901 hardener [shown in Figure 7.2(a)]. For typical applications such as electrical bonding and sealing, the resin and hardener are mixed to cure the epoxy; however, to ensure that the high-Z silver could be removed from the collector after the experiment, only the TIGA 901 resin paste was used in this work. An image of the collecting electrode coated with the silver is shown in Figure 7.2(b). Once the epoxy dried, the chamber was place in a hot box for 36 hr and the chamber response was measured at applied voltages of +25 V and +300 V (negative charge collection).

The silver was removed from the collecting electrode and the investigation was repeated for a more complete characterization. Saturation curves were measured for both polarities at applied voltages of 300 V, 150 V, 75 V, 35 V, 10 V, and 300 V. The silver was reapplied to the collecting electrode and the chamber was characterized with the same applied voltage scheme.

7.1.1.5 Electrode and insulator isolation

To isolate the behavior to a specific electrode or insulator, individual components of the J1 prototypes 2 and 4 were swapped and the chambers re-characterized. To swap the chamber components, the shell of each chamber was removed. The components of interest in prototype 2 were removed from prototype 2 and placed in prototype 4. Similarly, the same components from prototype 4 were removed from prototype 4 and placed in prototype 2. After each alteration, the shells were replaced and the chambers were placed in a hot box for a minimum of 36 hrs. The response of each chamber was measured for applied voltages of +25 V and +300 V (negative charge collection).

7.1.2 Larger-volume: A2 prototypes

The thimble Exradin A2 chamber, with a collecting volume of 0.53 cm^3 and electrodes composed of C552 air-equivalent plastic, is marketed as a relative dosimeter for scanning

(a)

(b)

Figure 7.2: Images of (a) the TIGA 901 silver epoxy resin (right) and hardener (left) and (b) the J1 prototype 5 with the shell removed and the TIGA 901 resin coated on the tip of the collecting electrode.

Table 7.2: Each ionization chamber model used in this work and the corresponding collecting volume, the inner diameter (ID) and outer diameter (OD) of the wall, and the OD of the collecting electrode. The materials are aluminum (Al) and air equivalent plastic (C552).

Chamber model	S/N	Collecting volume (cm^3)	Wall		Electrode	
			Material	ID/OD (mm)	Material	OD (mm)
Exradin A2 Prototype	60612	0.53	C552	094/1.14	Al	0.46
	60613	0.53	C552	0.94/1.14	C552	0.46

and point dose measurements in water, air or other phantom material. For this work, two custom Exradin A2 prototypes were investigated. These custom A2 chambers were developed by SI for Dr. Malcolm McEwen at the NRC for an investigation of ionization chamber effective point of measurement (McEwen et al., 2008). The custom A2 chambers were identical in design to the commercial version of the Exradin A2 with the exception of the collecting electrode outer diameter and materials. The collecting electrode in both chambers had a reduced outer diameter of 1 mm, compared to 4.6 mm for the commercial version. The only difference in design between the two A2 prototypes was the material of the collecting electrodes. The A2 prototype S/N 60613 and S/N 60612 contained collecting electrodes composed of C552 plastic and aluminum, respectively.

Due to the thorough investigation performed with the J1 microchamber prototypes, several variables were immediately eliminated as suspects for the cause of the voltage-dependent polarity effects in the custom A2 chambers. Thus, the custom A2 investigation were fast-tracked to a set of experiments designed to isolate the individual chamber electrodes responsible for the behavior.

7.1.2.1 Electrode and insulator isolation

Similar to the J1 prototypes, the individual components of A2 chambers were swapped between the two prototypes followed by a chamber characterization. The components of interest in chamber S/N 60613 were removed from the chamber and placed in chamber S/N 60612. Similarly, the same components from chamber S/N 60612 were removed from chamber S/N 60612 and placed in S/N 60613. After each alteration the chambers were placed in a hot box for a minimum of 36 hrs. The response of each chamber was then measured for applied voltages of +300 V and +50 V (negative charge collection).

7.2 Results and discussion

7.2.1 Microchamber: J1 prototype

7.2.1.1 Volume threshold

The saturation curves performed with each of the shell electrodes placed on the chamber, are shown in Figure 7.3. It is clear that with the original shell size, the chamber exhibited voltage-dependent polarity effects. As the shell size, and thus the collecting volume, increased, the polarity effects were reduced. With the largest shell, at a collecting volume of 0.06 cm^3 (similar to the Exradin A1SL scanning chamber), the voltage-dependent polarity effects were not observable. This indicates that the behavior is inversely proportional to the volume of the chamber, and that there is a threshold for each chamber design at which the voltage-dependent polarity effects either begin to occur or are observable. For the J1 prototype 5 that volume threshold is between 0.026 cm^3 and 0.06 cm^3.

7.2.1.2 Initial J1 prototype characterization

The initial saturation curves measured for each of the J1 microchambers showed varying chamber behavior amongst the five prototypes. As shown in Figures 7.4 , 7.5, and 7.6, the

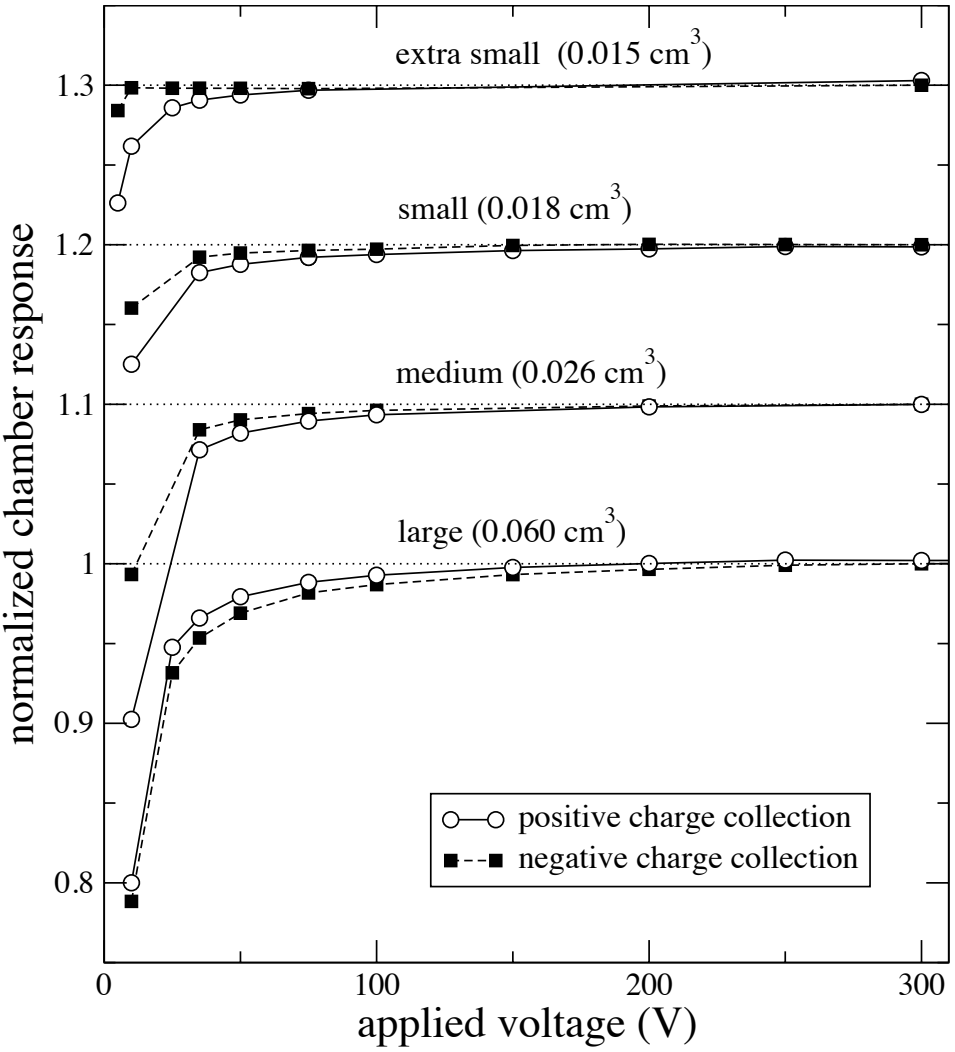

Figure 7.3: Normalized saturation curves measured with the J1 prototype 5 with varying shells sizes. All data were normalized to the average signal received when the chamber was biased to a polarizing voltage of +300 V (negative charge collection) for the corresponding shells size. The saturation curves are offset by 0.1 to allow for better visualization.

magnitude and variation of the polarity effects varied significantly among the chambers. In prototypes 3, and 4 the polarity effects were highly-voltage dependent and the inverse proportionality between chamber response and applied voltage was present. Lesser degrees of this effect were seen in prototypes 1 and 5.

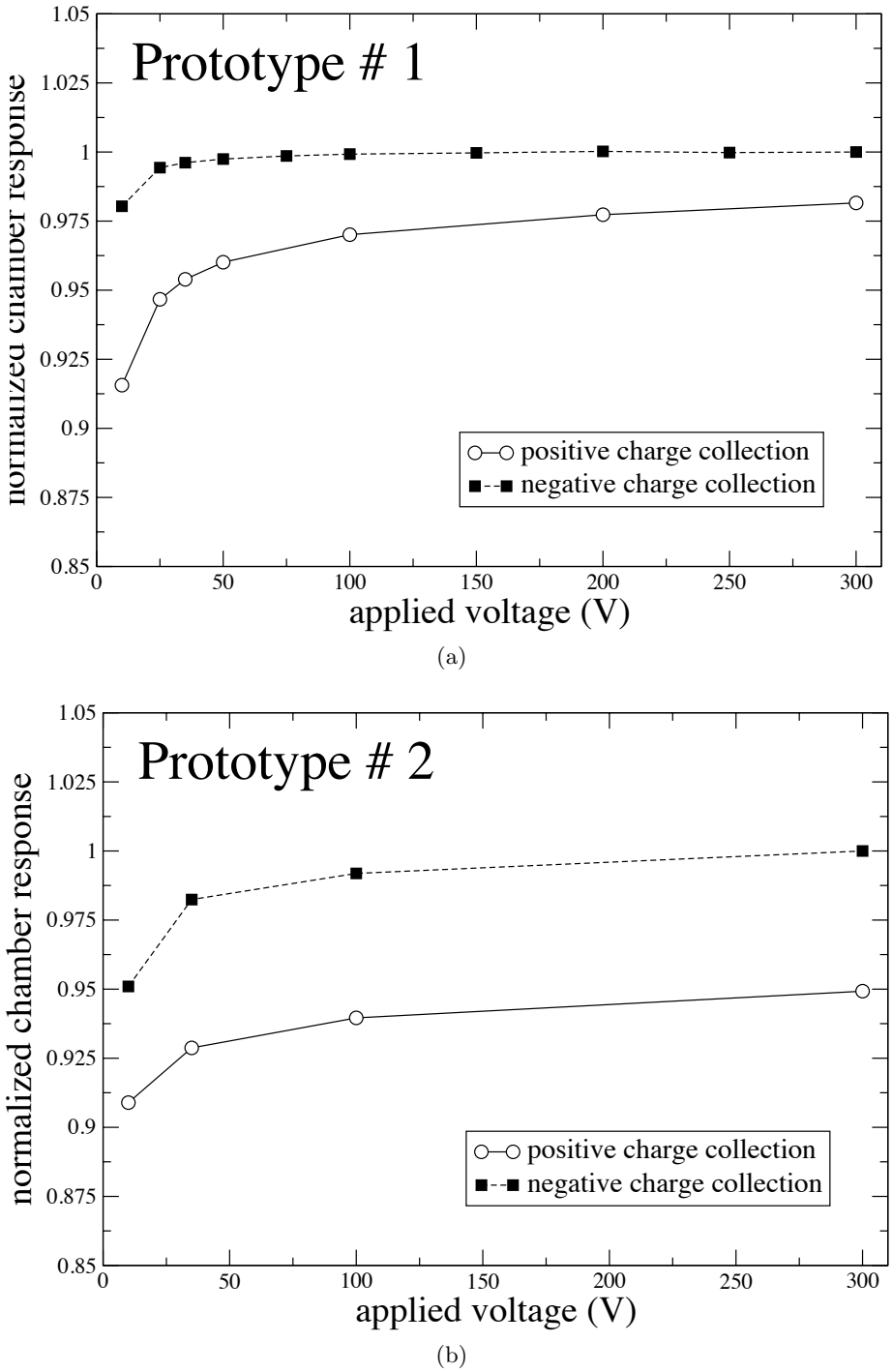

Figure 7.4: Normalized saturation curves measured with two J1 chambers, (a) Prototype 1 and (b) Prototype 2. All data were normalized to the average signal received when the chamber was biased to a polarizing voltage of +300 V (negative charge collection).

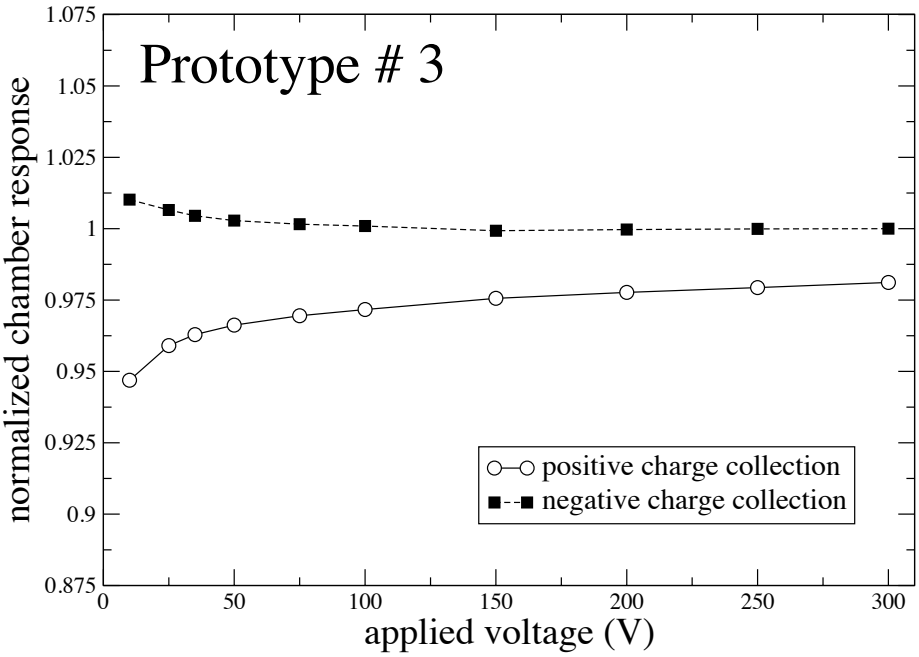

(a)

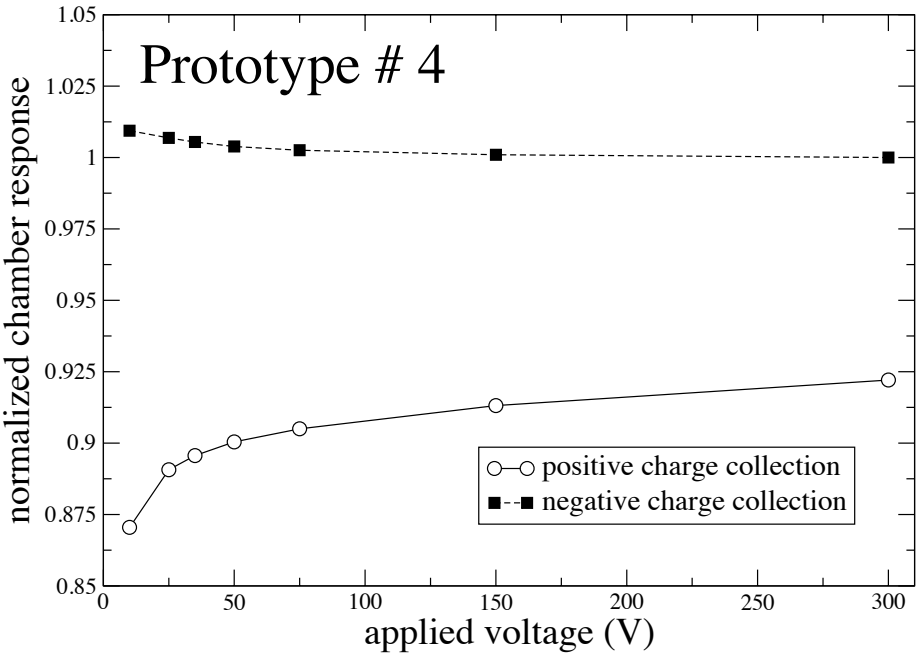

(b)

Figure 7.5: Same as Figure 7.4 except for the (a) Prototype 3 and (b) Prototype 4 chamber.

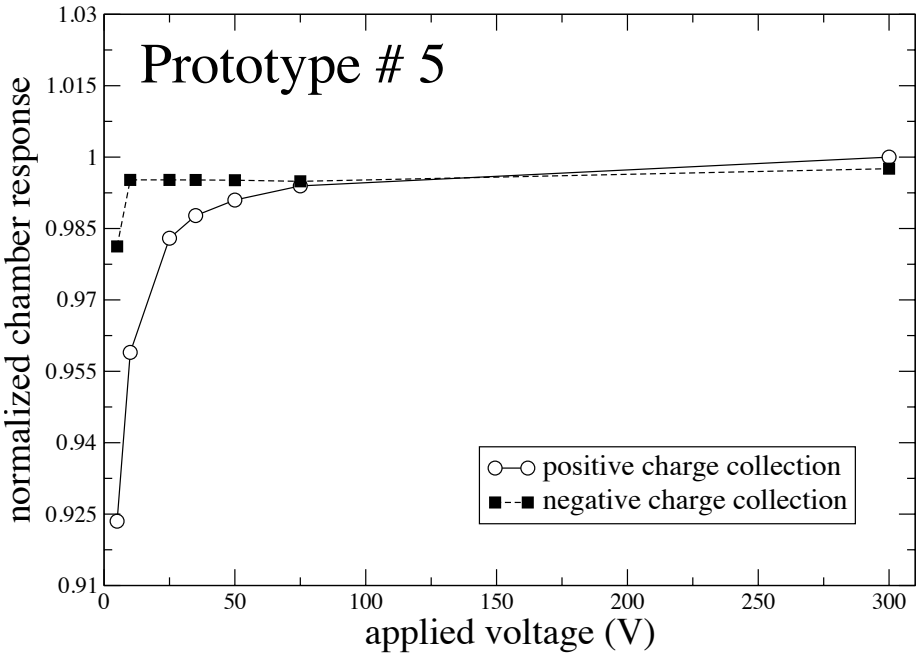

Figure 7.6: Same as Figure 7.4 except for the Prototype 5 chamber.

7.2.1.3 Stem effects and cable irradiation

To isolate the effects of cable irradiations on microchamber behavior, investigations were performed with the J1 prototype 3. Prototype 3 exhibited the voltage-dependent polarity effects during the initial saturation curve measurements, and that behavior did not significantly change with changes in the field size as shown in Table 7.3. The percent difference between the chamber response measured at applied voltages of 300 V and 35 V was relatively consistent with radiation field sizes ranging from 5 x 5 cm^2 to 20 x 20 cm^2. This suggests that the increase in chamber response with decreasing applied voltage is independent of the length of cable irradiated.

Table 7.3: The percent difference between the response of the J1 prototype 3 at applied voltages of 300 V and 35 V measured for field sizes ranging from 5 cm by 5 cm to 20 cm by 20 cm at the center of the chamber volume.

Prototype 3	
Field size (cm^2)	Percent difference($I_{300\,V}$, $I_{35\,V}$) [%]
5 x 5	+0.45
10 x 10	+0.51
15 x 15	+0.50
20 x 20	+0.45

Similarly, altering the length of the chamber stem irradiated did not significantly alter the voltage-dependent polarity effects of the J1 prototype 3. The results are shown in Table 7.4. The percent difference between the chamber response measured at applied voltages of 300 V and 25 V was relatively constant for chamber placements at the center of the field (entire chamber stem irradiated) to the edge of the field (only the stem surrounding the collecting volume irradiated). This suggests the stem irradiation does not play a significant role in the inverse proportionality in chamber response with applied voltage.

Table 7.4: The percent difference between the response of the J1 prototype 3 at applied voltages of 300 V and 25 V measured at the center and edge of a 10 cm by 10 cm field.

Prototype 3	
Placement of chamber in radiation field	Percent difference($I_{300\,V}$, $I_{25\,V}$) [%]
Center of field	+0.95
Edge of field	+0.90

7.2.1.4 Chamber assembly and contamination

In all cases, cleaning the components of the J1 prototype 3 had a negligible effect on the voltage-dependent polarity effects of the chamber. The percent difference between the chamber response measured at applied voltages of 300 V and 25 V, shown in Table 7.5,

demonstrated that the increase in chamber response with decreasing voltage persisted after each round of cleaning.

Furthermore, Table 7.5 shows the results of the assembly investigation. It was shown that disassembling each of the electrodes and the insulating material between the electrodes, and reassembling the chamber did not fix the anomalous behavior. This investigation indicates that neither contaminants on the surface of the chamber components nor electrical connections created during the assembly of that chamber contribute to the variability in chamber response as seen between the J1 chamber prototypes.

Table 7.5: The percent difference between the response of the J1 prototype 3 at applied voltages of 300 V and 25 V prior to and after the chamber was disassembled and cleaned to varying degrees.

Prototype 3	
Chamber assembly	Percent difference($I_{300\,V}$, $I_{25\,V}$) [%]
Original	+0.66
Cleaned with compressed air	+0.95
Disassembled and reassembled	+0.86
Disassembled, ultrasonically cleaned, reassembled	+0.44

7.2.1.5 Presence of high-Z materials

It was shown in Chapter 5 that high-Z materials can cause the chamber response to vary significantly with the energy of the beam, specifically for low- and medium-energy x-ray beams. As a result, the effects of high-Z materials on saturation curve measurements were investigated. As shown in Table 7.6, coating the tip of the collecting electrode of Prototype 5 with the high-Z silver epoxy did not cause the chamber to exhibit worse behavior. In fact, the chamber signal exhibited a greater decrease with decreasing applied voltage after the silver was applied.

To improve the understanding of the effects of the silver epoxy, the results of the repeated experiment which incorporated full saturation curves are shown in Figure 7.7. The magnitude of the polarity effects decreased slightly with the silver epoxy on the collecting

electrode, but the general shape of the curves remained constant with and without the silver. These results suggested that high-Z materials could be eliminated as the main cause of voltage-dependent polarity effects in small volume chambers.

Table 7.6: The percent difference between the response of the J1 prototype 3 at applied voltages of 300 V and 25 V with and without a silver epoxy coated on the collecting electrode.

Prototype 5	
Assembly	Percent difference($I_{300\,V}$, $I_{25\,V}$) [%]
Original	-0.31
Silver epoxy on collector	-0.85
Silver epoxy on collector (biggest portion of silver toward beam)	-0.81
Original (silver epoxy removed from collector)	-0.45

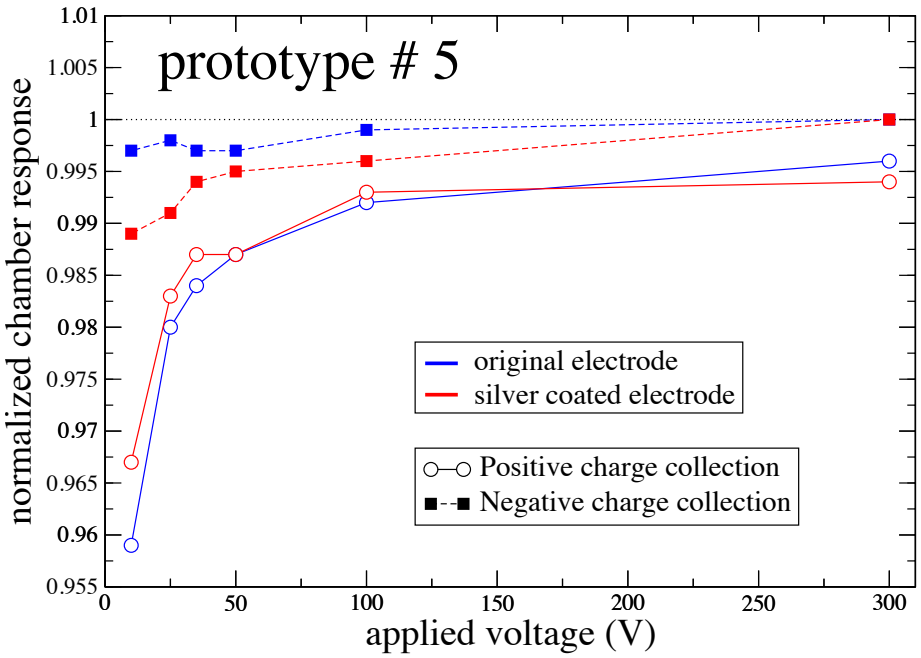

Figure 7.7: Same as Figure 7.4 except for the Prototype 5 chamber. Measurements performed with the silver removed from and repainted on the collecting electrode are represented by blue and red, respectively.

7.2.1.6 Electrode and insulator isolation

Since the anomalous behavior of these microchamber prototypes was not significantly altered by chamber stem and cable irradiation, contaminants, chamber assembly, or high-Z materials, experiments were performed to trace the voltage-dependent polarity effects to an individual chamber component. To determine the source of the behavior, individual components were swapped between prototype 4 [which exhibited voltage-dependent polarity effects, see Figure 7.5(b)] and prototype 2 [which exhibit voltage-independent polarity effects but no inverse proportionality between chamber response and applied voltage, see Figure 7.6(a)]. The characterization of the chambers after each component was swapped is shown in Table 7.7 and Table 7.8 for prototypes 2 and 4, respectively. A graphical representation of the data is shown in Figure 7.8.

Table 7.7: The percent difference between the chamber response of the J1 microchamber prototype 2 at an applied bias of 300 V and 25 V for each chamber assembly.

Prototype 2	
Assembly	Percent difference(300 V, 25 V) [%]
Original	-1.8
Internal components of prototype 4	+0.68
Original	-2.3
Guard and HV insulator of prototype 4	-0.27
Original	-2.0
Collector of prototype 4	-1.3
Guard/collector insulator of prototype 4	-1.8

Table 7.8: The percent difference between the chamber response of the J1 microchamber prototype 4 at an applied bias of 300 V and 25 V for each chamber assembly.

Prototype 4	
Assembly	Percent difference(300 V, 25 V) [%]
Original	+0.69
Internal components of prototype 2	-2.2
Original	+0.54
Guard and HV insulator of prototype 2	-1.5
Original	+0.43
Collector of prototype 2	+0.08
Guard/collector insulator of prototype 2	+0.32

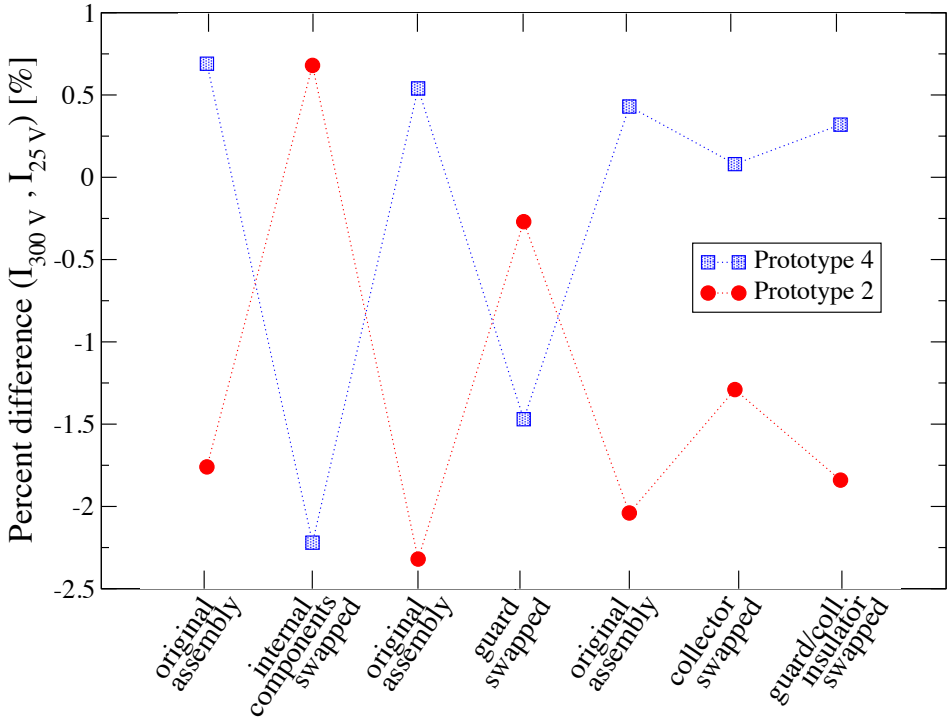

Figure 7.8: A graphical representation of the present difference between the chamber response at applied voltages of +300 V and + 25 V (negative charge collection) after a series of chamber alterations. Data measured with the J1 prototypes 2 and 4 are represented by red circles and blue squares, respectively.

The first alteration entailed swapping the internal components of each chamber (the guard electrode, collecting electrode, and the insulating materials between the electrodes).

The initial behavior of each chamber followed the internal components. With the internal components of prototype 4, prototype 2 exhibited the inverse proportionality between chamber response and applied voltage. In other words the percent difference between 300 V and 25 V was +0.68% for prototype 2, instead of the initial -1.76%. Likewise, prototype 4 no longer exhibited these voltage-dependent polarity effects with the internal components of prototype 2. This step eliminated the shell and the remainder of the stem as the source of the undesirable behavior. The components were returned to their original chambers and the behavior of each chamber returned to that of the initial characterization. Returning the components to the original assemblies further solidified the theory that the source of the behavior was isolated to the internal components and validated the reproducibility of these results.

Once the behavior was isolated to the internal components, the individual components were swapped one at a time between the two chambers. Each component was swapped individually with the exception of the guard and the high voltage insulator (guard/HV). These pieces were permanently fused during manufacturing and could not be separated without adding additional variables (such as solvents) to the experiment. The resulting characterizations showed that the behavior of the chambers strongly followed that of the guard/HV component. In the case of of prototype 2, the original -1.76% difference in chamber response at applied voltages of 300 V and 25 V increased to +0.68% with the guard/HV component of prototype 4. Likewise, the original undesirable increase of +0.69% in the response of prototype 4 for applied voltages of 300 V to 25 V fell to -1.47% with the guard/HV component of prototype 2. No other chamber component showed as significant of an impact on the voltage-dependent polarity effects of these chambers.

It is interesting to note that swapping the collecting electrodes did affect the chamber behavior slightly. With the collecting electrode of prototype 4, prototype 2 showed a difference in response for applied voltages of 300 V to 25 V similar to that of prototype 4 with

the guard/HV component of prototype 2. In both cases, the electrode was from prototype 4 and the guard/HV component was from prototype 2. Similarly, the change in response of the chambers showed a similar trend when prototype 4 contained the collecting electrode of prototype 2 and prototype 2 contained the guard/HV component of prototype 4. In both of these cases, the chambers contained the collecting electrode of prototype 2 and the guard/HV component of prototype 4. These results suggest that for these prototypes the voltage-dependent polarity effects are primarily caused by a characteristic of the guard/HV component, and are generally defined by the relation between the guard/HV component and the collecting electrode. This strongly suggests that the insulating materials and shell electrode can be eliminated as sources for the voltage-dependent polarity effects.

7.2.2 Larger-volume chamber: A2 prototypes

This section discusses the initial characterization of the Exradin A2 prototypes and the experiments performed to isolate the cause of the voltage-dependent polarity effects.

7.2.2.1 Initial Custom Exradin A2 prototype characterization

The initial saturation curves measured for each of the Exradin A2 prototypes showed varying chamber behavior between the two prototypes. As shown in Figures 7.4(a) the A2 S/N 60613 prototype with components composed entirely of C552 showed typical ionization chamber behavior with minimal polarity effects. The Exradin A2 S/N 60612, containing a collecting electrode composed of aluminum, showed the undesirable voltage-dependent polarity effects seen in microionization chambers [see Figure 7.5(b)]. The voltage-independent effects are significant enough to cause an increase in chamber response with decreasing voltage during negative charge collection.

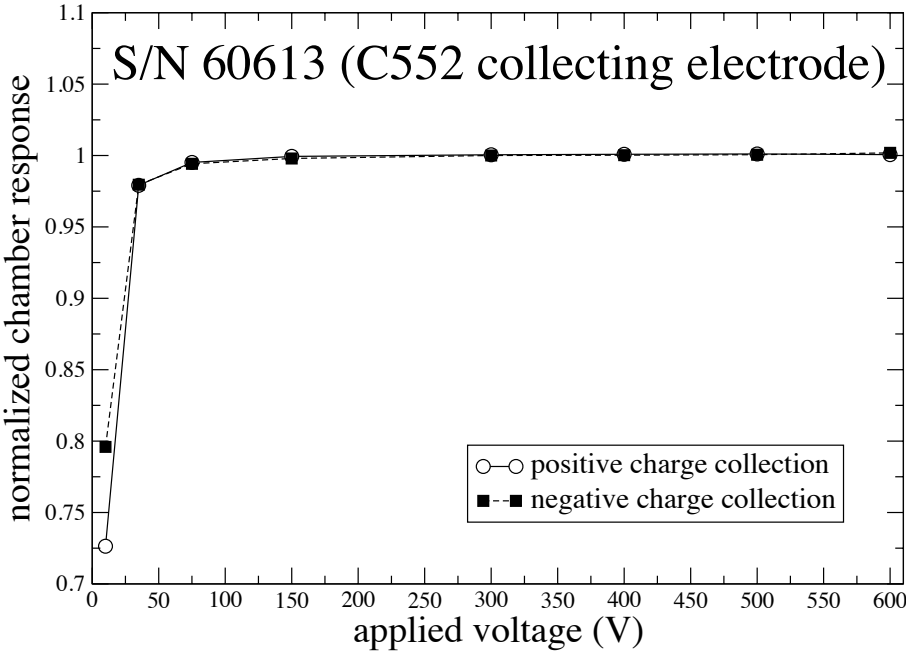

(a)

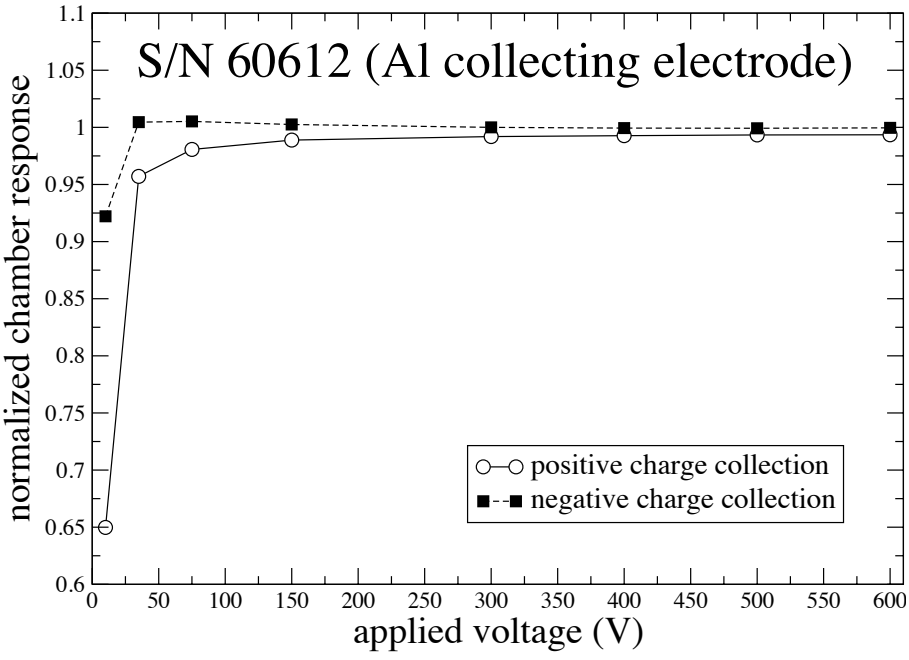

(b)

Figure 7.9: Normalized saturation curves measured with two Exradin A2 prototypes, (a) S/N 60613 and (b) S/N 60612. All data were normalized to the average signal received when the chamber was biased to a polarizing voltage of +300 V (negative charge collection).

7.2.2.2 Electrode isolation

Due to the results of the J1 microchamber investigation, several variables were immediately eliminated as suspects for the cause of the voltage-dependent polarity effects in the Exradin A2 S/N 60612. This investigation was fast-tracked to a set of experiments designed to isolate the individual chamber components responsible for the behavior. In the J1 microchamber investigation it was concluded that the behavior of the chambers was affected by the combination of the collecting electrode and the guard/HV, with an emphasis on the guard/HV component. Therefore, in the A2 investigation the collecting electrode and the guard/HV component were examined. Due to the initial characterization shown in Figure 7.9, applied voltages of 300 V and 50 V were chosen. For negative charge collection, the percent difference between the chamber response at 300 V and 50 V provided the means to differentiate between chambers demonstrating voltage-dependent polarity effects and chambers demonstrating optimal behavior. The applied voltage selection showed an increase in chamber response with decreasing voltage for the Exradin A2 S/N 60612 (aluminum electrode) and a decrease in chamber response with decreasing applied voltage for the A2 S/N 60613 (C552 electrode).

The guard/HV components were swapped first. The components were returned to the original chamber assemblies and the collecting electrodes were swapped, as described in Section 7.1.2.1. The results can be seen in Table 7.9 and 7.10. A graphical representation of the data can be seen in Figure 7.10. While the guard/HV component appeared to have a negligible effect on the chamber behavior, the behavior of the chambers was significantly altered by swapping the collecting electrodes. The voltage-dependent polarity effects followed the aluminum electrode. With the C552 electrode the percent difference between the chamber response at applied voltages of +300 V and +50 V was -0.58% and -1.09% for S/N 60613 and S/N 60612, respectively. With the C552 collector and the same guard/HV component (from the S/N 60612 assembly), the percent difference in response for the two

chambers was nearly identical at -1.07% and -1.09% for S/N 60613 and S/N 60612, respectively. This further validates that the chamber response is significantly controlled by not only the collecting electrode, but the relationship between the collecting electrode and the guard/HV component.

Table 7.9: The percent difference between the chamber response of the Exradin A2 prototype S/N 60613 at an applied bias of 300 V and 50 V for each chamber assembly.

Exradin A2 prototype S/N 60613	
Assembly	Percent difference(300 V, 50 V) [%]
Original	-0.58
Guard and HV insulator of S/N 60612	-1.1
Collector of S/N 60612	-0.19

Table 7.10: The percent difference between the chamber response of the Exradin A2 prototype S/N 60612 at an applied bias of 300 V and 50 V for each chamber assembly.

Exradin A2 prototype S/N 60612	
Assembly	Percent difference(300 V, 25 V) [%]
Original	+0.28
Guard and HV insulator of S/N 60613	+0.25
Collector of S/N 60613	-1.1

As a final characterization, saturation curves were performed for each of the Exradin A2 prototypes with the collecting electrodes swapped. The resulting saturation curves are shown in Figure 7.11. These curves provided a check that the method of spot checking specific applied voltages based on initial saturation curve characterization was an adequate method for determining behavior patterns. The data also supports the conclusion that the behavior of these chamber followed that of the collecting electrode.

7.3 Conclusions

To isolate the cause of voltage-dependent polarity effects and the inverse proportionality between chamber response and applied voltage, a series of empirical investigations were

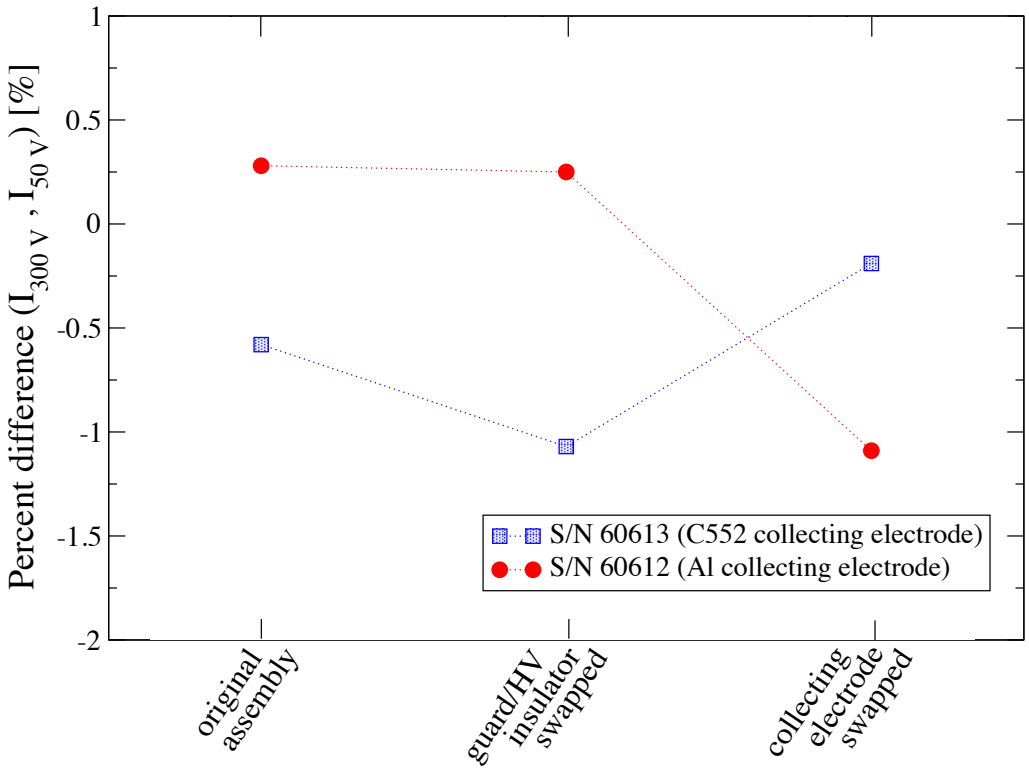

Figure 7.10: A graphical representation of the present difference between the chamber response at applied voltages of +300 V and + 50 V (negative charge collection) after a series of chamber alterations. Data measured with the Exradin A2 prototypes S/N 60613 and S/N 60612 are represented blue squares and red circles, respectively.

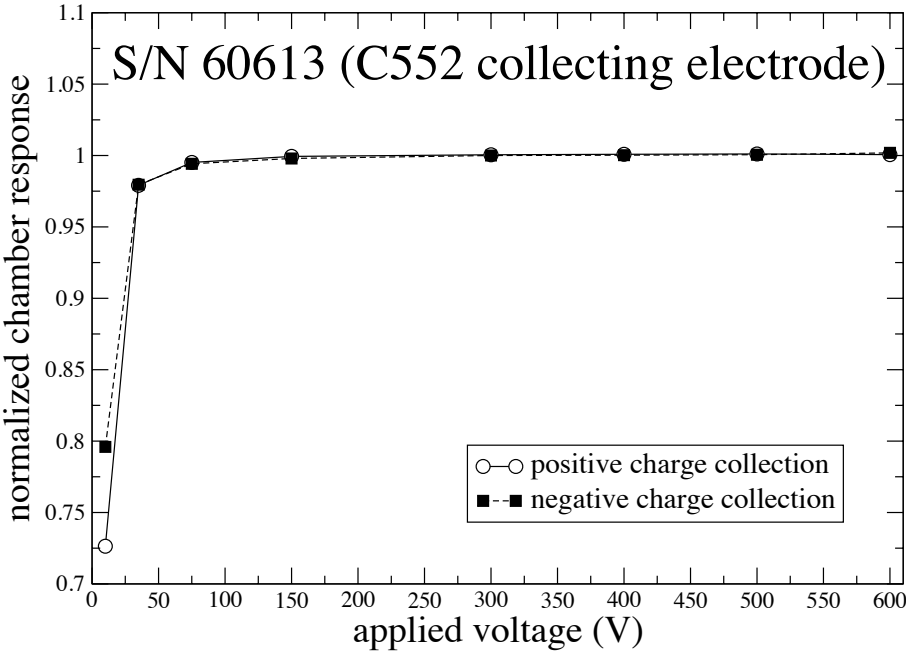

(a)

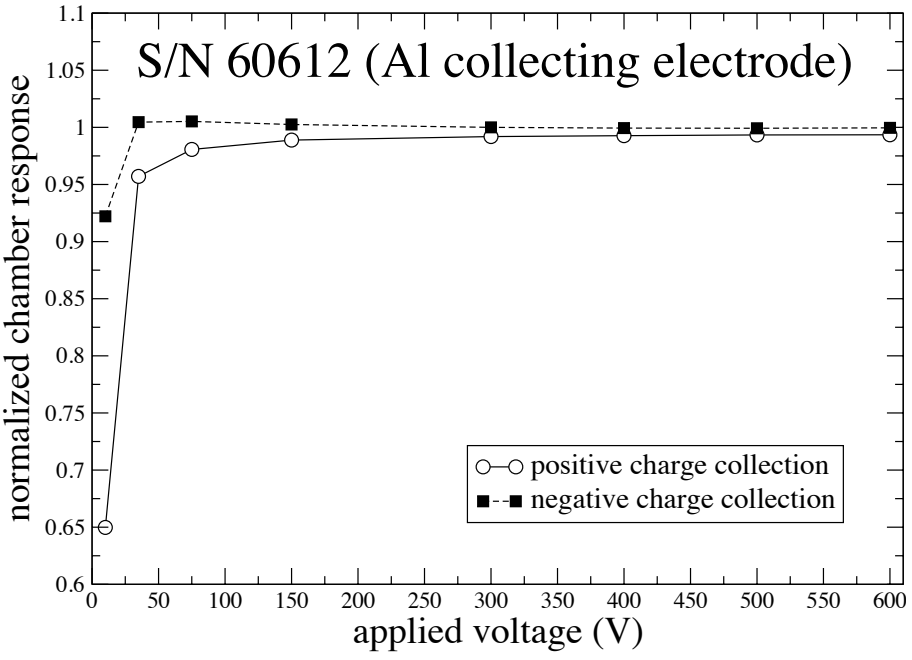

(b)

Figure 7.11: Same as Figure 7.9 except for the A2 S/N 60613 chamber with the C552 collecting electrode of the A2 S/N 60612 chamber and (b) the A2 S/N 60612 chamber with the aluminum collecting electrode of the S/N 60613 chamber.

performed with five microchamber prototypes, model J1. The experiments explored the effects of stem and cable irradiations; chamber assembly; dirt, oil, and other contaminants; and high-Z materials on the chamber behavior. For all cases, the relative change in chamber response with applied voltage was not significantly altered. Each of these variables was eliminated as a possible source for the voltage-dependent polarity effects exhibited by microchambers.

To isolate individual chamber components as suspects for the cause of this behavior, the components were swapped between two chambers; one chamber exhibiting voltage-dependent polarity effects (prototype 4) and one chamber not exhibiting this behavior (prototype 2). The undesirable behavior was shown to significantly follow the guard/HV insulator assembly. Thus, the general voltage-dependent polarity effects initially shown by prototype 4 were demonstrated by prototype 2 when prototype 2 contained the guard/HV assembly of prototype 4. The behavior of each chamber was entirely a function of the collecting electrode and guard/HV combination. Thus, with the guard/HV assembly and the collecting electrode of prototype 4, prototype 2 mimicked prototype 4's behavior more closely. This investigation suggests that the behavior of the J1 prototypes was significantly dependent on some quality of the guard/HV insulators and the combination of collecting electrode and guard/HV components.

Further investigations were performed with two custom A2 chambers. One chamber contained a collecting electrode composed of C552 low-Z conductive plastic and exhibited no voltage-dependent polarity effects. The other A2 chamber contained a collecting electrode composed of aluminum and exhibited voltage-dependent polarity effects. The components were swapped between the two chambers and the behaviors characterized. It was shown that the chamber behavior more closely followed the collecting electrodes of the A2 chambers. It was likely that the aluminum electrode oxidized over time and caused a reduction in the

final bias of the electrode with respect to the C552 guard electrodes, producing a difference in the final potential bias of the guard and collecting electrode.

Since the anomalous behavior was not isolated solely to the collecting electrode, as demonstrated with the prototype J1 chambers, this suggests that the voltage-dependent polarity effects were not solely, if at all, due to secondary charged particles created in, and traveling between, the shell and collecting electrode. Instead it was likely that a voltage-dependent potential difference was created between the guard and collecting electrodes causing a voltage-dependent polarity effect. The following chapter discusses further investigations that were performed to validate this theory.

Chapter 8

Potential difference between guard and collecting electrodes

In the previous chapter, the voltage-dependent polarity effects of the Exradin A2 and J1 prototypes were isolated to either the guard electrode or the collecting electrode. This suggested that the behavior was not solely caused by one electrode, but rather a relationship between the electrodes. Boag (1964) and Kim et al. (2005) demonstrated that a potential difference between the bias of the collecting electrode and guard electrode could distort the electric field lines within the collecting volume and ultimately effect the chamber response. However, little has been done to investigate the prevalence of this effect in commercial ionization chambers. For the chambers examined in this work, it is possible that a difference in conductance between the two electrode materials created a difference in the bias of the electrode surfaces. A bias difference between the electrodes would produce a voltage-dependent polarity effect. This effect would be more significant in small-volume chambers where distortion of the electric field lines would create a greater relative change in the collecting volume of the chamber. The following sections investigate the validity of this theory.

8.1 Methods and materials

8.1.1 Electrode conductance

Several experiments were performed to measure directly the difference in conductance between the electrodes; however, due to limitations in the ability to accurately measure controlled and continuous points along the electrodes, no statistically significant difference was determined. Thus, an indirect method was developed to isolate the conductance of the electrodes as a cause of the behavior. Using this method, the conductance of the electrodes was altered and the effect on chamber response was measured. To alter the conductance of the electrodes, a thin layer of graphite called Electrodag 154® (Ladd Research, Williston, VT) was painted on the surface of the electrodes of interest. Electrodag is a high-conductivity coating designed to provide controlled electrical properties to nonconductive materials, including most plastics. The coating, which is a dispersion of colloidal graphite in an isopropanol solution, dries in air to form a uniform layer of graphite on the surface of the electrode.

The electrodes of the J1 microchambers were small and in close approximation to other electrodes and insulator surfaces. To allow for a more controlled application of a thin layer of graphite, additional isopropanol was added to the Electrodag solution. Measurements were performed with the original Electrodag solution as well as the diluted solution; in both cases the effects on chamber response were consistent. Therefore, it was concluded that adding additional isopropanol to the solution did not compromise the electrical properties of the graphite coating, while allowing for a more fine control in graphite application.

The application of the Electrodag was limited to the electrodes that were found in the previous chapter to be primarily responsible for the voltage-dependent polarity effects. Within the J1 prototypes, the Electrodag was painted on the outside edge of the guard electrode. For the Exradin A2 prototypes, the surface of the aluminum collecting electrode

within chamber S/N 60613 was coated with Electrodag. Saturation curves were measured for a ^{60}Co beam with both chamber models using the methods describe in Section 3.1.2.

8.1.2 Induced potential difference between guard and collecting electrode bias

An investigation was performed to demonstrate further that the potential difference between the guard and collecting electrodes could cause the voltage-dependent polarity effects exhibited by microchambers. In this investigation a potential difference between the electrodes was induced in a Farmer-type chamber and a microchamber. The behavior of these chambers was characterized with the induced potential differences.

To create a potential difference between the guard and collecting electrodes of a chamber, an external power supply was introduced into the guard electrode circuit, independent of the collecting electrode circuitry. The thread of the guard electrode was separated from the triaxial cable, routed through a battery, and threaded back into a triaxial cable. The threads of the shell and collecting electrodes were routed through a wire and back into the cable introducing no additional voltage. Therefore, the shell and guard electrodes were not altered by the battery. The battery and additional wires were placed in a metal box to isolate and stabilize the signal path, as shown in Figure 8.1.

Two batteries were used, a 9 V and 1.5 V battery introducing a voltage difference of $\pm$9.5 V and $\pm$1.64 V. Depending on the position of the battery, the voltage could be added or subtracted to the voltage applied by the electrometer to the guard electrode. Saturation curves were measured with the batteries positioned to add a positive voltage to the applied bias of the guard electrode. Thus, for negative charge collection, when the guard electrode was positively biased, the battery voltage was added to the voltage applied by the electrometer, increasing the bias of the guard with respect to the collecting electrode. Conversely, for positive charge collection, when the guard was negatively biased, the battery

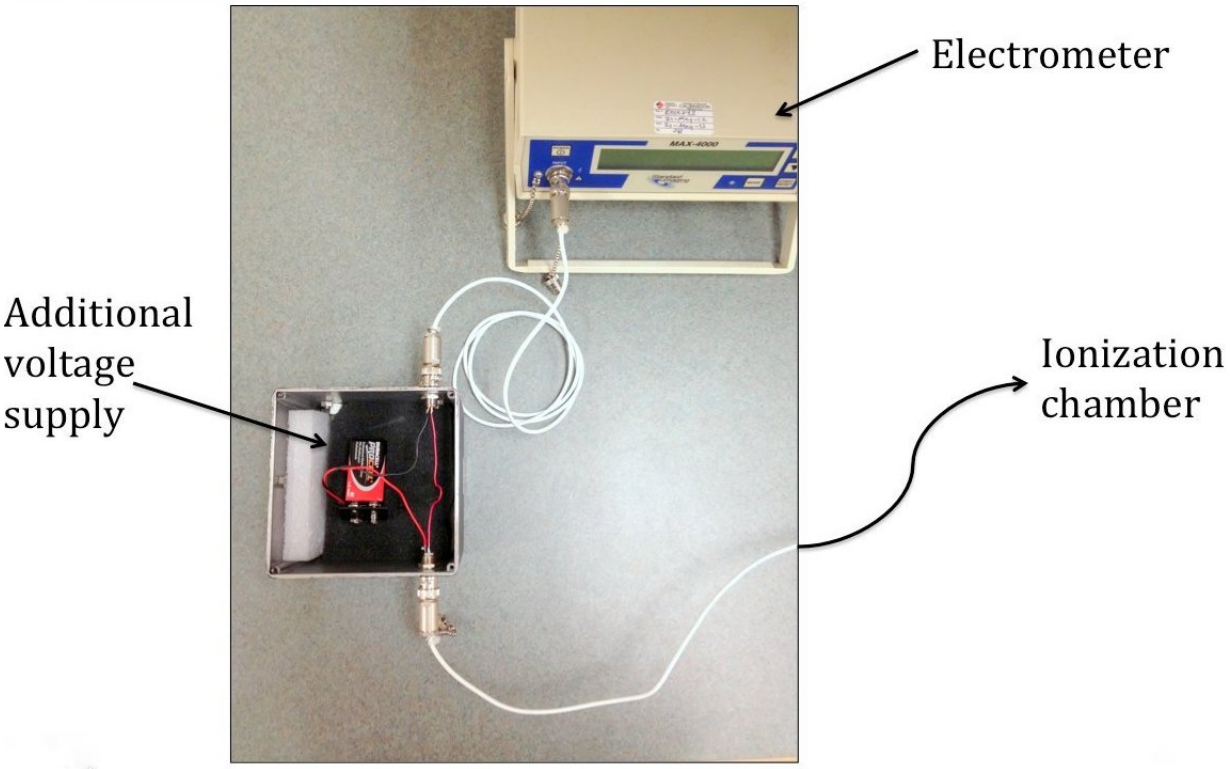

(a)

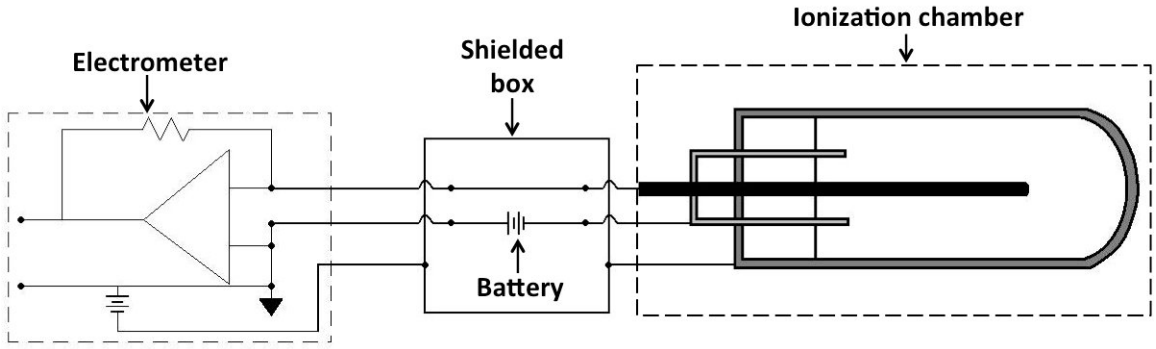

(b)

Figure 8.1: (a) A photograph and (b) a schematic of the experimental setup used to alter the applied voltage of the guard electrode with respect to the collecting electrode.

voltage was subtracted from the magnitude of the bias of the guard electrode with respect to the collecting electrode.

Two chambers were investigated with this setup: a low-Z microchamber called the J2 prototype and the Exradin A12 Farmer-type chamber. The J2 prototype is similar to the J1 prototype, described in Chapter 7, with slight differences in chamber dimensions and possibly the composition of plastic. The J2 prototype is discussed further in Chapter 9, but for this investigation it is sufficient to know that the chamber has a collecting volume of 0.018 cm^3 and exhibited minimal voltage-dependent polarity effects. The Exradin A12, which was characterized in Chapters 3-5, is a reference-class Farmer-type chamber, which exhibited no voltage-dependent polarity effects.

8.1.3 Simulated voltage-dependent volume effect

The previous sections empirically investigated if voltage-dependent polarity effects and an inverse proportionality between the chamber response and applied voltage could be induced by bias inequality between the guard and collecting electrodes. This section will simulate these polarity effects using COMSOL multiphysics software.

Figure 8.2 shows the COMSOL generated electric field in a generic microchamber for three bias setups. Each chamber diagram displays the cross-section of the chamber. Since cylindrical ionization chambers are axially symmetric, only one-half of the chamber is required to reconstruct the three-dimensional electric field inside of the chamber volume. In each of the three chamber simulations in Figure 8.2, the shell electrode was held at ground (0 V) and the collecting electrode was set to a bias of +300 V. The bias of the guard electrode was varied from +290 V to +310 V. The colors inside of the collecting volume represent the contoured normalized electric field. The dark red line represents the electric field line above which all of the electric field lines run from the shell electrode to the collecting electrode. Below the dark red line, the electric field lines run from the shell electrode

to the guard electrode. Therefore, the dark red line represents a theoretical border defining the collecting volume of the chamber.

Figure 8.3 provides a magnified version of this electric-field line which defines the collecting volume in each chamber simulation. The areas above and below the line are contoured in blue and black, respectively. In these figures it is clear that changing the bias of the guard electrode with respect to the collecting electrode affects the electric field lines and the shape and size of the collecting volume. With the guard bias lagging that of the collecting electrode, the collecting volume of the chamber is increased. Likewise, when the bias of the guard exceeds that of the collecting electrode, the collecting volume of the chamber is decreased.

To calculate the collecting volume for each chamber bias setup, the coordinates of the volume-defining electric field lines and collecting and wall electrodes were exported and redesigned using a 3D CAD software. The air volume above the electric field line was calculated for each simulation.

The COMSOL-simulated change in the collecting volume for the J2 microchamber and the Exradin A12 Farmer-type were modeled. The electric fields were simulated using the methods described in Chapter 6.1. The shell electrodes were set to ground (0 V) and the collecting electrodes were set to a bias of +300 V. The bias of the guard was varied from +160 V to +440 V (±47% of +300 V). Simulating the bias of the guard electrode at ±47% of the bias of the collecting electrode is equivalent to simulating the collecting electrode at a bias of +25 V and the guard at +16 V (25 V - 9 V) and +34 V (25 V + 9 V). This provided an approximation of what could be expected for a collecting volume change with a +9 V battery added to the applied voltage of the guard with an electrometer applied bias of 25 V. Similarly, simulations were performed at percent differences of ±19% and ±3% which were equivalent to the addition of the external +9 V of the battery to the guard with an electrometer applied voltage of ±50 V and ±300 V, respectively.

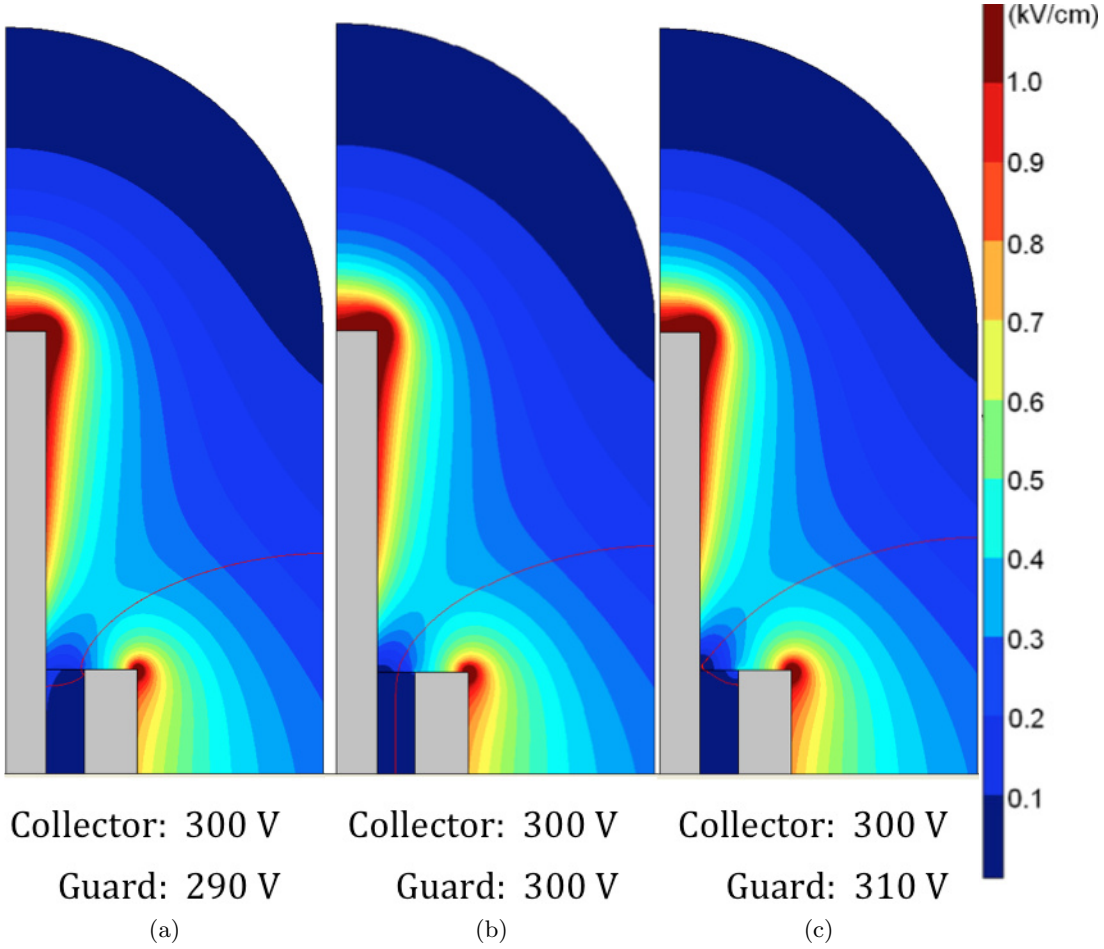

Figure 8.2: The simulated contoured normalized electric field and the electric field line which theoretically defines the collecting volume for a microchamber. The wall electrode was set to ground, the collecting electrode was biased to 300 V, and a guard electrode was biased to (a) +290 V, (b) +300 V, and (c) +310 V.

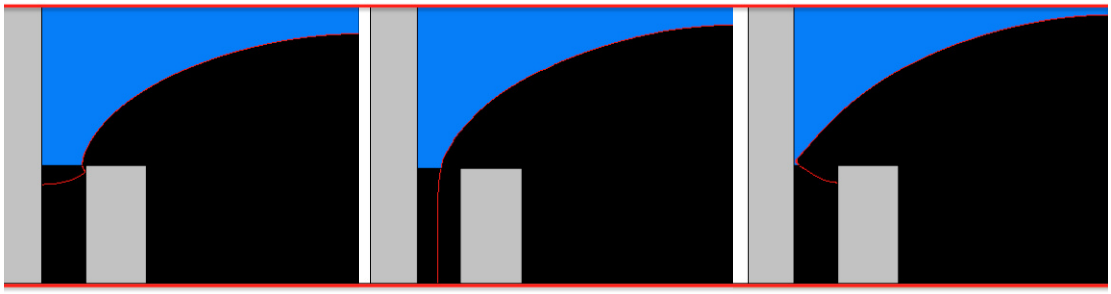

Figure 8.3: A magnified schematic of Figure 8.2 with the collecting volume colored blue.

8.2 Results and discussion

8.2.1 Electrode conductance

8.2.1.1 Microchamber: J1 prototype

The J1 prototypes containing graphite-coated guard electrodes exhibited improved behavior. The normalized saturation curves measured with the original and graphite-coated guard electrodes for the J1 prototype 3 are displayed in Figure 8.4. In all cases, the voltage-dependent polarity effects were reduced. As a result, the increase in chamber response with decreasing applied voltage, which occurred during negative charge collection, was eliminated.

Unlike with negative charge collection, the original saturation curves measured for positive charge collection did not exhibit an increase in chamber response with decreasing voltage. Therefore, it was less apparent if voltage-dependent polarity effects were occurring for positive charge collection. This investigation demonstrated an insightful graphite-induced change in chamber response for positive charge collection. The graphite coating minimized the falloff of positive charge collection at lower applied voltages. With a reduction in the

positive response falloff, the slope of the curves for positive and negative charge collection were in better agreement. With similar slopes, the voltage-dependent polarity effects were reduced, suggesting that the original (non-graphite) curves for positive charge collection were demonstrating voltage-dependent polarity effects. These results indicate that with decreasing applied voltage, a secondary effect increased negative charge collection and reduced positive charge collection in the J1 prototypes exhibiting anomalous behavior. This has not been reported in the literature and could lead to errors in chamber characterization when only positive charge is collected. In the case of the J1 prototype 3, traditional ion recombination correction methods would overestimate the contribution of ion recombination to the chamber collection inefficiency during positive charge collection. Several authors have characterized ion recombination factors for chambers using only positive charge collection. In several of these cases, ion recombination coefficients were accepted as correct without analysis of corresponding negative charge collection values. This work demonstrates that a comparison of the chamber response to both polarities may be necessary to accurately characterize a chamber's behavior.

In the previous chapter the voltage-dependent polarity effects were isolated to the guard electrode and HV insulator assembly. By altering only the surface of the guard electrode, the behavior of the chamber was significantly changed. As a result, the HV insulator was eliminated as a possible source of the voltage-dependent polarity effects. This further validated the theory that the polarity effects were produced by a potential difference between the guard and collecting electrodes.

8.2.1.2 Larger-Volume: Exradin A2 prototypes

Similar to the J1 microchamber prototypes, the chamber response of the Exradin A2 S/N 60613 was significantly improved by coating the aluminum electrode with graphite. The voltage-dependent polarity effects were reduced as demonstrated in Figure 8.5. As the applied

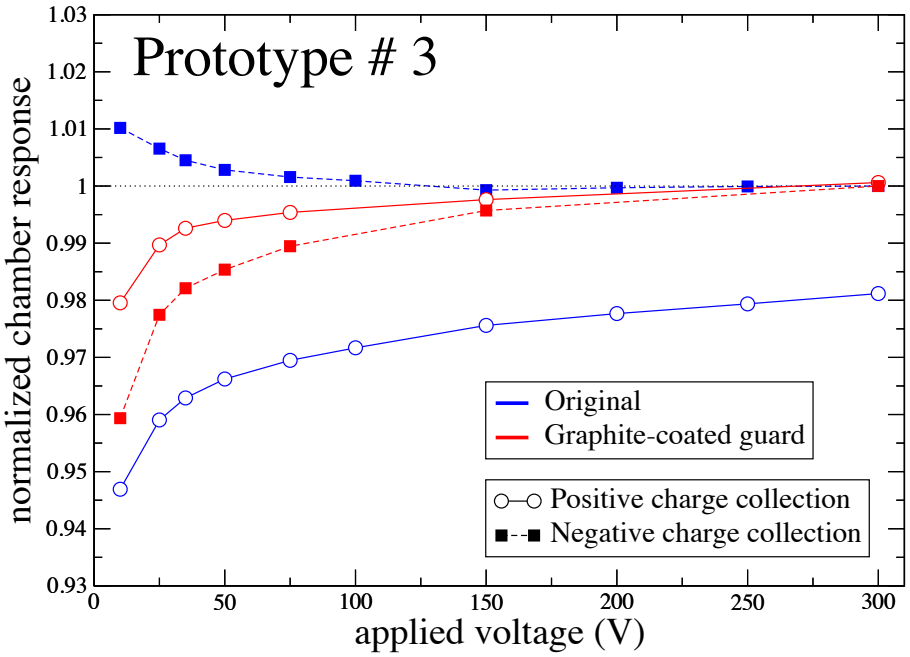

Figure 8.4: Saturation curves measured for the J1 prototype 3 before (represented in blue) and after (represented in red) the guard electrode was coated with graphite. Each data point was normalized to the average negative charge collected before the guard was coated with graphite at an applied voltage of +300 V.

voltage decreased, the graphite coating caused the chamber response to decrease during negative charge collection and increase during positive charge collection. The magnitude and slopes of the curves were brought into better agreement. As mentioned in Section 7.2.2.2, the electrode had likely oxidized over time causing a reduction in the conductance of the electrode with respect to the C552 guard electrode. Coating the outside with graphite improved the conductance and reduced the bias difference between the collecting electrode and the guard electrode.

8.2.2 Induced potential difference between guard and collecting electrode bias

8.2.2.1 Microchambers: J2 prototype

The saturation curves measured with the J2 prototype are shown in Figure 8.6. The original saturation curves (with no battery) are represented by the blue curves. Measurements performed with the addition of the 1.5 V and 9 V battery are represented by the green and red curves, respectively. The original saturation curves did demonstrate voltage-independent and voltage-dependent polarity effects; however, the voltage-dependent effects, which were associated with anomalous behavior, were very small. With the addition of the 1.5 V battery, significant voltage-dependent effects were produced in the saturation curve measurements. With a constant potential difference between the guard and collecting electrodes of 1.5 V the voltage-dependent effects were large enough to create the inverse proportionality between the chamber response and the applied voltage. With the 9 V battery, the polarity effects became even greater.

8.2.2.2 Farmer-type: Exradin A12

Similar results were seen with the Farmer-type chamber as shown in Figure 8.7. However, with this large-volume chamber, the effect of the potential difference between the guard

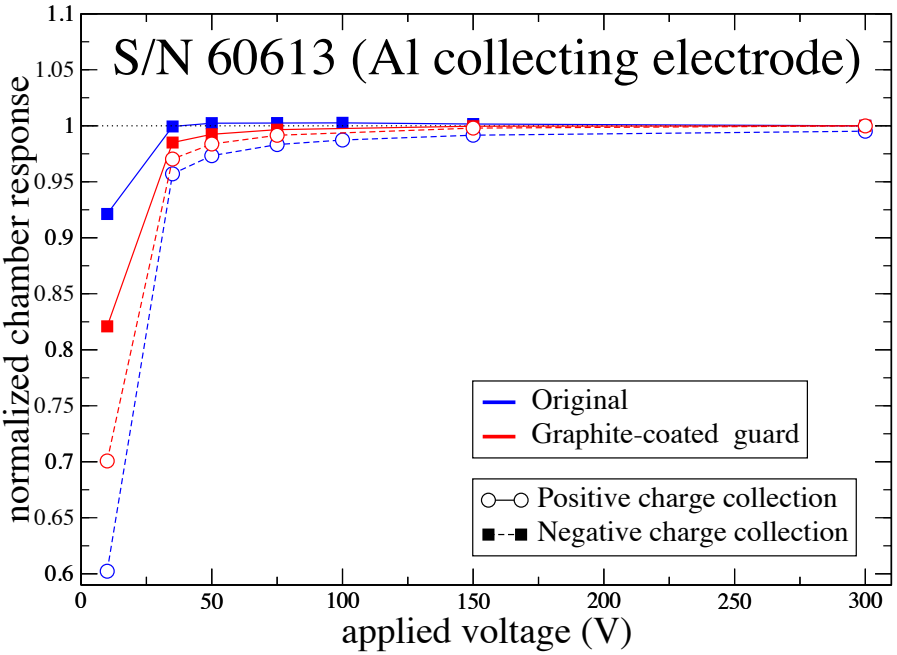

(a)

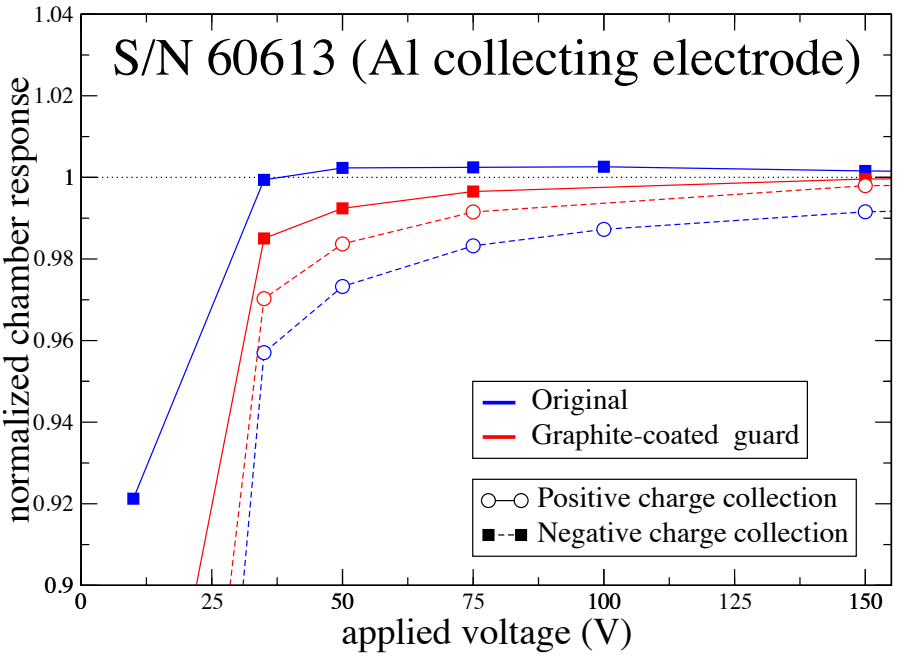

(b)

Figure 8.5: (a) Same as Figure 8.4 except for an Exradin A2 prototype S/N 60613. (b) A magnified view of the chamber response at the applied voltages of interest.

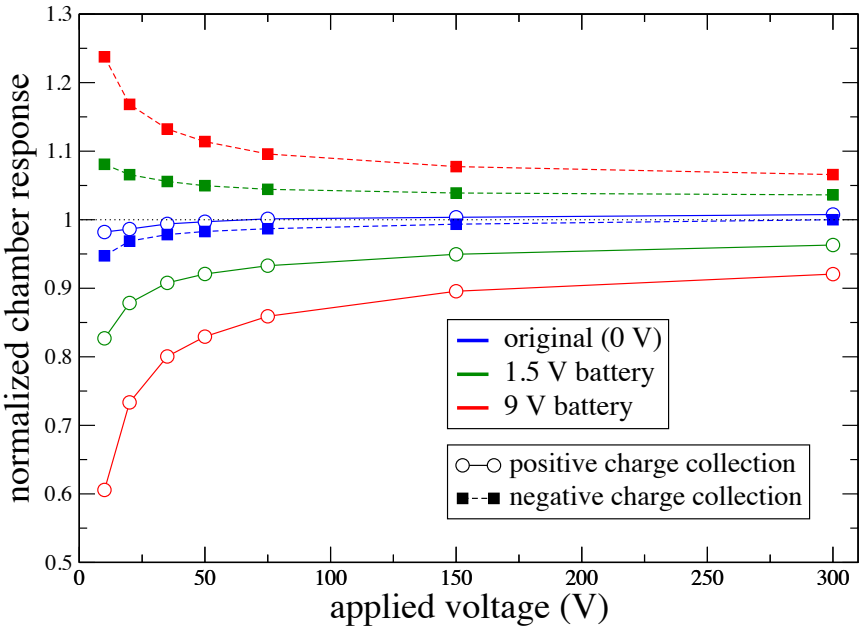

Figure 8.6: Saturation curves measured for the J2 prototype with an addition of a 0 V, 1.5 V, and 9 V battery to the applied bias of the guard electrode with respect to the collecting electrode shown in red, blue, and green, respectively. Each data point was normalized to the average negative charge collected for each battery setup at an applied voltage of +300 V.

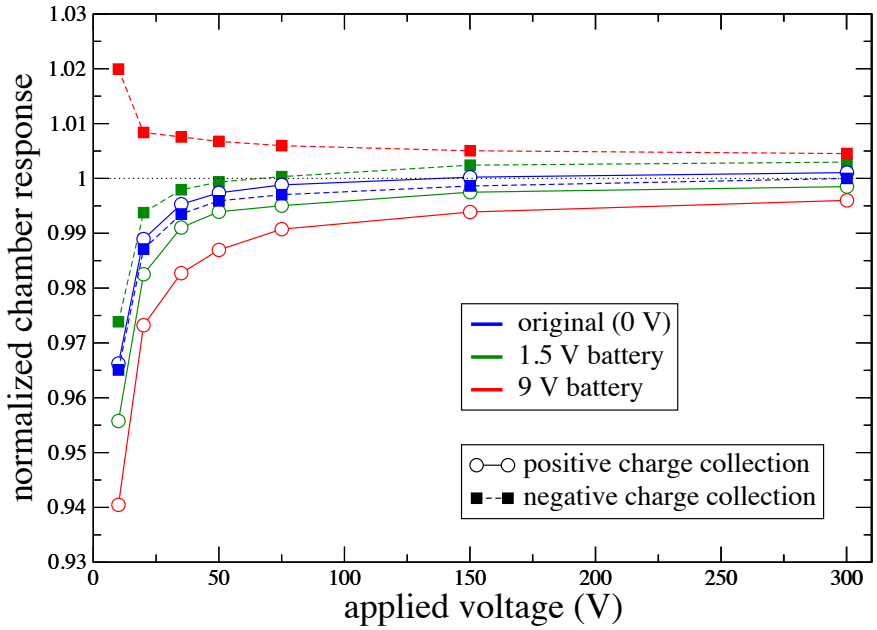

Figure 8.7: Same as Figure 8.6 except for an Exradin A12 Farmer-type chamber.

and the collecting electrodes was less significant by approximately a factor of ten when compared to the microchamber. With the addition of the 1.5 V battery, a slight voltage-independent polarity effect occurred between the two curves. With the introduction of the 9 V battery, a significant polarity effect was measured, which was voltage-dependent. The inverse proportionality between chamber response and bias voltage was evident for negative charge collection.

8.2.3 Simulated voltage-dependent volume effect

A voltage-dependent change in the simulated collecting volume was seen for both the J1 microchamber and Exradin A12 Farmer-type chamber with a potential difference between the electrodes. The results are shown in Figure 8.8 for the microchamber (red circles) and the Farmer-type chamber (blue squares). Both chambers demonstrated an increasing change in the collecting volume with an increasing percent difference in bias between the guard and collecting electrode. The change in volume was inversely proportional to the change in magnitude of the guard bias. In other words, as the bias of the guard increased with respect to the collecting electrode, the collecting volume decreased. The magnitude of the volume change was not the same when a given voltage was added as opposed to subtracted from the guard electrode. The reason for this can be seen in Figure 8.2, which demonstrates that changes in the guard electrode bias created complex changes in electric field lines.

While both chambers experienced a volume change with changes in the bias of the guard with respect to the collecting electrode, the magnitude of this effect was approximately a factor of ten greater for the microchamber compared to the Farmer-type chamber. These results agree well with the experimental data in Section 8.1.2. In both investigations, the voltage-dependent polarity effects were a factor of ten greater for the chamber with a collecting volume that was 36 times smaller.

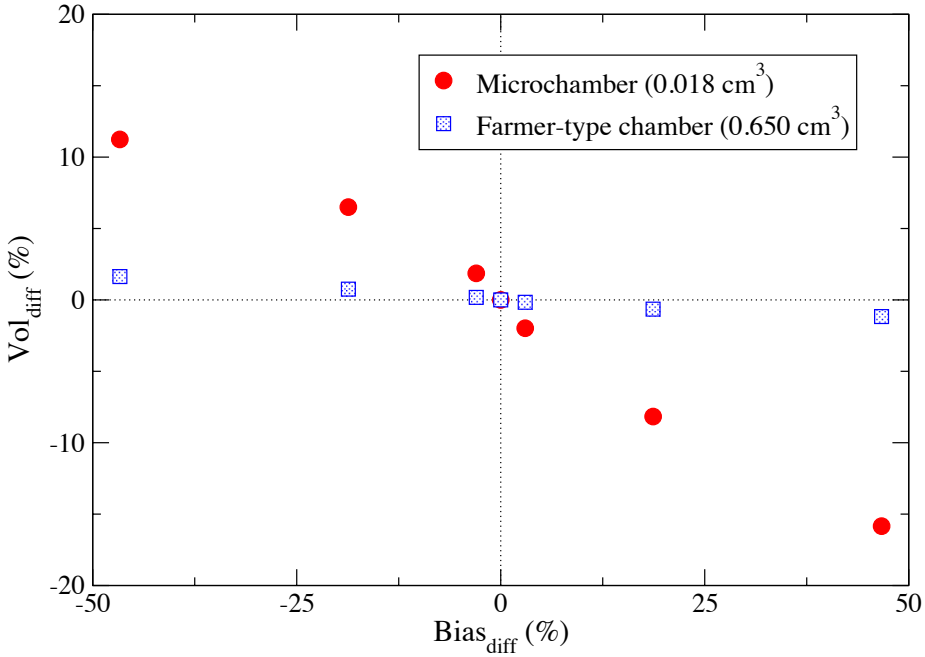

Figure 8.8: COMSOL-simulated percent differences in the collecting volume of a microchamber and Farmer-type chamber as a function of the percent difference in the bias of the guard electrode with respect to the bias of the collecting electrode.

8.3 Conclusions

Both chamber models, the J1 microchamber and the Exradin A2 larger-volume prototypes, demonstrated improved saturation curves with Electrodag coated electrodes. In the case of the J1 prototypes, the voltage-dependent polarity effects were reduced by coating the top outer edge of the guard electrode. This further isolated the guard electrode as the source of the voltage-dependent polarity effects for the J1 prototypes, eliminating the insulating material as a suspect. Coating the oxidized aluminum collecting electrode of the Exradin A2 prototype with graphite reduced the polarity effects. In both cases, as the applied voltage decreased, the graphite caused the chamber response to decrease instead of increase during negative charge collection and to decrease less significantly during positive charge collection, ultimately reducing the voltage-dependent polarity effects.

However, the polarity effects were not eliminated completely. This is likely due to the inability to completely cover the edge of the guard with graphite. As mentioned in the previous section, the small dimensions of the chamber components make confining the graphite to one electrode difficult.

These results suggest that the polarity effects demonstrated by these chambers are caused by an inequality in the conductance of the guard and collecting electrode. In the case of the J1 prototypes, the lack of conductance was most likely a result of an inhomogeneous manufacturing process. Low-Z conductive plastics are often doped with carbon to create conductivity throughout the plastic. If the carbon is not distributed evenly then regions of reduced conductivity may occur. It is possible that this was the issue with the batch of plastic used to create the guard electrodes. In the case of the Exradin A2 chamber, the aluminum collecting electrode was not treated to reduce oxidation and likely oxidized over time. This oxidation layer acted as a insulator and reduced the conductance of the surface of the electrode. This reduction in the conductance may have caused a potential difference between the guard and collecting electrodes.

A methodology to induce the voltage-dependent polarity effects by altering the bias of the guard electrode with respect to the collecting electrode was developed. By altering the bias of the guard, voltage-independent and voltage-dependent polarity effects were introduced into the saturation curves for both the microchambers and Farmer-type chambers. It was also demonstrated that a constant potential difference between the electrodes could cause voltage-dependent polarity effects, including the inverse proportionality between chamber response and applied voltage. This bias inequality has been shown to affect ionization chambers of varying collecting volumes; however, in this investigation the polarity effects were an order of ten times greater for the microchamber compared to the Farmer-type chamber.

The voltage-dependent polarity effects in chamber response were also modeled with COMSOL simulations. A Farmer-type and microchamber were modeled with the percent difference between the bias of the guard electrode with respecting to the collecting electrode ranging from ±47%. The simulated collecting volumes varied significantly depending on the potential difference of the electrodes. For both chambers, reducing the bias of the guard electrode with respect to the collecting electrode increased the collecting volume. Conversely, increasing the bias of the guard electrode with respect to the collecting electrode decreased the collecting volume. The change in the collecting volumes due to a potential difference between the electrodes was approximately 10% greater for the microchamber compared to the Farmer-type chamber. These results agreed well with the induced potential difference measurements.

This chapter demonstrated three investigations which support the theory that the potential difference between the collecting electrode and guard electrode is a significant source of the voltage-dependent polarity effects found with microchambers on the market today. These investigations also explain why the effects are only observed in chambers with small collecting volumes. The same potential difference between the electrodes will have a much smaller effect on a larger-volume chamber.

Chapter 9

Optimized microchamber design

9.1 Methods and materials

In the previous chapters it is was shown that the presence of high-Z materials may cause variations in chamber response with the energy of the beam. Furthermore, an offset in the potential bias of the guard electrode with respect to the collecting electrode may cause significant voltage-dependent and independent polarity effects in microchambers. These behaviors persist over a wide range of clinically relevant photon beam energies and dose rates and it is essential that these behaviors be eliminated in order for microchambers to be used in reference dosimetry measurements.

As a result, a microchamber prototype was created with an optimized design to reduce the energy dependence and polarity effects. Three of the prototypes were manufactured, called J2 prototypes 1, 2, and 3. To eliminate the dependence of the chamber response on the beam energy, the chambers were manufactured with low-Z components. The collecting, guard, and wall electrodes were composed of a conductive air-equivalent plastic. For all three prototypes, N_{k} measurements were performed for photon beams with effective energies ranging from 11.5 kV to 1.25 MV as discussed in Chapter5. To reduce polarity effects, the plastic was manufactured to minimize conductance issues such as over heating or improper

mixing. Furthermore, each of the electrodes were manufactured out of the same batch of plastic to avoid differences in conductance between batches. Saturation curves were measured for each of the chambers for the ^{60}Co beam using the methods described in Chapter 3. Additional investigations were performed with shells of varying sizes, similar to those described in Chapter 7, corresponding to collecting volumes of 0.018 cm^3 to 0.101 cm^3. Saturation curves were performed for prototypes 1 and 2 with the different shell sizes for the ^{60}Co beam.

9.2 Results and discussion

9.2.1 Air-kerma calibration coefficients

The air-kerma calibration coefficients measured for each of the three optimized prototypes are shown in Figure 9.1. The variation in N_{k} from 100 kV to 300 kV was less than the recommended 3% for prototypes 1 and 2 and less than 5% for prototype 3. In all cases, these variations were a significant improvement over the 50% variation demonstrated by the commercial microchambers containing high-Z materials (see Chapter 5).

9.2.2 Characterization in a ^{60}Co beam

The saturation curves for each of the three optimized prototypes are displayed in Figures 9.2(a) and (b) and 9.3. The voltage-dependent polarity effects were negligible for each of the chambers. A voltage-independent polarity effect was demonstrated by prototype 1. This is likely due to imperfections in the low-Z plastic. However, in all cases, the absence of voltage-dependent polarity effects led to an elimination of the inverse proportionality between the chamber response and the applied voltage.

The saturation curves measured with the varying shells and chamber volumes for prototypes 1 and 2 are shown Figures 9.4 and 9.5, respectively. In both cases, the chamber

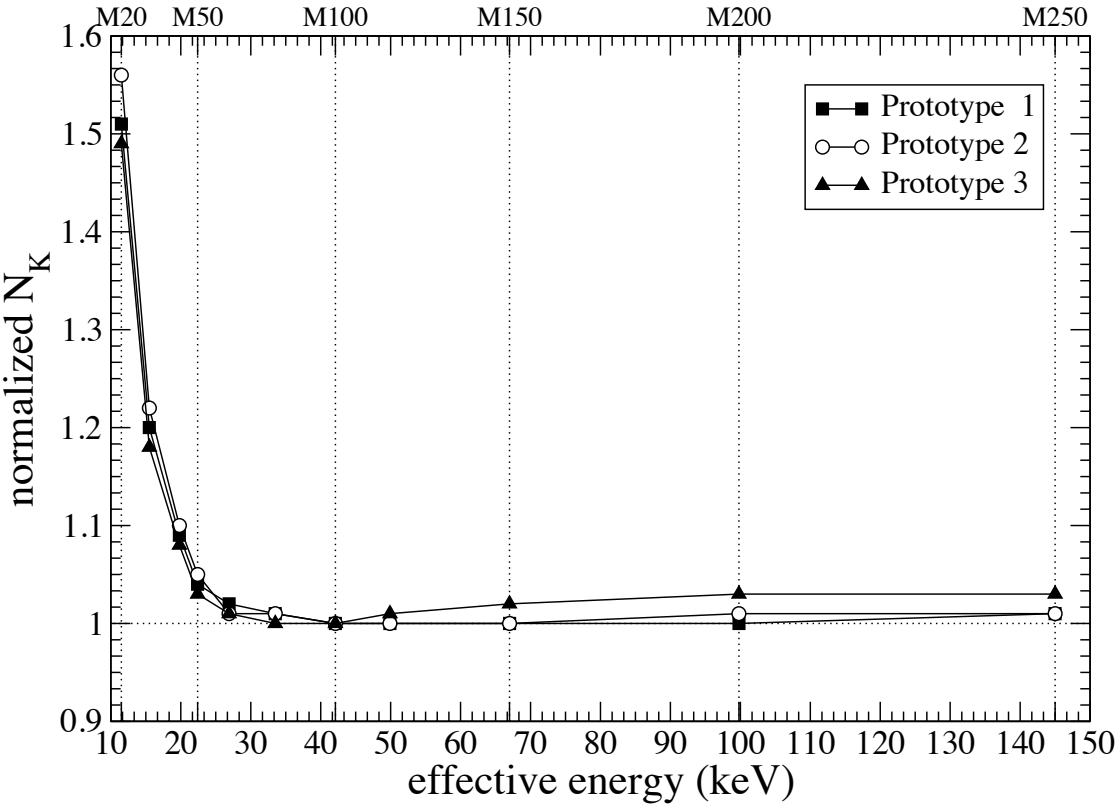

Figure 9.1: Normalized air-kerma calibration coefficients, N_K, measured with the optimized microchamber prototypes biased to +300 V (negative charge collection) for x-ray beams with effective energies ranging from (11.5 to 145) keV. The uncertainty at the k=2 level for the N_K measurements was 1.5%.

response remained fairly constant with respect to polarity for all volumes investigated, with a lack of trending in polarity effects.

9.3 Conclusions

An optimized microchamber was designed and manufactured from low-Z materials with electrodes composed from the same batch of improved plastic. Several of the anomalous

behaviors demonstrated by commercial chambers were reduced or eliminated. The optimized microchamber design demonstrated a variation in the chamber response of less than the TG-61 required 3% for x-ray beams ranging from 100 kV to 300 kV. Furthermore, the voltage-dependent polarity effects were significantly reduced and were constant for collecting volumes ranging from 0.018 cm^3 to 0.101 cm^3. In all cases, the inverse proportionality between chamber response and applied voltage was eliminated.

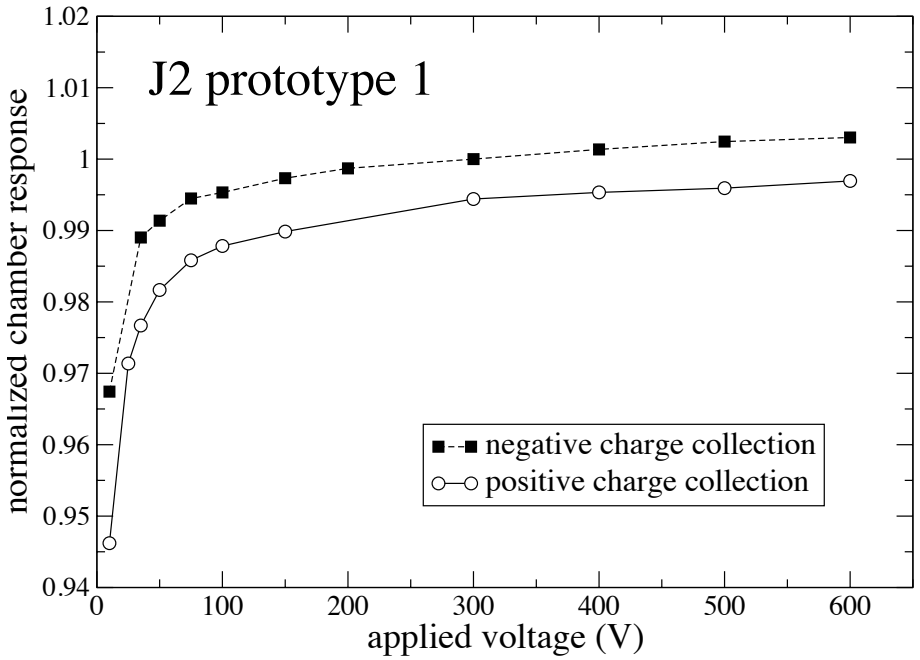

(a)

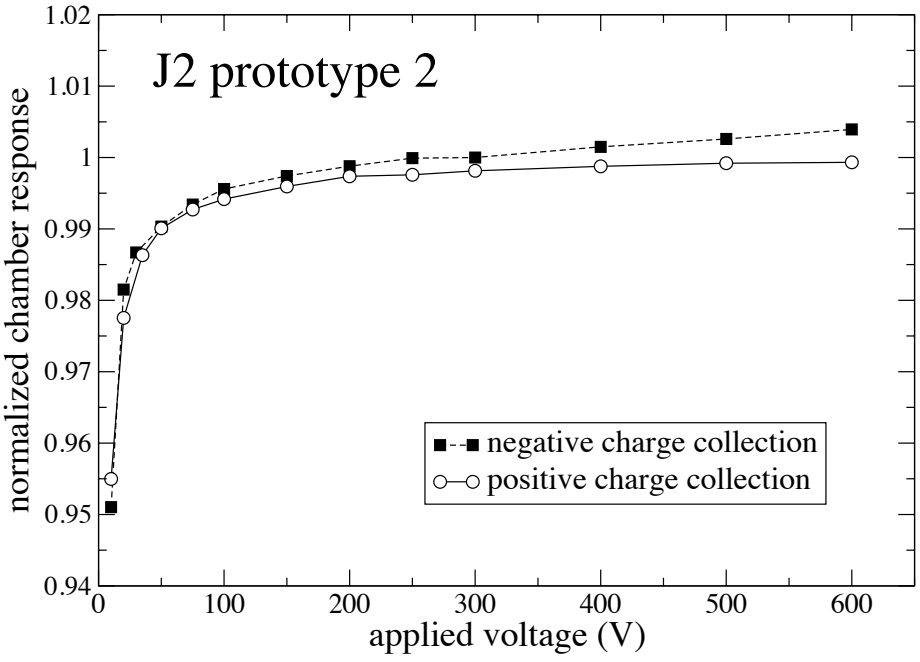

(b)

Figure 9.2: Normalized saturation curves measured with two optimized microchambers, (a) prototype 1 and (b) prototype 2. All data were normalized to the average signal received when the chamber was biased to a polarizing voltage of +300 V (negative charge collection).

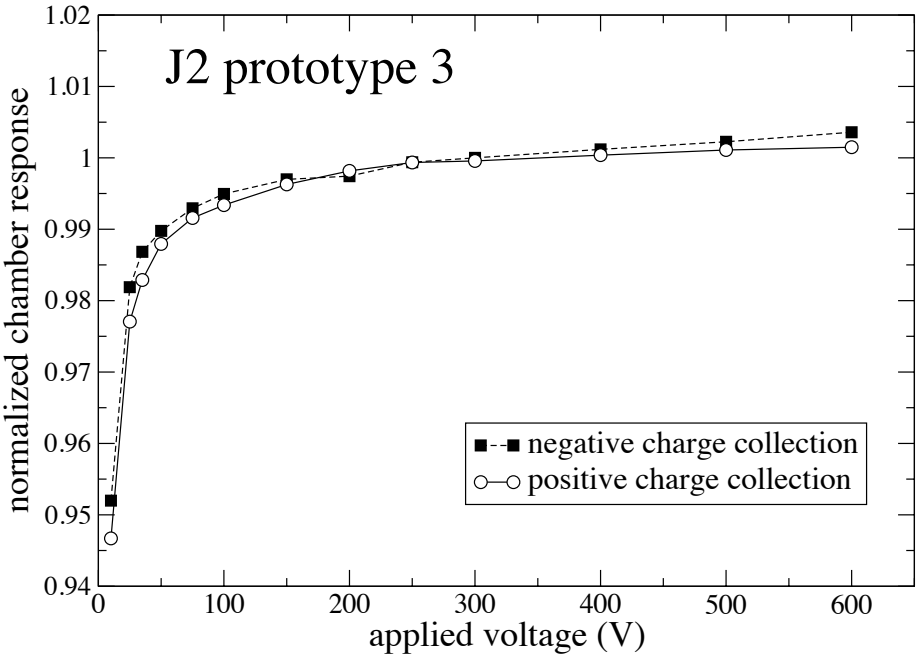

(a)

Figure 9.3: Same as Figure 9.2 except for the prototype 3 chamber.

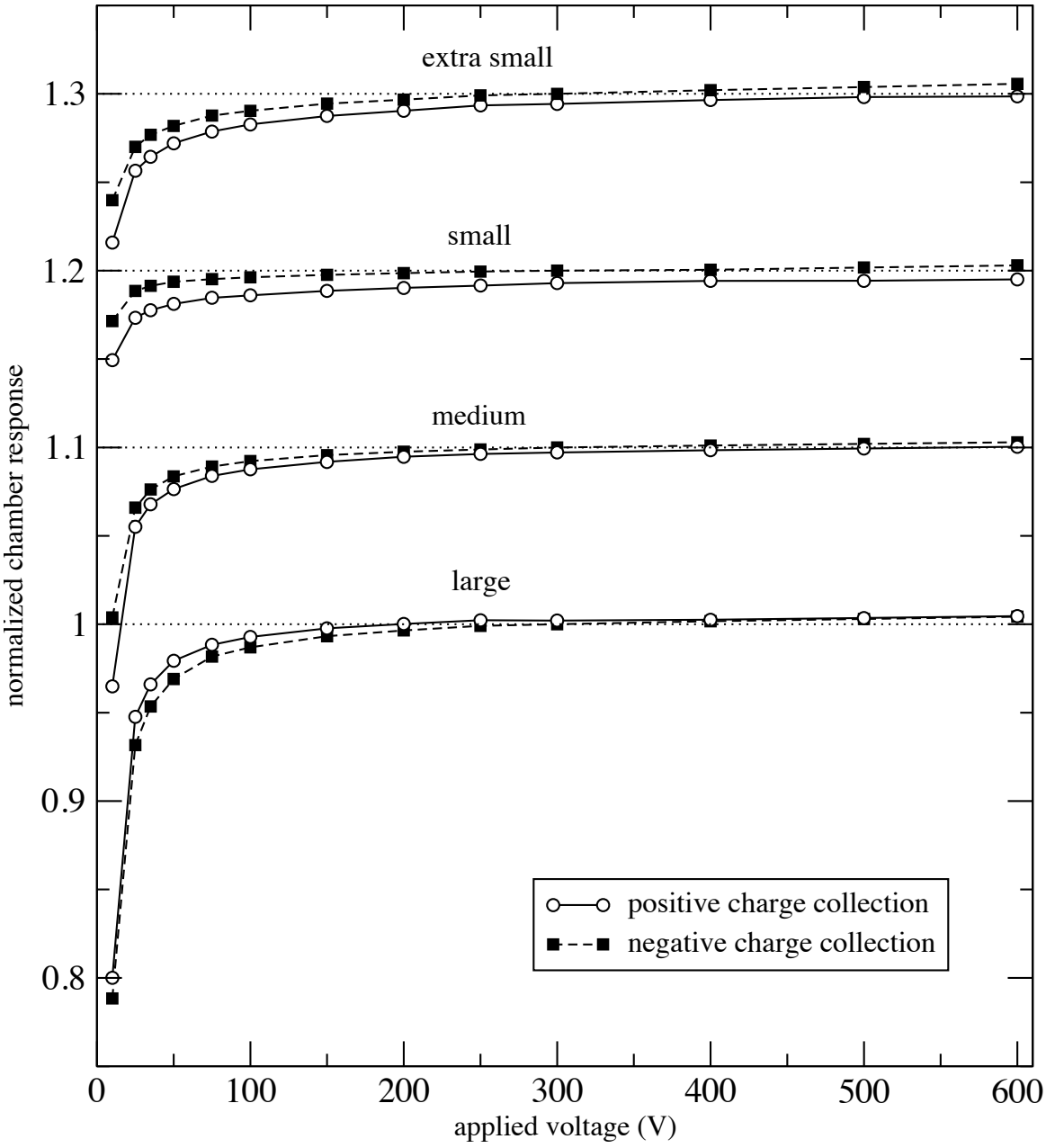

Figure 9.4: Normalized saturation curves measured with prototype 1 with varying shells sizes. All data were normalized to the average signal received when the chamber was biased to a polarizing voltage of +300 V (negative charge collection) for the corresponding shells size. The saturation curve are offset by 0.1 to allow for better visualization.

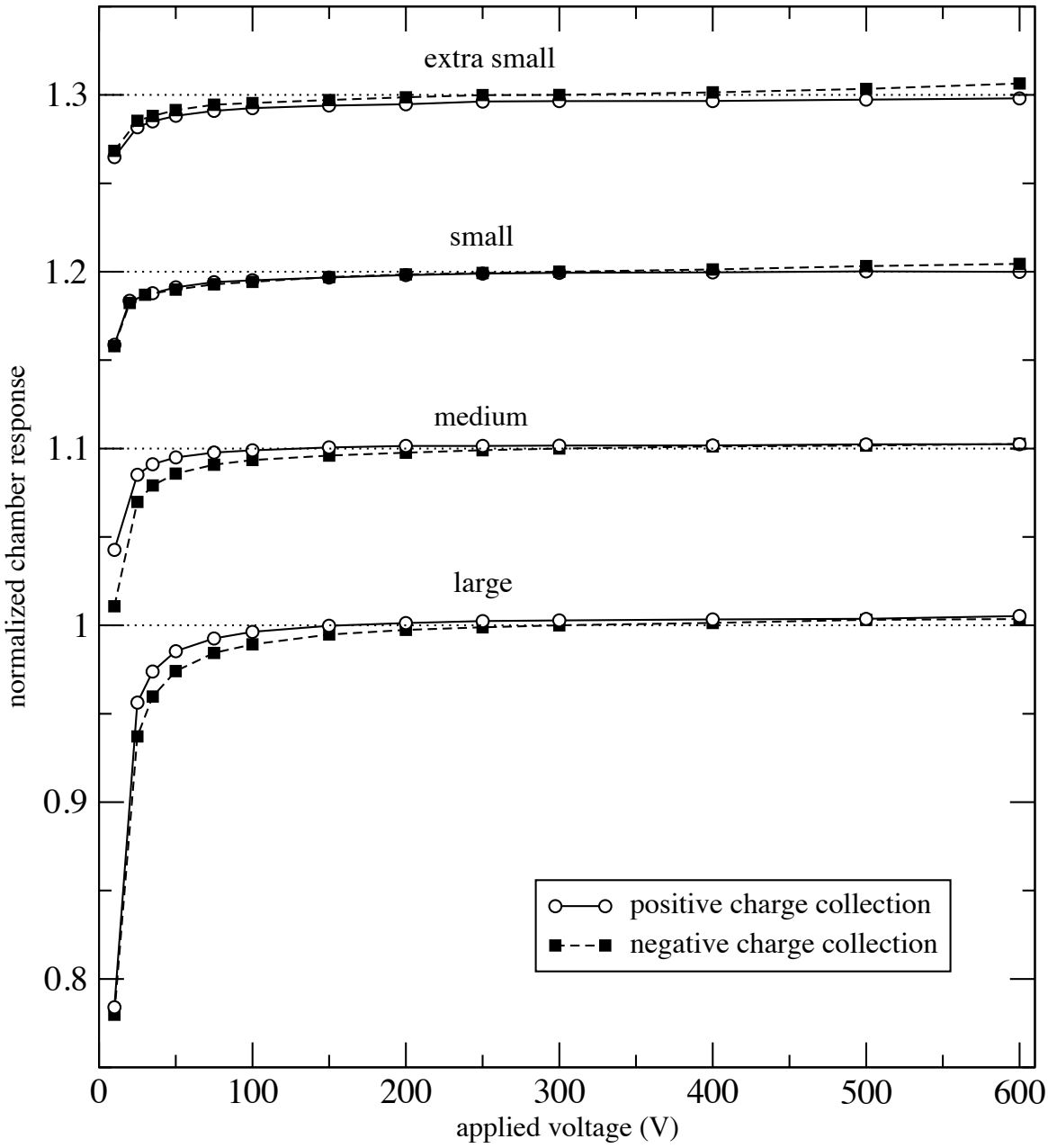

Figure 9.5: Same as Figure 9.4, except for prototype 2.

Chapter 10

Conclusions

10.1 Chamber characterization

Five microchamber models currently used in clinical radiation therapy dosimetry were characterized for photon beams ranging in energy from 11.5 keV to 10 MV. To benchmark the methodology used in this work against published data, as well as, to provide a reference for microchamber behavior, two Farmer-type chambers and one scanning chamber were also characterized. The behavior of each chamber was analyzed for leakage current, chamber response reproducibility and stability, voltage-dependent and independent polarity effects, ion recombination, exponential excess charge collection due to effects such as stem irradiation and charge multiplication, and energy dependence.

The leakage current of each chamber was monitored before and after each irradiation and maintained below 10 fA for all radiation beams investigated. For microchambers, 10 fA corresponded to less than 0.1% of the chamber signal for the high-energy pulsed beams, meeting the reference-class leakage requirement. For the ^{60}Co beam and the kilovoltage x-ray beam, 10 fA corresponded to a maximum of 0.25% and 0.5% of the chamber signal, respectively. However, the leakage current was often less than 10 fA and below 0.1% of the chamber signal for the ^{60}Co beam.

Once the chamber response stabilized, the average relative standard deviation in the chamber current over a given measurement set was 0.05%, 0.06%, 0.17% for the ^{60}Co beam, the high-energy pulsed beams, and the kilovoltage x-ray beam, respectively. Similarly, the reproducibility of the microchamber response at ±300 V was within 0.25%, 0.50%, and 1.2% for the ^{60}Co beam, the high-energy pulsed beams, and the kilovoltage x-ray beam, respectively. The increased variation in chamber response for the kilovoltage beam rendered the suitability of these microchambers uncertain for low- and medium-energy x-ray applications. Unlike with the higher-energy beams, the Farmer-type and scanning chambers also demonstrated reduced chamber response reproducibility for the kilovoltage x-ray beam. This variability was likely due to the decreased signal-to-noise ratio of chambers in low-dose-rate beams and the increased sensitivity to chamber dimensions and materials of low-energy beams.

The microchambers characterized in this work also exhibited significant voltage-dependent and independent polarity effects for all radiation beams investigated. Several microchamber models demonstrated voltage-dependent polarity effects large enough to induce an inverse proportionality between the chamber response and the applied voltage. The magnitude of these effects varied slightly with the energy of the beam, but the relative shape of the saturation curves remained consistent. It was also determined that while the behavior of the microchambers varied from chamber to chamber, even among the same model, the behavior of an individual chamber was consistent.

The P_{pol} values for the microchambers were generally greater than those of the scanning and Farmer-type chambers; however, several of the microchamber P_{pol} values were within the AAPM and reference-class recommended limits. In typical clinical situations where only these recommended limits are used to characterize chamber behavior, these reasonable P_{pol} values may be misleading. The low P_{pol} values suggest that the polarity correction factors can properly account for the chamber polarity effects; however, it was shown in this

work that for microchambers this may not be the case. The saturation curves demonstrated significant voltage-dependent differences in the magnitude of the saturation curves, which indicated the presence of an additional effect which P_{pol} may not account for correctly. Thus, P_{pol} values calculated for the applied voltage of interest alone are not sufficient to assess whether the polarity effects of the chamber are acceptable. A larger range of voltages should be measured for both polarities and the change in chamber response analyzed to deduce if the chambers meet reference-class dosimetry requirements.

During ion recombination calculations, excess charge collection due to exponential terms such as charge multiplication and stem effects were observed for the Exradin A1SL scanning chamber. The excess charge was present at low enough applied voltages to compete with ion recombination. It was demonstrated that the robust ion recombination correction technique, employing a fit of Equation 2.19 to the Jaffé plot, was beneficial for smaller volume chambers where exponential excess charge occurred. This would suggest that for well behaving microchambers, this method would be ideal for ion recombination correction. While several of the microchambers employing this method produced reasonable P_{ion} values, which were above unity and below 1.05, it was clear from the the saturation curves and Jaffé plots that voltage-dependent polarity effects prevented this robust method from accurately accounting for ion recombination. Thus, P_{ion} calculations alone are not sufficient to deduce the applicability of a microchamber. A full saturation curve must be measured for microchambers prior to reference-dosimetry measurements.

Furthermore, the expected increase in ion recombination with D_{pp} was demonstrated for the Exradin A12 Farmer-type chamber investigated, but not for the Exradin A14SL microchamber. The coefficients γ and δ for the Exradin A12 were in good agreement with the published values, and the Exradin A12 met each of the ion recombination requirements for a reference-class chamber. Conversely, the Exradin A14SL microchamber failed to meet any of ion recombination requirements. This investigation further demonstrated the need for

an understanding of the source of these voltage-dependent polarity effects in order to either account for them in dose calculations or eliminate them through optimized microchamber design.

Air-kerma calibration coefficients were measured for ^{60}Co and kilovoltage x-ray beams (with effective photon energies ranging from 11.5 keV to 145 keV) for all chambers characterized in this work. The chambers containing low-Z materials (Z$\leq$13) exhibited chamber responses with little dependence on the beam quality, independent of the size of the chamber. These chambers typically exhibited variations in calibration coefficients of less than 3% with the beam quality in the range of medium-energy beams. However, variations greater than 50% in N_{k} were found for all microchambers containing high-Z collecting electrodes (Z>13).

10.2 Behavior isolation

As a result of the chamber characterization investigation, it was determined that the prominent microchamber behaviors requiring resolution prior to reference-dosimetry measurements were the energy dependence and the voltage-dependent polarity effects. The voltage-dependent polarity effects were linked to many other anomalous behaviors such as the inverse proportionality between chamber response and applied voltage and the anomalous P_{ion} factors. Eliminating the voltage-dependent polarity effects would, therefore, likely eliminate these remaining anomalous behaviors

10.2.1 Energy dependence

To determine if the strong energy dependence exhibited by the microchambers was inherent to small-volume chambers or due solely to high-Z materials, a custom low-Z microchamber was manufactured. A layer of silver was coated onto the collecting electrode, and the chamber was characterized before and after the silver coating. The initial flat response of

the chamber (<3% variation) was altered significantly by the high-Z material. With the silver, variations in N_k increased from less than 3% to greater than 50%. These results demonstrated that the energy dependence of the microchambers is not inherent to small-volume chambers, but rather is a complex function of the material and relative dimensions of each component. Only the microchambers containing high-Z collecting electrodes showed significant variations in N_k with beam quality which were outside of the required TG-61 limits. As a result, it is recommended that only microchambers containing low-Z collecting electrodes be considered for reference dosimetry measurements in low- and medium- energy x-ray beams.

10.2.2 Voltage-dependent polarity effects

10.2.2.1 EGSnrc electric field simulations

To determine the cause of the voltage-dependent polarity effects, the effect of high-Z materials in the presence of strong electric fields was investigated through electric field/EGSnrc chamber simulations. First, the electric field and electric potential were modeled for several commercial ionization chambers using COMSOL Multiphysics software. The models were used to investigate electric field strengths and the potential for charge multiplication in a variety of chamber volumes. It was discovered that for microchambers, the small electrode separations induced electric fields strength of greater than 1000 V/mm over a significant portion of the collecting volume at clinically relevant applied voltages. At an electric field strength of 1000 V/mm, charge multiplication may occur.

Second, for the MC simulations, the EGSnrc source code was altered to account for the effects of external electric fields on charged-particle transport. The COMSOL-generated electric fields and electric potentials were imported into the modified EGSnrc source code. The charged particle transport in the presence of the electric field was benchmarked against published analytical calculations. The COMSOL models were shown to correctly model the

induced chamber fields. The modified EGSnrc source code was shown to accurately account for charge particle deflection and energy change in the external electric fields.

The benchmarked methodology was used to simulate the effects of high-Z materials and polarity at several applied voltages for a simplified Exradin A16 geometry in a water phantom. The voltage-dependent polarity effects demonstrated by this chamber in previous chapters was not modeled by the EGSnrc simulations. The simulated dose varied with the applied voltage and polarity; however, the trend in the voltage-dependent polarity effects demonstrated by the microchambers measurements in this work was not observed in the EGSnrc simulations. This suggests that either the current EGSnrc code does not account for or accurately model the processes causing the polarity effects investigated in this work, or the polarity effects are due to secondary charge particles created in chamber components which have energies below the energy threshold of the code. In either case, the source of the anomalous polarity effects for the microchambers investigated in this study was not identified through MC simulations.

10.2.2.2 Empirical behavior isolation

To empirically determine the cause of voltage-dependent polarity effects, a series of investigations were performed with five microchamber prototypes, called the J1 model, and two custom A2 larger-volume chambers. The J1 prototypes were identical in design. The A2 chambers were identical with the exception of the collecting electrode material: one chamber contained a collecting electrode composed of C552 plastic and the other of aluminum.

The experiments explored the effects of collecting volume size, stem and cable irradiations; chamber assembly; dirt, oil, and other contaminants; and high-Z materials on the chamber behavior. It was shown that the extent of the voltage-dependent polarity effects were inversely proportional to the collecting volume of the chamber. For the J1 model investigated, the polarity effects were negligible at the collecting volume of a typical scanning

chamber (0.06 cm^3). It was shown that stem and cable irradiations, chamber assembly, and contaminants did not alter the chamber behavior with respect to the voltage-dependent polarity effects.

To isolate the voltage-dependent polarity effects to an individual chamber component, the internal components of the chamber were swapped between two of J1 microchamber prototypes and between the two Exradin A2 chambers. For each chamber model: one chamber exhibited voltage-dependent polarity effects and one chamber did not exhibit this behavior. For the J1 microchamber, the voltage-dependent polarity effects were shown to significantly follow the guard insulator assembly, with a slight dependence on the collecting electrode. For the A2 chambers, the polarity-effects followed the aluminum collecting electrode. In both cases, the complete behavior of each chamber was entirely a function of the collecting electrode and guard electrode combination. This investigation suggested that the behavior of the chambers was significantly dependent on some quality of the combination of collecting and guard electrodes.

Both chamber models, the J1 microchamber and the Exradin A2 larger-volume prototype, demonstrated improved saturation curves with Electrodag® coated electrodes. In the case of the J1 prototypes, the voltage-dependent polarity effects were reduced by coating the top outer edge of the guard electrode. For the Exradin A2 prototype, coating the collecting electrode with graphite reduced the polarity effects. These results suggested that the polarity effects demonstrated by these chambers were caused by an inequality in the conductance of the guard and collecting electrode. In the case of the J1 prototypes, the lack of conductance was most likely a result of an inhomogeneous manufacturing process. In the case of the Exradin A2 chamber, the chamber displaying voltage-dependent polarity effects contained an aluminum electrode, opposed to C552 like the well behaving chamber. The aluminum collecting electrode was not treated during manufacturing and likely oxidized over time. This oxidation layer acted as a insulator reducing the bias of the surface of the

electrode. The reduction in the bias of the collecting electrode may have caused a potential difference between the guard and collecting electrodes.

A methodology to induce voltage-dependent polarity effects in a well behaving microchamber and Farmer-type chamber was explored by altering the bias of the guard electrode with respect to the collecting electrode. By altering the bias of the guard, voltage-independent and voltage-dependent polarity effects were introduced into the saturation curves for both chamber models. It was also demonstrated that a constant potential difference between the guard and collecting electrodes could cause voltage-dependent polarity effects, including the inverse proportionality between chamber response and applied voltage. This bias inequality has been shown to affect ionization chambers of varying collecting volumes; however, in this investigation, the polarity effects were an order of ten times greater for the microchamber compared to the Farmer-type chamber. The difference in polarity effects agreed well with the volume threshold investigation perviously discussed.

The voltage-dependent polarity effects in chamber response were also modeled with COMSOL simulations. A generic Farmer-type chamber and microchamber were modeled with the bias of the guard electrodes set to varying percentages of the bias of the collecting electrodes. The simulated collecting volumes varied significantly depending on the potential difference of the electrodes. For both chambers, reducing the bias of the guard electrode with respect to the collecting electrode increased the collecting volume. Similarly, increasing the bias of the guard electrode with respect to the collecting electrode, decreased the collecting volume. The change in the collecting volumes due to a potential difference between electrodes was approximately 10% greater for the microchamber compared to the Farmer-type chamber. These results again agreed well with the measured results of the previous investigations.

In summary, this work demonstrated three empirical investigations which support the theory that the potential difference between the collecting electrode and guard electrode is a

significant source of the voltage-dependent polarity effects for microchambers on the market today. These investigations also explain why the effects are only observed in chambers with small collecting volumes. The same potential difference between the electrodes will have a much smaller effect on a larger-volume chamber.

10.3 Design optimization

A microchamber prototype was designed and manufactured using the results of this work. To eliminate the dependence of the chamber response on the energy of the photon beam, the chamber electrodes were manufactured out of a low-Z plastic. To address the issue of voltage-dependent polarity effects and the inverse proportionality between chambers response and applied voltage, an effort was made to reduce the potential difference between the collecting and guard electrodes. By manufacturing all of the electrodes from the same batch of low-Z plastic, a reduction in the difference in conductance between the electrodes was achieved. Furthermore, the manufacturing methodology of the plastic was improved to increase a homogeneous conductance throughout the plastic.

The optimized microchamber prototype was characterized for photon beams ranging in energy from 25 keV to 1.25 MV. In all cases, the chamber response was flat for medium-energy x-ray beams relative to the ^{60}Co beam. The voltage-dependent polarity effects were also significantly reduced compared to the commercial microchambers investigated in this work. Furthermore, the inverse proportionality of the chamber response with the applied voltage was eliminated. While further characterization of these optimized chambers is necessary, the improvements made to the design and consequently the behavior of these microchambers provide a significant benchmark in microchamber dosimetry.

10.4 Future work

For the kilovoltage x-ray beam, the chambers of all sizes suffered from low chamber response reproducibility and significant polarity effects. These behaviors were not limited to microchambers, they were exhibited by the Farmer-type and scanning chambers characterized in this work. As a results, the application of ionization chambers for low- and medium-energy x-ray beams is in question. Further work is required to determine the cause of these effects as well as the limitations of these chambers for kilovoltage beams.

The simplified EGSnrc electric-field simulations did not model the voltage-dependent polarity effects under investigated in this work; however, a voltage-dependent difference in the simulated chamber response was observed with the incorporation of the corresponding electric fields. Even though the specific processes investigated in this work were not modeled, it is still important to investigate the processes that are accounted for in the modified EGSnrc source code. Further work could be done to investigate the ability of EGSnrc, with the incorporation of an external electric field, to improve the accuracy of ionization chamber simulations as well as to provide additional insight into the behavior of small-volume chambers.

Furthermore, it was determined that a potential difference between the collecting electrode and guard electrode produced voltage-dependent polarity effects for microchambers. An optimized microchamber design reduced these effects; however, further characterization with these optimized microchambers should be performed to ensure that the microchambers meet all of the reference-class requirements. Reference-class requirements which remain to be verified with the optimized microchamber include: the variation in P_{ion} with the D_{pp} of the beam, the chamber pre-irradiation effects, and the response reproducibility and stability. Additionally, alternative materials could be investigated to reduce microchamber polarity effects further with greater consistency. It is also possible that other effects are contributing to the polarity effects of microchambers, such as a net exchange of secondary

particles from the wall and collecting electrode. Once the voltage-dependent polarity effects due to potential differences between the guard and collecting electrodes are eliminated, a characterization of the microchambers will determine if further anomalous processes are altering microchamber behavior.

Once a microchamber design can be verified as meeting all reference-class requirements in standard radiation fields, the next step will be to use these chambers in small- and nonstandard-field measurements. With confidence in the accuracy of microchamber response, calibration coefficients, and correction factors, we will be one step closer to overcoming the challenges facing small- and nonstandard-field dosimetry.

Bibliography

W. Abdel-Rahman, J. P. Seuntjens, F. Verhaegen, and E. B. Podgorsak. Radiation induced currents in parallel plate ionization chambers: measurement and Monte Carlo simulation for megavoltage photon and electron beams. *Med. Phys.*, 33:3094–3104, 2006.

S. Agostinelli, S. Garelli, M. Piergentili, and F. Foppiano. Response to high-energy photons of PTW31014 PinPoint ion chamber with a central aluminum electrode. *Med. Phys.*, 35: 3293–3301, 2008.

J. H. Aitken and W. H. Henry. Spectra of the internally scattered radiation from large ^{60}Co sources used in teletherapy. *International Journal of Applied Radiation and Isotopes*, 15: 713–724, 1964.

X. Allen Li, C.-M. Ma, and D. Salhani. Measurement of percentage depth dose and lateral beam profile for kilovoltage x-ray therapy beams. *Phys. Med. Biol.*, 42:2561–2568, 1997.

X. Allen Li, L. Reiffel, J. Chu, and S. Naqvi. Conformal photon-beam therapy with transverse magnetic fields: A monte carlo study. *Med. Phys.*, 28:127–133, 2001.

P. R. Almond, P. J. Biggs, B. M. Coursey, W. F. Hanson, M. S. Huq, R. Nath, and D. W. O. Rogers. AAPM's TG-51 protocol for clinical reference dosimetry of high-energy photon and electron beams. *Med. Phys.*, 26:1847–1870, 1999.

F. H. Attix. *Introduction to Radiological Physics and Radiation Dosimetry.* Wiley-VCH, Weinheim, Germany, 2004.

M. Berg and O. Noerrevang. Recombination factors for the cylindrical FC65-G ionization chamber in pulsed photon beams and the plane-parallel roos ionization chamber in pulsed electron beams. *Phys. Med. Biol.*, 49:5309–5318, 2004.

M. J. Berger. *Methods in Computational Physics*, chapter Monte Carlo calculation of the penetration and diffusion of fast charged particles, pages 135–215. Academic, New York, 1963.

A. F. Bielajew. The effect of free electrons on ionization chamber saturation curves. *Med. Phys.*, 12:197–200, 1985.

A. F. Bielajew. *Monte Carlo Transport of Electron and Photons*, chapter Electron transport in E and B fields, pages 421–434. Plenum Press, New York, 1987.

A. F. Bielajew. The effect of strong longitudinal magnetic fields on dose deposition from electron and photon beams. *Med. Phys.*, 20:1171–1179, 1993.

J. W. Boag. Ionization measurements at very high intensities. *Br. J. Radiol.*, 23:601–611, 1950.

J. W. Boag. Space charge distortion of the electric field in a plane-parallel ionization chamber. *Phys. Med. Biol.*, 8:461–467, 1963.

J. W. Boag. Distortion of the electric field in an ionization chamber due to a difference in potential between guard ring and collector. *Phys. Med. Biol.*, 9:25–32, 1964.

J. W. Boag. The recombination correction for an ionization chamber exposed to pulsed radiation in a 'swept beam' technique. *Phys. Med. Biol.*, 27:201, 1982.

J. W. Boag and J. Currant. Current collection and ionic recombination in small cylindrical ionization chambers exposed to pulsed radiation. *Br. J. Radiol.*, 53:471–478, 1980.

J. W. Boag, E. Hochhäuser, and O. A. Balk. The effect of free-electron collection on the recombination correction to ionization measurements of pulsed radiation. *Phys. Med. Biol.*, 41:885–897, 1996.

J. W. Boag, K. R. Kase, B. E. Bjarngard, and F. H. Attix. *The Dosimetry of Ionizing Radiation*. New York: Academic, 1987.

J. W. Boag and T. Wilson. The saturation curve at high ionization intensity. *Br. J. Appl. Phys.*, 3:222–229, 1952.

J. Borg and D. Rogers. Spectra and air-kerma strength for encapsulated ^{192}Ir sources. *Med. Phys.*, 26:2441–2444, 1999.

G. Bruggmoser, R. Saum, A. Schmachtenberg, F. Schmid, and E Schule. Determination of the recombination correction factor k_S for some specific plane-parallel and cylindrical ionization chambers in pulsed photon and electron beams. *Phys. Med. Biol.*, 52:N35–N50, 2007.

L. A. Buckley and D. W. O. Rogers. Wall correction factors, P_{wall}, for thimble ionization chambers. *Med. Phys.*, 33:455–464, 2006.

J. E. Burns and K. E. Rosser. Saturation correction for the ne 2560/1 dosimeter in photon dosmietry. *Phys. Med. Biol.*, 35:687–693, 1990.

R. Capote, F. Sanchez-Doblado, A. Leal, J. I. Lagares, R. Arrans, and B. G. H. Hartmann. An EGSnrc Monte Carlo study of the microionization chamber for reference dosimetry of narrow irregular IMRT beamlets. *Med. Phys.*, 31:2416–2422, 2004.

F. Crop, N. Reynaert, G. Pittomvils, L. Paelinck, C. De Wagter, L. Vakaet, and H. Thierens. The influence of small field sizes, penumbra, spot size and measurement depth on perturbation factors for microionization chambers. *Phys. Med. Biol.*, 54:2951–2969, 2009.

F. DeBlois, C. Zankowski, and E. Podgorsak. Saturation current and collection efficiency for ionization chambers in pulsed beams. *Med. Phys.*, 27:1146–1155, 2000.

K. Derikum and M. Roos. Measurement of saturation correction factors of thimble-type ionization chambers in pulsed photon beams. *Phys. Med. Biol.*, 38:755–763, 1993.

L. DeWerd, S. Davis, L. Bartol, and F. Grenzow. Ionization chamber instrumentation, Proceedings of the AAPM Summer School, 2009. 181-204.

F. Di Martino, M. Giannelli, A. C. Traino, and M. Lazzeri. Ion recombination correction for very high dose-per-pulse high-energy electron beams. *Med. Phys.*, 32:2204–2210, 2005.

M. Ehrlich, S. M. Seltzer, M. J. Bielefeld, and J. I. Trombka. Spectrometry of a ^{60}Co gamma-ray beam used for instrument calibration. *Metrologia*, 12:169–179, 1976.

I. H. Ferreira, C. E. de Almeida, D. Marre, M. H. Marechal, A. Bridier, and J. Chavaudra. Monte Carlo calculations of the ionization chamber wall correction factors for ^{192}Ir and ^{60}co gamma rays and 250 kV x-rays for use in calibration of ^{192}Ir hdr brachytherapy sources. *Phys. Med. Biol.*, 44:1897–1904, 1999.

J. R. Greening. A contribution to the theory of ionization chamber measurements at low pressures. *British Journal of Radiology*, 27:163–170, 1953.

F. Grenzow. The wonderful world of electrometers, Oct. 2009.

J. M. Havercroft and S. C. Klevenhagen. Ion recombination corrections for plane-parallel and thimble chambers in electron and photon radiation. *Phys. Med. Biol.*, 38:25–38, 1993.

R. Hill, Z. Mo, M. Haque, and C. Baldock. An evaluation of ionization chambers for the relative dosimetry of kilovoltage x-ray beams. *Med. Phys.*, 36:3971–3981, 2009.

E. Hochhäuser and O. A. Balk. The influence of unattached electrons on the collection efficiency of ionisation chambers for the measurement of radiation pulses of high dose rate. *Physics in Medicine and Biology*, 31:223–233, 1986.

IEC, International Electrotechnical Commission. Medical electrical equipment. dosimeters with ionisation chambers as used in radiotherapy. *IEC Report No. 60731*, 1997.

P. N. Jeffery, J. W. Boag, and H. E. Johns. Electron avalanche amplification in x-ray imaging devices. *Phys. Med. Biol.*, 19:593–604, 1974.

T. M. Jenkins, T. M. Nelson, and A. Rindi. *Monte Carlo Transport of Electrons and Photons*. Plenum Press, 1988.

H. E. Johns, N. Aspin, and R. G. Baker. Currents induced in the dielectrics of ionization chambers through the action of high-energy radiation. *Radiat. Res.*, 9:573–588, 1958.

I. Kawrakow. Accurate condensed history monte carlo simulation of electron transport. i. egsnrc, the new egs4 version. *Med. Phys.*, 27:485–198, 2000a.

I. Kawrakow. Accurate condensed history Monte Carlo simulation of electron transport. II. Application to ion chamber response simulations. *Med. Phys.*, 27:499–513, 2000b.

I. Kawrakow and A. Bielajew. On the condensed history technique for electron transport. *Nuclear Instruments and Methods in Physics Research B*, 142:253–280, 1998.

I. Kawrakow, E. Mainegra-Hing, D. W. O. Rogers, F. Tessier, and B.R.B. Walters. The EGSnrc code system: Monte Carlo simulation of electron and photon transport. Technical Report PIRS-701, National Research Council, Ottawa, Canada, 2010. URL `http://irs.inms.nrc.ca/software/egsnrc/egsnrc.html`. see http://irs.inms.nrc.ca/software/egsnrc/egsnrc.html.

Inc. Keithley Instruments. Low level measurements handbook: Precision dc current, voltage, and resistance measurements, 2004. www.keithley.com.

Y. K. Kim, S. H. Park, H. S. Kim, S. M. Kang, J. H. Ha, C. E. Chung, S. Y. Cho, and J. K. Kim. Polarity effect of the thimble-type ionization chamber at a low dose rate. *Phys. Med. Biol.*, 50:4995–5003, 2005.

C. Kirkby, B. Murray, S. Rathee, and B. G. Fallone. Lung dosimetery in a linac-mri radiotherapy unit with a longitudinal magnetic field. *Med. Phys.*, 9:4722–4732, 2010.

C. Kirkby, T. Staneschu, S. Rathee, M. Carlone, B. Murray, and B. G. Fallone. Patient dosimetry for hybrid mri-radiotherapy systems. *Med. Phys.*, 35:1019–1027, 2008.

M. Kristensen. Measured influence of the central electrode diameter and material on the response of a graphite ionisation chamber to cobalt-60 gamma rays. *Phys. Med. Biol.*, 28:1269–1278, 1983.

S. F. Kry, R. Popple, A. Molineu, and D. S. Followill. Ion recombination correction factors (P_{ion}) for varian truebeam high-dose-rate therapy beams. *J. Appl. Clin. Med. Phys.*, 13: 318–325, 2012.

D. J. La Russa, M. McEwen, and D. W. O. Rogers. An experimental and computational investigation of the standard temperature-pressure correction factor for ion chambers and kilovoltage x rays. *Med. Phys.*, 34:4690–4699, 2007.

P. J. Lamperti and M. O'Brien. Nist measurement services: Calibration of x-ray and gamma-ray measuring instruments. NIST Special Publication 250-58, National Institute of Standards and Technology, Gaithersburg, Maryland, 2001.

P. Langevin. The recombination of ions in gases. *Comptes Rendus*, 134:533–536, 1902.

A. C. Lapsley. Effect of space charge on saturation properties of ionization chambers. *Rev. Sci. Instrum.*, 24:602–605, 1953.

M. Le Roy, L de Carlan, F. Delaunay, M. Donois, P. Fournier, A. Ostrowsky, A. Vouillaume, and J. M. Bordy. Assessment of small volume ionization chambers as reference dosimeters in high-energy photon beams. *Phys. Med. Biol.*, 56:5637–5650, 2011.

L. B. Leybovich, A. Sethi, and N. Dogan. Comparison of ionization chambers of various volumes for imrt absolute dose verification. *Med. Phys.*, 30:119–123, 2003.

C. Ma and A. E. Nahum. Effect of size and composition of the central electrode on the response of cylindrical ionization chambers in high-energy photon and electron beams. *Phys. Med. Biol.*, 38:267–290, 1993.

C.-M. Ma, C. W. Coffey, L. A. DeWerd, C. Liu, R. Nath, S. M. Seltzer, and J. P Seuntjens. AAPM protocol for 40–300 kV x-ray beam dosimetry in radiotherapy and radiobiology. *Med. Phys.*, 28:868–893, 2001.

C. Martens, C. De Wagter, and W. De Neve. The value of the PinPoint chamber for characterization of small field segments used in intensity-modulated radiotherapy. *Phys. Med. Biol.*, 45:2519–2530, 2000.

M. R. McEwen. Measurement of ionization chamber absorbed dose k_Q factors in megavoltage photon beams. *Med. Phys.*, 37:2179–2193, 2010.

M. R. McEwen, I. Kawrakow, and C. K. Ross. The effective point of measurement of ionization chambers and the build-up anomaly in MV x-ray beams. *Med. Phys.*, 35: 950–958, 2008.

G. M. Mora, A. Maio, and D. W. O. Rogers. Monte Carlo simulation of a typical ^{60}Co therapy source. *Med. Phys.*, 26(11):2494–2502, 1999.

B. R. Muir and D. W. O. Rogers. Monte carlo calculations of k_{Q}, the beam quality conversion factor. *Med. Phys.*, 37:5939–5950, 2010.

B. R. Muir and D W O Rogers. The central electrode correction factor for high-z electrodes in small ionization chambers. *Med. Phys.*, 38:1081–1088, 2011.

A. A. Nunn, S. D. Davis, J. A. Micka, and L. A. DeWerd. LiF:Mg,Ti TLD response as a function of photon energy for moderately filtered x-ray spectra in the range of 20 to 250 kVp relative to ^{60}Co. *Medical Physics*, 35:1859–1869, 2008.

T. O'Shea. *Monte Carlo Simulation of Medical Accelerator Electron Treatment Heads*. Ph.D. dissertation, National University of Ireland, Galway, Ireland, August 2011.

T. P O'Shea, J. F. Mark, and B. A. Faddegon. Accounting for the fringe magnetic field from the bending magnet in a monte carlo accelerator treatment head simulation. *Med. Phys,*, 38:3260–3269, 2011.

Å. Palm and O. Mattsson. Experimental study on the influence of the central electrode in farmer-type ionization chambers. *Phys. Med. Biol.*, 44:1299–1308, 1999.

H. Palmans, R. A. Thomas, S. Duane, E. Sterpin, and S. Vynckier. Ion recombination for ionization chamber dosimetry in a helical tomotherapy unit. *Med. Phys.*, 37:2876–2889, 2010.

D. W. O. Rogers, I. Kawrakow, J. P. Seuntjens, B. R. B. Walters, and E. Mainegra-Hing. Nrc user codes for egsnrc. Technical Report PIRS-702(rev B), National Research Council, Ottawa, Canada, 2003.

D. W. O. Rogers, I. Kawrakow, J. P. Seuntjens, B. R. B. Walters, and E. Mainegra-Hing. NRC User Codes for EGSnrc. *National Research Council*, 2011.

C. K Ross and K. R. Shortt. The effect of waterproofing sleeves on ionization chamber response. *Phys. Med. Biol.*, 37:1403–1411, 1992.

K. E. Rosser. Investigation of the chamber correction factor (k_{ch}) for the uk secondary standard ionization chamber (ne2561/ne2611) using medium-energy x-rays. *Phys. Med. Biol.*, 43:3195–3206, 1998.

J. W. Scrimger and D. V. Cormack. Spectrum of the radiation from a cobalt 60 teletherapy unit. *Br. J. Radiol.*, 36:514–521, 1963.

J. P. Seuntjens, C. K. Ross, K. R. Shortt, and D. W. O. Rogers. Absorbed-dose beam quality conversion factors for cylindrical chambers in high energy photon beams. *Med. Phys.*, 27:2763–2779, 2000.

T. Shimono, K. Koshida, H. Nambu, K. Matsubara, H. Takahashi, and Hiroshi Okuda. Polarity effect in commercial ionization chambers used in photon beams with small fields. *Radiol. Phys. Technol.*, 2:97–103, 2009.

V. G. Smyth and A. C. McEwan. Verification of a result of kristensen by Monte Carlo modeling. *Phys. Med. Biol.*, 29:1279–1282, 1984.

M. Stasi, B. Baiotto, G. Barboni, and G. Scielzo. The behavior of several microionizaton chambers in small intensity modulated radiotherapy fields. *Med. Phys.*, 31:2792–2795, 2004.

N. Takata and T. Sugita. Change in the number of ion pairs produced in free-air ionization chambers due to the applied electric field. *IEEE*, 2000.

F. Ubrich, J. Wulff, R. Kranzer, and K. Zink. Thimble ionization chambers in medium-energy x-ray beams and the role of constructive details of central electrode: Monte carlo simulations and measurements. *Phys. Med. Biol.*, 53:4893–4906, 2008.

M. Westermark, J. Arndt, B. Nilsson, and A. Brahme. Comparative dosimetry in narrow high-energy photon beams. *Phys. Med. Biol.*, 45:685–702, 2000.

J. A. Williams and S. K. Agarwal. Energy-dependent polarity correction factors for four commercial ionization chambers used in electron dosimetry. *Med. Phys.*, 24:785–790, 1997.

C. Zankowski and E. B. Podgorsak. Determination of saturation charge and collection efficiency for ionization chambers in continuous beams. *Med. Phys.*, 25:908–915, 1998.